UNIVERSITEIT VAN PRETORIA
UNIVERSITY OF PRETORIA
YUNIBESITHI YA PRETORIA

The Effect of Environmental Loading on Concrete Structures

by

KYLE SHAUN HAMBIDGE

Supervisor: Kearsley, Elsabe P.

Co-Supervisor: Skorpen, Sarah A.

A dissertation submitted in fulfilment of the requirements for the degree of

Masters of Engineering (Structural Engineering)

Department of Civil Engineering
Faculty of Engineering, Built Environment, and Information Technology
University of Pretoria

2024

UNIVERSITY OF PRETORIA

Abstract

Faculty of Engineering, Built Environment, and Information Technology

Department of Civil Engineering

Masters of Engineering

The Effect of Environmental Loading on Concrete Structures

by KYLE SHAUN HAMBIDGE

This study investigates the thermal and mechanical behaviour of concrete elements under environmental loading, with a focus on South African aggregates - dolerite and dolomite. As South Africa transitions to adopting *EN1992-1-1: Design of Concrete Structures (2004)*, understanding the applicability of international standards to local materials and climatic conditions is critical. The concrete structures in the region are exposed to significant thermal variations, solar radiation, and drying conditions, inducing temperature gradients, shrinkage, and thermal stresses. An experimental programme was conducted, featuring concrete elements of three shapes, cube, flange, and L-section, cast with dolerite and dolomite aggregates. Thermocouples and vibrating wire strain gauges were used to monitor temperature and strain over a three-month winter period, while material characterisation tests determined key thermal and mechanical properties. Finite element models developed in ABAQUS/CAE (2023) were calibrated using experimental data to refine thermal conductivity and solar absorptivity values. Sensitivity analyses evaluated the effects of thermal properties on effective temperatures, temperature gradients, and thermal strains. The results show that aggregate type had a limited influence on thermal and shrinkage responses. Dolomite mixes, with higher thermal conductivity and solar absorptivity, experienced slightly greater temperature variations, while Dolerite mixes showed steeper gradients but lower stress development due to reduced thermal expansion, modulus of elasticity, and conductivity. Geometry also affected strain and stress distributions, with L-sections exhibiting higher residual stresses under environmental loading. These findings highlight the need to calibrate *EN1992-1-1* assumptions for local materials and conditions. The study recommends developing standardised thermal property tests for South African aggregates and incorporating calibrated material properties into structural design models.

Declaration of Authorship

I, KYLE SHAUN HAMBIDGE, declare that the dissertation, which I hereby submit for the degree *Masters of Engineering* at the University of Pretoria, is my own work and has not previously been submitted by me for a degree at this or any other tertiary institution. I did not refer to work of current or previous students, lecture notes, handbooks or any other study material without proper referencing. Where other people's work has been used this has been properly acknowledged and referenced

Signed:

Date:

Acknowledgements

I would like to express my deepest gratitude to the individuals and organisations who contributed to the success of this research.

Academic Mentorship:

- Professor Elsabe Kearsley, my supervisor, for her invaluable guidance, time, and effort throughout this journey. Her mentorship has been pivotal in shaping the success of this study.
- Dr. Sarah Skorpen, my co-supervisor, is acknowledged for her insightful guidance and expertise, which greatly enriched this research.

Family Support:

- To my family, for their never-ending support, patience, and encouragement. Your belief in me has been my anchor through this challenging yet rewarding process.

Senior Postgraduate Colleagues:

- Ms. Amé Kleynhans for her unwavering support, late nights of work, and always being available to help.
- Mr. Jurie Adendorff, for his valuable advice and assistance with the physical experiments.
- Mr. Daniel Rademan, for his dedicated laboratory assistance and continuous support.

University Laboratory Staff:

- Mr. Johan Scholtz, for his time, effort, and willingness to accommodate last-minute changes.
- Mr. Jordan Mostert, for his technical expertise and assistance.

Concrete Laboratory Staff:

- Mr. Richard Ncabeleng, Mr. Chris Baloyi, Mr. Kgwara Mokomane, Mr. Jonas Selwadi, and Mr. Frank Vein, for their invaluable help with preparations and casting.

Research Funding:

- The South African National Roads Agency (SANRAL), for supporting this study as part of the broader SANRAL research initiative.

Thank you to everyone who played a part in this journey; your support and contributions will always be remembered with gratitude.

Contents

List of Figures

List of Tables

List of Abbreviations

AOD	Aerosol Optical Depth
BEM	Boundary Element Method
CTE	Coefficient of Thermal Expansion
CV	Coefficient of Variability
EBT	Effective Bridge Temperature
FDM	Finite Difference Method
FEA	Finite Element Analysis
FEM	Finite Element Method
IQR	Interquartile Range
MBE	Mean Bias Error
NRMSE	Normalised Root Mean Square Error
PDF	Probability Density Function
PSD	Particle Size Distribution
RD	Relative Density
RH	Relative Humidity
RMSE	Root Mean Square Error
VWSG	Vibrating Wire Strain Gauge

List of Symbols

$\alpha_{c,wi}$	Coefficient of thermal expansion in week i
α_c	Coefficient of thermal expansion
α_d	Thermal diffusivity
$\alpha_{\text{ds1}}, \alpha_{\text{ds2}}$	Coefficients dependent on cement type *
A_c	Cross-sectional area of the concrete element
A_d	Optical depth
A_i	Area associated with sensor i
A_m	Optical air mass
a_r	Solar reflectivity
a_s	Absorptivity of the concrete surface
β	Tilt angle of the surface relative to the horizontal plane
$\beta_{as}(t)$	Time-dependent factor for autogenous shrinkage *
β_{RH}	Relative humidity adjustment factor *
$\beta_s(t, t_s)$	Time-dependent factor for drying shrinkage *
B	Vibrating wire strain gauge calibration factor
C_0	Stefan-Boltzmann constant
C_1	Coefficient of thermal expansion for the vibrating wire strain gauge
C_{lux}	Conversion factor from lux to W/m^2
c_i	Specific heat of specimen at temperature T_i, $i = 1, 2$
c_p	Specific heat capacity
c_{cal}	Heat capacity of calorimeter
c_{concrete}	Specific heat capacity of concrete
c_{water}	Specific heat capacity of water
Δ	Relative prediction metric
ΔT	Temperature difference
ΔT_{eff}	Change in effective temperature
Δx	Thickness of the material
δ	Solar declination angle
e	Emissivity of the concrete surface
e_C	Euler's constant
E	Young's modulus of concrete
E_{cm}	Mean elastic modulus *
$f(x, y)$	Initial temperature distribution
$f(x_T)$	Temperature distribution probability density
f_{ck}	Characteristic compressive strength *
f_{cm}	Mean cylinder compressive strength of concrete *
$f_{cm,cube}$	Mean cube compressive strength *
f_{cmo}	Reference compressive strength *
$f_{ctk,0.05}$	5% fractile characteristic tensile strength *
f_{ctm}	Mean tensile strength of concrete *
F_{wb}	Sky angle factor

F_{wd}	Ground angle factor
G_{sc}	Solar constant
γ	Difference between solar azimuth angle and surface azimuth angle
h_0	Notional member size *
h_c	Convective heat transfer coefficient
I_{BH}	Beam radiation on a horizontal surface
I_{BT}	Beam radiation on a tilted surface
I_{Beam}	Direct beam radiation component
I_{DH}	Diffuse radiation on a horizontal surface
I_{DT}	Diffuse radiation on a tilted surface
$I_{Diffuse}$	Scattered Diffuse radiation component
I_G	Ground reflectance radiation on a tilted surface
$I_{GroundReflected}$	Reflected ground radiation component
I_{lux}	Light intensity (weather station)
I_{measured}	Measured solar radiation (weather station)
I_{sc}	Extraterrestrial solar radiation
I_{Total}	Total incident solar radiation
$I_{Total,\beta=0}$	Total radiation on the top surfaces
$I_{Total,\beta=90}$	Total radiation on north-facing surfaces
$I_{Total,Reflected}$	Total radiation on the bottom and south-facing surfaces
k	Thermal conductivity of material
$k_b t_c$	Heat diffused to the environment
k_h	Coefficient related to the notional member size *
$k_{insulation}$	Thermal conductivity of insulating material
k_{td}	Diffuse fraction
k_v	Vaporisation heat of water
K_t	Clearness index
λ	Solar azimuth angle
λ_s	Surface azimuth angle
m_1	Mass of the concrete specimen
m_b	Mass of vaporised water
m_{concrete}	Mass of the concrete cube
m_{water}	Mass of liquid water
μ	Mean temperature
n_s	Total number of sensors in the concrete shape
N	Day of the year (1–365)
q	Applied heat flux
q_c	Convective heat flux
q_l	Long-wave radiation component
q_s	Short-wave radiation component
q_t	Total heat flux on boundaries
Q_1	Heat released by the hot specimen during the range B–C
Q_2	Heat absorbed by the liquid water
Q_3	Heat carried by vaporized water
Q_4	Heat diffused to the environment
RH	Ambient relative humidity *
RH_0	Reference relative humidity *

ϕ	Local latitude
s	Standard deviation of sample group
S	Slope of AB and CD
$\sigma_{1,\,\text{Cube}}$	Residual stress in Cube section
$\sigma_{1,\,\text{Flange}}$	Residual stress in Flange section
σ_{residual}	Residual stress
σ_{thermal}	Thermal stress
τ_B	Beam transmission coefficient
θ	Solar incident angle
θ_z	Solar zenith angle
T	Temperature at any point within the material
T_0	Initial water temperature
T_1	Initial temperature of specimen
T_2	Maximum achieved system temperature
T_a	Ambient temperature
T_b	Temperature of boiling water
T_i	Temperature recorded by sensor i
T_n	Initial vibrating wire strain gauge temperature reading
T_{n+1}	Subsequent vibrating wire strain gauge temperature reading
T_{concrete}	Initial concrete temperature
T_{eff}	Effective temperature of concrete shape
T_{peak}	Peak system temperature
T_{water}	Initial water temperature
$T_{t=0}$	Initial temperature distribution, varying with x and y coordinates
T_{s}	Surface temperature
T_{bottom}	Bottom sensors temperature reading
T_{top}	Top sensors temperature reading
T_{wi}	Measured temperature for week i
t	Age of concrete
t_s	Age of concrete at which drying begins *
t_{bc}	Duration of range BC
t_{solar}	Solar time
t_{n+1}, t_n	Successive time intervals
t_n	Initial time interval
t_{n+1}	Subsequent time interval
u	Perimeter of the section exposed to drying
v	Wind speed
w	Hour angle of the sun
x_T	Temperature value for probabilistic density
$\varepsilon_{\text{apparent}}$	Measured VWSG strain (not temperature compensated)
ε_{ae}	Adjusted EN1992-1-1 2004 ultimate drying shrinkage strain
ε_{ca}	Autogenous shrinkage strain *
$\varepsilon_{\text{ca}}(t)$	Predicted autogenous shrinkage strain at time t *
$\varepsilon_{\text{ca}}(\infty)$	Ultimate autogenous shrinkage strain *
$\varepsilon_{\text{cd},0}$	Ultimate drying shrinkage strain *
ε_{cd}	Drying shrinkage strain *
$\varepsilon_{\text{cd}}(t)$	Predicted drying shrinkage strain at time t *
ε_{cs}	Total shrinkage strain *

$\varepsilon_{cs,calc}$	Calculated shrinkage strain
$\varepsilon_{cs,obs}$	Measured shrinkage strain
$\varepsilon_{elastic}$	Elastic strain, reversible upon unloading
$\varepsilon_{Flange\ Effect}$	Strain component attributed to the presence of the Flange
$\varepsilon_{Free\ Cube}$	Measured residual strain in the standalone cube
$\varepsilon_{L\text{-}Shape\ Cube}$	Measured residual strain in L-shaped cube
$\varepsilon_{residual}$	Residual strain
$\varepsilon_{true,\ temp}$	Measured VWSG strain (temperature compensated)
ε_{28}	Shrinkage strain 28 days post casting
$\varepsilon_{0,wi}$	Baseline strain intercept for week i
ε_{creep}	Creep strain
$\varepsilon_{measured}$	Total measured strain
$\varepsilon_{measured,cyl}$	Measured strain in concrete cylinders
$\varepsilon_{measured,wi}$	Measured strain for week i
$\varepsilon_{shrinkage}$	Shrinkage strain
$\varepsilon_{shrinkage,cyl}$	Shrinkage strain in the cylinders
$\varepsilon_{shrinkage}(t)$	Predicted shrinkage (adapted from EN1992-1-1 2004)
$\varepsilon_{thermal}$	Thermal strain
$\varepsilon_{thermal,cyl}$	Thermal strain in the cylinders

Note: Symbols marked with (*) are derived from EN1992-1-1 2004.

1 Introduction

1.1 Background

South Africa's adoption of *EN1992-1-1 (2004a)* for concrete structure design represents a significant step toward aligning with international best practices. However, this shift requires assessing the applicability of the standard to local conditions, particularly for reinforced concrete elements exposed to unique environmental and material challenges in South Africa. While *EN1992-1-1 (2004a)* provides guidelines on parameters such as thermal gradients, shrinkage, and restricted deformation, its direct application in South Africa requires careful consideration of local materials, aggregate properties, and environmental loads.

Concrete structures in South Africa are exposed to extreme climatic conditions, including intense solar radiation, significant fluctuations in the diurnal temperature, and seasonal extremes. These conditions induce temperature gradients within concrete elements, which result in thermal stresses that can cause cracking, reduced durability, and compromised structural integrity. Although *EN1992-1-1 (2004a)* accounts for such effects, it assumes specific material properties and environmental conditions that may not fully reflect the South African context.

The variability of aggregate materials, such as Dolerite and Dolomite, significantly influences the thermal properties of concrete, including its conductivity, coefficient of thermal expansion, and shrinkage characteristics. This variability requires a deeper understanding of how these properties affect concrete's response to environmental loading and its structural performance.

The adoption of *EN1992-1-1 (2004a)* emphasises the importance of predicting and mitigating thermal stresses and shrinkage effects during the design stage, particularly in restrained concrete elements, those where deformation due to thermal effects or shrinkage is restricted by external or internal factors. These restrictions induce internal stresses and strains that, if not properly managed, can lead to cracking and reduced durability. This challenge is amplified in concrete elements with complex geometries, such as T-beams, as shown in Figure 1.1. T-beams, commonly used in bridge decks and similar structures, are valued for their bending and shear resistance while remaining cost-effective. However, their geometry, specifically the flange and beam sections, introduces additional complexity in terms of thermal response. The flange, being more exposed to thermal loading, experiences greater temperature variations and drying compared to the deeper web section.

This differential thermal expansion, coupled with geometric constraints at the junction of the two sections, can lead to stress concentration and cracking. Therefore, understanding how environmental loads, material properties, and structural geometry interact in such configurations is essential to ensure that design decisions adequately mitigate these risks without resulting in overly conservative designs that could increase costs or impair structural performance.

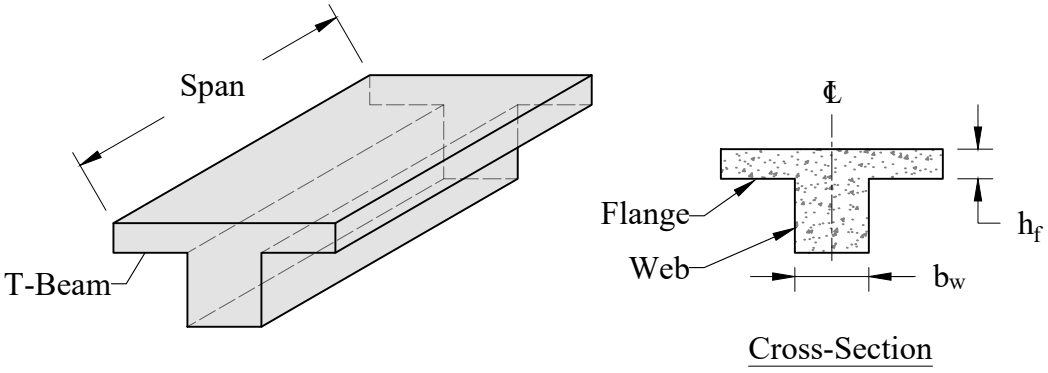

Figure 1.1: Typical cross-section of a concrete T-beam.

The growing focus on sustainability and the impacts of climate change further amplify the need for resilient, energy-efficient structures. As extreme temperature variations and other environmental stresses continue to intensify, particularly in regions such as South Africa, incorporating these considerations into structural design becomes increasingly vital. Understanding the thermal behaviour of concrete, especially in complex geometries such as T-beams, is therefore crucial not only to mitigate immediate risks such as cracking and loss of durability but also to ensure long-term sustainability and performance of the infrastructure. By addressing these challenges, engineers can design structures that are both resilient to climate impacts and efficient in their use of materials, aligning with the broader goals of sustainability in civil engineering.

Objectives of the Study

The overarching goal of this study is to investigate the thermal and mechanical behaviour of concrete elements with varying material properties under environmental loading. The research focuses on understanding and quantifying the effects of thermal loading, material-specific properties, and environmental conditions on structural performance. The specific objectives of the study are as follows:

Primary Objectives:

1. To assess the applicability of *EN1992-1-1* (2004a) to local environmental conditions and material properties in South Africa.
2. To investigate the effect of the shape of the concrete element on thermal behaviour.
3. To analyse the development of stress in concrete elements under environmental loading.
4. To compare the thermal properties of concrete mixes made with distinct aggregate types and assess their influence on thermal behaviour.

Secondary Objectives:

1. To predict solar radiation on tilted concrete surfaces.
2. To predict concrete shrinkage using the *EN1992-1-1* (2004a) shrinkage model.
3. To calibrate the finite element model for thermal properties using experimental data.

By addressing these objectives, this study aims to improve the understanding of how material properties and environmental loads influence the performance of concrete elements, thus supporting regionally relevant and effective structural design practices.

Scope and Limitations of the Study

This study focuses on the thermal and mechanical behaviour of concrete elements subjected to environmental loading, with particular attention to the properties of the material and their influence on structural performance. The scope and limitations of the study is defined as follows:

- **Vertical Temperature Gradients:** The investigation focuses on vertical temperature gradients along the centre lines of concrete elements. Effective temperatures, calculated as weighted averages of temperature readings at various heights, are used to assess the global deformation behaviour of cross-sections. This approach provides a simplified but representative measure of the thermal response of the elements, aligning with typical design code practices.
- **Concrete Specimens and Mixes:** Concrete specimens were cast using two types of South African aggregates: Dolerite and Dolomite. Four concrete elements were prepared for this study: Cylinder, Cube, Flange, and L-Shape (see Figure 1.2). Only one specimen of each geometry was cast per mix due to practical constraints related to time, cost, and resources.
- **Material Properties Testing:** Mechanical properties, specific heat capacity, and the coefficient of thermal expansion were determined through laboratory testing. The specific heat capacity was measured using a single 150mm cube per mix. Although this approach does not capture potential variability within a mix, it was chosen due to the controlled nature of laboratory conditions and the assumption of homogeneity. The results are considered reliable for finite element model calibration, as the study focuses on comparing material performance rather than minor within-mix variations.
- **Experimental Duration and Data Collection:** Temperature and strain data were collected over a three-month winter period in South Africa. This timeframe was chosen to eliminate variability due to seasonal effects. The thermal properties of the concrete were assumed to remain constant during this period and were verified using finite element models. Instrumentation included thermocouples for temperature measurements, Vibrating Wire Strain Gauges (VWSGs) for strain measurements, and a weather station for real-time ambient data on temperature, humidity, wind speed, and solar radiation.
- **Numerical Analysis and Calibration:** Thermal conductivity and solar absorptivity were calibrated using measured experimental data, with a focus on transient thermal responses. The finite element model was used to verify the consistency of thermal properties over the experimental period and across different element shapes.

- **Strain Considerations:** Only unrestrained strains are considered, focusing on drying shrinkage, thermal expansion, and residual strains. All cast elements were free to expand and contract, as restrained elements would not produce measurable strains. If the elements were restrained, internal stresses would develop due to restricted movement, but no deformation would be measurable. Reinforced concrete, which introduces additional constraints due to reinforcement, is not considered in this study. Creep behaviour is excluded from the analysis.
- **Limitations of Sample Size:** Given the small sample size (one specimen per geometry and mix), the findings provide indicative rather than statistically significant results. The study aims to highlight general trends in thermal and mechanical behaviour, rather than to offer definitive conclusions about variability within each mix. Although the consistency of experimental conditions improves reliability, the results should be interpreted with caution when considering broader applications.
- **Exclusion of Relative Humidity in Shrinkage Calculations:** Although Relative Humidity (RH) was recorded, it was not explicitly considered in shrinkage calculations due to its significant fluctuations over time. While RH can influence shrinkage, this study primarily focuses on temperature-driven deformation and the effects of different aggregate types. Practical engineering approaches typically rely on averaged RH values rather than real-time variations, making its direct inclusion unnecessary. The results are assumed to be applicable under similar RH conditions, and future studies could assess RH sensitivity in more detail.

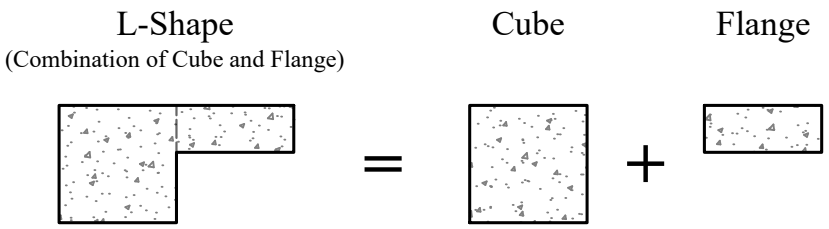

Figure 1.2: Experimental shapes used in the study: Cube, Flange, and L-Shape.

This study ensures a focused investigation into the thermal and mechanical behaviour of concrete elements under environmental loading, emphasising the properties of the material, the environmental effects, and their implications for structural performance.

1.2 Methodology

This study used a combined experimental and numerical approach to investigate the thermal and mechanical responses of concrete elements under environmental loading. The methodology was designed to assess the influence of the type of aggregate, the geometry of the elements, and the environmental conditions on the distribution of temperature and the development of stress.

The L-Shape was chosen as a combination of a cube and a flange to isolate the individual contributions of each component (Figure 1.2). The Cube, Flange, and L-Shape elements were used to investigate the effect of element geometry on thermal behaviour, while the Cylinder was used to model shrinkage and determine the coefficient of thermal expansion.

The dimensions of the L-Shape, Cube, and Flange elements were selected to ensure they all had the same span length. The depth of the Cube and Flange elements was varied, while the width and span length (extending into the page from Figure 1.2) remained constant. This ensured consistency in geometric parameters for comparative analysis. The L-Shape was chosen over a full T-beam to avoid the complexity of symmetrical deformations, which would be difficult to measure accurately. Using an L-shape, the contributions of the flange and beam sections were isolated for a focused analysis of their thermal and shrinkage behaviour. Additionally, the support conditions allowed for free expansion and contraction, as full restraint is difficult and would yield measurable strains. The Cube was designed as a simple cubic shape to simplify the study under the assumption that thermal transfer occurs primarily in the vertical direction.

Instrumentation included thermocouples for temperature measurements and VWSG for strain measurements. A weather station provided real-time data on ambient conditions such as temperature, humidity, wind speed, and solar radiation, which were used to calculate effective temperatures and thermal gradients.

Mechanical and thermal properties, including compressive strength, modulus of elasticity, coefficient of thermal expansion, and specific heat capacity, were determined by laboratory testing. Smaller representative samples, including water-cured samples, were used for mechanical property testing and determination of the specific heat capacity.

In ABAQUS/CAE (2023) , a finite element-based heat transfer model was developed to simulate the thermal behaviour of concrete elements. This model incorporated experimental data for calibration and validated thermal properties over the 3-month period. The focus was on simulating transient thermal responses and thermal gradients, excluding long-term deformation mechanisms such as creep.

1.3 Structure of the Thesis

This thesis is structured to provide a logical progression of the study, from establishing the research context and objectives to presenting experimental results, material properties, environmental data, numerical modelling, and their application to strain and stress analysis. Each chapter builds upon the findings of the previous chapters to ensure a cohesive narrative.

- **Chapter 1: Introduction** Establishes the research problem, objectives, and scope of the study, highlighting the importance of understanding the thermal and mechanical responses of concrete under environmental conditions, with a focus on South African aggregates and winter exposure.
- **Chapter 2: Literature Study** Reviews existing knowledge on the thermal and mechanical properties of concrete, the impact of environmental loading, and the gaps in current design practices, providing the foundation for experimental and numerical work.
- **Chapter 3: Experimental Investigation** Details the experimental methodology, including sample preparation, sensor placement, and environmental exposure, forming the framework for data collection and analysis.
- **Chapter 4: Material Results** Presents experimentally determined material properties, used as input for numerical modelling.
- **Chapter 5: Environmental Loading and Thermal Response** Analyses of environmental conditions, vertical temperature gradients, effective temperatures, and adjustments to the *EN1992-1-1 (2004a)* shrinkage model.
- **Chapter 6: Calibration and Sensitivity Analysis** Explores FEA model calibration using material properties and environmental data, with sensitivity analyses of thermal conductivity and solar absorptivity.
- **Chapter 7: Stress Results** Evaluates strain and stress development, highlighting temperature-strain relationships and structural performance implications under environmental loading.
- **Chapter 8: Conclusions and Recommendations** Summarises findings, emphasising the importance of material properties and environmental loading in design, and offers recommendations and areas for future research.

2 Literature Study

2.1 Introduction

South Africa is currently in the process of adopting the *EN1992-1-1: Design of Concrete Structures (2004a)* as its primary standard for concrete design. This transition highlights the need for a deeper understanding of the properties of the material and the environmental effects that significantly influence the performance of concrete structures. Inclusion of environmental loading, thermal properties, shrinkage, and restraint effects in concrete is essential to align local design practices with the European standard.

This chapter reviews key aspects of environmental loading on concrete structures, highlighting the influence of climatic conditions such as solar radiation, temperature fluctuations, humidity, and wind. These factors interact with the thermal properties of concrete, including thermal conductivity, specific heat capacity, and coefficient of thermal expansion, to create temperature gradients and internal stresses within structural elements. Such interactions are critical in understanding the behaviour of concrete under environmental exposure.

The impact of shrinkage, a time-dependent deformation influenced by environmental conditions and aggregate type, is also examined. Drying shrinkage and autogenous shrinkage are addressed as critical components, with particular emphasis on how South African aggregate properties affect shrinkage behaviour. The restrictions due to geometry and support conditions are explored, as they play a vital role in stress development and potential cracking in concrete elements.

These interconnected phenomena highlight the importance of material properties in determining the durability and performance of concrete under environmental loading. This chapter investigates the state of research in these areas, linking experimental observations, numerical models, and design considerations to provide a comprehensive understanding of how material properties and environmental factors influence the thermal and mechanical behaviour of concrete. This review serves as the foundation for the subsequent study of concrete elements exposed to environmental loads, particularly in the context of South African aggregates and climate.

2.2 Effect of Aggregate Type on Concrete Material Properties

The type of aggregate used in concrete influences both its mechanical and thermal properties, which are critical for the performance and durability of concrete structures. Aggregates typically make up 60% to 85% of concrete's volume, making them a key determinant of the material's properties (Albarwary et al., 2017; Neville, 2012; Xie et al., 2012).

The mechanical properties of concrete, including compressive strength, tensile strength, and elastic modulus, are influenced by the size, shape, and mineral composition of the aggregates used. However, recent data suggest that while aggregate type significantly affects the elastic modulus, its influence on compressive and tensile strength is less pronounced. The influence of South African aggregate types on compressive strength is well documented, with Davis and Alexander (1994) reporting that the selection of aggregates can cause strength variations of 10 MPa to 15 MPa. Higher-strength concretes are typically produced using andesite, dolerite, and felsite, whereas certain types of granite may result in below-average strengths due to variations in their mineral composition.

Table 2.1 presents the ranges of modulus of elasticity and splitting tensile strength for different South African aggregate types, highlighting the variation in stiffness among aggregates. Although the data confirm that aggregates with higher stiffness, such as dolomite and dolerite, contribute to increased elastic modulus, the differences in splitting tensile strength remain relatively small across all aggregate types. This further supports the conclusion that aggregate type plays a more pronounced role in influencing the stiffness of concrete rather than its tensile strength (Davis and Alexander, 1994; Neville, 2012).

Table 2.1: Comparison of elastic modulus and splitting tensile strength for different South African aggregate types (adapted from Brink, 2024).

Aggregate	Source	E-Value (GPa)	Splitting Tensile Strength (MPa)
Andesite	Eikenhof *(Johannesburg)*	30.3 – 33.9	4.00 – 5.02
Dolerite	Pietermaritzburg *(KZN)*	31.4 – 35.0	4.25 – 4.61
Dolomite	Olifantsfontein *(Guateng)*	35.6 – 40.0	3.96 – 4.69
Felsite	Zeekoewater *(MP)*	30.9 – 35.4	4.12 – 4.90
Granite	Rheebok *(WC)*	29.9 – 31.2	4.37 – 4.89
Tillite	Verulam *(KZN)*	28.6 – 30.2	4.15 – 4.86

Beyond mechanical properties, the thermal behaviour of concrete is also influenced by aggregate type. Since aggregates make up the majority of concrete volume, their thermal conductivity, heat capacity, and coefficient of thermal expansion play a role in determining how concrete responds to temperature fluctuations (Neville, 2012). This is particularly important in environmentally exposed structures, where temperature-induced stresses can impact long-term durability (Pavlů et al., 2019; Zhang and Poon, 2015).

2.3 Environmental Loading

Environmental loading includes the external forces and conditions that concrete structures experience during their service life, including temperature variations, solar radiation, humidity, wind, and other climatic factors. Figure 2.1 shows typical environmental loads on exposed concrete elements (Lu et al., 2021). While the figure shows temperature, wind, and solar radiation effects, moisture-related effects, such as evaporation and absorption, are not explicitly shown. The economical design of concrete structures, such as bridge decks, roofs, and pavements, must account for environmental loads alongside permanent and variable actions (EN-1991-1-1 (2004a)). The demand for maintenance-free infrastructure further highlights the need to understand and incorporate climatic effects throughout the asset's lifecycle. The structural response depends on the restriction of free movement, geometry, geographic location, daily and seasonal variations in weather conditions, and the thermal properties of the construction material (Elbadry and Ghali, 1983).

The presence of moisture further exacerbates these effects. Wet conditions, coupled with temperature fluctuations, can lead to freeze-thaw cycles in colder climates, significantly weakening the material (Gui et al., 2020). Although frost damage is not a concern in many South African regions, the interaction between temperature and moisture can be significant, as it influences drying shrinkage and internal stresses in concrete elements.

Solar radiation is a significant factor that influences the environmental load on concrete structures. Prolonged exposure to sunlight causes surface heating, which can intensify thermal gradients within concrete sections, especially on bridge decks and pavements (Li et al., 2020). These gradients may lead to tensile stresses within the concrete. In this study, solar radiation is a key variable, with a solar prediction model developed to quantify its effects on the thermal response and effective temperatures in the experimental concrete shapes.

Humidity also plays an important role in the durability of concrete, as it affects the rate of loss of moisture, carbonation, and penetration of chloride (Zhang et al., 2020b). These factors are particularly relevant for shrinkage behaviour, which is influenced by environmental conditions during curing and subsequent exposure. Wind, while often considered

in the context of lateral forces in tall structures, also accelerates surface drying, potentially contributing to moisture gradients and shrinkage (Deng et al., 2012).

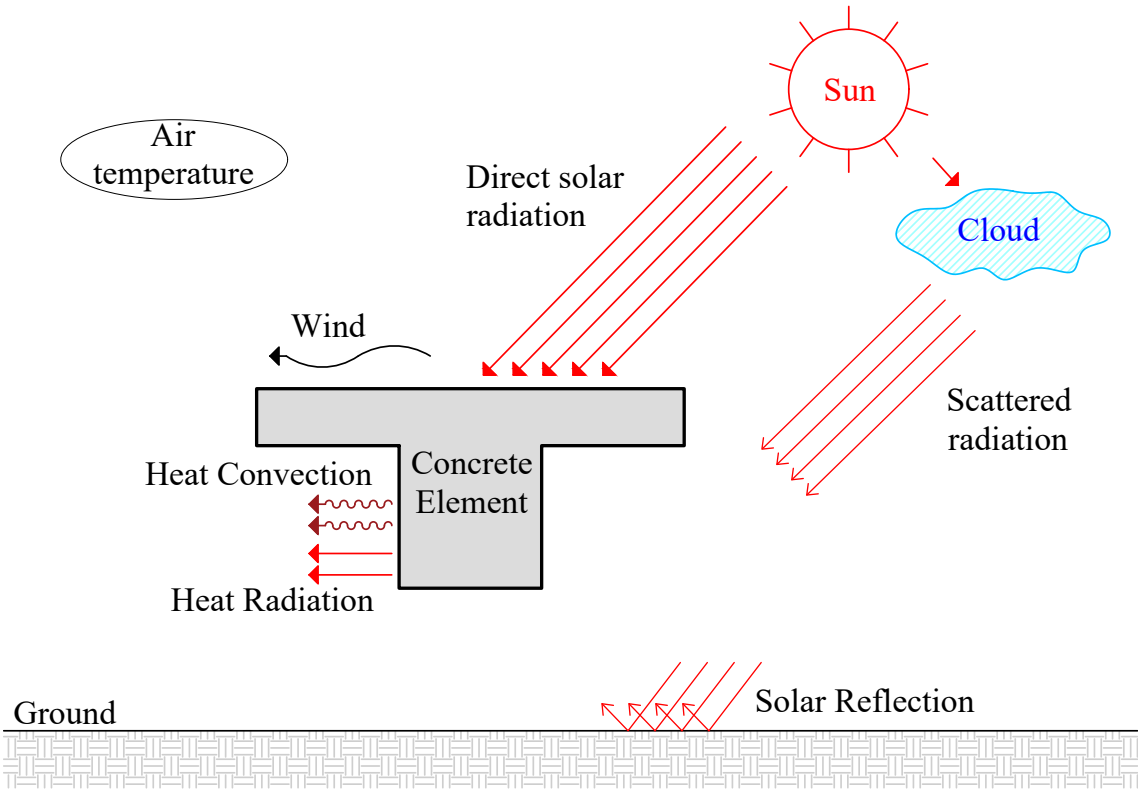

Figure 2.1: Environmental loading on exposed concrete element (adapted from Lu et al. (2021)). Moisture effects are not explicitly illustrated.

Shrinkage is significantly affected by environmental loading, especially in outdoor conditions where moisture loss is significant. As concrete cures, drying shrinkage creates tensile stresses, which, if the tensile strength of the material is exceeded, can cause cracking (Li et al., 2012). This study investigates drying shrinkage effects in detail, applying an adjusted EN1992-1-1 (2004a) shrinkage model to South African aggregates and comparing it with experimental results.

2.4 Thermal Response

The thermal response in concrete structures can be characterised by two key concepts:

- **Effective Temperature**
- **Temperature Gradients**

These concepts quantify how concrete elements, such as bridge decks, respond to environmental loading, including temperature fluctuations due to solar radiation, seasonal changes, and other climatic factors.

The effective temperature is a significant parameter in the evaluation of the thermal behaviour of concrete exposed to environmental loading. Defined by Emerson (1976), the effective bride temperature (EBT) governs the longitudinal movement of the structure, influencing thermal expansion and contraction. EBT is calculated by summing the product of the areas between cross-sectional isotherms and their respective mean temperatures, divided by the total cross-sectional area of the deck. If a bridge is constructed from homogeneous material, the effective temperature can be calculated according to Equation 2.1.

$$T_{\text{eff, EBT}} = \frac{\sum_{i=1}^{n} A_i \cdot T_i}{\sum_{i=1}^{n} A_i} \tag{2.1}$$

Where,

$T_{\text{eff, EBT}}$ = Effective bridge temperature
T_i = Temperature of area i (to n)
A_i = Cross-sectional area i (to n)

Although the concept of EBT is mainly applied to bridge decks, it can also be adapted to other concrete structures such as pavements or roofs that experience similar environmental loads. The effective temperature is particularly important for assessing thermal expansion and induced stresses due to uniform temperature changes.

Temperature gradients describe the variation in temperature through the depth of a concrete element at any given time. These gradients are crucial because they influence the structural integrity of concrete, especially under rapid temperature changes or prolonged exposure to sunlight. Emerson (1976) and Potgieter and Gamble (1983) define temperature gradients in bridge decks as the difference in temperature between the surface and specific depths within the deck. Significant temperature differences can lead to internal stresses, especially when the element is restricted from free movement.

The effective temperature and the temperature gradients are interrelated, as both quantify the thermal response of concrete, but from different perspectives. The effective temperature provides an averaged temperature that governs overall thermal expansion, while temperature gradients focus on the spatial variation of temperature, highlighting potential differential heating and resulting internal stresses.

This study does not include a review of design codes related to the effects of temperature in concrete structures. Although various standards, such as ACI Committee 209 (2002) and American Association of State Highway and Transportation Officials (AASHTO)

(2007), provide guidance on temperature gradients and effective temperatures in concrete elements, their applicability was not evaluated in this study.

The thermal properties of concrete, such as thermal conductivity, specific heat capacity, and coefficient of thermal expansion, influence the development of temperature gradients. Materials with higher thermal conductivity dissipate heat more evenly, reducing the magnitude of temperature gradients, while materials with lower conductivity may amplify these gradients, increasing the risk of thermal stresses and cracking.

2.5 Thermal Properties of Concrete

South African standards, such as SANS 10100-2 (2000), mainly focus on the structural use of concrete, including materials and the execution of the works. However, they do not provide detailed specifications for the thermal properties of concrete, such as thermal conductivity, specific heat capacity, or thermal expansion coefficients. These properties are important in assessing how concrete responds to temperature variations and environmental conditions. This section describes the key thermal properties of concrete, including thermal conductivity, specific heat capacity, and thermal expansion.

2.5.1 Thermal Conductivity

Thermal conductivity (k) is a measure of the ability of a material to conduct heat, quantified in units of $W/m^{\circ}C$ (Neville, 2012). In concrete, this property is crucial to understand how heat flows through structural elements, influencing temperature distribution, internal stresses, and durability under varying environmental conditions.

Figure 2.2 shows the concept of thermal conductivity. When a thermal energy flux (W) is applied on the surface area of an element, heat flows from a region of higher temperature (*Temperature 1*) to a lower temperature (*Temperature 2*). The thermal conductivity of the material determines the rate of this heat transfer. The heat flux is influenced by the thickness of the element and the temperature gradient, as described by Fourier's Law in Equation 2.2 (Fourier, 1878).

$$q = -k \cdot \frac{\Delta T}{\Delta x} \tag{2.2}$$

Where,

q = Applied heat flux (W/m^2)
k = Thermal conductivity ($W/m^{\circ}C$)
ΔT = Temperature difference (Temperature 1 - Temperature 2)
Δx = Thickness of the material

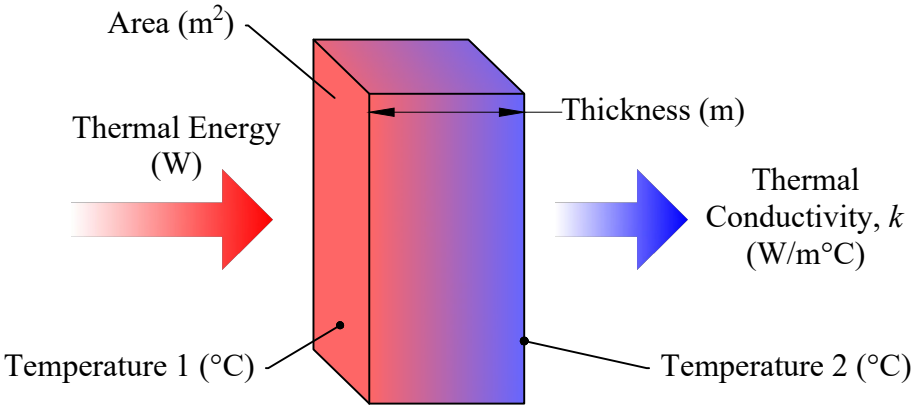

Figure 2.2: Illustration of thermal conductivity through an applied energy flux on a rectangular element (adapted from Whitaker (1977)).

Studies indicate that the thermal conductivity in concrete varies widely depending on factors such as (Kim et al., 2003; Neville, 2012; Tatro, 2006):

- Concrete composition
- Type of aggregate used
- Water content

The presence of air voids and porosity generally reduces conductivity, as higher porosity leads to lower thermal conductivity due to the insulating effect of trapped air (Neville, 2012). In contrast, a lower water-to-cement (w/c) ratio typically increases conductivity by reducing air voids, leading to a denser and more conductive concrete matrix. Kim et al. (2003) conducted an experimental study to investigate the factors influencing the thermal conductivity of concrete. Their findings indicate that moisture content, specimen condition, and aggregate volume fraction significantly affect thermal conductivity, supporting Neville (2012) and Tatro (2006). Figure 2.3 shows an adapted summary of the relevant experimental results from Kim et al. (2003).
Note: The study was limited in statistical evidence; thus, only trends were analysed.

In Figure 2.3 (a), it is suggested that the thermal conductivity of the cement, mortar, and concrete mixtures is independent of curing age. The thermal conductivity of concrete ranges between 2.34 $W/m°C$ and 2.3 $W/m°C$ over 28 days, while cement paste ranges between 1.21 $W/m°C$ and 1.15 $W/m°C$, approximately half that of concrete. These variations show the differences in thermal conductivity across mixtures, independent of curing age.

In Figure 2.3 (b), it is suggested that the thermal conductivity of cement paste is influenced by the water-to-cement (w/c) ratio. Tests conducted on cement pastes, rather than concrete specimens, revealed that the thermal conductivity of paste specimens increases with a lower w/c ratio. For instance, at 20 $°C$, wet samples with a w/c ratio of 0.25 exhibit a thermal conductivity of 1.22 $W/m°C$, while samples with a w/c ratio of 0.4 show a lower thermal conductivity of 1.16 $W/m°C$. Dry samples show a similar trend, with thermal conductivity decreasing from 0.98 $W/m°C$ at a w/c ratio of 0.25 to 0.77 $W/m°C$ at a w/c ratio of 0.4. This trend occurs because cement has a higher thermal conductivity value than water (Neville, 2012). The results suggest that with the addition of cement (that is, a lower w/c ratio), the thermal conductivity of the paste specimens increases.

As shown in Figure 2.3 (b), the thermal conductivity decreased as the status changed from fully saturated to fully dried. For example, at 20 $°C$, wet samples exhibit a thermal conductivity of 1.22 $W/m°C$ compared to 0.98 $W/m°C$ for dry samples, showing a 20% reduction. This is attributed to changes in air voids filled with water, whose thermal conductivity is superior to that of air, which accounts for the effect of the degree of saturation on the thermal conductivity. The influence of these factors shows the role of saturation levels and material composition in determining thermal conductivity.

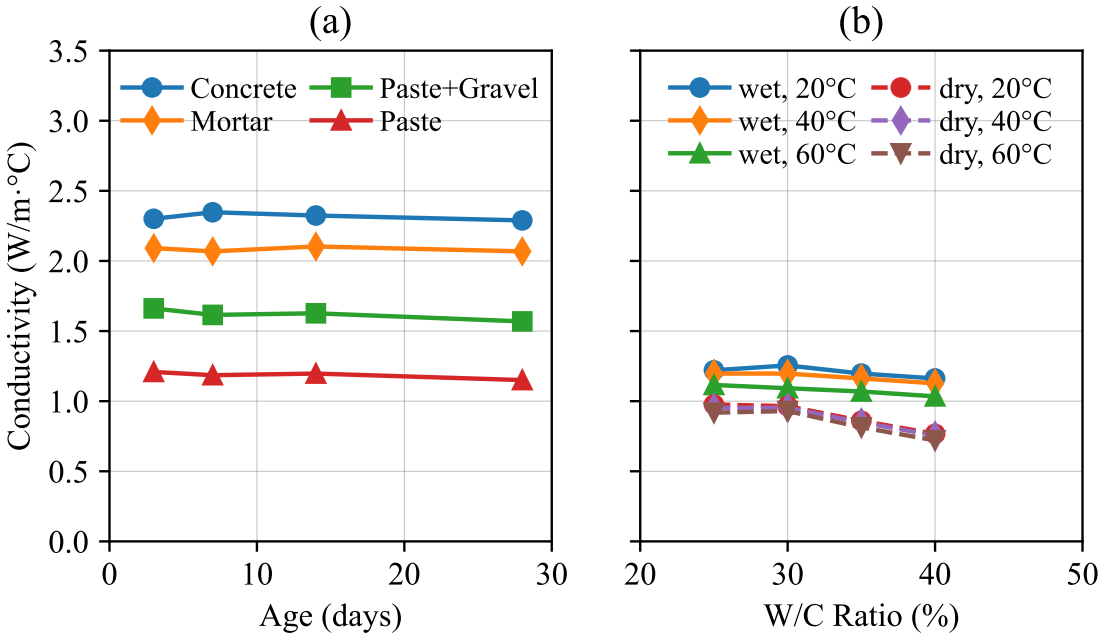

Figure 2.3: Experimental results for concretes thermal conductivity (adapted from Kim et al. (2003)). (a) Age and (b) water-to-cement ratio.

The aggregate particles play a dominant role in determining the thermal conductivity of concrete (Neville, 2012). As aggregates are the largest constituent by volume, their thermal properties heavily influence the overall heat transfer characteristics of the composite

material. Tatro (2006) summarised the effects of different aggregate types on thermal conductivity (see Table 2.2). Table 2.2 shows that the thermal conductivity of concrete is dependent on the type and density of the aggregate used. Neville (2012) suggests that the type of aggregate is the most critical factor influencing the thermal conductivity of concrete. Dense aggregates such as quartzite (4.1W/m·°C) and dolomite (3.3W/m·°C) contribute to higher conductivity, allowing efficient heat transfer through the material. In contrast, lightweight aggregates such as expanded shale (0.85W/m·°C) reduce the conductivity, improving the insulation properties of the material.

Researchers have shown the temperature dependence of thermal conductivity (Bahnick et al., 2020; Benoudjafer et al., 2021; Wang et al., 2023; Yun et al., 2014; Zehfuß et al., 2020). The EN1992-1-2 (2004c) accounts for the temperature dependence by the upper and lower limits for thermal conductivity. The upper and lower bounds for thermal conductivity are presented as functions of temperature, ranging from $20°C$ to $1200°C$. At lower temperatures, the thermal conductivity remains relatively stable, with values between $1.4 - 2.0$W/m·K, depending on the aggregate type.

Table 2.2: Thermal conductivity of concrete made with various aggregates (Tatro, 2006).

Aggregate Type	**Wet Density (kg/m^3)**	**Thermal Conductivity (W/m·°C)**
Hematite	3040	4.10
Quartzite	2400	4.10
Quartzite	2440	3.50
Dolomite	2500	3.30
Quartzite	-	3.30
Limestone	2450	3.20
Quartzite	2350	3.10
Sandstone	2130	2.90
Sandstone	2400	2.90
Granite	2420	2.60
Limestone	2420	2.60
Marble	2440	2.20
Limestone	2440	2.20
Basalt	2520	2.00
Rhyolite	2340	2.00
Barite	3040	2.00
Dolerite	2350	2.00
Basalt	2350	1.90
Expanded Shale	1590	0.85

The high and low thermal conductivity in concrete each have different implications for structural performance. High thermal conductivity promotes a more uniform temperature distribution throughout the concrete structure, minimising thermal gradients (Liu and Wang, 2022; Ren et al., 2022; Shahedan et al., 2017). This can significantly reduce the

risk of thermal stresses, which are often induced by temperature differences within the material (Li, 2019). In mass concrete applications, high thermal conductivity allows effective dissipation of heat generated from hydration reactions. This heat management helps prevent excessive internal temperatures that could otherwise lead to thermal cracking (Aniskin and Nguyen, 2018). Although high thermal conductivity is beneficial for heat dissipation, it can also lead to rapid heat loss in colder climates. This rapid cooling may cause thermal shock, where sudden changes in temperature induce cracking in the concrete, potentially compromising its structural integrity (Hussein and Saeed, 2016). Variations in thermal conductivity would affect design considerations for concrete structures exposed to environmental loading.

High thermal conductivity can mitigate internal thermal stresses and aid in heat dissipation, whereas low thermal conductivity can create thermal gradients and complicate temperature control. Understanding these implications helps in the design of concrete structures exposed to environmental loading, minimising the risks of thermal stress and cracking.

2.5.2 Specific Heat Capacity

Specific heat capacity is a fundamental thermodynamic property that quantifies the amount of heat energy required to raise the temperature of a unit mass of a substance by one degree Celsius (or one Kelvin) (Neville, 2012; Tatro, 2006). Ordinary Portland cement concrete typically has specific heat capacity values ranging between 840 and 1170 J/kg · °C (Neville, 2012). Research suggests that higher specific heat capacities can improve thermal stability, contributing to energy-efficient designs (Bentz et al., 2011).

According to Neville (2012), the factors that influence the specific heat capacity include:

- Density
- Water content
- Temperature
- Mineral composition of the aggregates (to a lesser extent)

For example, a high moisture content and certain aggregates increase the specific heat capacity, enhancing the thermal buffer capacity of concrete. Additives, such as phase change materials, further improve heat storage without drastically altering capacity (Cao et al., 2017).

The specific heat capacity is closely related to the thermal diffusivity (α_d), which represents the rate at which the heat diffuses through a material. Thermal diffusivity is defined as the ratio of thermal conductivity (k) to the product of specific heat capacity (c_p) and density (ρ), as shown in Equation 2.3 (Neville, 2012).

$$\alpha_d = \frac{k}{\rho c_p} \tag{2.3}$$

Where,

α_d = Thermal diffusivity (m^2/s)
k = Thermal conductivity ($W/m \cdot °C$)
ρ = Density (kg/m^3)
c_p = Specific heat capacity ($J/kg \cdot °C$)

Zhang and Jiang (1999) reviewed three commonly used techniques for calorific property testing: the conventional calorimetry method, differential thermal analysis, and differential scanning calorimetry. Although these methods are widely used for materials, such as metals and polymers, they require that the sample is homogeneous, small, and ground (Zhang and Jiang, 1999). Consequently, these methods are inappropriate for heterogeneous and porous materials such as concrete, which consists of aggregates, cement paste, and entrapped air pockets. The T-history method, developed to measure the specific heat of phase-change materials, provides a simpler approach to calorimetric analysis. However, this method also assumes a degree of homogeneity that concrete does not inherently possess. The large aggregate size and internal porosity of concrete introduce variability in heat transfer behaviour, making it difficult to achieve consistent results with existing small-scale test methods (Zhang and Jiang, 1999).

The absence of a specific standardised test method for measuring concrete-specific heat capacity highlights the need for innovative approaches that take into account the heterogeneity of the material and the large sample sizes. This limitation is critical when evaluating materials, such as concrete, for applications in thermal energy storage, where accurate calorimetric data are essential for design and analysis.

Pan et al. (2017) conducted an experimental investigation into the specific heat capacity of concrete at elevated temperatures. The research employed a half-open dynamic method based on the mixing principle, an innovative approach to address the challenges of measuring specific heat capacity under near-adiabatic conditions. The mixing principle involves immersing a high-temperature concrete specimen in water (Pan et al., 2017). The heat released by the specimen is absorbed by the water until a new thermal equilibrium is reached. By measuring the initial temperatures of the concrete and water, along with the final equilibrium temperature, the specific heat capacity of the concrete can be calculated. Although this process traditionally requires adiabatic conditions to ensure accuracy, such conditions are difficult to achieve in practice because of challenges in temperature measurement. To address this issue Pan et al. (2017) suggested a half-open dynamic method. This method addresses the issue by allowing for some heat exchange

with the environment while maintaining measurable control over the system. The approach is based on energy conservation principles, where the total heat released by the system equals the heat absorbed by the water, the vaporised water, and any heat lost to the environment. In this process, A represents the initial temperature of the water, while B indicates the temperature of the water after allowing the system to cool. Note that the temperature shown in the figure refers to the water temperature, and T_1 corresponds to the initial temperature of the specimen. Taking into account the thermal balance process between the points B and C in Figure 2.4, the thermal equilibrium equation is expressed as indicated in Equation 2.4.

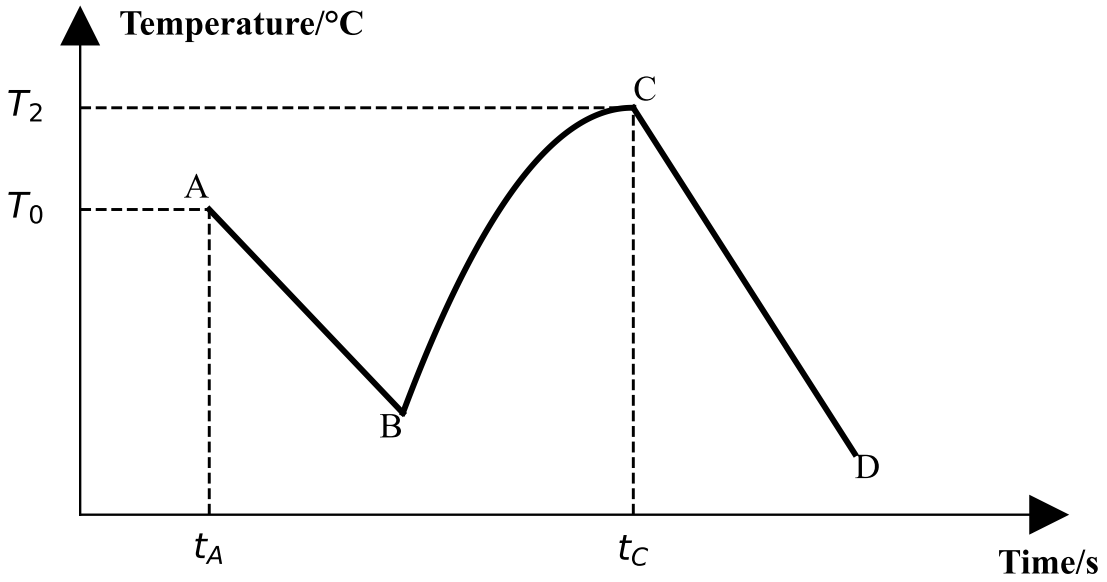

Figure 2.4: The mixing principle for the half-open dynamic method: Water temperature changing process (Pan et al., 2017)

$$Q_1 = Q_2 + Q_3 + Q_4 \tag{2.4}$$

Where,

Q_1 = Heat released by the hot specimen during range B–C
Q_2 = Heat absorbed by liquid water
Q_3 = Heat carried by vaporised water (phase change energy and heat absorbed)
Q_4 = Heat lost to the environment

These components are further defined by Pan et al. (2017) as indicated in Equation 2.5 to Equation 2.8:

$$Q_1 = m_1 c_1 (T_1 - T_2) \tag{2.5}$$

$$Q_2 = m_{\text{water}} c_{\text{water}} (T_2 - T_0) \tag{2.6}$$

$$Q_3 = m_b c_b (T_b - T_0) + m_b H_v \tag{2.7}$$

$$Q_4 = m_{\text{water}} S t_c \tag{2.8}$$

Where,

c_i = Specific heat of specimen at temperature T_i, $i = 1, 2$
m = Mass of specimen
T_0 = Water temperature when specimen is added
T_1 = Specimen temperature when added to water
T_2 = Maximum system temperature
c_{water} = Specific heat of water, 4.2×10^3 J/(kg·°C)
m_{water} = Mass of water
m_b = Mass of vaporised water
T_b = Boiling water temperature, 100°C
H_v = Vaporisation heat at 100°C, 2.57×10^6 J/kg
S = Slope of AB and CD
t_{bc} = Duration of range BC, $t_{bc} = t_C - t_B$

This experimental methodology highlights the balance between practical challenges and the accuracy of thermal property measurements. Using the half-open dynamic method, Pan et al. (2017) successfully derived reliable data on concrete specific heat capacity at elevated temperatures.

2.5.3 Coefficient of Thermal Expansion

The Coefficient of Thermal Expansion (CTE) refers to the tendency of materials to expand when heated and to contract when cooled. Concrete typically exhibits a low CTE (α_c), generally between 10 and 12$\mu\varepsilon$/°C (Chung and Shin, 2011; Ghannam, 2019; Khalifa et al., 2020). However, temperature variations can induce stresses within the concrete, potentially leading to cracking and other forms of damage. As highlighted by Kodur (2014), the response of concrete to elevated temperatures is complex, as thermal, mechanical, and deformation properties interact and change with temperature. This interplay can increase the risk of thermal cracking, particularly in large structures where temperature gradients are significant. The CTE is an important property that influences structural performance, particularly in structures exposed to thermal stresses, such as bridges and large infrastructure projects (Ding et al., 2014; Naik et al., 2011; Zhao et al., 2021).

The coefficient of thermal expansion recommended by EN 1992-1-1 (2004a) is $10\mu\varepsilon/°C$ ("Unless more accurate information is available") for normal concrete and can be used for design and analysis in the context of concrete structures exposed to environmental loading. However, in areas subject to high temperature fluctuations, variability in thermal expansion may become a concern, as the resulting thermal stresses could be more pronounced due to larger temperature gradients and differential expansion across the structure.

Aggregate Type: Given the high volume of aggregate in concrete, the properties of aggregate play an dominant role in influencing concrete's CTE (Neville, 2012). Different aggregates have different thermal expansion coefficients, which, when combined in concrete, determine the composite CTE. Naik et al. (2011) found that aggregates such as dolomite and limestone exhibit different thermal expansion characteristics, which can lead to thermal incompatibility within the concrete matrix, reducing the durability. Similarly, Wang et al. (2019) emphasised the type of aggregate as a decisive factor for CTE in concrete due to the unique thermal properties of different minerals. Aggregates impede the thermal movement of the cement paste matrix due to their lower thermal expansion coefficients (Alexander and Mindess, 2014). Consequently, the use of aggregates with lower CTE can reduce the overall thermal expansion of concrete. Table 2.3 provides an adapted summary, from Hall and Tayabji (2011) of the CTE values for concrete containing various aggregate types, which can guide material selection in concrete mix design.

Table 2.3: Coefficient of thermal expansion of concrete by aggregate type (adapted from Hall and Tayabji (2011)).

Aggregate	**Average α_c ($/°C \times 10^{-6}$)**	**Standard Deviation ($/°C \times 10^{-6}$)**
Andesite	7.78	0.75
Basalt	7.80	0.77
Chert	10.83	0.75
Diabase	8.35	0.94
Dolomite	8.92	0.73
Gabbro	8.00	0.75
Gneiss	8.77	0.15
Granite	7.80	0.94
Limestone	7.80	0.80
Quartzite	9.34	0.90
Rhyolite	6.91	1.47
Sandstone	9.58	0.94
Schist	7.98	0.70
Siltstone	9.03	0.56

Water-to-Cement Ratio: The w/c ratio impacts concrete's porosity and density, both of which affect concrete's CTE. Higher w/c ratios typically increase porosity, resulting in higher CTE values (Neville, 2012). Wang et al. (2011b) found that optimising the w/c ratio can reduce thermal expansion, as lower ratios produce a denser and more stable matrix, limiting thermal movement.

Curing Conditions: Curing conditions, including temperature and humidity, significantly influence concrete's CTE (Li et al., 2021). Yeon et al. (2009) and Yeon et al. (2013) found the maximum value of CTE was obtained at approximately 70% relative humidity (RH). Effective curing is therefore important for controlling thermal expansion, ultimately enhancing concrete stability and durability.

Temperature Effects: Lee et al. (2019) reported that at high temperatures (particularly between 20°C and 100°C), thermal expansion in concrete becomes complex due to phase changes in the cement matrix and aggregate.

Additives and Supplementary Materials: Supplementary materials, such as fly ash or silica fume, can modify the thermal properties of concrete. Ghannam (2019) demonstrated that various additives and saturation conditions influence thermal expansion behaviour, suggesting that careful material selection can enhance thermal stability.

Restrained concrete structures are those in which volume changes due to factors such as temperature fluctuations, moisture loss, or chemical reactions are limited by external or internal constraints. These constraints can lead to the development of tensile stresses within the concrete, which may ultimately result in cracking. The mechanisms of restraint can be categorised into several types, including end restraint, continuous edge restraint, and internal restraint caused by reinforcement or other structural elements (Elwakeel et al., 2022; Jędrzejewska et al., 2023; Park et al., 2010). In restrained concrete structures, thermal expansion can lead to challenges, including internal stresses, cracking, and reduced durability:

- **Development of Internal Stresses**: Restrained expansion generates tensile stresses within the concrete, as movement is limited by structural elements, reinforcement, or external constraints. Yu et al. (2021) showed that the restrained expansion in concrete creates three-dimensional stress conditions, potentially leading to internal stresses that exceed the tensile strength.
- **Cracking Mechanisms**: Internal stresses due to restricted expansion can cause cracking, particularly in early-age concrete. Yuan et al. (2021) found that external supports or internal temperature gradients often cause restraint-based cracking, exacerbating drying shrinkage and reducing structural integrity.

- **Impact on Durability**: Cracking from restricted thermal expansion can compromise long-term durability. Kodur and Sultan (2003) noted that excessive expansion can lead to cracking and reinforcement corrosion, especially if cracks allow moisture ingress, accelerating degradation.
- **Environmental Influence**: Environmental conditions, such as high temperature and low humidity, exacerbate the susceptibility of restrained concrete to cracking, compounding thermal expansion and drying shrinkage effects (Yuan et al., 2021).

2.5.4 Solar Absorptivity

Solar absorptivity in concrete refers to the material's ability to absorb solar radiation, significantly affecting its thermal performance and the energy efficiency of concrete structures (Kim et al., 2014; Qin et al., 2023). This characteristic is especially relevant in urban areas, where high absorptivity contributes to the urban heat island effect, leading to elevated surface temperatures and increased cooling demands (Wu et al., 2017).

Solar absorptivity (a_s) can be calculated from the reflectivity, or albedo (a_r), of the concrete surface, as shown in Equation 2.9.

$$a_s = 1 - a_r \tag{2.9}$$

Where,
a_s = Solar absorptivity
a_r = Solar reflectivity (albedo)

Equation 2.9 highlights that as the reflectivity (a_r) increases, the absorptivity decreases, which means that less solar radiation is absorbed by the surface. This relationship describes how concrete surfaces interact with solar energy in various environments. Table 2.4 shows a summary of solar absorptivity values in current literature. Most references provide a range of values for concrete in general, without explicitly detailing the effect of aggregate type on these properties.

Several factors influence the solar absorptivity of concrete:

- **Surface Texture and Colour**: The surface characteristics of concrete, including texture and colour, play a crucial role in determining solar absorptivity. Lighter and smoother concrete surfaces tend to reflect more solar radiation, resulting in lower absorptivity, while darker, rougher surfaces absorb more energy. Adjusting surface properties, such as using lighter-coloured aggregates or finishes, can help reduce heat absorption (Lu et al., 2023; Qin et al., 2023; Zhang et al., 2015).
- **Coatings and Reflective Treatments**: The application of coatings or reflective treatments can alter the solar absorptivity of concrete. Reflective paints or sealants are

often used to reduce absorptivity, effectively lowering surface temperatures, and enhancing energy efficiency (Li et al., 2019). These treatments are particularly beneficial in urban areas and high-temperature environments where managing surface temperatures is crucial for durability and comfort.

- **Environmental Factors**: External conditions, such as temperature, humidity, and pollution, can influence the long-term absorptivity of concrete. Environmental exposure may alter the surface characteristics, affecting solar absorptivity over time (Richard et al., 2015). For example, prolonged exposure to the sun or pollution can darken the concrete surface, inadvertently increasing its absorptivity.

Table 2.4: Solar radiation properties of concrete (adapted from several researchers).

Author	Solar Absorptivity	Emissivity
Emerson (1973)	0.5 – 0.8	0.85 – 0.9
Elbadry and Ghali (1983)	0.5	0.88
Branco and Mendes (1993)	0.7	0.9
Ivanov and Thelandersson (2011)	0.5 – 0.7	0.9
Li et al. (2014)	0.71 – 0.74	0.8
ASHRAE (2001)	0.91	0.85 – 0.95
Duffie et al. (2020)	0.65 – 0.8	–
Mehta and Monteiro (2014)	0.5	–

High solar absorptivity means that concrete absorbs more solar energy, which can increase surface temperatures and induce thermal stress within the structure. This stress can accelerate material ageing, increase the risk of cracking, and ultimately reduce the durability of concrete structures (Zhao et al., 2021). In urban areas, concrete with high absorptivity can exacerbate the urban heat island effect, where the accumulation of heat in urban materials leads to warmer temperatures. This effect not only affects the comfort of residents, but also increases the energy consumption for cooling (Wu et al., 2017).

2.5.5 Emissivity

Emissivity, defined as the ratio of the thermal radiation emitted by a surface to that emitted by a perfect black body at the same temperature, plays a significant role in applications ranging from thermal imaging to energy efficiency in buildings. For concrete, the average emissivity is typically reported to be around 0.95, indicating that it is quite effective at emitting thermal radiation (Abuhmida, 2023). This value can vary according to several factors, including the texture, colour, and moisture content of the concrete surface (Zhang, 2021).

Despite its theoretical importance in heat transfer calculations, Tayşi and Abid (2015) demonstrated that the influence of emissivity on the thermal behaviour of concrete is often negligible. In their parametric investigation of a concrete box-girder bridge segment, it was shown that variations in emissivity did not produce statistically significant changes in temperature distributions or gradients. This finding was supported by an analysis of variance, which identified surface emissivity as having a minimal impact compared to other thermal properties such as solar absorptivity, specific heat, and thermal conductivity. The range of emissivity values used by several researchers can be seen in Table 2.4 and the assumed values fall in a narrow range between 0.8 to 0.95.

The negligible effect of emissivity can be attributed to the dominance of other heat transfer mechanisms, such as conduction and solar absorption, in determining the thermal behaviour of concrete structures. These results highlight the importance of prioritising material properties such as thermal conductivity and absorptivity in the thermal analysis and design of concrete elements, while the role of emissivity can often be simplified for practical applications. Consequently, emissivity was excluded from further parametric studies within the study.

2.5.6 Summary of Thermal Properties Found in Literature

Table 2.5 summarises the thermal properties of concrete as reported in various sources. The values for thermal conductivity, specific heat, emissivity, and absorptivity vary depending on factors such as aggregate type, moisture content, and temperature conditions. These properties significantly influence the thermal behaviour of concrete in applications such as pavements, bridge decks, and buildings, as they affect how concrete responds to temperature fluctuations and external thermal loads. The variability in these properties highlights the need to consider specific material characteristics and environmental conditions when designing and analysing concrete structures.

Table 2.5: Values of the thermal properties of concrete as found in literature.

Reference	Density (kg/m^3)	Thermal Conductivity (W/mK)	Specific Heat ($J/kg \cdot ^\circ C$)	Emissivity	Absorptivity
ASHRAE (2001)	2400 2240 2080	1.4–2.9 1.3–2.6 1.0–1.9	800–1000	0.85–0.95	0.65–0.8
Duffie et al. (2020)	2400	1.73	840		
Ghali et al. (2017)	2400	1.5–2.5	840–1200	0.9	0.65–0.8
Incropera et al. (2007)	2300	1.4	880	0.88–0.93	
Kothandaraman (2006)	2300	1.279	1130		
Mehta and Monteiro (2014)		Basalt: 1.9–2.2 Dolomite: 3.2 Quartzite: 3.5	900–1000		
Naterer (2002)	2200	1.7	753	0.85–0.95	0.5
Neville (2012)		1.4–3.6	840–1170		
Porges (2000)	2240	1.2–1.4	1130		
Ramachandran (1996)		1.55–2.17			
Somerton (1992)	2100	Dry: 1.33–1.63 Saturated: 2.54–2.87			
Tatro (2006)	2240–2400	Sandstone: 2.9 Quartzite: 3.3 Gravel: 2.7			
Turns and Kraige (2007)	2300	1.4	880	0.88–0.93	
Welty et al. (2007)	2310	1.21	880		
Rezaei et al. (2020)	2205 – 2498	1.6 –3.2	920 – 1160		

2.6 Shrinkage and Restraint Effects in Concrete Structures

The effects of shrinkage and restraint are key considerations in the long-term durability and performance of concrete structures. Concrete shrinkage refers to the volume reduction that occurs as concrete dries and hardens. Shrinkage is composed of several components, including autogenous shrinkage, drying shrinkage, and thermal shrinkage, each contributing to the overall deformation. When shrinkage is restricted, tensile stresses develop within the material. If these stresses exceed the tensile strength of the concrete, they can cause cracking, compromising structural integrity.

Concrete structures can experience restraint in various ways. External restrictions may arise from boundary conditions or connections to other elements, while internal restrictions are often introduced by the geometry of the concrete section or the inclusion of reinforcement. For example, in reinforced concrete, the restraining effect of steel reinforcement significantly influences stress distribution and cracking potential. In geometrically complex sections, such as those with flanges or non-uniform shapes, internal restriction can amplify stress development. These interactions require careful consideration during design to mitigate cracking risks. Figure 2.5 provides a broad overview of the primary factors that contribute to cracking in restrained concrete structures such as bridge decks, including shrinkage, thermal stresses, and restraint.

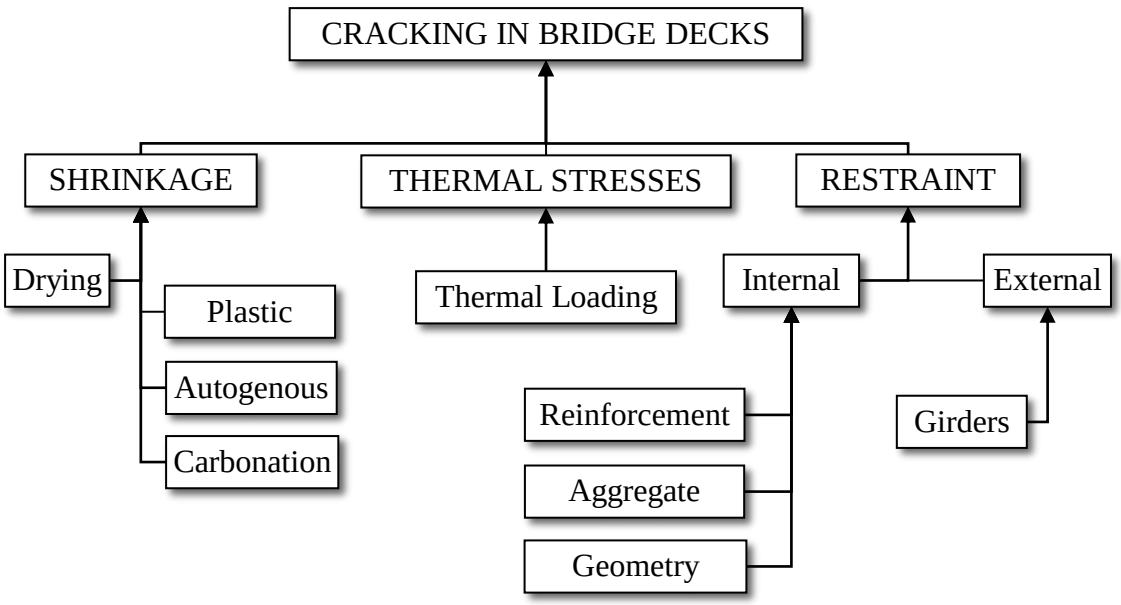

Figure 2.5: Overview of factors contributing to cracking in concrete bridge decks, including shrinkage, thermal stresses, and restraint (adapted from Brown et al. (2001)).

With South Africa adopting the EN1992-1-1 (2004a) design code for the design of reinforced concrete structures, it is important to recognise that the shrinkage behaviour of concrete made with South African aggregates may differ from the European context where the code was developed. Variations in aggregate properties, environmental conditions, and construction practices can influence both the magnitude of shrinkage and the effect of restraint. This divergence can lead to unexpected stress development and cracking, posing challenges to achieving long-term structural performance.

This section provides an overview of the deformation components in structural concrete, the different types of shrinkage, and the impact of restraint, particularly internal restraint due to geometry, on shrinkage-induced stresses. Furthermore, it highlights the potential implications of adopting EN1992-1-1 (2004a) for South African concrete structures, considering local aggregate properties and their effects on shrinkage and restraint.

2.6.1 Strain Components in Structural Concrete

In concrete structures, strain is a measure of deformation resulting from applied stresses or internal changes in the material. The strain components in concrete can be broadly categorised into time-dependent and time-independent strains.

1. **Time-Independent Strains** arise from external loads applied to the concrete and include elastic deformation, which occurs immediately upon loading and is typically reversible when the load is removed (Pan et al., 2022; Zhang et al., 2019).
2. **Time-Dependant Strains** result from internal changes within the concrete, not directly related to external loads. They include shrinkage and creep strains, which are critical for understanding concrete's behaviour under environmental changes and hydration processes. Shrinkage, in particular, can occur without external forces but can lead to stress build-up when movement is restricted (Hwang et al., 2021).

The total strain in concrete, $\varepsilon_{\text{total}}$, can be expressed as the sum of its components (Equation 2.10).

$$\varepsilon_{\text{total}} = \varepsilon_{\text{elastic}} + \varepsilon_{\text{thermal}} + \varepsilon_{\text{shrinkage}} + \varepsilon_{\text{creep}} \tag{2.10}$$

Where,

$\varepsilon_{\text{total}}$ = Total strain in concrete
$\varepsilon_{\text{elastic}}$ = Elastic strain, reversible upon unloading
$\varepsilon_{\text{thermal}}$ = Thermal strain, dependent on temperature changes and α_c
$\varepsilon_{\text{shrinkage}}$ = Shrinkage strain, which includes drying and autogenous shrinkage
$\varepsilon_{\text{creep}}$ = Creep strain, a time-dependent strain under sustained load
Note: Creep strain falls outside the scope of this study.

Each component of the strain contributes differently to the overall deformation in concrete. This study focusses on shrinkage and thermal deformation as primary factors that affect concrete performance under environmental conditions. Creep strain, which contributes to long-term deformation under sustained load, was not within the scope of this analysis, but is recognised as a critical component in the overall behaviour of concrete.

The relationship between strain and stress in concrete can be expressed using Hooke's law (Equation 2.11), where the stress, σ, is directly proportional to the strain, ε, with the modulus of elasticity, E, acting as the proportionality constant.

$$\sigma = \varepsilon \cdot E \tag{2.11}$$

Where,
σ = Stress in the concrete (Pa)
ε = Strain in the concrete (dimensionless)
E = Modulus of elasticity of the concrete (Pa)

The interplay of strain components often leads to complex stress states in concrete, especially in restrained structures. Understanding the contributions of each strain component to stress development is essential for accurate predictions of structural behaviour and the design of durable concrete elements. This study focusses on thermal and shrinkage strains as the dominant contributors to stress development under environmental loading.

2.6.2 Types of Shrinkage and Contributing Factors

Concrete shrinkage is a complex phenomenon influenced by multiple factors, including water content, cement composition, environmental conditions, and the geometry of the concrete element. Shrinkage can be broadly categorised into two main components: drying shrinkage and autogenous shrinkage, each with distinct mechanisms and contributing factors (Neville, 2012).

Drying shrinkage occurs due to the evaporation of water from hardened concrete, particularly from capillary pores. Especially pronounced in concrete with a high water-to-cement (w/c) ratio, where excess water leads to void formation upon evaporation. The drying shrinkage is influenced by environmental factors, such as ambient temperature, humidity, and air circulation around the concrete surface. In addition, the type of aggregate used can influence the drying shrinkage properties of concrete. Studies have indicated that certain aggregates, such as limestone, can lead to a lower drying shrinkage compared to others, such as recycled aggregates, which often show a higher shrinkage due to their porous nature and the presence of adhered mortar (Etxeberria et al., 2016; Zhang et al., 2013).

Figure 2.6 shows the drying shrinkage component as the dominant shrinkage component over time for normal strength concrete.

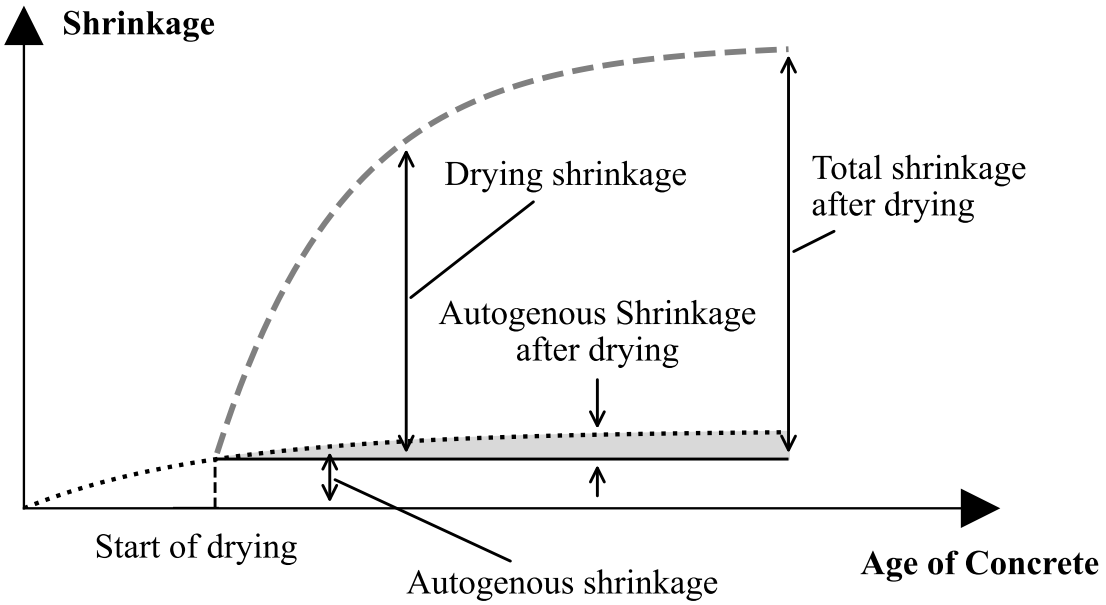

Figure 2.6: Shrinkage strain components in normal strength concrete (adapted from Gribniak et al. (2008) and Sakata and Shimomura (2004)).

In practical applications, drying shrinkage is of particular concern when exposed to environmental conditions, such as sunlight, wind, and fluctuating temperatures. These factors exacerbate drying shrinkage, leading to cracking of the surface and reduced structural durability. For conventional concrete, drying shrinkage constitutes the majority of total long-term shrinkage, often overshadowing the effects of autogenous shrinkage after curing (Gribniak et al., 2008; Sakata and Shimomura, 2004).

In contrast, autogenous shrinkage occurs after the concrete has set, under conditions where no moisture exchange with the environment takes place. It is caused by the withdrawal of water from the capillary pores during hydration, a process known as self-desiccation. This shrinkage occurs in the interior of a concrete mass and is restricted by the rigid skeleton of the already hydrated cement paste and the aggregate particles. Consequently, autogenous shrinkage in concrete is an order of magnitude smaller than in neat cement paste (Neville, 2012). This phenomenon is independent of external environmental factors and is mainly influenced by the ratio w/c, the cement content, and the curing conditions (Neville, 2012). Autogenous shrinkage is most significant in low w/c ratio mixes, such as high-performance and high-strength concretes, where reduced porosity limits external moisture ingress (Silliman and Newtson, 2006).

Silliman and Newtson (2006) and Gribniak et al. (2008) showed that autogenous shrinkage in high-strength concrete can be a considerable fraction of total shrinkage, particularly in the early stages before drying begins. However, for conventional concrete, the autogenous shrinkage strain is relatively small, ranging from 20 to 110 microstrains, and constitutes only about 10–20% of the total shrinkage strain over time (Gribniak et al., 2008; Silliman and Newtson, 2006). Small autogenous shrinkage can persist even after the start of drying, as hydration continues within the concrete matrix. However, this contribution becomes negligible for most conventional concrete applications due to the dominance of drying shrinkage under normal environmental conditions (Gribniak et al., 2008; Kovler and Zhutovsky, 2006). High-strength concrete, defined as concrete with strengths exceeding 55MPa (Sakata and Shimomura, 2004), exhibits a more significant ratio of autogenous to drying shrinkage, necessitating separate consideration of these components in shrinkage analysis.

2.6.3 Effects of Restraint on Shrinkage-Induced Stresses

When natural shrinkage of concrete is restricted, either by external supports or adjacent materials, tensile stresses develop within the concrete matrix. If these stresses exceed the tensile strength of the material, cracking can occur. Figure 2.7 shows the stress relaxation process as proposed by Weiss (1999) for a restrained concrete member, progressing through six states.

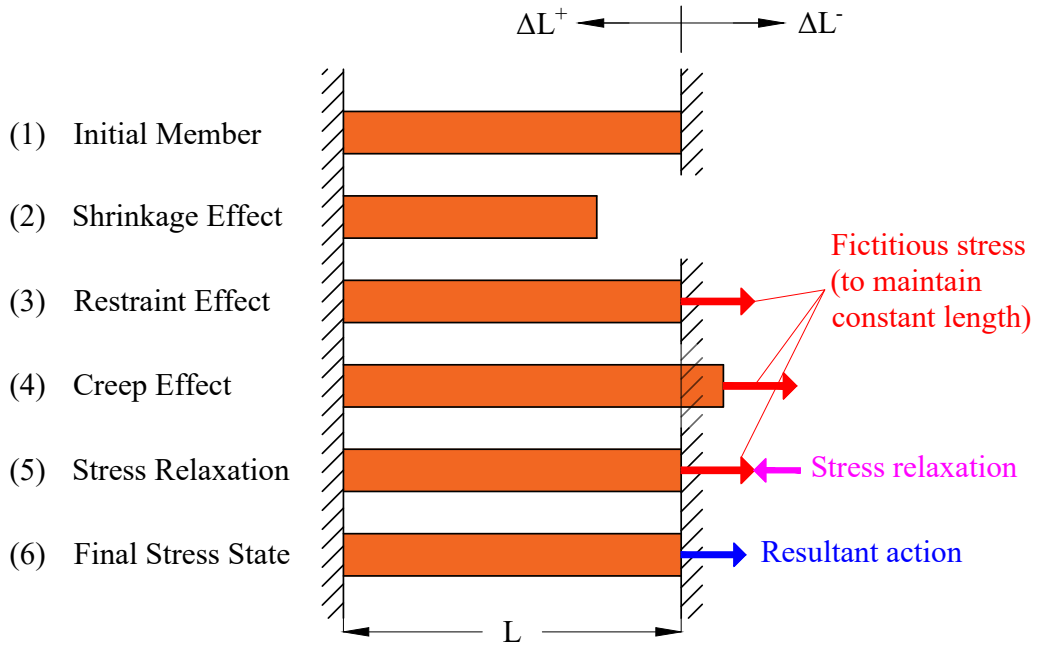

Figure 2.7: Six states of shrinkage in a restrained concrete member showing resulting stresses and relaxation due to creep (adapted from Weiss (1999)).

Initially, the concrete is undeformed *(1)*. When subjected to free shrinkage *(2)*, as shown by the release of the right support, the concrete experiences a reduction in length due to shrinkage. In a perfectly restrained condition *(3)*, this shrinkage-induced movement is prevented, leading to the development of tensile stresses as the concrete resists deformation.

To maintain the restrained condition, Weiss (1999) suggested the conceptual application of a "fictitious" tensile stress. This hypothetical stress counteracts the tendency of the concrete to shrink, imposing a state of perfect restraint where the length of the member remains constant despite the shrinkage tendency. However, under this fictitious stress alone, the concrete would gradually deform outward over time due to creep *(4)*. Creep deformation occurs as an internal response to the sustained stress imposed by restraint.

By superimposing fictitious tensile stress and creep deformation, the interactive effects of restraint and time-dependent deformation can be visualised. Over time, stress relaxation occurs *(5)*, where the stress gradually reduces while the deformation remains constant. This results in a final reduced shrinkage stress state *(6)*. Stress relaxation, a time-dependent process, can significantly reduce initial shrinkage stresses, with reductions ranging from 30% to 70% as reported by Gribniak et al. (2011) and Weiss (1999).

Figure 2.8 compares the development of shrinkage-induced stress over time with the time-dependent strength of the concrete. As concrete ages, its tensile strength usually increases; however, shrinkage-induced stresses also develop over time. Cracking occurs when these stresses exceed the tensile strength of the concrete, as shown by their intersection in the graph (time to cracking).

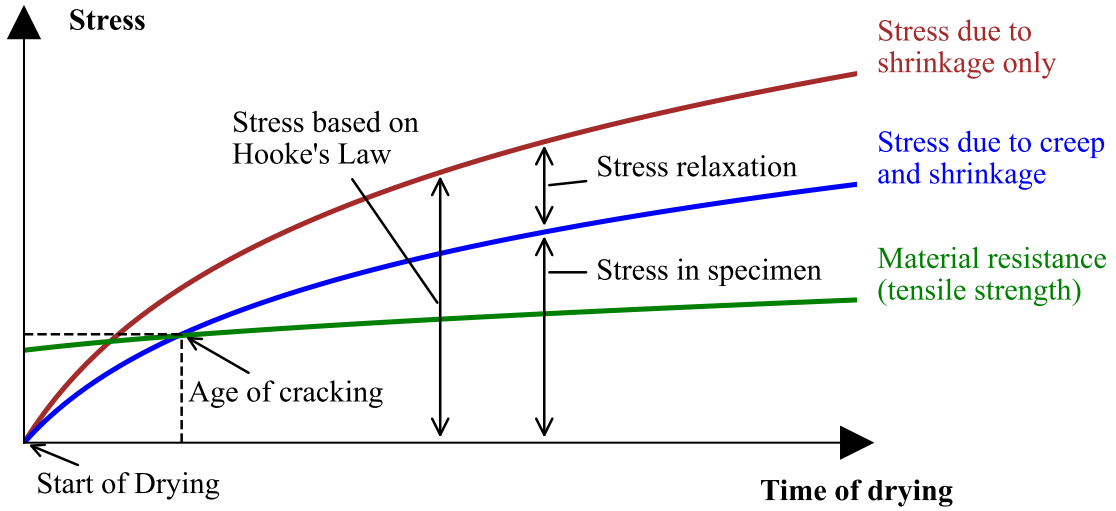

Figure 2.8: Shrinkage-induced stress development and time-dependent strength in a restrained concrete member (adapted from Weiss (1999)).

It is important to note, as Gribniak et al. (2007) stated, that stresses from restrained shrinkage cannot be calculated directly using Hooke's law (Equation 2.11) because stress relaxation modifies the state of stress over time. Stress relaxation, while conceptually similar to creep, describes the reduction in stress under constant deformation. Although this study did not explicitly consider stress relaxation and creep, understanding these mechanisms is critical to interpreting restrained shrinkage behaviour.

2.6.4 Shrinkage Prediction Model

The *EN 1992-1-1:2004 (2004a)* shrinkage prediction model was selected for this study due to its upcoming adoption as a South African design standard. Comparative research on shrinkage models highlights the strengths and limitations of each model in various contexts, including:

- EN1992-1-1 (2004a)
- *ACI 209.2R-08 Guide for Modeling and Calculating Shrinkage and Creep in Hardened Concrete* (2002)
- *B3 model* (Bazant and Baweja, 1995a; Bazant and Baweja, 1995b)
- *GL 2000 model* (Gardner and Lockman, 2001)

In particular, Gribniak et al. (2011) conducted a comprehensive evaluation of the precision of these models by comparing the calculated and measured free shrinkage strains in concrete. The precision of each model was assessed using a relative prediction metric, defined as in Equation 2.12. Gribniak et al. (2011) used crushed granite aggregates of two sizes, 5/8 mm and 11/16 mm, with a w/c ratio of 0.42, which presents a limitation as the findings are specific to this aggregate type and may not account for the influence of other aggregate types on shrinkage behaviour.

$$\Delta = \frac{\varepsilon_{cs,calc}}{\varepsilon_{cs,obs}} \tag{2.12}$$

Where,
Δ = Relative prediction metric
$\varepsilon_{cs,calc}$= Calculated shrinkage strain based on the model
$\varepsilon_{cs,obs}$ = Measured shrinkage strain

As shown in Figure 2.9, EN1992-1-1 (2004a) (Eurocode 2 in Figure) demonstrated the closest alignment with the measured shrinkage strains, with a central tendency to underestimate the shrinkage at an average of 14.6%. In contrast, the ACI 209 (2002), B3 (Bazant and Baweja, 1995a; Bazant and Baweja, 1995b) , and GL 2000 (Gardner and Lockman, 2001) models exhibited greater deviations from the measured data (43.6%, 128.1% and

16.2%, respectively). This suggests that while these models are useful in certain contexts, they may be less accurate for standard shrinkage predictions.

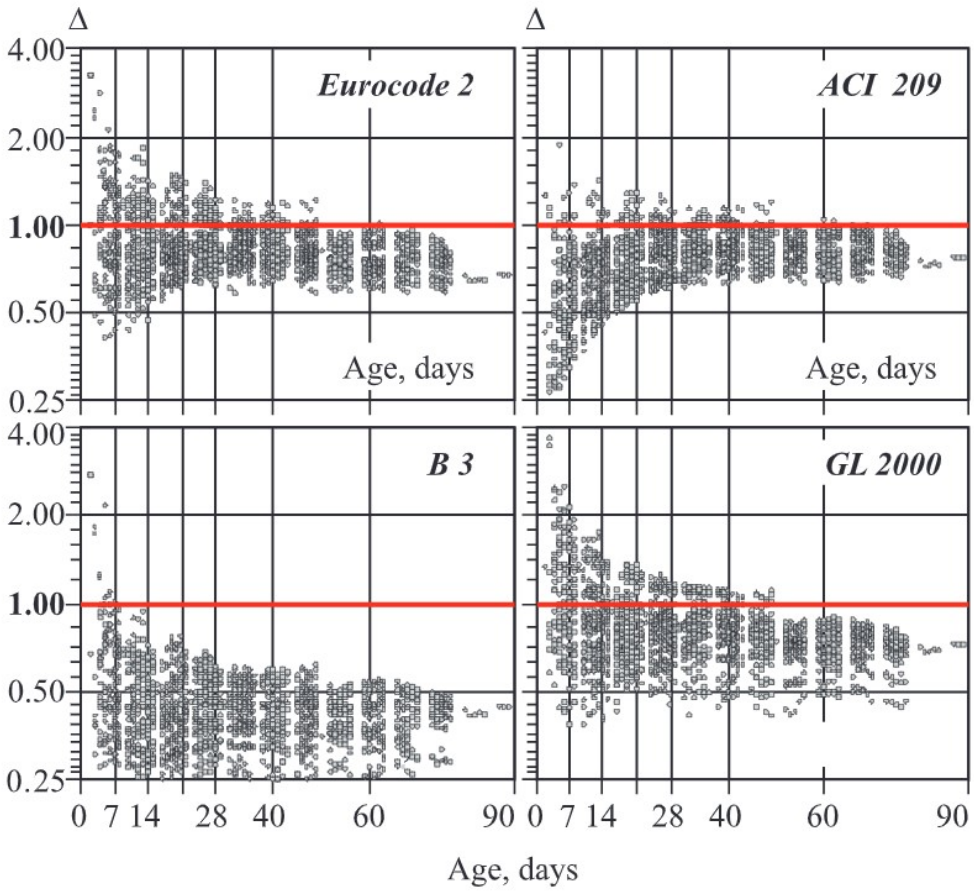

Figure 2.9: Comparison of shrinkage prediction accuracy for EN1992 (Eurocode 2), ACI 209, B3, and GL 2000 models based on relative prediction metric (Gribniak et al., 2011).

The findings of Gribniak et al. (2011) align with the decision to adopt EN1992-1-1 (2004a) as South African standard, particularly in the context of the use of crushed granite aggregates. The EN1992-1-1 (2004a) framework is well supported by empirical data and appears to be the most accurate of the four models that Gribniak et al. (2011) considered. While some studies suggest that EN1992-1-1 (2004a) may underestimate shrinkage in specific concrete types, such as high-strength or recycled aggregate concretes, its overall accuracy make it a suitable choice for analysing shrinkage in typical concrete mixes (Gribniak et al., 2011; Hołowaty, 2015).

The EN1992-1-1 (2004a) model categorises **total shrinkage** (ε_{cs}) into two main components: **drying shrinkage** (ε_{cd}) and **autogenous shrinkage** (ε_{ca}). This distinction allows for individual consideration of the effects of moisture loss (drying shrinkage) and self-desiccation (autogenous shrinkage) on the total shrinkage strain. The shrinkage prediction model provided in EN1992-1-1 (2004a) does not explicitly incorporate the influence

of aggregate type in its equations. Instead, it relies mainly on the strength class of the concrete, environmental conditions, and cement content to predict shrinkage. Although aggregate type significantly affects shrinkage due to its impact on stiffness and volume stability, it is only implicitly considered through its influence on overall concrete properties, such as compressive strength and modulus of elasticity.

The total shrinkage strain, ε_{cs}, is expressed as the sum of drying shrinkage (ε_{cd}) and autogenous shrinkage (ε_{ca}), as presented in Equation 2.13 (EN1992-1-1 (2004a)):

$$\varepsilon_{cs} = \varepsilon_{cd} + \varepsilon_{ca} \tag{2.13}$$

Where,

ε_{cs} = Total shrinkage strain
ε_{cd} = Drying shrinkage strain
ε_{ca} = Autogenous shrinkage strain

Drying shrinkage, ε_{cd}, is attributed to the gradual loss of moisture from hardened concrete. This component of shrinkage is influenced by factors such as relative humidity, concrete strength, and size of the members. Equation 2.14 (EN1992-1-1 (2004a)) can be used to estimate drying shrinkage strain.

$$\varepsilon_{cd}(t) = \beta_s(t, t_s) \cdot k_h \cdot \varepsilon_{cd,0} \tag{2.14}$$

Where,

$\varepsilon_{cd}(t)$ = Predicted drying shrinkage strain at time t
$\varepsilon_{cd,0}$ = Basic drying shrinkage strain (Equation 2.17)
k_h = Coefficient related to the notional member size h_0 (Table 2.7)
$\beta_s(t, t_s)$ = Time-dependent factor (drying shrinkage) (Equation 2.15)

The time-dependent factor $\beta_s(t, t_s)$ considers the non-linear reduction in shrinkage over time, as drying shrinkage gradually decreases. This factor is calculated using Equation 2.15 (EN1992-1-1 (2004a)):

$$\beta_s(t, t_s) = \frac{t - t_s}{t - t_s + 0.04\sqrt{h_0^3}} \tag{2.15}$$

Where,

$\beta_s(t, t_s)$ = Time-dependent factor (drying shrinkage)
t = Age of the concrete (days)
t_s = Age at which drying begins (typically after curing)
h_0 = Notional member size (m)

The parameter h_0, known as the notional member size, is determined by Equation 2.16 as the ratio of the cross-sectional area A_c to the exposed perimeter u (EN1992-1-1 (2004a)).

$$h_0 = 2 \cdot \frac{A_c}{u} \tag{2.16}$$

Where,

h_o = Notional member size (m)
A_c = Cross-sectional area of the concrete element in m^2
u = Perimeter of the section exposed to drying in m

The basic drying shrinkage strain, $\varepsilon_{cd,0}$, is estimated according to Equation 2.17 (EN1992-1-1 (2004a)). This base value accounts for influences such as cement class, concrete strength, and ambient relative humidity through β_{RH} (Equation 2.18):

$$\varepsilon_{cd,0} = 0.85 \cdot \left[(220 + 110 \cdot \alpha_{ds1}) \cdot \exp\left(-\alpha_{ds2} \frac{f_{cm}}{f_{cmo}} \right) \right] \cdot 10^{-6} \cdot \beta_{RH} \tag{2.17}$$

Where,

$\varepsilon_{cd,0}$ = Basic drying shrinkage strain
$\beta_s(t, t_s)$ = Relative humidity adjustment factor (Equation 2.18)
f_{cm} = Mean compressive strength of concrete (MPa)
f_{cmo} = Reference strength (10MPa)
α_{ds1}, α_{ds2} = Coefficients depending on the type of cement (Table 2.6)

Table 2.6: Values for α_{ds1} and α_{ds2} in Equation 2.17 (EN1992-1-1 (2004a)).

Cement Class	α_{ds1}	α_{ds2}
S	3	0.13
N	4	0.12
R	6	0.11

The relative humidity adjustment factor β_{RH}, defined in Equation 2.18, adjusts to ambient conditions (EN1992-1-1 2004):

$$\beta_{RH} = 1.55 \cdot \left(1 - \left(\frac{RH}{RH_0} \right)^3 \right) \tag{2.18}$$

Where,

β_{RH} = Relative humidity adjustment factor
RH = Ambient relative humidity (%)
RH_0 = Reference relative humidity (100%)

The coefficient k_h is based on the notional size h_0 and can be selected from Table 2.7, which provides values for different member sizes.

Table 2.7: Values for k_h in Equation 2.14 (EN1992-1-1 (2004a)).

h_0 **(mm)**	k_h
100	1.0
200	0.85
300	0.75
≥ 500	0.70

Autogenous shrinkage, ε_{ca}, is the strain that results from self-desiccation due to ongoing hydration within the concrete. This component is particularly significant in mixes with low water-to-cement ratios, where the concrete's internal moisture depletes without external drying. Using EN1992-1-1 (2004a), autogenous shrinkage is estimated using Equation 2.19 to Equation 2.21.

$$\varepsilon_{ca}(t) = \beta_{as}(t) \cdot \varepsilon_{ca}(\infty) \tag{2.19}$$

$$\varepsilon_{ca}(\infty) = 2.5 \cdot (f_{ck} - 10) \cdot 10^{-6} \tag{2.20}$$

$$\beta_{as}(t) = 1 - \exp\left(-0.2 \cdot \sqrt{t}\right) \tag{2.21}$$

Where,

$\varepsilon_{ca}(t)$ = Autogenous shrinkage strain at time t
$\beta_{as}(t)$ = Time-dependent factor (autogenous shrinkage)
$\varepsilon_{ca}(\infty)$ = Final autogenous shrinkage strain (at infinite time)
f_{ck} = Characteristic compressive strength of concrete (MPa)
t = Time since the start of shrinkage (days)

Although EN1992-1-1 (2004a) provides practical equations for shrinkage prediction, the model does not include specific terms for aggregate type, which can limit its accuracy when applied to concrete mixes with non-standard aggregates. It is hypothesised that the integration of aggregate-specific characteristics into the model could enhance the precision of shrinkage predictions, particularly for concrete mixes that use South African aggregates under unique environmental conditions.

2.6.5 EN1992-1-1 Assumptions on Modulus of Elasticity (E-value)

The modulus of elasticity (E-value) of concrete is a fundamental parameter that influences stress-strain behaviour, and EN1992-1-1 (2004a) provides an empirical formula for estimating E-value based on the characteristic compressive strength of the concrete. This subsection discusses the assumptions underlying this formula, the influence of aggregate type and concrete age.

EN1992-1-1 (2004a) suggests Equation 2.22 for estimating the mean modulus of elasticity of concrete (E_{cm}).

$$E_{cm} = 22 \cdot \left(\frac{f_{\text{ck}}}{10}\right)^{0.3} \tag{2.22}$$

Where,
E_{cm} = Mean modulus of elasticity of the concrete (Pa)
f_{ck} = Characteristic compressive strength of the concrete (Pa)

Equation 2.22 is based on concrete made with quartzite aggregates under standard curing and environmental conditions (EN1992-1-1 2004). The use of quartzite aggregates serves as the baseline for estimating E_{cm}, and deviations in aggregate type or curing conditions can significantly affect the accuracy of this prediction.

The aggregate type has a significant effect on the modulus of elasticity, as it significantly contributes to the stiffness of the concrete (Jurowski and Grzeszczyk, 2018; Kim et al., 2022; Raheem et al., 2021). EN1992-1-1 (2004a) acknowledges this variability and recommends adjustments for specific aggregate types:

- **Limestone Aggregates:** Increase E_{cm} by 20%.
- **Basalt Aggregates:** Decrease E_{cm} by 10%.

Moreover, the European standard EN1992-1-1 (2004a) provides adjustment factors to estimate the modulus of elasticity at different ages relative to its 28-day value. The modulus of elasticity of concrete is age-dependent, with significant increases measured as the concrete matures due to ongoing hydration and bond development (Li et al., 2018; Sun and Fanourakis, 2021; Zhou et al., 2022).

The EN1992-1-1 (2004a) assumptions for E-value may not accurately reflect the properties of concrete made with South African aggregates. South African aggregates have different mineralogical compositions compared to European quartzite or limestone, leading to potential deviations in the predicted modulus of elasticity.

2.7 Numerical Modelling of Heat Transfer

Heat transfer in materials occurs through three fundamental mechanisms: conduction, convection, and radiation (Whitaker, 1977). In concrete structures, these mechanisms govern how heat is absorbed, stored, and dissipated, ultimately influencing temperature distributions and structural behaviour. Figure 2.1 shows the different heat transfer processes and climatic factors that affect a concrete structure, specifically the heat exchange between a typical concrete beam and the outside environment.

Conduction occurs when heat absorbed on the surface of the concrete (from solar radiation and other sources) is transferred through the material to the interior. The thermal conductivity of concrete is a key factor in determining its ability to conduct heat (Wang et al., 2011a). In Figure 2.1, although not explicitly shown with an arrow in the diagram, conduction is the process responsible for the movement of heat from the surface of the concrete to the centre.

Convection plays a crucial role in the heat transfer processes that involve concrete and the surrounding atmosphere. The exchange of heat between the concrete surface and the ambient air occurs because of temperature differences, leading to either heat gain or loss. In the context of Figure 2.1, convection is visually represented by the wavy red arrows labelled "Heat convection" on the side of the concrete element. Additionally, the wavy black arrow above the concrete element, labelled "Wind", indicates how the wind can enhance the convective process. The heat transfer process is influenced by factors including differences in temperature between individual cells, pore size, and temperature-dependent thermal conductivity (Rivera-Salinas et al., 2021). Yang et al. (2024) showed that the wind speed is a significant factor that affects the convective heat transfer coefficient of the concrete surfaces.

Solar radiation is the heat energy emitted by the sun, which includes short-wave radiation (directly from the sun) and long-wave radiation (infrared radiation). Short-wave radiation heats the surface of the concrete, while the concrete emits long-wave radiation as it cools (Whitaker, 1977). From Figure 2.1:

- Short wave radiation: Represented by the straight red arrows labelled "Direct solar radiation", "Solar reflection", and "Scattered radiation". These arrows show how sunlight (short-wave radiation) strikes the concrete surface directly.
- Long wave radiation: The heat emitted from the concrete as it cools, represented by the red wavy arrows labelled "Heat radiation". This is the infrared radiation emitted from the concrete back into the environment.

Studies have explored the influence of solar radiation absorption on the temperature field of concrete structures, emphasising its role in determining the thermal behaviour of concrete elements (Liang et al., 2023; Lu et al., 2021; Westgate et al., 2015). Liang et al. (2023) showed solar radiation can cause significant temperature variations on concrete surfaces, with surface temperatures reaching up to 52° C under the influence of solar radiant heat.

2.7.1 Governing Equation for Heat Transfer

Heat transfer is governed by Fourier's law, which states that heat flow is proportional to a negative temperature gradient and thermal conductivity (Dincer and Erdemir, 2021; Fourier, 1878). In two-dimensional analysis, the governing equation for heat conduction (Equation 2.23) and thermal diffusivity (Equation 2.3) are essential to calculate the temperature profiles within the material.

$$\frac{\partial T}{\partial t} = \alpha_d \left(\frac{\partial^2 T}{\partial x^2} + \frac{\partial^2 T}{\partial y^2} \right) \tag{2.23}$$

Where,

T = Temperature at any point within the material.
t = Time
α_d = Thermal diffusivity (see Equation2.3)
k = Thermal conductivity
ρ = Density of the material
c_p = Specific heat capacity

2.7.2 Initial and Boundary Conditions

For accurate heat flow modelling, initial and boundary conditions must be defined. The initial conditions (Equation 2.24) specify the temperature distribution at the beginning of the simulation, while the boundary conditions (Equation 2.25) address the radioactive and convective heat flux on concrete surfaces (Whitaker, 1977).

$$T_{t=0} = f(x, y) \tag{2.24}$$

$$k\frac{\partial T}{\partial r} = q_t \tag{2.25}$$

Where,

$T_{t=0}$ = Initial temperature distribution, varying with x and y coordinates
k = Thermal conductivity
r = Normal direction to the surface
q_t = Total heat flux on surface boundaries

As shown by Abid et al. (2021) and Zhang et al. (2020a), the total heat flux (q_t) can be decomposed into components of convective heat flux (q_c), long-wave radiation (q_l), and short-wave radiation (q_s) (Equation 2.26), providing a complete thermal boundary description.

$$q_t = q_c + q_l + q_s \tag{2.26}$$

Where,

q_t =Total heat flux
q_c = Convective heat flux component
q_l = Long-wave radiation heat flux component
q_s = Short-wave radiation heat flux component

Each component in Equation 2.26 can be expressed as in Equation 2.27 to 2.29 (Cengel, 2004; Zhang et al., 2020a):

$$q_c = h_c(T_s - T_a) \tag{2.27}$$

$$q_l = eC_0[(T_s + 273)^4 - (T_a + 273)^4] \tag{2.28}$$

$$q_s = a_s I_{Total} \tag{2.29}$$

Where,

T_s = Surface temperature ($^\circ C$)
T_a = Ambient temperature ($^\circ C$)
h_c = Convective heat transfer coefficient
e = Emissivity of the concrete surface
a_s = Absorptivity
C_0 = Stefan-Boltzmann constant ($5.67 \times 10^{-8} W/m^2K^4$)
I_{Total} = Total incident solar radiation applied on surface

Convective heat transfer is primarily driven by temperature differences between the concrete surface and the surrounding air. The convective heat transfer coefficient (h_c) is surface dependent, influenced by factors such as wind speed (v) and surface orientation (Abid et al., 2016; Zhang et al., 2020a). The empirical formulation in Equation 2.30, originally proposed by Kehlbeck (1975). Numerous researchers, such as Zhang et al. (2020a) and Cai et al. (2022), have applied this equation in their analyses, showing its relevance. Although developed for box girder bridges, the formulation's parameters align with most concrete structures exposed to environmental loading.

$$h_c = \begin{cases} 3.83v + 4.67 & \text{top surface} \\ 3.83v + 2.17 & \text{bottom surface} \\ 3.83v + 3.67 & \text{lateral surface} \\ 3.5 & \text{internal surface} \end{cases} \tag{2.30}$$

Where,
h_c = Convective heat transfer coefficient
v = Wind speed (m/s)

The wind speeds considered by Cai et al. (2022) ranged from approximately 0m/s to 12m/s and yielded accurate thermal predictions, showing the applicability of this formulation under typical environmental conditions for exposed concrete elements. It should be noted that this formulation does not explicitly include the leeward surface, where wind velocities are typically lower. Although this is a limitation, it is unlikely to impact the accuracy of the predictions, given that the primary focus is on windward and exposed surfaces.

2.7.3 Solar Radiation Modelling

The solar radiation incident on a surface comprises three main components: beam radiation, diffuse radiation, and ground reflected radiation, with intensity affected by the orientation, location, and solar position of the structure. The total solar radiation (I_{Total}) on a horizontal surface can be expressed as in Equation 2.31 (Cai et al., 2022; Zhang et al., 2020a). The total solar radiation (I_{Total}) is subsequently used as input in Equation 2.29, which estimates the amount of solar radiation absorbed by a surface (q_s).

$$I_{Total} = I_{Beam} + I_{Diffuse} + I_{GroundReflected} \tag{2.31}$$

Where,
I_{Beam} = Direct beam radiation
$I_{Diffuse}$ = Scattered diffuse radiation
$I_{GroundReflected}$ = Reflected ground radiation

Beam radiation refers to direct solar radiation that travels along a straight path from the sun to the surface without being scattered. Diffuse radiation, on the other hand, results from the scattering in the atmosphere due to air molecules, dust, and aerosols. Figure 2.10 shows extraterrestrial solar radiation (I_{sc}) entering the Earth's atmosphere and splitting into beam radiation (I_{Beam}) and diffuse radiation ($I_{Diffuse}$) due to atmospheric interactions. The Figure does not include ground-reflected radiation.

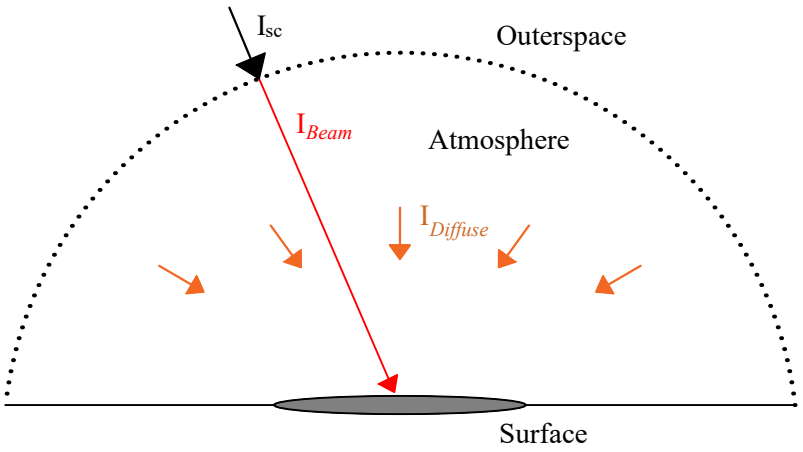

Figure 2.10: Extraterrestrial radiation (I_{sc}) splitting into direct beam (I_{Beam}) and scattered diffuse ($I_{Diffuse}$) components (adapted from Stephen et al. (2010))

Extraterrestrial solar radiation (I_{sc}) is the radiation received at the outer edge of the Earth's atmosphere, which varies slightly due to the elliptical orbit of the Earth. Calculated as in Equation 2.32 (Kalogirou, 2009). The equation accounts for the elliptical orbit of the Earth and calculates the solar radiation received at the outer edge of the Earth's atmosphere as a function of the day of the year (N). Equation 2.32 is independent of the hemisphere since it is based on the Earth's position relative to the sun and applies universally across the globe.

$$I_{sc} = G_{sc} \cdot \left(1 + 0.033 \cdot \cos\left(\frac{360 \cdot N}{365}\right)\right) \tag{2.32}$$

Where,

I_{sc} = Extraterrestrial solar radiation
G_{sc} = Solar constant (1361 W/m^2 from Thekaekara and Drummond (1971))
N = Day of the year (1 to 365)

Beam Radiation (I_{BT}) on an Inclined Surface

The beam radiation incident on an inclined surface is influenced by solar angles, which depend on the Earth's position relative to the sun and the orientation of the surface. These angles include the solar declination angle (δ), hour angle (w), zenith angle (θ_z), and the angle of incidence (θ). The incident angle (θ) is used as an input to calculate the solar exposure on structural surfaces and is given by Equation 2.33, incorporating the geometry and solar position parameters shown in Figure 2.11 (Kalogirou, 2009).

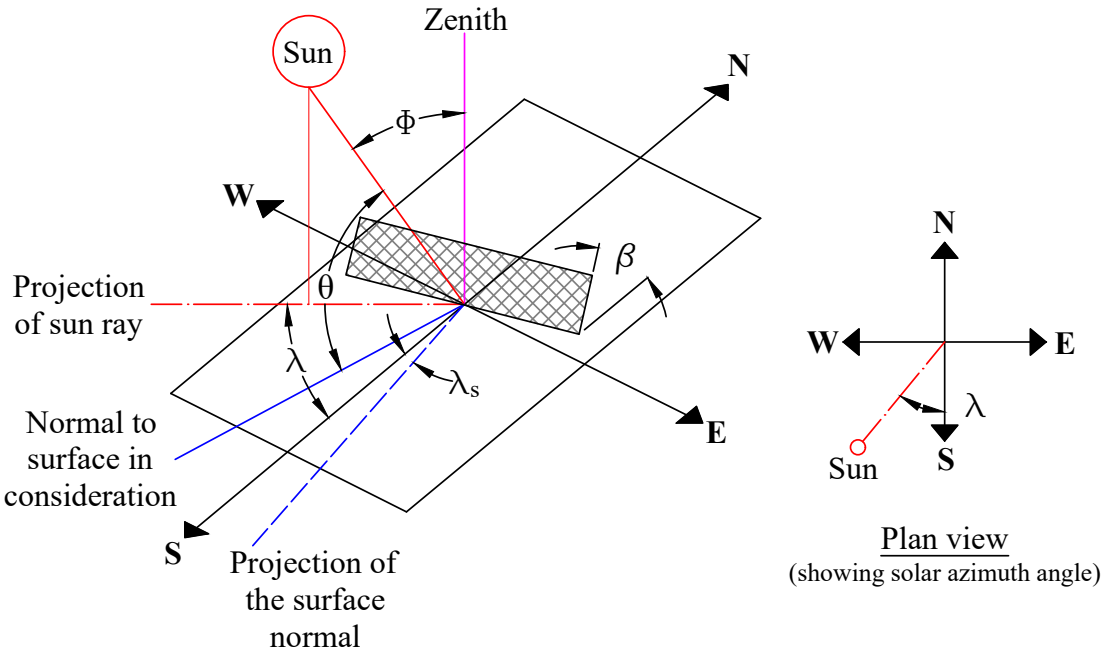

Figure 2.11: The relative position relationship between the sun and the inclined plane (adapted from Kalogirou (2009)).

$$\begin{aligned}\cos(\theta) = &\sin(\delta)\cdot\sin(\phi)\cdot\cos(\beta)\\ &-\sin(\delta)\cdot\cos(\phi)\cdot\sin(\beta)\cdot\cos(\gamma)\\ &+\cos(\delta)\cdot\cos(\phi)\cdot\cos(w)\cdot\cos(\beta)\\ &+\cos(\delta)\cdot\sin(\phi)\cdot\sin(\beta)\cdot\cos(w)\cdot\cos(\gamma)\\ &+\cos(\delta)\cdot\sin(\beta)\cdot\sin(\gamma)\cdot\sin(w)\end{aligned} \tag{2.33}$$

Where,

θ = Solar incident angle
β = Tilt angle of the surface relative to the horizontal plane
ϕ = Local latitude
γ = Angle between surface azimuth angle (λ_s) and solar azimuth angle (λ)
δ = Solar declination angle
w = Hour angle of the sun

The solar declination angle (δ) represents the angular position of the sun relative to the plane of the Earth's equator. It varies throughout the year due to the Earth's axial tilt and elliptical orbit around the sun, reaching its maximum and minimum values at the solstices. The solar declination angle is calculated using Equation 2.36, where N is the day of the year. In the southern hemisphere, the seasonal variation of the solar declination angle

is reversed compared to the northern hemisphere. The sun reaches its highest declination ($\delta = +23.45°$) during the December solstice and its lowest declination ($\delta = -23.45°$) during the June solstice. This reversal affects the solar angles and solar radiation patterns specific to the hemisphere but does not require modifications to Equation 2.36, as the equation inherently accounts for this reversal based on the Earth's orbit (Kalogirou, 2009).

The zenith angle θ_z and solar azimuth angle λ are further defined as in Equation 2.34 and Equation 2.35, respectively (Kalogirou (2009)).

$$\cos\theta_z = \sin\delta\sin\phi + \cos\delta\cos\phi\cos w \tag{2.34}$$

$$\cos\lambda = \frac{\cos\theta_z\sin\phi - \sin\delta}{\sin\theta_z\cos\phi} \tag{2.35}$$

$$\delta = 23.45\sin\left(360\times\frac{284+N}{365}\right) \tag{2.36}$$

Where,

θ_z = Solar zenith angle
λ = Solar azimuth angle
ϕ = Local latitude
δ = Solar declination angle
w = Hour angle of the sun
N = Day of the year

The beam radiation directly from the sun (I_{Beam}) can be decomposed into its components on different surfaces: (a) beam radiation on a horizontal surface (I_{BH}) and (b) beam radiation on a tilted surface (I_{BT}), as shown in Figure 2.12. Using solar angles, the beam radiation incident on a horizontal surface can be calculated with Equation 2.39. Kalogirou (2009) shows that beam radiation on any inclined surface can be determined using a tilt factor (R_B) and I_{BH} using Equation 2.39. R_B depends on the solar incident angle and the zenith angle (Equation 2.38).

$$I_{BT} = I_{BH}\cdot R_B \tag{2.37}$$

$$R_B = \frac{\cos(\theta)}{\cos(\theta_z)} \tag{2.38}$$

Where,

I_{BT} = Beam radiation on a tilted surface
I_{BH} = Beam radiation on a horizontal surface (Equation 2.39)
R_B = Beam radiation tilt factor
θ = Solar incident angle

θ_z = Solar zenith angle

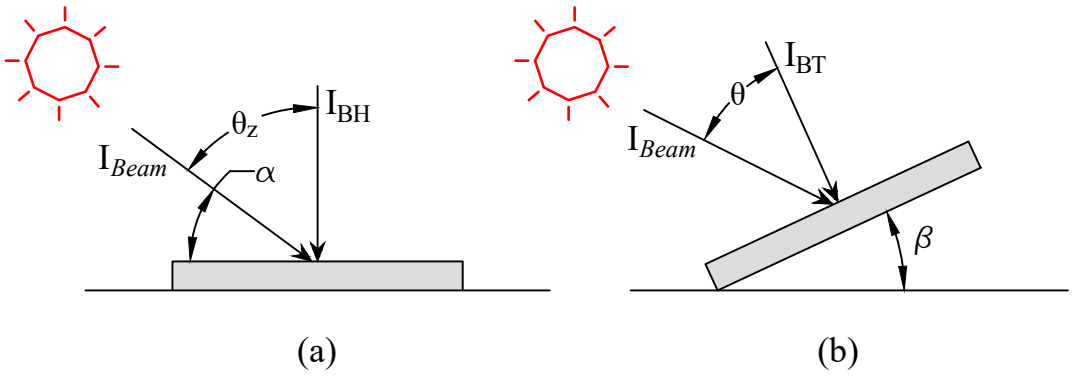

Figure 2.12: Beam radiation on horizontal and tilted surfaces (adapted from Kalogirou (2009)).

The beam transmission coefficient (τ_B) plays a critical role in adjusting the beam radiation on a horizontal surface (I_{BH}) by accounting for the attenuation of solar radiation as it passes through the atmosphere. This attenuation is influenced by the amount of air mass and the clarity of the atmosphere, both of which are captured in the following equations.The beam transmission coefficient is calculated using Equation 2.40. The beam transmission coefficient is a function of the optical air mass (Equation 2.41) and optical depth (Fu, 2006).

$$I_{BH} = I_{sc} \cdot \tau_B \cdot \cos(\theta_z) \tag{2.39}$$

$$\tau_B = e^{-A_m \cdot A_d} \tag{2.40}$$

$$A_m = \frac{1}{\cos \theta_z} \tag{2.41}$$

Where,

I_{sc} = Extraterrestrial solar radiation
τ_B = Beam transmission coefficient
A_m = Optical air mass
A_d = Optical depth (Clearness index)
θ_z = Solar zenith angle

The optical depth (A_d) represents the combined effects of atmospheric components, such as aerosols, water vapour, and other gases that scatter and absorb solar radiation. It is often determined using empirical models or measured data. Common approaches include Angstrom's Turbidity Model, which relates the optical depth to aerosol concentration

and particle size distribution Ångström (1929). Additionally, optical depth can be directly obtained from atmospheric monitoring stations or satellite-based measurements. The Moderate Resolution Imaging Spectroradiometer provides global atmospheric data, including aerosol properties, at high spatial and temporal resolution (Remer et al., 2005). The Aerosol Robotic Network, a ground-based monitoring network, offers high-quality, site-specific measurements of aerosol optical depth (Holben et al., 1998).

Diffuse Radiation (I_D) on an Inclined Surface

Kalogirou (2009) provides a method for calculating diffuse radiation on a tilted surface using the sky angle factor (F_{wb}) and the diffuse fraction (k_{td}). The diffuse radiation incident on a tilted surface is calculated using Equation 2.42.

$$I_{DT} = I_{DH} \cdot F_{wb} \tag{2.42}$$

$$F_{wb} = \frac{1 + \cos(\beta)}{2} \tag{2.43}$$

Where,

I_{DT} = Diffuse radiation on a tilted surface
I_{DH} = Diffuse radiation on a horizontal surface
F_{wb} = Sky angle factor, based on tilt angle (β)

The diffuse radiation on a horizontal surface is determined using the Erbs separation model (1982), which defines the diffuse fraction (k_{td}) as a function of the clearness index (K_t) (Kalogirou, 2009). This model was chosen because of its good performance (Gueymard, 2009). Using Equation 2.45, the diffuse radiation on a horizontal surface is calculated as shown in Equation 2.44.

$$I_{DH} = k_{td} \cdot I_{BH} \tag{2.44}$$

Where,

I_{DH} = Beam radiation on a horizontal surface
k_{td} = Diffuse radiation on a horizontal surface

The diffuse fraction (k_{td}) is calculated using a piecewise function, as shown in Equation 2.45. The clearness index (K_t) is defined as the ratio of beam radiation to extraterrestrial radiation, calculated using Equation 2.46.

$$k_{td} = \begin{cases} 1 - 0.09 \cdot K_t & \text{if } K_t \leq 0.22 \\ 0.9511 - 0.1604 \cdot K_t + 4.388 \cdot K_t^2 - 16.638 \cdot K_t^3 + 12.336 \cdot K_t^4 & \text{if } 0.22 < K_t \leq 0.8 \\ 0.165 & \text{if } K_t > 0.8 \end{cases} \tag{2.45}$$

$$K_t = \frac{I_{BH}}{G_{sc} \cdot \cos(\theta_z)} \tag{2.46}$$

Where,

I_{BH} = Beam radiation on a horizontal surface
k_{td} = Diffuse fraction
K_t = Clearness index
G_{sc} = Solar constant (1361 W/m^2 from Thekaekara and Drummond (1971))
θ_z = Solar zenith angle

Ground Reflectance

The total solar radiation incident on a surface includes a reflected component of the ground, which depends on the ground reflectance (ρ_g) and the angle of the surface relative to the ground. Ground reflectance accounts for the solar radiation reflected by the ground and subsequently received by the surface. The ground reflected radiation on a tilted surface (I_G) is calculated using Equation 2.47. This depends on the ground angle factor (F_{wd}), which is a function of the tilt angle (β), and the combined beam and diffuse radiation incident on a horizontal surface ($I_{BH} + I_{DH}$). The ground angle factor (F_{wd}) is calculated using Equation 2.48, where the tilt angle determines the proportion of reflected radiation reaching the surface.

$$I_G = F_{wd} \cdot \rho_g \cdot (I_{BH} + I_{DH}) \tag{2.47}$$

$$F_{wd} = \frac{1 - \cos(\beta)}{2} \tag{2.48}$$

Where,

I_G = Ground reflectance radiation on a tilted surface
I_{DH} = Diffuse radiation on a horizontal surface
I_{BH} = Beam radiation on a horizontal surface
I_R = Ground-reflected radiation
ρ_g = Ground reflectance, typically 0.2 for standard conditions (Zhang, 2021)
F_{wd} = Ground angle factor, determined by the tilt angle (β)

The reflectance of the ground is influenced by surface properties such as vegetation, soil type, or artificial materials such as concrete or asphalt. For most natural and built environments, ρ_g ranges between 0.1 (low reflectance, for example, dark soil) and 0.4 (high reflectance, for example, snow or light concrete). For this study, ρ_g is assumed to be 0.2, consistent with typical conditions for urban and suburban environments (Zhang, 2021).

2.7.4 Methods of Heat Transfer Analysis

In the context of heat transfer analysis, several numerical methods are widely used to model and simulate the thermal behaviour of materials, including concrete. The following subsections summarise these methods, focussing on their applications and effectiveness in analysing heat transfer in concrete structures.

Finite Element Method

The Finite Element Method (FEM) is a widely used numerical technique for heat transfer analysis. This method discretises the domain into smaller elements and applies the governing equations of heat transfer to each. FEM is particularly effective for modelling complex geometries, heterogeneous materials, and varying boundary conditions, making it suitable for analysing concrete structures exposed to environmental loads. Furthermore, FEM handles transient heat transfer with high accuracy, which is crucial to capture time-dependent thermal responses. Its integration into commercial software, such as ABAQUS/CAE (2023), ensures robust simulation capabilities for both calibration and sensitivity analyses (Dunić et al., 2015; Flitta et al., 2013; Namiki et al., 2020; Yan, 2014).

Finite Difference Method

The Finite Difference Method (FDM) approximates derivatives using finite differences at discrete points. While effective for problems involving regular geometries, it is less suitable for complex geometries or non-uniform boundary conditions compared to FEM. FDM is often used in time-stepping solutions for transient heat transfer problems (Hou et al., 2013).

Meshless Methods

Meshless methods, such as the Node-Based Smoothed Finite Element Method, do not require a mesh for discretisation, offering advantages for cases with large deformations or complex boundaries. However, they remain less validated and computationally efficient for large-scale practical applications compared to FEM (Gao and Wei, 2014; Šarler and Pepper, 2004).

Boundary Element Method

The Boundary Element Method (BEM) reduces the dimensionality of a problem by solving for boundary values rather than throughout the domain. This approach is efficient for infinite or semi-infinite domains but is not as versatile as FEM for capturing detailed internal temperature gradients (Prata et al., 2012).

Superposition Method

The Superposition Method simplifies linear heat transfer problems by dividing them into solvable components. Although useful for summing effects from multiple heat sources, it lacks the capability to handle non-linear or complex scenarios (Jiang et al., 2018).

2.8 Environmental Loading Studies on Concrete Structures

Environmental loading significantly influences the thermal and mechanical behaviour of concrete structures, especially those exposed to variable climatic conditions. Factors such as solar radiation, ambient temperature fluctuations, wind, and precipitation can induce complex thermal gradients and strain distributions within concrete elements. These effects are further compounded by the geometry, size, and material properties of the structure, as well as the duration and intensity of exposure to environmental loads (Hossain et al., 2021; Lee et al., 2011; Tayşi and Abid, 2015).

Previous studies have investigated the impact of environmental loading on concrete structures from various perspectives, including the development of thermal gradients, the role of boundary conditions, and the effects of prolonged exposure on structural performance. Research has also focused on quantifying temperature-induced strains and stresses, examining the thermal response of different concrete mixes, and validating analytical and numerical models with experimental data (see Table 2.8).

This section reviews key findings from these studies, with an emphasis on their methodologies, results, and relevance to structural engineering. Particular attention was paid to studies addressing the role of aggregate type, geometry, and exposure conditions in shaping the thermal and mechanical responses of concrete elements. By synthesising insights from the existing literature, this review provides a foundation for understanding the influence of environmental loading on concrete structures and identifies the knowledge gaps addressed in this research.

2.8.1 Experimental Investigations on Thermal Response

Previous experimental studies have focused mainly on the influence of environmental loading on bridge structures, often considering only a single concrete mix and element

shape. This section provides an overview of key studies to illustrate the scope of past research and highlight how experimental methods have evolved. However, these studies do not offer direct comparisons with one another, as they differ significantly in terms of material properties, structural configurations, and environmental conditions.

Numerous recent experimental studies have been conducted to investigate thermal gradients in concrete elements. These studies typically involve embedding temperature sensors in concrete specimens or structures to monitor temperature variations over time, under different environmental conditions. For example, Abid et al. (2016) studied the effects of thermal gradients on concrete structures, especially examining how these gradients can influence the mechanical behaviour of concrete under various environmental conditions. Abid et al. (2016) used experimental methods to measure the response of concrete samples subjected to controlled thermal gradients, demonstrating that as the temperature differential increased, the probability of cracking also increased due to induced thermal stresses. The study by Abid et al. (2016) investigated temperature gradients in a concrete box-girder segment with a top slab width of 7.25m, an overall depth of 2.4m, and a length of 2.1m (Figure 2.13). The box-girder was supported by a 2m high reinforced concrete frame (see Figure 2.14) to simulate environmental conditions, including ground-reflected radiation and convection on the lower surface, while thermally isolating the frame from the girder.

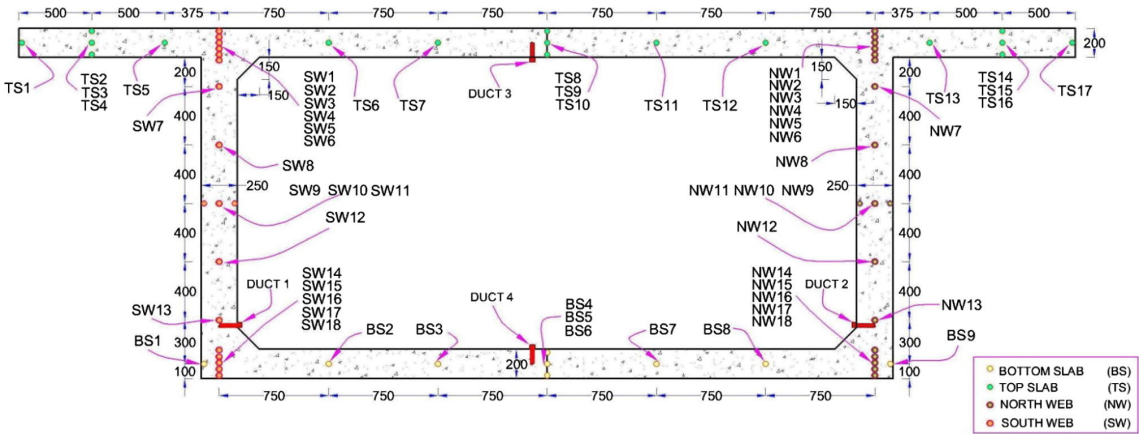

Figure 2.13: Cross-section details of box-girder and locations of the thermocouples in Abid et al. (2016) (all dimensions are in mm).

In another study, Feng et al. (2022) examined the effects of thermal gradients on three-cell concrete box girders exposed to seasonal temperature changes as shown in Figure 2.15. The research used air temperature, solar radiation, and wind speed to model temperature prediction equations.

Yang et al. (2023) conducted an experimental study to examine the influence of environmental factors, particularly solar radiation and ambient temperature, on the thermal

(a) (b)

Figure 2.14: Abid et al. (2016) experimental box-girder segment: (a) formwork construction, (b) sealing with isolation boards.

gradients within a thin-walled concrete sample. Yang et al. (2023) characterised thin-walled concrete structures by their relatively small thickness in relation to their other dimensions, making them particularly susceptible to environmental temperature variations and thermal gradients. In this setup, they used a concrete block with insulation applied on the sides to simulate thermal behaviour representative of a thin-walled structure. Temperature sensors were embedded throughout the sample to capture the vertical and lateral temperature distribution over an annual cycle. The experimental setup is shown in Figure 2.16. This experimental design provided insight into the effects of seasonal and diurnal temperature changes on the thermal profile of the structure.

Yang et al. (2023) used seasonal trends to show statistically significant seasonal equivalent days. This allowed for a better prediction of seasonal variations in effective temperature and gradient temperatures. In the context of this study, this research highlights the relevance of understanding thermal gradients for structural applications. The insights gained from the study conducted by Yang et al. (2023) provide a basis for evaluating the thermal performance of concrete elements in real environmental settings, particularly with regard to the impact of solar radiation on the temperature distribution. The findings support the development of design considerations to manage thermal effects.

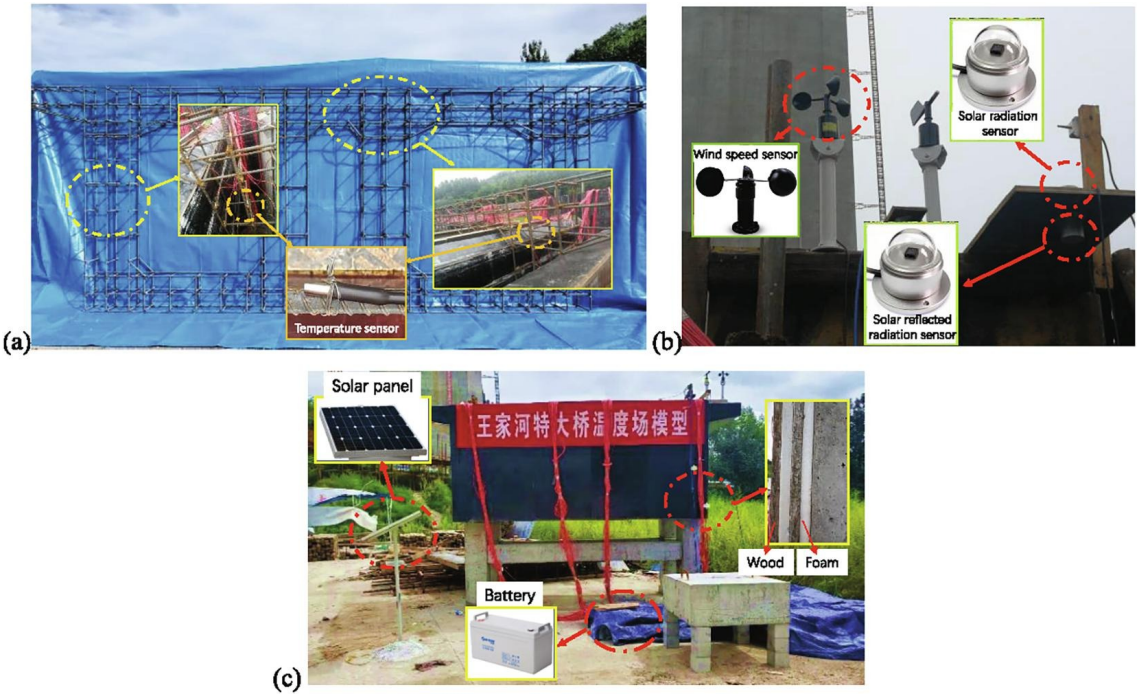

Figure 2.15: Feng et al. (2022) Model photograph: (a) temperature sensors, (b) 1 wind speed sensor and 2 solar radiation sensors, (c) overall photograph.

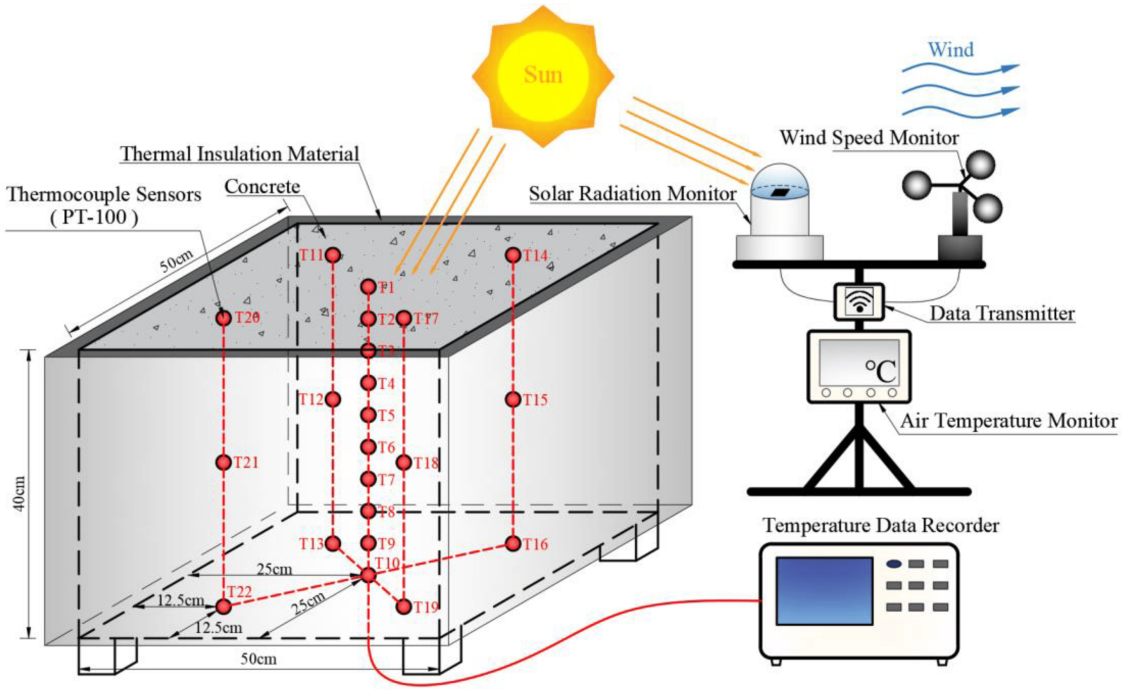

Figure 2.16: Diagram of the measurement tests for concrete temperature and environmental factors in Yang et al. (2023).

2.8.2 Summary of Environmental loading Studies

A summary of the previous literature on environmental loading on concrete structures is shown in Table 2.8. The summary highlights the importance of understanding the thermal properties of concrete elements under environmental load. Several key themes emerge from these studies, demonstrating the depth and breadth of current research in this area.

- **Thermal Properties and Structural Behaviour:** Studies such as those of Zhu (2024), Liang (2024), and Min et al. (2016) highlight the role of thermal properties, such as thermal conductivity, specific heat capacity and coefficient of thermal expansion, in influencing the thermal and structural response of concrete. These properties govern temperature distributions and their associated stresses, which are critical for assessing concrete's durability and structural performance.
- **Environmental Interactions:** Research by Hu et al. (2012), Norouzi et al. (2016), and Sheng et al. (2022) highlights the dynamic interaction between environmental factors (e.g., solar radiation, wind speed and ambient temperature) and thermal behaviour in concrete structures. These findings emphasise the need to incorporate realistic boundary conditions in numerical simulations to accurately capture complex thermal responses.
- **Applications and Design Considerations:** Studies such as those of Murphy et al. (2014), Lu et al. (2021), and Zheng (2023) demonstrate how understanding the thermal properties of concrete can optimise design strategies for applications ranging from energy foundations to large-scale infrastructure such as bridges. These works highlight the relevance of thermal considerations in reducing structural risks and enhancing performance under varying environmental conditions.
- **Advancements in Numerical and Experimental Methods:** The development and application of advanced numerical models, such as those discussed by Jin et al. (2021) and Sheng et al. (2020), demonstrate the value of simulation techniques to predict thermal behaviour. These approaches complement experimental methods, offering deeper insight into the factors influencing temperature gradients and thermal stresses.

Table 2.8: Summary of Literature on Thermal Properties and Behaviour of Concrete

Study	**Focus Area**	**Key Findings**
Hu et al. (2012)	Thermal properties in concrete pavements	Highlights that thermal properties, including the coefficient of thermal expansion and thermal conductivity, significantly influence the thermal response of concrete pavements. Improper selection of materials with varying thermal properties can lead to stresses and cracking, ultimately affecting the durability of concrete structures.
Murphy et al. (2014)	Thermal properties in energy foundations	Indicates that longer horizontal run-out lengths can reduce apparent thermal conductivity due to increased concrete mass and altered heat transfer dynamics. Highlights the importance of understanding thermal properties for optimising the performance of concrete in thermal applications.
Min et al. (2016)	Influence of damage levels on thermal properties of concrete	Highlights that thermal conductivity is significantly affected by damage levels due to loading, which influences the temperature response of concrete structures under heating and cooling. Emphasises the critical relationship between thermal properties and durability, underscoring the need to account for these effects in structural assessments.
Norouzi et al. (2016)	Temperature effects on structural properties of concrete	Discusses how variations in temperature significantly affect the structural properties of concrete. Emphasises the need to monitor these changes to assess potential structural damage and highlights the correlation between daily thermal responses of concrete towers and environmental temperature fluctuations.

Continued on next page

Continued from previous page

Study	**Focus Area**	**Key Findings**
Chung et al. (2017)	Grading of lightweight aggregates in lightweight concrete	Discusses how the grading of lightweight aggregates significantly influences the thermal properties of lightweight concrete, particularly its thermal conductivity and density. Highlights the critical relationship between aggregate characteristics and the thermal response of concrete, emphasising the importance of optimising aggregate selection for desired thermal performance.
Foteinaki et al. (2019)	Dynamic thermal response in low-energy buildings	Emphasises how the thermal properties of concrete elements influence temperature fluctuations and heat storage potential. Highlights the importance of considering concrete's thermal characteristics for effective space heating strategies and energy management in residential buildings.
Sheng et al. (2020)	Time-varying temperature fields in curved concrete box girder bridges	Develops a three-dimensional finite element model to analyse time-varying temperature fields in small radius curved concrete box girder bridges. Highlights the influence of environmental factors, such as solar radiation and wind speed, on temperature distribution profiles, providing insights into the thermal behaviour of concrete bridges under varying conditions.

Continued on next page

Continued from previous page

Study	**Focus Area**	**Key Findings**
Jin et al. (2021)	Temperature distributions in mass concrete during construction	Discusses temperature control strategies in the Jinsha River Bridge's mass concrete, emphasising the importance of managing internal temperatures, temperature differences, and cooling strategies. Demonstrates effective numerical simulations and monitoring techniques for optimising concrete temperature management during construction to prevent thermal stresses and cracks.
Lu et al. (2021)	Temperature distribution in concrete box girder bridges under solar radiation	Highlights the relationship between solar intensity and temperature variations across different surfaces of the girder. Simulations using meteorological data reveal that tensile stresses from thermal loads can exceed design strength values, emphasising the importance of considering thermal effects in bridge design and evaluation.
Liu and Wang (2022)	Influence of water content and hydration degree on thermal properties of concrete	Establishes a calculation model showing that higher hydration levels lead to lower thermal conductivity. Highlights the relationship between thermal properties and the thermal response of concrete, crucial for understanding its thermal behaviour in engineering applications.
Zeng et al. (2022)	Temperature distributions and thermal stress in concrete bridges	Emphasises the significant impact of thermal stress due to ambient temperature variations on structural stability. Highlights a comprehensive analysis of thermodynamic properties and thermal stress performance, revealing how these factors interplay in complex environmental conditions, which is crucial for enhancing bridge design and maintenance strategies.

Continued on next page

Continued from previous page

Study	**Focus Area**	**Key Findings**
Elwakeel et al. (2022)	Restraint effects on concrete under environmental loading	Highlights how thermal and shrinkage strains in restrained concrete can lead to stresses exceeding the tensile strength, resulting in excessive cracking. Discusses the significant concern of cracking in concrete structures due to internal or external restraint under environmental loads.
Zhu (2024)	Incorporation of Microencapsulated Phase Change Materials (MPCM) in lightweight aggregate concrete panels	Demonstrates that increased MPCM dosage enhances thermal response by reducing energy demand for maintaining interior temperatures. Highlights the significant impact of thermal properties (thermal conductivity and specific heat capacity) on concrete's thermal behaviour under varying environmental conditions.
Liang (2024)	Environmental thermal effects on structural behaviour of concrete	Emphasises the significant impact of environmental thermal effects on a prestressed double-T slab made from sustainable carbon-capturing concrete. Highlights the necessity of thermal compensation in structural health monitoring systems to accurately assess the temperature-strain relationship and overall performance under thermal loads.
Ruano (2024)	Coefficient of thermal expansion in prestressed concrete beams	Discusses how the coefficient of thermal expansion affects the stress state and mechanical response of prestressed concrete beams under thermal loads. Highlights the critical role of temperature-dependent properties in determining the thermal response and overall performance of concrete structures during high-temperature events.

2.9 Summary

The review of the existing literature highlights the critical interplay between material properties and environmental loading in the performance of concrete structures. Temperature changes, influenced by factors such as solar radiation, variation in diurnal temperature, and humidity, introduce significant thermal stresses within concrete elements. These stresses, coupled with shrinkage and restraint effects, can lead to cracking and durability challenges.

The choice of aggregate type significantly affects the thermal and mechanical properties of concrete, particularly the thermal conductivity, the specific heat capacity, modulus of elasticity (E-value) and shrinkage. In South Africa, variability in aggregate properties presents challenges and opportunities to improve design practices. Local engineers must incorporate these factors, along with environmental influences, to ensure the long-term resilience of concrete structures.

Recent studies, especially from 2019 onwards, have increasingly focused on the thermal response and stress accumulation due to environmental loading, emphasising the urgent need to address climate-induced stresses and improve infrastructure sustainability. The review of past literature shows the importance of understanding how environmental factors interact with material properties to influence concrete durability and performance.

Key findings from the literature include:

- **Thermal Properties:** Aggregate type, porosity, and environmental conditions significantly influence the thermal performance of concrete. The lack of standardised test methods for thermal properties in South African codes calls for region-specific research to improve the characterisation of thermal properties, especially in local mixes.
- **Shrinkage and Restraint Effects:** Shrinkage, particularly drying shrinkage, plays a crucial role in concrete performance. The EN1992-1-1 (2004a) shrinkage model provides a foundation, though deviations may arise due to unique aggregate properties. Restraint from boundary conditions or reinforcement also influences shrinkage-induced stresses.
- **Modulus of Elasticity:** The modulus of elasticity (E-value) plays an important role in determining the response to deformation of concrete under thermal and shrinkage stresses. Variation in E-values based on aggregate type and mix design can impact how concrete elements respond to environmental loading and internal stresses. The need for standardised testing of-E values in local conditions is emphasised for more accurate design and durability predictions.

This review establishes that understanding the interaction between material properties, environmental loading, and structural restraint is critical for the effective design and durability of concrete structures.

The hypothesis driving this research is that the thermal and mechanical behaviours of concrete - impacted by aggregate type, element shape, environmental load, and restraint - considerably affect the shrinkage and thermal response, leading to stress concentration in concrete structures. This understanding aims to inform future design practices, testing methods, and material characterisation, especially in regions with extreme temperature variations.

3 Experimental Investigation

3.1 Introduction

This chapter outlines the experimental methodology undertaken to investigate the thermal and strain development of concrete elements cast with two distinct South African aggregates: Dolerite and Dolomite. The experimental design aimed to explore the effects of aggregate type, shape of concrete elements, and exposure to environmental conditions on the response to temperature and restrained stresses. To achieve this concrete shapes representing typical T-beam elements (Cube, Flange and L shape) were cast, along with cylinders and smaller samples for the characterisation of material properties.

The chapter begins by detailing the material selection process, including the properties of the aggregates and the mix designs, which were tailored to highlight thermal and mechanical differences between Dolerite and Dolomite concrete mixes. Following this, the specimen preparation process is described, including the casting, curing, and insulation of the samples. The experimental setup for outdoor exposure is then presented, which highlights how the samples were arranged and instrumented to monitor their response to natural environmental loading.

Instrumentation, including thermocouples and vibrating wire strain gauges (VWSG), was used to measure temperature changes and strain development in samples. The data acquisition system ensured consistent and precise logging of temperature and strain data, while a weather station provided complementary environmental data. In addition, specific heat capacity tests were conducted to provide thermal property data for calibration of the heat transfer model.

By the end of this chapter, a comprehensive understanding of the experimental methods used to evaluate the thermal and mechanical performance of concrete elements under winter environmental conditions will be established, which forms the basis for the analyses in subsequent chapters.

3.2 Specimen Preparation

The concrete shapes cast for this study included a Cube, a Flange, and an L-Shape (combining a Cube and a Flange). The shapes and dimensions of the concrete shapes are shown in Figure 3.1. These beam elements were cast into timber moulds, instrumented with temperature and strain sensors to capture thermal gradients and the development of strains (see Figure 3.2). In addition, concrete containing each type of aggregate was poured into large cylindrical moulds to allow prediction of deformation properties, such as the coefficient of thermal expansion and the drying shrinkage strain, which were then applied to the Cube, Flange and L-Shape elements. Smaller samples were cast to measure the mechanical properties and specific heat capacity.

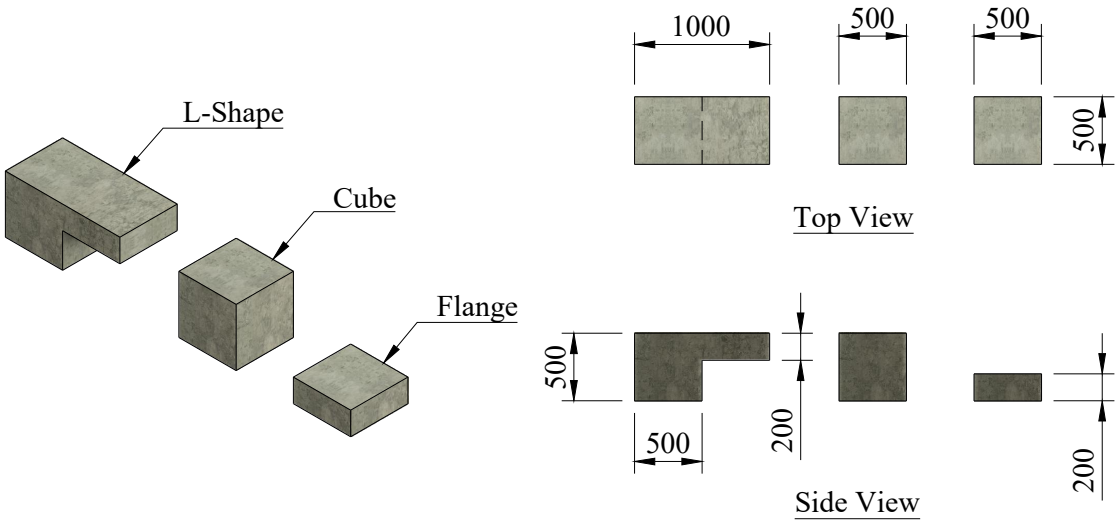

Figure 3.1: Dimensions of casted shapes: Cube, Flange, and L-Shape (all dimensions in mm).

The dimensions of the Cube and the Flange (0.5m x 0.5m x 0.5m and 0.5m x 0.2m x 0.5m, respectively) were chosen to allow the study of thermal behaviour in simple uniform geometries. The combination of the Cube and the Flange in an L-Shape allowed a comparative analysis with the separate Cube and Flange sections, facilitating the study of the impact of the combined shape on stress development (Cube alone vs Cube with Flange). Timber moulds were used to create the different shapes and each mould was sealed to prevent water loss during curing.

Two concrete cylinders (one per mix) with a diameter of 230mm and a height of 500mm were cast in plastic PVC pipes. These cylinders were used to determine the thermal properties and shrinkage of each mix. Using the cylindrical shapes, it was possible to remove thermal and shrinkage strains from the Cubes, Flanges and L-Shapes, allowing for a focused analysis of the residual and restrained strain components.

In addition, smaller samples were cast to determine the specific material properties of each concrete mix. Table 3.1 summarises the types of samples prepared for the testing of material properties.

Table 3.1: Samples used for material property tests on concrete (per mix).

Property	Sample	No. of Samples
Compressive Strength	100mm Cube	22
Density	100mm Cube	22
E-Value	100mm x 200mm Cylinder	10
Splitting Tensile Strength	100mm x 200mm Cylinder	20
Specific Heat Capacity	150mm Cube	1

For compressive strength testing, 22 cubes (100mm) were cast for each mix and cured under the same environmental conditions as the larger concrete elements to maintain consistency. These samples were tested at various intervals to track the development of compressive strength over time: four samples each at 0, 1, 7, 14, and 56 days, and six samples at 28 days. Because the 28-day compressive strength is a critical benchmark in concrete design, particularly in EN1992-1-1 (2004a), the increased number of samples ensured sufficient data for comparison and analysis. In addition, six additional cubes were water-cured for comparisons between water-cured and dry-cured samples, although these are not included in Table 3.1. Density measurements were also performed on the same cubes used for compressive strength testing, ensuring efficient use of material and consistency in the testing process.

To determine the elastic modulus (E-value) of the concrete, ten cylinders (100mm x 200mm) per mix were cast and subjected to tests at 1, 7, 14, 28, and 56 days. Two cylinders were tested at each interval to account for variability and ensure reliable results. These cylinders were also exposed to the same curing environment as the larger elements. After the E-value test, the cylinders were halved and tested for splitting tensile strength. This approach used the same material to measure two critical properties. As a result, the table reflects twenty samples for splitting tensile strength, corresponding to the two halves of each of the ten cylinders.

To determine the specific heat capacity of each mix, a single 150mm cube per mix was cast and subjected to calorimetric testing. Although only one sample per mix was tested, this was deemed appropriate for the study, which was conducted under controlled laboratory conditions. The focus of the study was to highlight the difference in thermal properties between the two concrete mixes and to emphasise the importance of measuring these properties when designing concrete elements exposed to environmental loads. Although the use of a single sample per mix limited the ability to account for variability, the results provided indicative measures of the thermal behaviour of the concrete. This

study demonstrates the importance of evaluating the thermal properties in the mix design and shows the need for future studies to incorporate a broader range of samples for more comprehensive analysis.

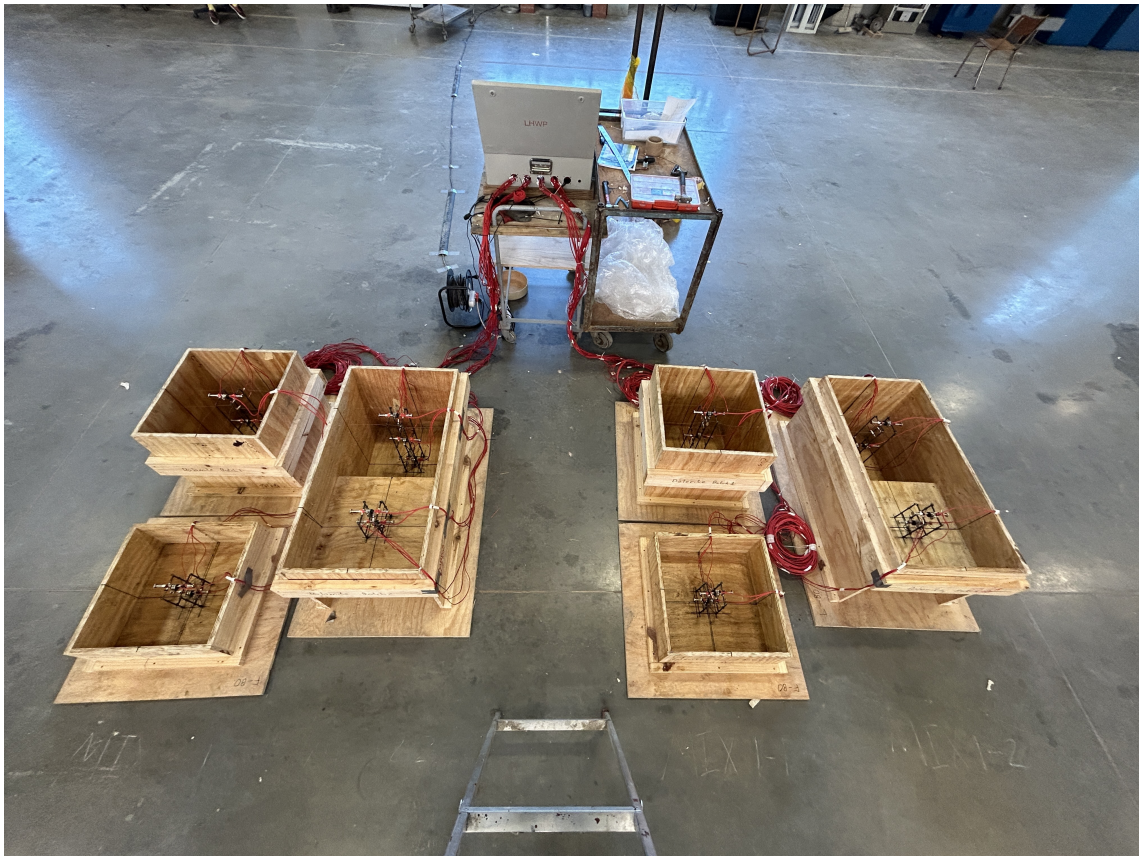

Figure 3.2: Layout of timber moulds with positioned instrumentation before casting.

3.3 Instrumentation

This section details the instrumentation used in the experimental study, covering the types, locations, and characteristics of each sensor. Each concrete shape (L-Shape, Cube and Flange) was instrumented along its vertical centreline with thermocouples and Vibrating Wire Strain Gauges (VWSGs), as shown in Figure 3.3. Thermocouples and VWSGs were positioned to capture temperature gradients and strain development across the sections, while the 230mm diamter cylinders were equipped with a single VWSG and thermocouples to determine baseline thermal and shrinkage properties for each mix.

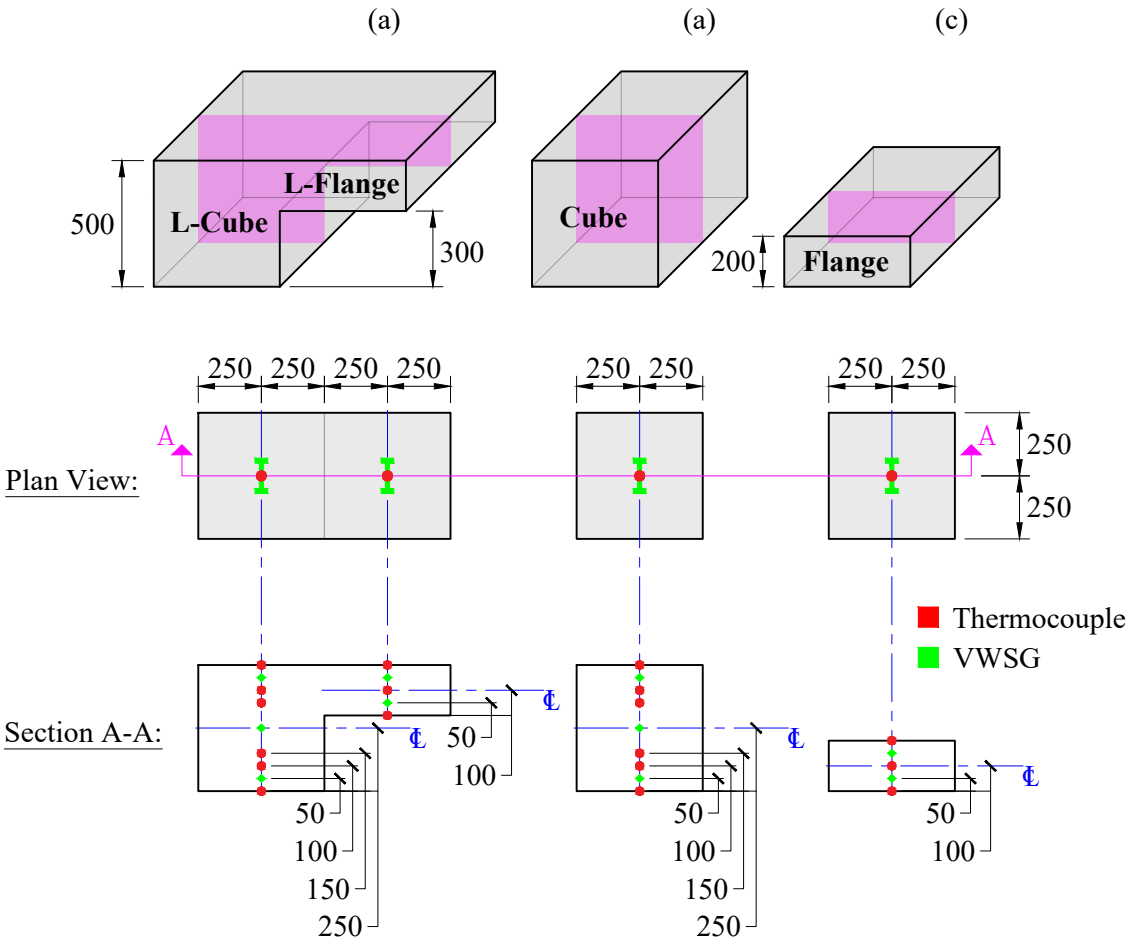

Figure 3.3: Instrumentation layout within (a) L-Shape, (b) Cube and (c) Flange (all dimensions in mm).

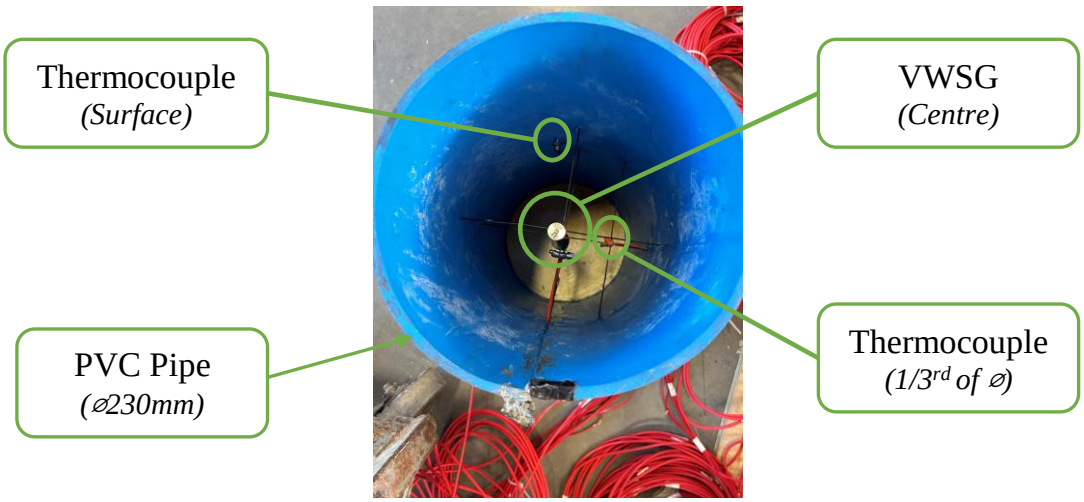

Figure 3.4: Instrumentation inside 230mm diameter cylinder.

Figure 3.3 shows the placement of the sensors within each shape. The plan view depicts the orientation of VWSGs, which were positioned to monitor strain across the cross-sections. Sections A-A illustrate the specific layout of each sensor in detail. The Cube and L-Cube section (see Figure 3.3 (a)) were instrumented in the same way, and the Flange and L-Flange section (see Figure 3.3 (a)) were instrumented in the same way. This allowed for a comparative analysis. Furthermore, each 230mm diameter cylinder was instrumented with a central VWSG, a thermocouple positioned one-third from the surface, and another thermocouple on the surface (see Figure 3.4).

3.3.1 Temperature Sensors

Temperature data were measured using two types of sensors: Type K thermocouples and Vibrating Wire Strain Gauges (VWSG). Both sensors provided reliable temperature data critical for analysing thermal gradients in concrete specimens.

Type K thermocouples (Chromel-Alumel), known for their versatility and wide temperature range (-200°C to 1100°C), were used to measure the temperature at specific points in each sample (see Figure 3.3). These thermocouples, with an accuracy of ±2°C, were positioned as follows:

- **L-Shape, Cube and Flange**: Thermocouples were installed at the top surfaces of each shape and at intervals along the depth (Figure 3.3 - red markers) to capture vertical temperature gradients.
- **230mm diameter cylinders**: Thermocouples were installed on the surface and one-third in the depth of the cylinder *(not within the scope of this study)*.

The thermocouples were connected to two 20-channel Graphtec GL820 midi loggers (2010).

Vibrating Wire Strain Gauges (VWSG) were installed in the centre of each sample to capture strains, but were also equipped with built-in thermistors to measure internal temperature. These VWSGs are highly durable and designed for long-term monitoring in harsh environments, making them suitable for this study.

- **Temperature Range**: -80°C to 150°C
- **Temperature Accuracy**: ±0.5°C

The VWSG thermistors provided data for assessing the internal temperature gradients and thermal expansion within the concrete specimens. These internal readings were complementary to the thermocouple measurements, enhancing the accuracy of the thermal analysis. Temperature readings were recorded at 10 minute intervals for the duration of the study.

3.3.2 Strain Sensors

VWSGs were embedded in each concrete shape to monitor both strain and temperature at points shown in Figure 5.13 (green markers). The VWSGs used in this experiment have the following strain specifications:

- **Range**: 3000 $\mu\varepsilon$
- **Resolution**: 1.0 $\mu\varepsilon$
- **Accuracy**: ±0.5%

VWSGs operate on the principle of vibrating wires, where changes in wire tension due to concrete deformation affect its resonant frequency. This frequency is converted to strain ($\varepsilon_{apparent}$) using Equation 3.1 (RST Instruments LTD, 2019).

$$\varepsilon_{apparent} = (R_{n+1}^2 - R_n^2)B \tag{3.1}$$

The thermally compensated strain ($\varepsilon_{true,temp}$, factoring out the temperature effects of the instrument) is given by Equation 3.2 (RST Instruments LTD, 2019).

$$\varepsilon_{true,temp} = (R_{n+1}^2 - R_n^2)B + (T_{n+1} - T_n)C_1 \tag{3.2}$$

Where,

R_{n+1} = Subsequent frequency reading ($Hz \times 10^{-3}$)
R_n = Initial frequency reading ($Hz \times 10^{-3}$)
B = Calibration factor from the manufacturer (per sensor)
T_n = Initial temperature reading (°C)
T_{n+1} = Subsequent temperature reading (°C)
C_1 = Coefficient of thermal expansion for the strain gauge (12.2 $\mu\varepsilon$/°C)

The strain data was logged using a Campbell Scientific CR6 data logger (2025), which provided an excitation pulse to the VWSGs and measured the resulting resonant frequency. Strain readings were recorded at 10 minute intervals for the duration of the study.

Strain Zeroing Process

As stress can only develop in concrete after setting, strains were zeroed when the concrete had hardened. The strains ($\varepsilon_{true,temp}$) were zeroed at the set time to establish a baseline for each gauge. The set time for each specimen was determined as the point of maximum temperature change rate during the heat of the hydration phase. The concrete setting time was determined by adopting the Derivatives method described by Ge et al. (2009)

and supported by Kang et al. (2020). The rate of temperature change, or heat of hydration curve, was calculated by differentiating the VWSGs temperature readings over time (Equation 3.3).

$$\frac{dT}{dt} = \frac{T_{n+1} - T_n}{t_{n+1} - t_n} \tag{3.3}$$

Where,
T_n = Initial temperature reading (C)
T_{n+1} = Subsequent temperature reading (C)
t_{n+1}, t_n = Successive time intervals (10 min)

The maximum rate of temperature change in Figure 3.6 was used to identify the set time at which strains were zeroed. After zeroing, which occurred between 300 and 360 minutes after casting, the strains were recorded as $\varepsilon_{measured}$, representing baseline-corrected values. Each sensor was individually zeroed to account for differential setting times within the concrete.

In the plot shown in Figure 3.6, the sensors are displayed as shades of the respective shape's colour (e.g., lighter to darker shades of green for the Flange sensors). This approach visually differentiates sensors based on their depth, with lighter shades indicating sensors closer to the top and darker shades indicating sensors closer to the bottom. This shading helped to separate the shapes and their corresponding positions within the geometry, providing a clear representation of the data across different depths. Figure 3.5 shows the naming convention used in Figure 3.6.

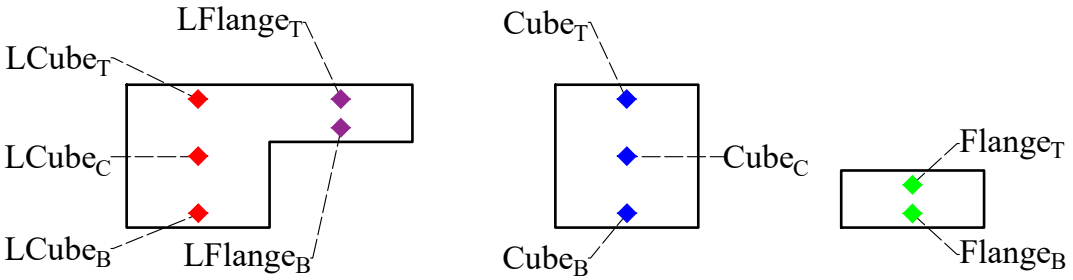

Figure 3.5: Naming convention of VWSG measurements.

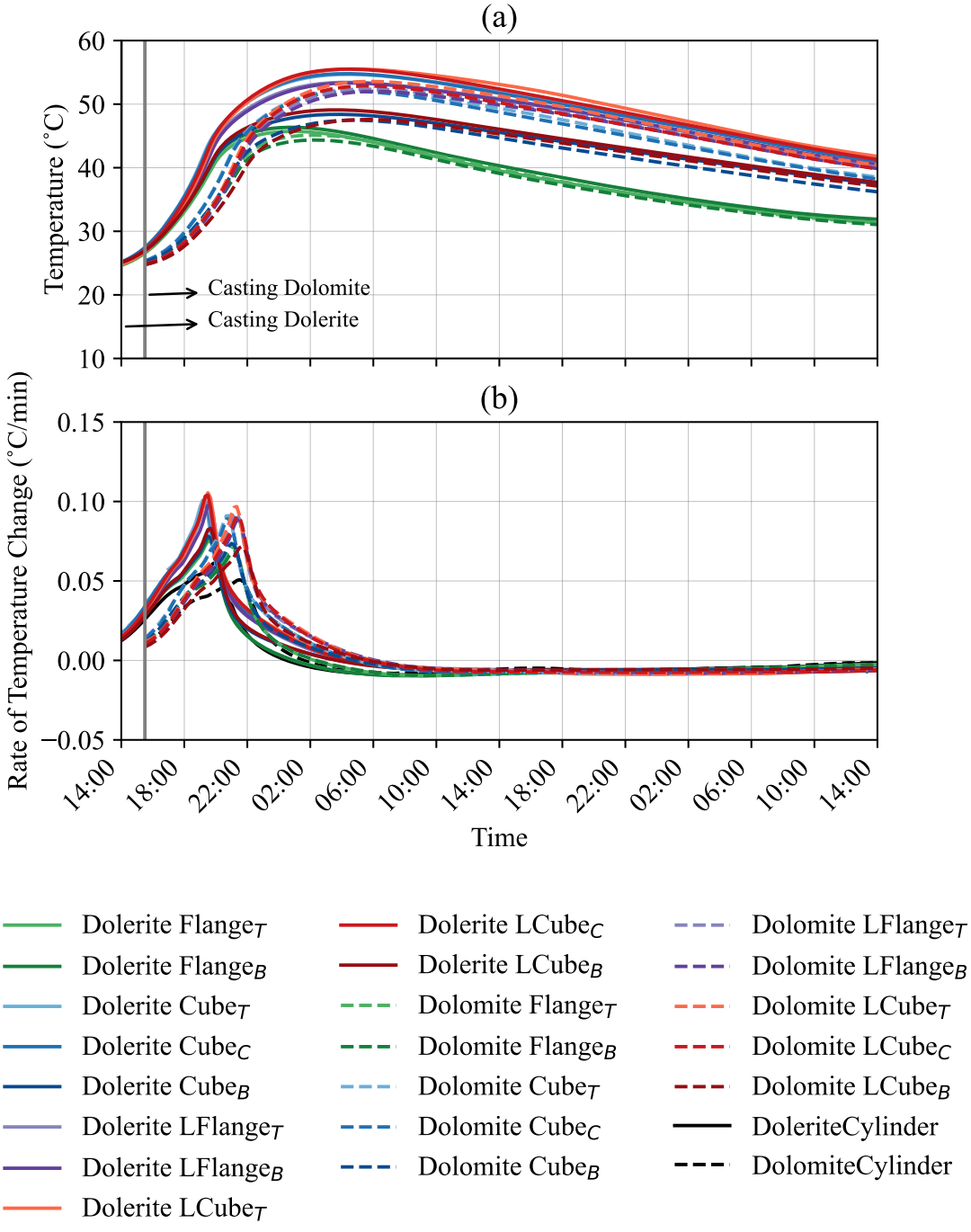

Figure 3.6: (a) Temperature over time recorded by each sensor. (b) Rate of temperature change over time for each sensor. Subscripts $_B$ and $_T$ refer to bottom and top, respectively.

3.3.3 Sensor Positioning and Support Cage

Steel cages made of steel bars of 4mm diameter were used for the L-Shape, Cube and Flange shapes to secure the sensors. Steel cages were considered to have negligible influence on thermal and mechanical properties. The cages included two parallel ladders of bars 150mm apart, connected by VWSGs that extend 100mm between them (see Figure 3.7). The thermocouples were attached to steel wires, which were crossed between diagonal bars to secure their position. The layout of the instruments on the vertical ladders is illustrated in Figure 3.8. The Cube and L-Shaped Cube sections used identical ladders (cages) as well as the Flange and L-Shape Flange.

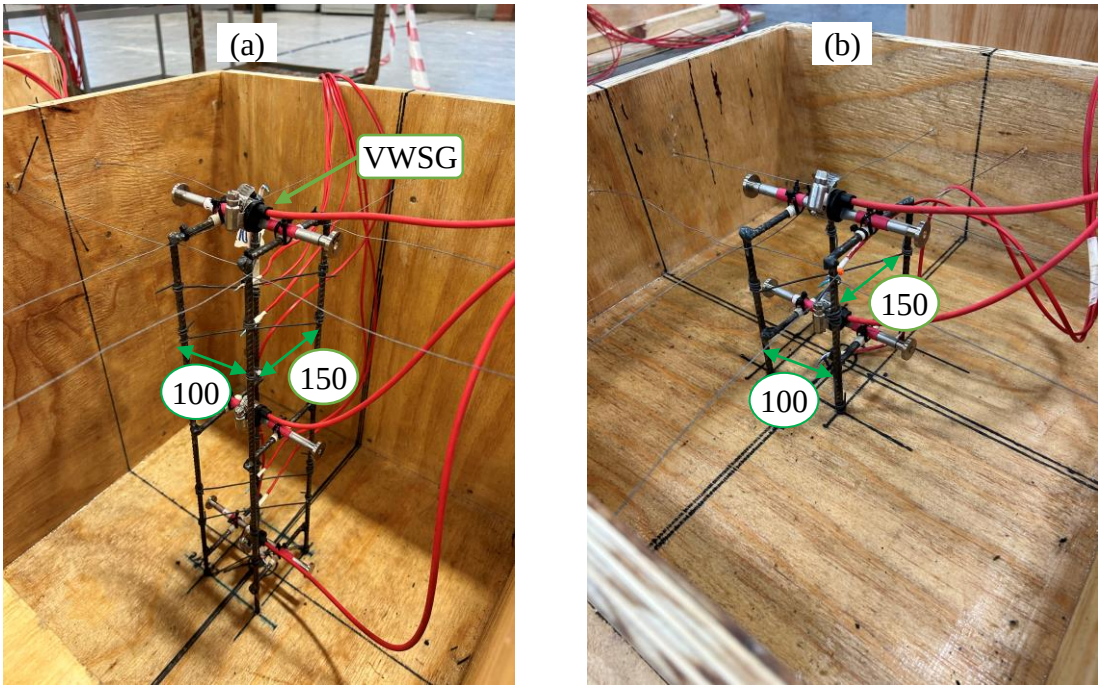

Figure 3.7: Steel cage and sensor layout within (a) Cube and (b) Flange moulds.

The cages were anchored by drilling 4mm diameter holes, 5mm deep, at the bottom of each timber mould to provide support without significant concrete interference (see Figure 3.8). The top of the cages was stabilised by spanning 0.71mm steel wire across the wooden moulds.

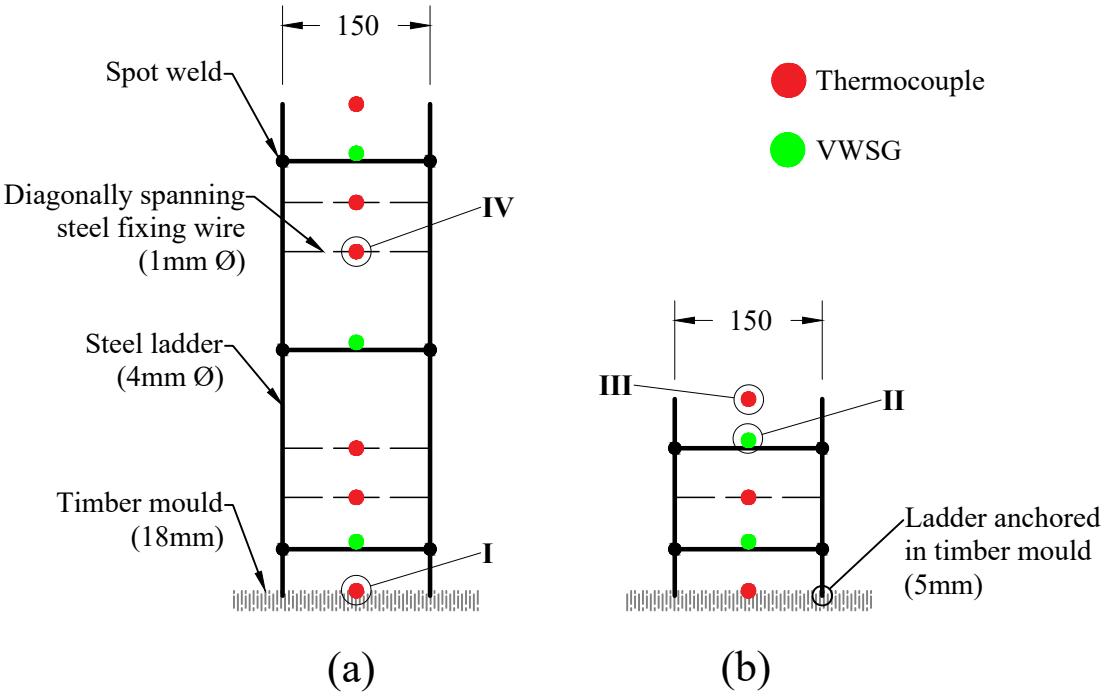

Figure 3.8: Layout of instrumentation ladders showing (a) the Cube and L-Shape Cube layout, and (b) Flange and L-Shape Flange layout

The thermocouples and VWSGs were attached to the ladder structure as follows (refer to Figure 3.8):

I. Bottom thermocouple held by steel fixing wire that spans diagonally between ladders.

II. VWSG's spanning 100mm between ladders resting on steel bars wrapped with masking tape. Secured with cable ties.

III. Thermocouples floated onto specimen immediately after casting shape (before concrete set).

IV. Thermocouples attached to steel fixing wire with cable ties.

3.4 Concrete Materials and Procedures

3.4.1 Aggregate Properties

The selection of aggregate type in a concrete mix design can significantly affect thermal and mechanical properties (Neville, 2012). For this investigation, Dolerite and Dolomite were used as fine and coarse aggregates. The aggregates were sourced from two separate quarries in South Africa (see Table 3.2). The Dolerite and Dolomite aggregates were chosen based on their distinct thermal properties, specifically thermal conductivity (Table 2.2). The difference in thermal conductivity influences the change in temperature and therefore the thermal deformation in the concrete specimen (as outlined in Chapter 2).

Table 3.2: Aggregate sources and relative densities (RD) with corresponding sample standard deviations (s) and Coefficient of Variation (CV).

Aggregate	**Source**	**RD**	**s**	CV
Dolerite stone (10mm)	Pietermaritzburg *(KZN)*	2.94	0.0006	0.0002
Dolerite sand	Pietermaritzburg *(KZN)*	2.97	0.0004	0.0001
Dolomite stone (10mm)	Lyttelton *(Gauteng)*	2.86	0.0007	0.0002
Dolomite sand	Lyttelton *(Gauteng)*	2.85	0.0003	0.0001

The concrete mix design incorporated 10mm size aggregates to ensure material uniformity within the relatively small specimens. Smaller aggregates help reduce segregation and ensure a consistent distribution of materials, which was important for obtaining consistent thermal and mechanical measurements.

The *relative density (RD)* of each aggregate was determined, as it is a critical parameter for the design of concrete mixes. RD affects the proportions of aggregate, cement, and water in the mix, which in turn influences the density, strength, and thermal performance of the concrete. A pycnometer was used to measure the RD values, and three samples were tested for each aggregate to ensure reliability and account for any variability in the measurements. The RD values in Table 3.2 represent the mean of three tests, with the corresponding sample standard deviations (s) and Coefficient of Variation (CV) provided to the level of consistency in the results. The RD values were subsequently used to design the concrete mixes. The results show the Dolerite aggregates have slightly higher RD values compared to the Dolomite aggregates, with the Dolerite sand showing the highest RD (2.97) and the Dolomite sand the lowest (2.85). The low Sample standard deviations and variances indicate minimal variability in the measurements. The differences in RD were

taken into account during mix design to ensure uniformity in the concrete properties, accounting for the inherent variability of the materials.

The *particle size distribution (PSD)* provides information on the size range and distribution of the aggregate particles, which influences concrete properties such as strength, workability and thermal behaviour. By comparison of the PSDs of the Dolerite and Dolomite aggregates, the consistency in particle size distribution was quantified. The PSD for each of the aggregates' fines was determined using a Malvern 3000 and is shown in Figure 3.9. In Figure 3.9, it was determined that the differences in PSD between the two aggregates were negligible, confirming their suitability for a comparative study.

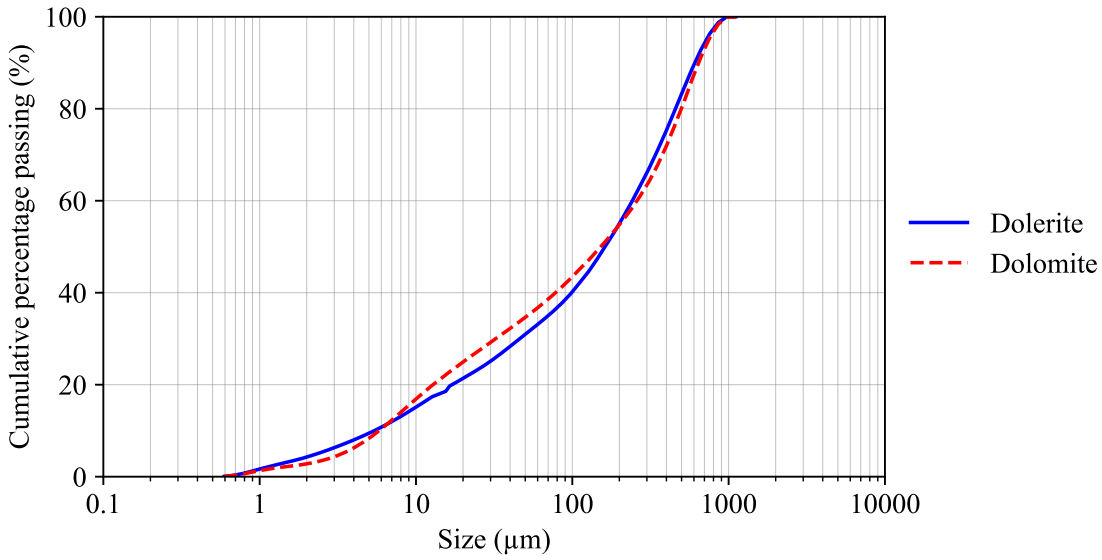

Figure 3.9: Particle Size Distribution (PSD) of fine aggregates.

The moisture content and absorption characteristics of the aggregates were not directly measured in this study. However, according to AfriSam (South Africa) (Pty) Ltd (2017), both Dolerite and Dolomite aggregates are not deleteriously reactive. The water absorption for Dolerite from the Pietermaritzburg quarry in KZN is approximately 0.2% (AfriSam (South Africa) (Pty) Ltd, 2017). According to Afrimat (2022), the water absorption of Dolomite aggregate from the Lyttelton quarry in Centurion, Gauteng, is reported as 0.68% (Afrimat, 2022).

3.4.2 Concrete Mix Design and Casting

The concrete mix designs developed for this study aimed to ensure consistency between samples while allowing comparison of thermal effects due to aggregate variations. Two distinct mixes were prepared: one with Dolerite as aggregate and the other with Dolomite. The detailed proportions of the mixture for both aggregates are shown in Table 3.3.

Mix Proportions:

- A water-to-binder ratio (w/b) of 0.5 was maintained for both mixes, balancing workability with a target compressive strength of more than 50 MPa.
- The coarse-to-fine aggregate ratio of 0.5 was used, ensuring an even distribution of fine aggregates between the two mixes.
- To minimise the environmental impact, 20% of the cement content (CEM I 52.5R) was replaced by fly ash from Lesotho Power Station.

Mixing Procedure:

- The concrete materials were batched and mixed in a laboratory mixer to ensure uniformity. Each mix required two batches of 0.23 m^3 to meet the volume requirements.
- The mixing process involved an initial dry mix of aggregates and binder material, followed by a gradual addition of water. Each batch was mixed for 2 minutes.
- Each batch was placed into specific moulds for various specimen shapes and compacted to minimise air gaps that could influence thermal behaviour (Neville, 2012).
- Slump tests were conducted to verify the workability of each mix: Mix 1 (Dolerite) recorded slump values of 65mm for Batch 1 and 60mm for Batch 2, while Mix 2 (Dolomite) recorded 70mm for both batches, ensuring consistency and workability.

Table 3.3: Concrete mix design for both aggregates.

Component	Dolerite Mix	Dolomite Mix
CEM I 52.5R (kg/m^3)	362	352
Water (kg/m^3)	227	220
Coarse Aggregate (kg/m^3)	885	897
Fine Aggregate (kg/m^3)	936	894
Fly Ash (kg/m^3)	91 (20%)	88 (20%)
Theoretical Density (kg/m^3)	2500	2451

3.4.3 Curing Procedure

The curing procedure for the experimental investigation is described in Figure 3.10. The casted concrete shapes (L-Shape, Cube and Flange), along with most of the smaller representative samples, were subjected to a controlled curing process. This procedure was designed to simulate early-age curing conditions and, subsequently, allow environmental exposure. Throughout the indoor curing period (first 28 days), the laboratory temperature ranged between 20°C and 25°C. While the relative humidity (RH) was not recorded, it was assumed to remain relatively stable under typical indoor conditions.

The curing process was as follows (see Figure 3.10):

- **2024-05-06 (Start of Curing):** All specimens were cast and immediately covered with bubble wrap and a curing blanket to retain moisture and promote hydration during the initial setting period (see Figure 3.11). The curing blanket remained in place for 14 days.
- **2024-05-20 (14 days):** The curing blanket was removed. At this stage, the specimens were allowed to continue curing indoors, exposed to air while still in their moulds.
- **2024-05-22 (16 days):** Moulds were removed from the L-Shape, Cube and Flange shapes, and the sides of each sample were insulated to control the lateral drying shrinkage (see Figure 3.12).
- **2024-06-03 (End of Curing):** After 28 days of controlled indoor curing, the casted concrete shapes (including the 230mm diameter cylinders) were moved outdoors. This allowed exposure to natural environmental conditions.

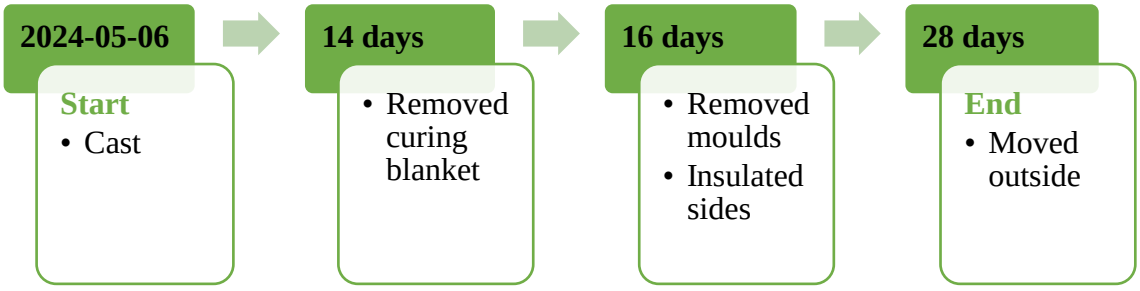

Figure 3.10: Curing regime for casted shapes and representative samples.

Several smaller samples were cured alongside the casted concrete shapes (see Figure 3.12). These samples were designated as representative samples to measure material properties between batches and cured on the same timeline as the L-Shape, Cube, Flange, and 230mm diameter cylinders.

For comparison and quality control purposes, an additional set of smaller samples, comprising six cubes (three per batch) and four cylinders (two per batch) from each mix, were cured in water for 28 days. This curing method adhered to the SANS 5861-3:2006 (2006b) requirements to obtain a reference 28 day design strength. The water-cured samples provided a reference strength for evaluating the compressive strength and other mechanical properties, ensuring that the concrete mixes met the target specifications.

Figure 3.11: Casted concrete shapes and representative samples under curing blanket.

Figure 3.12: Casted concrete shapes and representative samples curing indoors on timber supports.

3.5 Outside Layout of Specimens

After reaching the 28-day design strength, the concrete elements and samples were moved outdoors (north face of the lab) and arranged in a controlled layout to monitor their responses to environmental conditions. Figures 3.13 and 3.14 illustrate the outdoor setup, support conditions, and placement of casted shapes, as well as representative samples.

Figure 3.13: Outdoor placement of casted concrete shapes, and representative specimens.

The L-Shape, Cube, and Flange were positioned on separate steel frames elevated 950mm above ground level to ensure uniform exposure to ambient conditions. Each concrete mix (Dolerite and Dolomite) was assigned a dedicated steel frame, as shown in Figure 3.13. This layout ensured proper separation between the mixes to minimise cross-mix interference and facilitate data monitoring.

The L-Shape, Cube, and Flange was supported on 90mm angle irons resting on the steel frames. The placement and spacing of the L-Shape, Cube and Flange shapes were as follows (Figure 3.14):

- The L-Shape sections were placed closest to the 180mm thick wall, with a clearance of 880mm.
- The Cube, Flange, and L-Shape were positioned 500mm apart.

- The two sets of shapes (Dolerite and Dolomite) were spaced 2000mm apart.

The instrumentation cables were routed through the 180mm thick wall to keep the data loggers indoors, as shown in Figures 3.14 and 3.16.

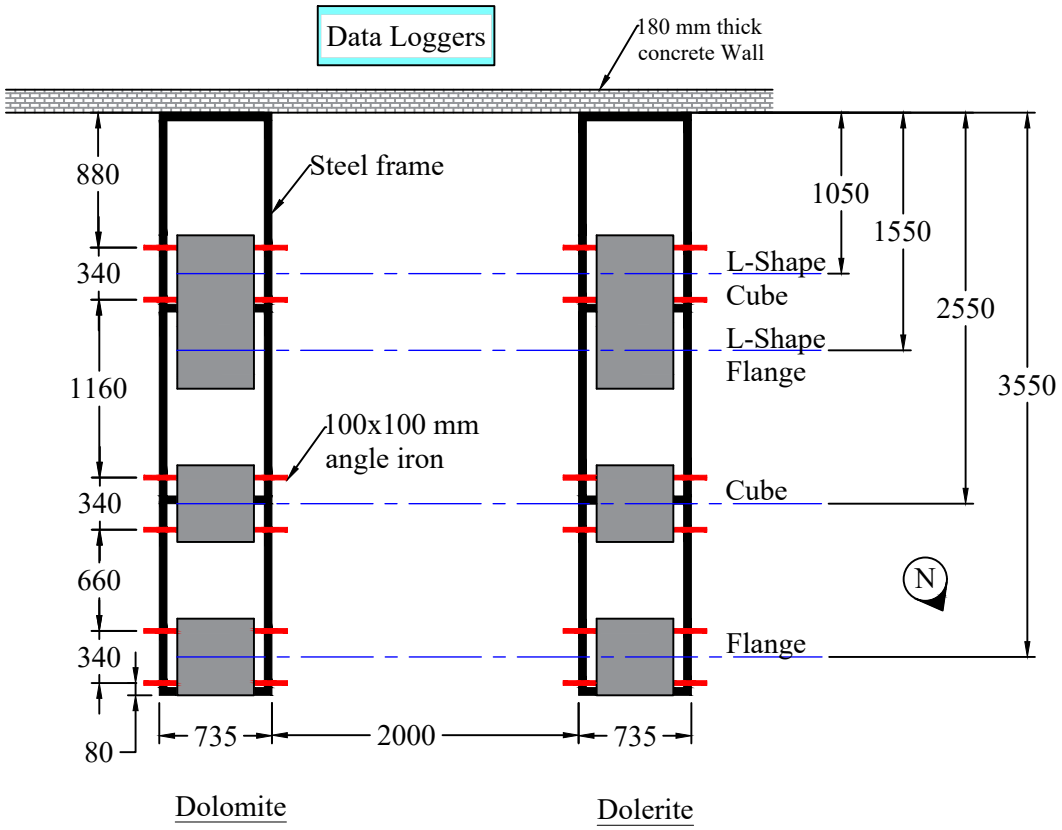

Figure 3.14: Layout of L-Shape, Cube, and Flange relative to 180mm thick concrete wall.

The support conditions for the L-Shape, Cube, and Flange were designed to limit the bending of the concrete elements under self-weight in the direction of the VWSG. Figure 3.15 shows the support conditions and the orientation of the VWSGs. The shapes rest on the edges of angle sections, providing minimal contact area to reduce friction and ensure minimal restraint to thermal expansion and contraction. The angle irons span in the same direction as the VWSGs, ensuring proper alignment with the strain measurement direction (see Figure 3.15).

Cylinders and representative samples were placed between the steel frames for Dolomite and Dolerite mixes, as shown in Figure 3.16. These specimens were placed on a wooden pallet to avoid direct contact with the ground or other concrete elements. The cylindrical elements were placed vertically, with the VWSG vertically aligned (see Figure 3.15),

allowing free vertical elongation to determine the coefficient of thermal expansion and shrinkage prediction.

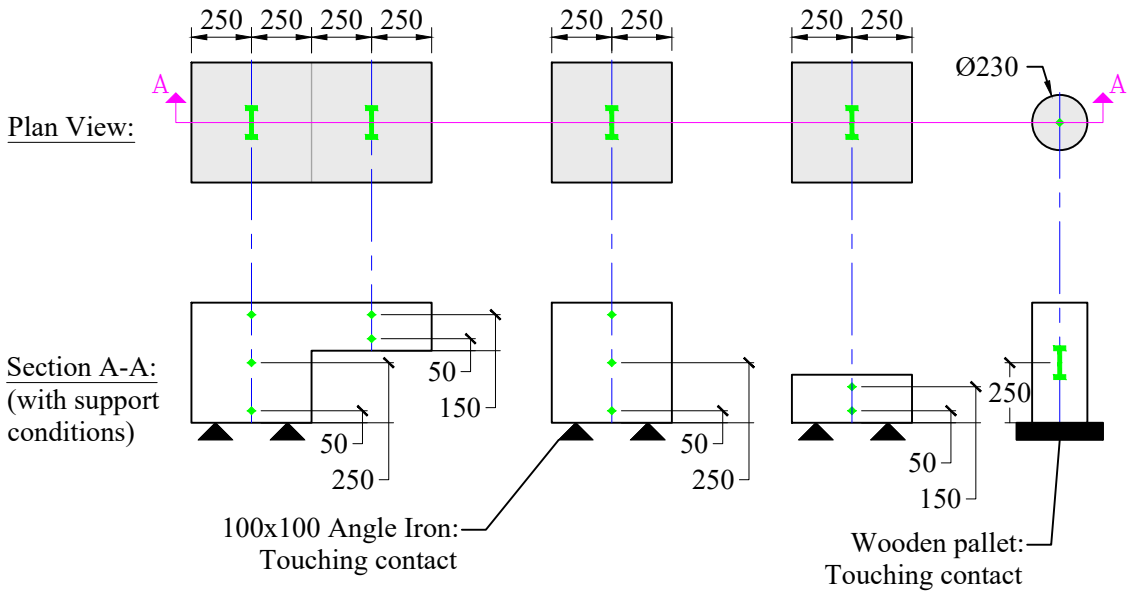

Figure 3.15: Support conditions and VWSG layout for Flange, Cube, L-Shape, and Cylinder elements.

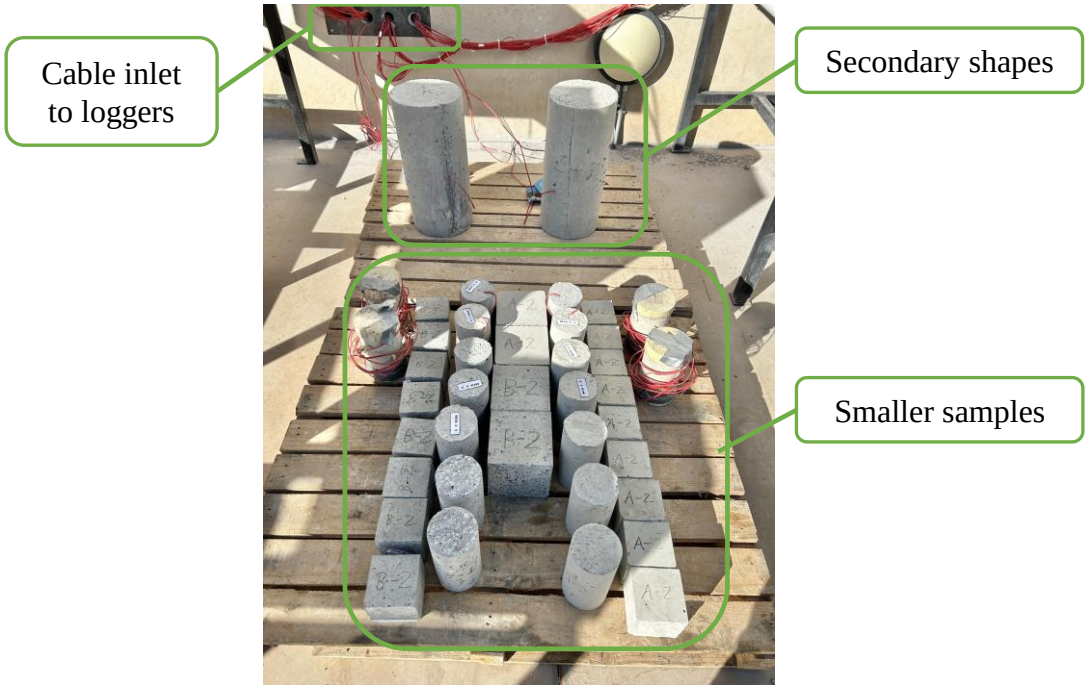

Figure 3.16: Cylinders and representative samples on a wooden pallet.

3.5.1 Insulation

To ensure controlled thermal conditions during the experimental investigation (after curing for 28 days), the western and eastern surfaces of the L-Shape, Cube and Flange shapes were insulated with a 100mm Isoboard XPS thermal insulation board. This insulation simulated the continuity of the cross-sections in a typical concrete beam, where the front and back surfaces are not directly exposed to environmental conditions. The insulation boards were affixed to the concrete samples using Alcolin Cornice Adhesive, which ensured a secure bond while preventing any potential degradation of the insulation material. Each 100mm layer was formed by adhering two 50mm Isoboard panels together. The Isoboard XPS thermal insulation board used in the study is characterised by the thermal properties shown in Table 3.4, which were obtained from a laboratory test report by Omega Test House (2022). Figure 3.17 shows the L-Shaped element (Dolomite mix) with the insulation boards in place, positioned outdoors after curing.

Table 3.4: Thermal properties of the Isoboard XPS thermal insulation board (Omega Test House, 2022).

Property	**Value**
Density (kg/m^3)	37.2
Thermal conductivity, $k_{\text{insulation}}$ ($W/°Cm$)	0.02624

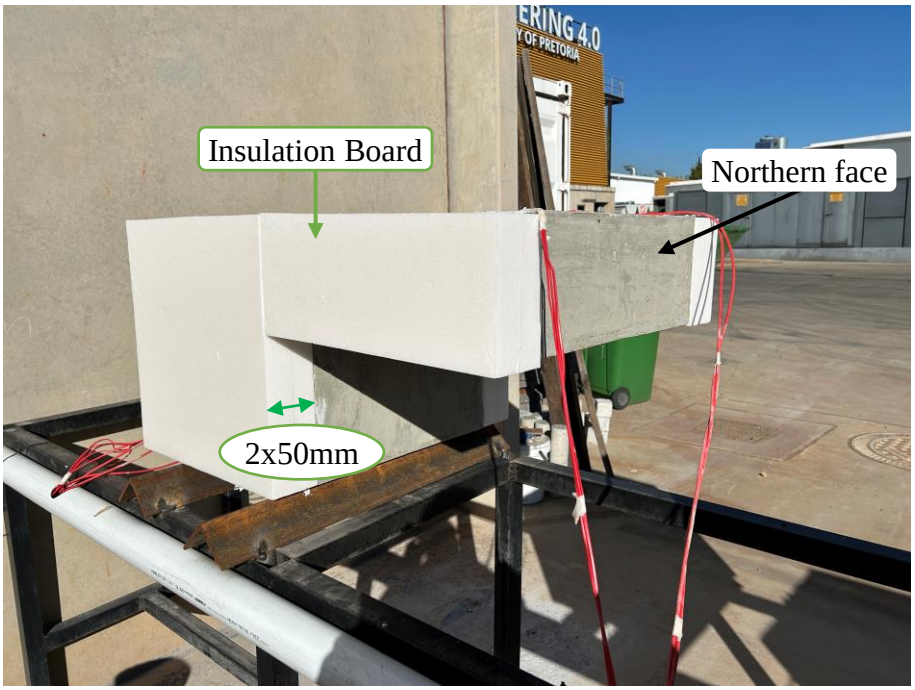

Figure 3.17: L-Shape showing insulation boards on eastern and western faces.

3.6 Weather Station

The weather data for this study was collected using a single SenseCAP S2120 8-in-1 LoRaWAN weather sensor (Seeed Technology Co., Ltd, 2022), a highly integrated weather monitoring device. The S2120 provides environmental data in multiple parameters, making it suitable for monitoring outdoor conditions relevant to concrete structures. The sensor operates via LoRaWAN communication, providing low-power long-range data transmission Seeed Technology Co., Ltd (2022). This single weather station was used to record data for all mixes throughout the outdoor experimental period, ensuring consistency in environmental monitoring across the different samples.

Figure 3.18 shows the Weather Sensor used in this study.

Figure 3.18: SenseCAP S2120 8-in-1 LoRaWAN Weather Sensor (Seeed Technology Co., Ltd, 2022)

The SenseCAP S2120 is an 8-in-1 sensor that measured the following key weather parameters (for the scope of this study):

- **Air Temperature**: Ranges from $-40°C$ to $+85°C$, with an accuracy of $\pm 0.5°C$.
- **Relative Humidity (RH)**: Measured from 1% to 99% with an accuracy of $\pm 3\%$.
- **Light Intensity**: Ranges from 0 to 200 000 lux with an accuracy of $\pm 10\,\%$
- **Rainfall**: Captures precipitation in millimetres with a resolution of 0.01mm.
- **Wind Speed and Direction**: Measures up to 60 m/s, with a resolution of 0.01 m/s.

3.7 Data Acquisition System

The data acquisition system for the experiment is designed to capture and record temperature and strain data from concrete specimen, specifically those of the Dolerite mix (A) and Dolomite mix (B). The system integrates several components, including thermocouples, VWSG, data loggers, multiplexers, and a personal computer for data storage and analysis. Figure 3.19 shows a schematic of the data acquisition system used in this study.

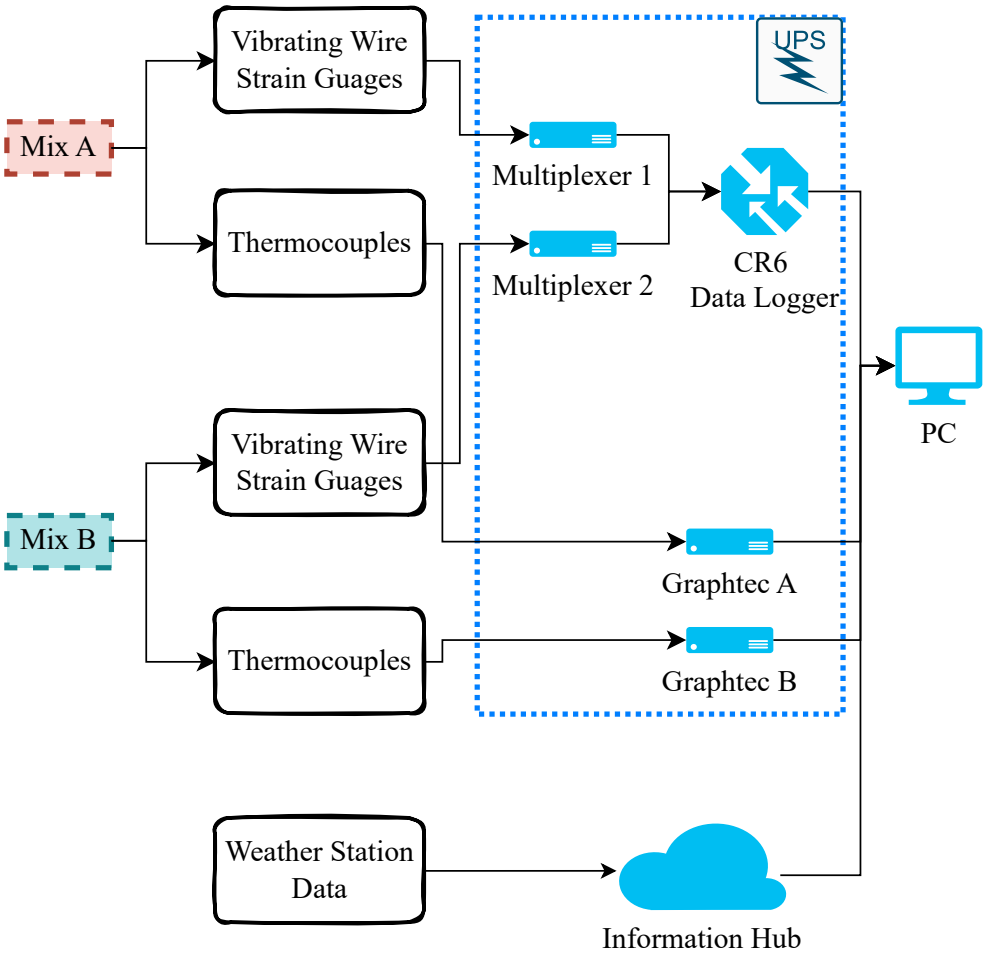

Figure 3.19: Schematic of data acquisition system.

The temperature and strain data from the concrete specimens were captured by the thermocouples and VWSGs connected to the data loggers (see Figure 3.20). The data were logged at 10min intervals using the following loggers:

- *Campbell CR6 Data Logger (2025):* The CR 6 data logger used two AM16/32 Multiplexers (Multiplexer 1 and 2) to allow for 20 channels for the 20 VWSGs.

- *GRAPHTEC GL840-SDthermocouplesWV Data Logger (Graphtec Corporation, 2010):* Each mix's thermocouples were connected to a 20-channel Graphtec (Graphtec A and B).

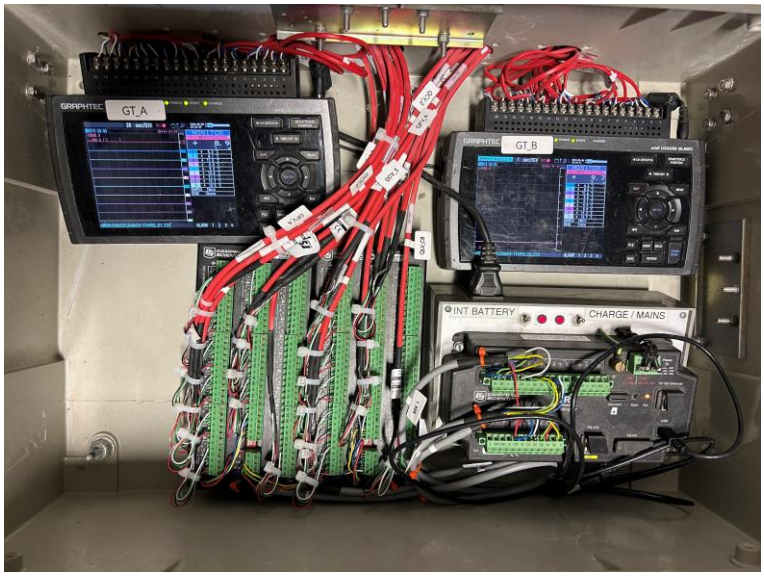

Figure 3.20: Sensors connected to respective loggers in a metal-cased box (kept indoors).

After the data was recorded by the Graphtec units, CR6, and the weather station, it was transferred to a personal computer. This transfer involved downloading the stored data files from these devices to the computer for further processing. The weather station data was downloaded from an internet server and stored in a combined data frame with the other sensors.

3.8 Testing of Concrete Mechanical Properties

This section presents the mechanical properties of the two concrete mixes (Dolerite and Dolomite), determined through compressive strength, modulus of elasticity (E-value), and tensile strength splitting tests. These tests provide insight into the behaviour of concrete under different loading conditions, allowing a comparison of the performance of the two types of aggregates.

3.8.1 Compressive Strength

The compressive strength tests were performed following the guidelines outlined in SANS 5863:2006 (2006a). The tests were performed at specified days (1, 14, 28 and 56) to assess the development of the strength over time and to assess consistency between batches (two batches per mix).

To evaluate batch consistency and calculate the *characteristic compressive strength* as per EN1992 (2004a), six 100 mm cubes per mix were cured in water baths maintained between 22°C and 25°C after demoulding, in accordance with SANS 5861-3:2006 (2006a). The water-cured samples provided a baseline strength metric under standardised conditions.

The remaining samples (referred to as *representative samples*) were placed outdoors along with the L-Shape, Cube and Flange shapes to simulate the environmental conditions experienced during the experimental programme.

This dual curing strategy aimed to differentiate between:

- **Batch Consistency and Characteristic Strength:** Water-cured samples provided a controlled environment to evaluate batch consistency and the derived characteristic compressive strength values for design purposes.
- **Representative Strength:** Outdoor-cured samples reflected the environmental exposure in the real world, providing information on the development of strength in field conditions.

3.8.2 Modulus of Elasticity

The modulus of elasticity (E-value) test was performed on 100 mm-diameter, 200 mm-high cylinders. As with compressive strength tests, the specimens were subjected to two curing regimes. Capping was performed using a capping machine to ensure uniform loading during testing. Specimens were loaded to 40% of their maximum compressive strength, and the resulting deformations were measured in accordance with ASTM C469/C469M-22 (2022). This enabled the calculation of the static modulus of elasticity, a critical parameter for assessing the stiffness and deformation behaviour under load. The measured E-value was used to transform restrained strain into stress values.

3.8.3 Splitting Tensile Strength

The splitting tensile strength test was carried out to evaluate the concrete's tensile capacity, a crucial factor in assessing its resistance to cracking. The test followed SANS 6253:2006 (2006b), using the same 100 mm-diameter, 200 mm-high cylinders as for the E-value tests. Specimens were prepared under both the curing conditions described above. The cylinders were placed horizontally on the test machine and subjected to a compressive load along their longitudinal axis until failure. This indirect method of applying tensile stress allowed an assessment of crack resistance and the comparison of tensile properties between the two mixes.

3.9 Specific Heat Capacity

The specific heat capacity of concrete is a critical thermal property that governs how the material absorbs and releases heat (Neville, 2012). As a multicomponent material, concrete presents unique challenges for thermal property measurements, particularly because standard thermal test methods are designed for homogeneous materials (Chen et al., 2008; Demirtürk et al., 2023; Xu and Solaimanian, 2010). To address these challenges, this study adopted a simple calorimetric test to determine the specific heat capacity of concrete mixes containing Dolerite and Dolomite aggregates. The test used the mixing principle described by (Pan et al., 2017). The experiment involved heating concrete samples to approximately 50°C and submerging them in water at room temperature within a Langavant 1040 calorimeter, as shown in Figure 3.21. This method relies on the principle of energy conservation, ensuring that the heat exchanged between concrete, water, and the calorimeter is accurately captured. The calorimeter was assumed to provide complete insulation, and energy losses were considered negligible. The results served two primary purposes: compare the thermal properties of the two mixes and provide essential input data for the numerical heat transfer model discussed in Chapter 4.

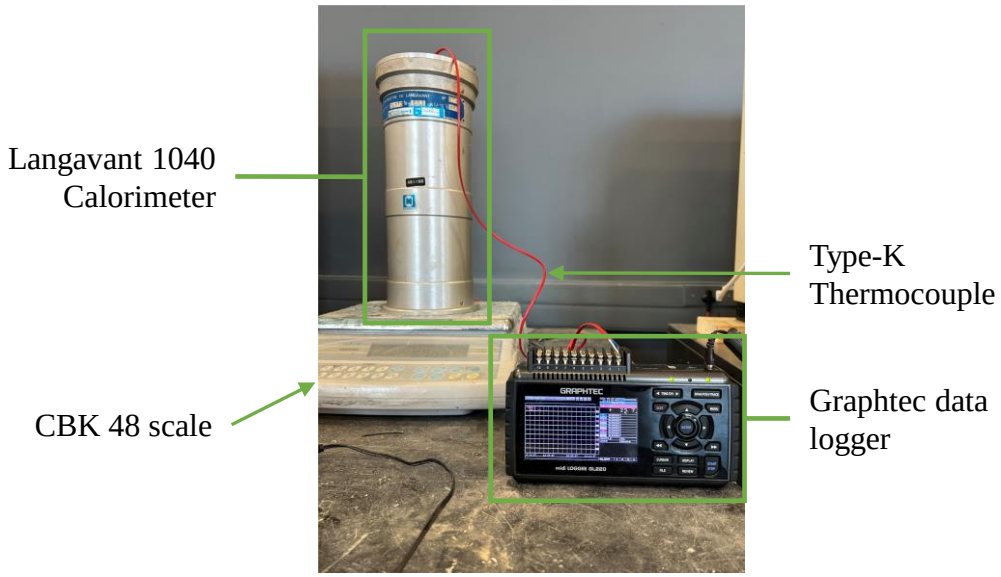

Figure 3.21: Experimental setup showing the Langavant 1040 calorimeter placed on a CBK 48 scale, with a thermocouple Graphtec data logger.

The experiment was carried out after 87 days of environmental exposure (115 days after casting)as the specific heat capacity is not age-dependent and no rainfall events influenced moisture (Neville, 2012). This approach ensured that the samples were representative of practical applications and that the effects of both material properties and environmental factors were captured. The experiment was carried out within a controlled

temperature range of 50°C (initial concrete temperature) to 19.7°C–20.4°C (water temperature). This range was selected to maintain stability within a moderate temperature regime, where the specific heat capacity of the concrete is known to be relatively constant (Bentz et al., 2011). Bentz et al. (2011) reported that the concrete specific heat capacity remains stable between 10°C and 66°C, averaging around 0.93 J/g·K. Deviations outside this range can be attributed to phase transitions and moisture loss, particularly at elevated temperatures. The experiment was carried out on 50 mm cubes cut from 150 mm samples (see Figure 3.22) to accelerate heating and thermal equilibrium. The procedure is described below:

(a) (b)

Figure 3.22: Samples used for specific heat capacity experiment: (a) Dolerite and (b) Dolomite 50mm cubes.

1. Preparation of Samples

- After 28 days of curing in the laboratory environment, the 150 mm cubes were placed outside along with the cast shapes (L-Shape, Cube, and Flange) to ensure consistent environmental exposure.
- One 150 mm cube was used per mix for testing.
- Each 150 mm cube was carefully cut into smaller 50 mm cubes to reduce the thermal mass and enable faster thermal equilibrium during testing. Figure 3.22 shows the 50 mm cubes prepared for testing.
- Three tests were performed for each mix, with each test using three 50 mm cubes.
- The 50 mm cubes were preheated to 50°C in an oven for 24 hours to ensure uniform heat distribution prior to testing.

2. Calorimeter Setup

- A Langavant 1040 calorimeter with a specific calorimeter heat capacity of 0.218 J/g·K and a total heat capacity of 442 J/°C was used (Figure 3.21).
- One kilogram of water was added to the calorimeter at room temperature (19.7°C–20.4°C)
- To eliminate thermal fluctuations, the system was allowed to stabilise for 10 minutes before adding the heated concrete samples.
- The system was placed on a CBK 48 scale with an accuracy of $\pm 4g$.

3. Measurement and Data Collection

- The mass of the system was measured at three intervals: initial (without samples), with samples (immediately after adding samples) and end of experiment (to ensure that minimum mass was lost).
- The concrete cubes were quickly removed from the oven, and their initial temperatures were measured using a Dikang infrared thermometer, which offers a rapid non-contact measurement with an accuracy of ± 0.4°C.
- Each heated cube was immediately submerged into the calorimeter containing room-temperature water, ensuring minimal heat loss during transfer. The calorimeter lid was kept closed throughout the experiment to further minimise heat loss and ensure reliable results.
- The system temperature was monitored at 10-second intervals using a thermocouple connected to a GRAPHTEC GL840-SD Data Logger.
- The initial test for the Dolerite mixture was conducted without stirring to allow the system to reach thermal equilibrium naturally. This test required approximately 45 minutes.
- Subsequent tests for the Dolerite and Dolomite mixes employed gentle stirring to expedite heat distribution within the calorimeter. This adjustment reduced the time required to achieve thermal equilibrium to approximately 25 minutes per test. The mixing process was validated as having a negligible effect on the final results, with deviations from the average remaining within 4.8%.

The specific heat capacity of concrete (c_{concrete}) was calculated using Equation 3.4, based on the principle of energy balance (adapted from Pan et al. (2017).

$$c_{\text{concrete}} = \frac{(c_{\text{cal}} + m_{\text{water}} c_{\text{water}})(T_{\text{peak}} - T_{\text{water}})}{m_{\text{concrete}}(T_{\text{concrete}} - T_{\text{peak}})} \tag{3.4}$$

Where,

c_{cal} = Heat capacity of the calorimeter (442 J/°C)
m_{water} = Mass of water (1 kg)
c_{water} = Specific heat capacity of water (4.18 J/g·°C)
T_{peak} = Peak system temperature (°C)
T_{water} = Initial water temperature (°C)
$T_{concrete}$ = Initial concrete temperature (°C)
$m_{concrete}$ = Mass of the concrete cube (kg)

3.10 Summary

This chapter presented the experimental setup and methodology used to investigate the thermal and mechanical behaviour of concrete elements containing Dolerite and Dolomite aggregates under environmental loading. The study involved the casting of two concrete mixes in L-Shape, Cube and Flange shapes that were instrumented with thermocouples and vibrating wire strain gauges (VWSG) to monitor temperature response and strain development throughout their depth. In addition, 230mm diameter cylinders were cast to isolate the coefficient of thermal expansion and shrinkage strain for each mix, providing a baseline to analyse the development of the strain in the casted shapes.

Concrete mixes were specifically designed to highlight the influence of aggregate type on thermal and mechanical deformation. Careful attention was paid to material quality control, batch consistency, and curing conditions to ensure reliable results. Reference water-cured samples were used to verify the mechanical properties, all samples were cured for 28 days before being exposed to natural environmental conditions.

Using both the water and outdoor curing regimes, the experimental programme captured the variability in mechanical properties due to environmental exposure, allowing a comparison between standardised and representative conditions. These results serve as a foundation for interpreting the structural behaviour of the casted concrete shapes, linking mechanical properties to the thermal and strain responses discussed in subsequent chapters.

Detailed instrumentation and data acquisition procedures were implemented to capture accurate and representative thermal and strain data, allowing an in-depth analysis of the effective development of temperature and strain in each concrete shape. In the subsequent sections of this study the data is analysed to compare the thermal and mechanical performance of Dolerite and Dolomite mixes, contributing to the knowledge of material selection and design considerations for concrete structures exposed to environmental loads.

4 Material Property Results

4.1 Introduction

The mechanical and thermal properties of concrete are fundamental to understanding its performance in structural applications, particularly when exposed to variable environmental conditions. These properties, including compressive strength, tensile strength, modulus of elasticity (E-value), specific heat capacity, and coefficient of thermal expansion, govern the material's response to both mechanical loading and thermal fluctuations. This chapter focusses on the evaluation of these properties for concrete mixes that incorporate Dolerite and Dolomite aggregates.

As described in Chapter 3, representative samples were prepared and cured along with primary and secondary shapes to ensure consistent environmental exposure and curing conditions. Additional water-cured samples, as well as representative samples, were tested to determine characteristic compressive strengths, which were later used to predict other mechanical properties, such as the modulus of elasticity and tensile strength, using established design code relationships. In addition, the specific heat capacity and thermal expansion coefficients were determined experimentally, providing essential thermal data for subsequent numerical modelling.

The integration of mechanical and thermal property evaluation is crucial for structural design, particularly in applications where temperature variations induce significant thermal stresses. For example, the modulus of elasticity influences the stiffness of the concrete, while the coefficient of thermal expansion dictates the magnitude of strain induced by temperature changes. Together, these properties determine the stress state within the thermally loaded structure.

The outcomes of this chapter serve dual purposes. First, they provide information on the mechanical and thermal performance of concrete made with Dolerite and Dolomite aggregates. Second, they establish a foundation for the numerical modelling work presented in Chapter 6, where these experimentally determined properties are utilised for the calibration of thermal conductivity and solar absorptivity in finite element simulations. The findings also facilitate a critical assessment of the applicability of design code assumptions for the South African context, where aggregate properties may differ substantially from those assumed in international standards.

While this study focused on short-term thermal and mechanical behaviour, long-term durability aspects such as alkali-aggregate reactivity were not explicitly investigated. Dolomite aggregates can exhibit alkali-carbonate reactivity, but these effects typically develop over extended periods and were beyond the scope of this research. No visible signs of expansion or cracking were observed during the experimental period.

4.2 Mechanical Concrete Properties

The mechanical properties of the concrete were evaluated by testing representative samples in conjunction with water-cured samples. As detailed in Chapter 3, representative samples were prepared and cured together with the primary and secondary shapes to ensure consistency in environmental exposure and curing conditions. These samples were assumed to represent the actual compressive strength of the concrete used in the experimental investigation.

To account for variations in test results and ensure safety and reliability in structural design, characteristic strengths are used as the basis for calculations. The characteristic strength, denoted as f_{ck}, represents a conservative estimate of material strength, defined as the value below which it is expected that no more than 5% of the test results fall. This approach accounts for the inherent variability in concrete properties due to differences in material composition, environmental conditions, and testing procedures (Mosley et al., 2012).

The characteristic compressive strength (f_{ck}) of the concrete was determined based on the mean compressive strength of water-cured cube samples ($f_{cm,cube}$), tested under controlled conditions. As the equations provided in EN1992-1-1 (2004a) are based on cylinder strengths, the compressive strengths obtained from the cube tests were converted to their approximate cylinder equivalents (f_{cm}) using the relationship given in Equation 4.1, as recommended by EN1992-1-1 (2004a).

Once the cylinder strengths were estimated, the sample standard deviation (s) was determined from the converted cylinder strength values to quantify the variability in the test results. Finally, the characteristic cylinder strength (f_{ck}) was calculated using Equation 4.2, which incorporates the mean cylinder strength (f_{cm}) and the sample standard deviation (s).

$$f_{cm} = 0.8 \cdot f_{cm,cube} \tag{4.1}$$

$$f_{ck} = f_{cm} - 1.64 \cdot s \tag{4.2}$$

Where,

$f_{cm,cube}$ = Mean cube compressive strength (MPa)
f_{cm} = Mean cylinder compressive strength (MPa)
f_{ck} = Characteristic cylinder compressive strength (MPa)
s = Sample standard deviation (MPa)

This process ensures that the strength values used in the design are conservative and account for variability, providing a margin of safety. Once the characteristic and mean cylinder strengths were calculated, they were used to predict additional mechanical properties of the concrete, such as the modulus of elasticity (E_{cm}) and the characteristic tensile strength ($f_{ctk,0.05}$), as per the relationships specified in EN1992-1-1 (2004a).

The mean elastic modulus (E_{cm}) was calculated using Equation 4.3, while the mean tensile strength (f_{ctm}) and the 5^{th} percentile characteristic tensile strength ($f_{ctk,0.05}$) were calculated using Equations 4.4 and 4.5, respectively.

$$E_{cm} = 22 \cdot \left(\frac{f_{cm}}{10}\right)^{0.3} \tag{4.3}$$

$$f_{ctm} = 0.3 \cdot f_{ck}^{(2/3)} \tag{4.4}$$

$$f_{ctk,0.05} = 0.7 \cdot f_{ctm} \tag{4.5}$$

Where,

E_{cm} = Mean elastic modulus (GPa)
f_{cm} = Mean cylinder compressive strength (MPa)
f_{ctm} = Mean tensile strength (MPa)
$f_{ctk,0.05}$ = 5% fractile characteristic tensile strength (MPa)

The use of the 5^{th} percentile fractile for tensile strength provides a conservative and reliable value for design, ensuring compliance with the safety requirements outlined in EN1992-1-1 (2004a). The results of the code-based equations were compared with the experimentally tested results to evaluate performance and variability under real-world conditions.

This chapter presents the average values, sample standard deviations, and Coefficients of Variation for the tested mechanical properties. Individual sample results can be referenced in AppendixA.

4.2.1 Compressive Strength

The compressive strength results for the representative samples (100mm cubes) of both mixes are shown in Figure 4.1, with the blue line representing the Dolerite mix and the red line representing the Dolomite mix. The results of the 28-day (water-cured and representative) samples and the calculated characteristic strengths (f_{ck}) are summarised in Table 4.1. For comparison, f_{ck} is plotted in Figure 4.1. The characteristic cylinder strength was used to predict the tensile strength and the elastic modulus according to EN1992-1-1 (2004a) (Table 4.1).

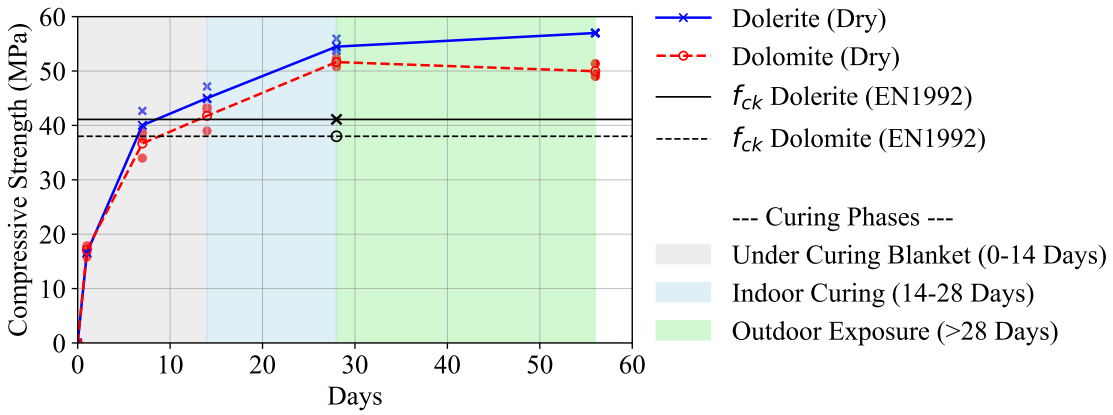

Figure 4.1: Compressive strength results for representative Dolerite (blue) and Dolomite (red) samples over time.

Table 4.1: Compressive strength of 28-day water-cured and representative samples for Dolerite and Dolomite mixes.

Property	**Water-Cured**		**Representative**	
	Dolerite	**Dolomite**	**Dolerite**	**Dolomite**
Mean Cube Strength, $f_{cm,Cube}$ (MPa)	54.8	52.1	53.4	50.9
Mean Cylinder Strength, f_{cm} (MPa)	43.9	41.7	42.8	40.7
Sample standard deviation [f_{cm}], s (MPa)	1.7	2.3	1.3	1.7
Coefficient of Variability [f_{cm}], CV	0.04	0.05	0.03	0.04
Characteristic Strength, f_{ck} (MPa)	41.1	38.0	40.7	37.9

At 28 days, the representative samples recorded average cube compressive strengths of 53.4 MPa for the Dolerite mix and 50.9 MPa for the Dolomite mix. Over time, the Dolerite mix showed a strength increase of 6.5%, reaching 57 MPa, while the Dolomite mix showed a slight decrease of 1.8%, stabilising at 50 MPa. The water-cured samples of the Dolerite and Dolomite mixes achieved a mean cube strength of 54.8 MPa and 52.1 MPa, respectively.

After estimating their equivalent cylinder strengths using Equation 4.1, the mean cylinder strengths were determined to be 43.9 MPa for the Dolerite mix and 41.7 MPa for the Dolomite mix under water-cured conditions. For representative samples, the mean cylinder strengths were slightly lower at 40.7 MPa for Dolerite and 42.8 MPa for Dolomite. The sample standard deviations (s) and coefficients of variability (CV) were calculated to evaluate the consistency of the results.

The Dolerite mix displayed a CV of 0.04 for the water-cured samples and 0.03 for the representative samples, indicating low variability and consistent material properties. Similarly, the Dolomite mix showed a CV of 0.04 for water-cured samples and 0.03 for representative samples. These low CV values reflect reliable test results, with minor differences attributed to curing conditions and inherent variability in the mixes. The characteristic cylinder strengths (f_{ck}) were calculated as 41.1 MPa and 38.0 MPa for the water-cured Dolerite and Dolomite mixes, respectively, and 40.7 MPa and 37.9 MPa for the representative samples.

4.2.2 Tensile Strength

Tensile strength in concrete can be measured using direct or indirect methods. While direct tensile tests are recognised for their higher accuracy in determining tensile capacity, they are often more complex and challenging to implement (Alhussainy et al., 2019; Gao et al., 2020). Consequently, this study adopted the code-specified splitting tensile strength test, as outlined in SANS 6253:2006 (2006b), despite its inherent limitations in accurately representing tensile capacity, as noted in the literature.

Figure 4.2 shows the development of tensile strength of representative samples over time, while Table 4.2 summarises the results of the 28-day water-cured and representative samples. As with the compressive strength samples, representative samples were cured alongside the concrete elements (Cubes, Flanges, L-Shapes and Cylinders), while the water-cured samples were maintained under standard water-cured conditions. For comparison, $f_{ctk,0.05}$ is plotted in Figure 4.2. The calculated values f_{ctm} and $f_{ctk,0.05}$ for both mixes are shown in Table 4.2.

At 28 days, the measured splitting tensile strengths of the representative samples were 4.2 MPa (sample standard deviation $s = 0.2$ MPa) for the Dolerite mix and 4.3 MPa ($s = 0.2$ MPa) for the Dolomite mix. The low sample standard deviations and coefficients of variability (CVs) of 0.05 for both mixes indicate that the results are consistent, with minimal spread between the tested samples. Over time, minor reductions in tensile strength were observed: the Dolerite mix decreased by 5%, reducing to 4.0 MPa, while the Dolomite mix decreased by 3.4%, reaching 4.15 MPa at 56 days. Despite these slight reductions, both mixes maintained good resistance to tensile cracking under prolonged exposure to environmental conditions.

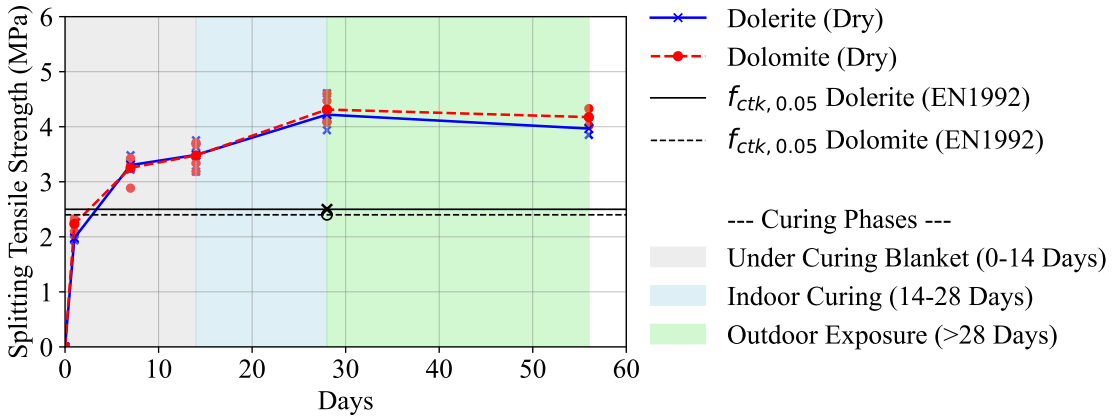

Figure 4.2: Splitting tensile strength results for Dolerite (blue) and Dolomite (red) samples over time.

Table 4.2: Splitting tensile strength of 28-day water-cured and representative samples for Dolerite and Dolomite mixes.

Property	**Water-Cured**		**Representative**	
	Dolerite	**Dolomite**	**Dolerite**	**Dolomite**
Mean Splitting Tensile Strength (MPa)	4.2	4.3	4.2	4.3
Sample Standard Deviation, s (MPa)	0.1	0.2	0.2	0.2
Coefficient of Variability, CV	0.03	0.04	0.05	0.05
Mean Tensile Strength, f_{ctm} (MPa)	3.6	3.4	-	-
5^{th} Percent Fractile, $f_{ctk,0.05}$ (MPa)	2.5	2.4	-	-

Note: Standard deviation and coefficient of variability were calculated from the measured splitting tensile strength.

The predicted mean tensile strengths (f_{ctm}) show noticeable deviations from the measured splitting tensile strengths of the water-cured samples. For the Dolerite mix, the predicted mean tensile strength was 3.6 MPa, which is approximately 14.3% lower than the measured splitting tensile strength of 4.2 MPa. For the Dolomite mix, the predicted mean tensile strength was 3.4 MPa, deviating by 20.9% from the measured splitting tensile strength of 4.3 MPa. Given the low Sample standard deviations ($s = 0.1$ MPa for Dolerite and $s = 0.2$ MPa for Dolomite), the measured results are consistent, and the discrepancies between the predicted and measured values suggest that the code-based equations can underestimate the tensile strength of these concrete mixes.

These deviations may be attributed to the empirical nature of the prediction equations, which do not account for specific material properties or environmental factors that influence the tensile strength. Although the predictive equations provide an estimate, the results indicate that they may not fully capture the tensile behaviour of these mixes.

4.2.3 Modulus of Elasticity

The E-value results are presented in Table 4.3 and Figure 4.3. The representative samples were exposed to environmental conditions, while the water-cured samples were cured under controlled conditions in accordance with the compressive strength and splitting tensile strength sample preparation (see Chapter 3). Figure 4.3 shows the development of the E-value for the representative samples over time, while Table 4.3 summarises the results of the 28-day water-cured samples.

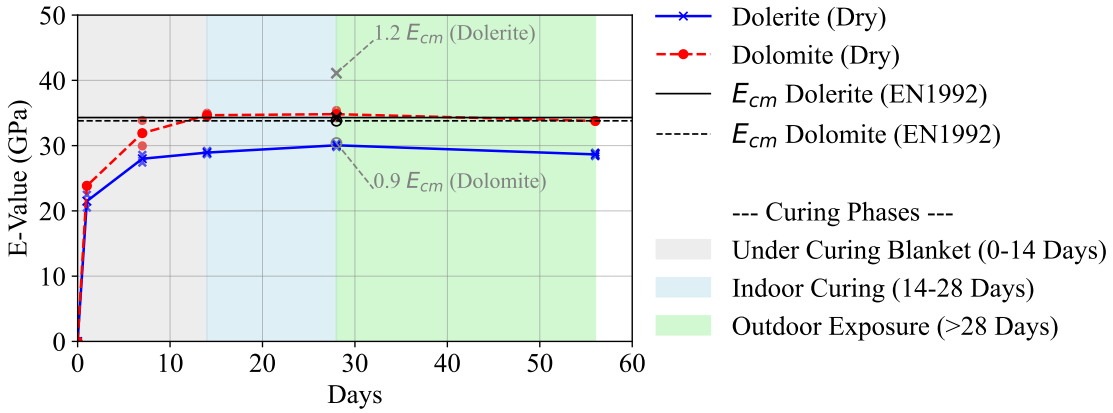

Figure 4.3: Modulus of elasticity (E-value) results for Dolerite (blue) and Dolomite (red) samples over time.

Table 4.3: Modulus of Elasticity of 28-day water-cured and representative samples for Dolerite and Dolomite mixes.

Property	**Water-Cured**		**Representative**	
	Dolerite	**Dolomite**	**Dolerite**	**Dolomite**
Measured Elastic Modulus (GPa)	31.0	37.3	30.1	34.8
Sample Standard Deviation, s (GPa)	0.7	0.6	0.3	0.6
Coefficient of Variability, CV	0.02	0.02	0.008	0.02
Mean Elastic Modulus, E_{cm} (GPa)				
Without Adjustment	34.3	33.8	-	-
With Adjustment	41.1	30.4	-	-
Aggregate Adjustment Factor	1.2	0.9	-	-

Note: Standard deviation and coefficient of variability were calculated from the measured elastic modulus values.

Representative samples showed minor variations in stiffness after 28 days, with the Dolerite mix showing an increase in E-value of 4.8% and the Dolomite mix experiencing a decrease of 4.1%. This suggests that environmental exposure had a minimal impact on the stiffness of both mixes. Notably, no rainfall events were recorded during the study period, reducing the potential for water-induced effects. The difference in measured E-values at 7 days suggests that early-age stiffness development varied between the two

mixes, likely due to differences in aggregate stiffness and hydration rates. The 28-day E-values of both Dolerite and Dolomite concrete are within the ranges reported in Table 2.1, confirming consistency with previously documented values for these aggregate types.

The low Sample standard deviations and coefficients of variability ($s = 0.4$ GPa, CV = 0.01 for Dolerite; $s = 0.8$ GPa, CV = 0.02 for Dolomite) reflect the consistency of results within each mix, indicating minimal variability in the stiffness of samples subjected to similar conditions. This consistency suggests that any differences in measured elastic modulus between water-cured and representative samples were mostly due to environmental exposure rather than inherent variability within the mixes. Notably, no rainfall events were recorded during the study period, reducing the likelihood of water-induced effects on the elastic modulus.

The 28-day water-cured E-value was also measured for both mixes, yielding 31.0 GPa for Dolerite and 37.3 GPa for Dolomite, as summarised in Table 4.3. Furthermore, the E-value was calculated in accordance with *EN1992-1-1 (2004a)* using Equation 4.3. The *EN1992-1-1 (2004a)* guidelines suggest aggregate-specific adjustments, recommending a 20% increase for basalt aggregates (Dolerite) and a 10% reduction for limestone aggregates (Dolomite). After these adjustments, the calculated E-values were 41.1 GPa for Dolerite and 30.4 GPa for Dolomite. These adjustments led to an overestimation of the E-value for Dolerite and an underestimation for Dolomite (see Figure 4.3).

The measured E-values of the representative samples compared well to the unadjusted calculated E-values, as well as to the water-cured values. For the Dolerite mix, the measured water-cured E-value (31.0 GPa) was 27% lower than the predicted adjusted value (41.1 GPa), suggesting that the actual elastic modulus of Dolerite mixes may be lower than expected when using South African aggregates. In contrast, for the Dolomite mix, the measured water-cured E-value (37.3 GPa) was 19% higher than the predicted adjusted value (30.4 GPa), indicating that the reduction factor for limestone may overestimate the reduction in stiffness. These discrepancies highlight the limitations of using *EN1992-1-1 (2004a)* generalised equations for stiffness prediction when applying them to South African aggregates.

4.3 Specific Heat Capacity

The specific heat capacity experiment aimed to evaluate the thermal properties of concrete mixes containing Dolerite and Dolomite aggregates. The experimental procedure relied on the assumptions of negligible energy losses in the calorimeter system and complete thermal equilibrium. These assumptions allowed the application of the energy balance principle, as detailed in Chapter 3. The results were analysed to determine the

specific heat capacities ($c_{concrete}$) of the two mixes, compare their thermal behaviour, and validate their suitability for numerical modelling in Chapter 6.

The temperature vs. time plot for two tests from each mix can be seen in Figure 4.4. The data demonstrate a general trend where the system's temperature initially drops slightly upon submerging the heated concrete samples into the calorimeter water. This initial drop can be attributed to several factors, including heat transfer to the calorimeter walls and components, which were initially at room temperature, and a potential lag in the response time of the temperature sensors. Additionally, evaporative cooling or minor heat loss through the calorimeter surface may have contributed to this transient temperature behaviour.

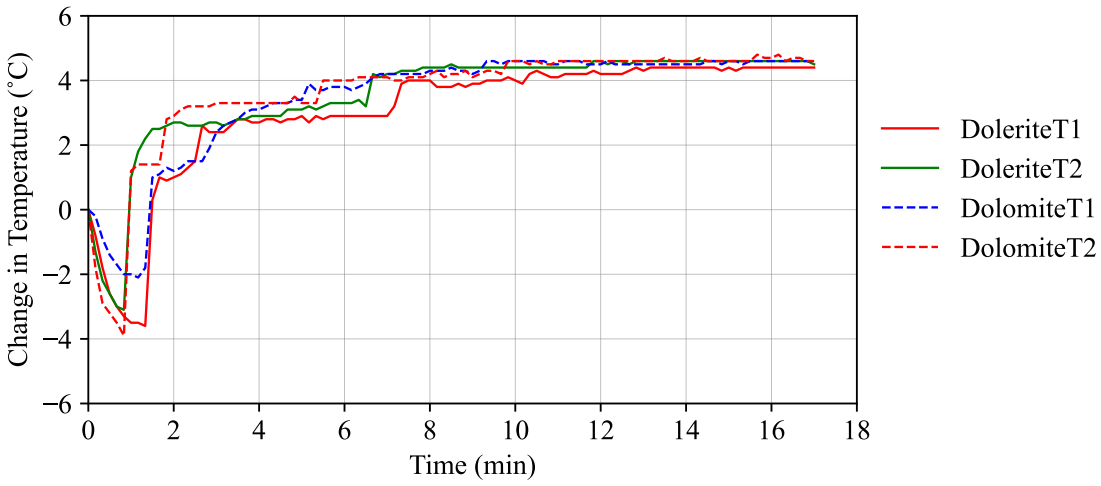

Figure 4.4: Temperature change of water during specific heat capacity experiments (T1 and T2) for Dolerite and Dolomite mixes.

After the initial drop, the system's temperature rises rapidly, followed by a gradual convergence or flattening in the rate of temperature change around 14 minutes. This flattening indicates that the system achieved thermal equilibrium as the energy exchange between the concrete, water, and calorimeter stabilised. The low variability observed in the equilibrium temperatures across repeated tests supports the adequacy of the experimental setup and the calculated specific heat capacities.

Using the measured parameters and Equation 3.4, the specific heat capacities were calculated for each test. Table 4.4 summarises the inputs and results for both mixes. The specific heat capacity values for the Dolerite mix ranged between 930 J/kg·°C and 998 J/kg·°C, with an average value of 970 J/kg·°C and a Sample standard deviation of 36 J/kg·°C. Similarly, the Dolomite mix showed a higher specific heat capacity range of 1092 J/kg·°C to 1183 J/kg·°C, with an average value of 1135 J/kg·°C and a Sample standard deviation of 45 J/kg·°C.

The Coefficient of Variation (CV) for both mixes was calculated as 0.04, indicating that the results for both mixes are consistent with low variability relative to their mean values. This consistency supports the reliability of the experimental setup and the calculated specific heat capacity values.

Table 4.4: Specific heat capacity inputs and results for Dolerite and Dolomite mixes.

Parameter	**Dolerite**			**Dolomite**		
	T1	T2	T3	T1	T2	T3
Mass of water (kg)	1	1	1	1	1	1
Mass of samples (kg)	0.902	0.806	0.836	0.832	0.800	0.798
Initial temp. of water (°C)	19.3	19.0	19.3	19.7	19.8	20.4
Initial temp. of samples (°C)	46.8	46.6	46.9	47.1	47.3	47.5
Final temp. (°C)	23.8	23.3	23.8	24.5	24.6	25.3
Calculated c_c (J/kg·°C)	930	982	998	1092	1131	1183
Average c_c (J/kg·°C)		970			1135	
Sample Standard Deviation, s (J/kg·°C)		36			45	
Coefficient of variation, CV		0.04			0.04	

The results indicate that the Dolomite mix has a higher specific heat capacity compared to the Dolerite mix. This aligns with expectations, as Dolomite's mineralogical composition typically contributes to greater heat absorption and storage capacity. The difference in the average specific heat capacities (970 J/kg·°C for Dolerite vs. 1135 J/kg·°C for Dolomite) highlights the influence of the aggregate type on the thermal performance of concrete. The ranges of specific heat capacity fall within the ranges found in the literature, summarised in Table 2.5 (American Society of Heating, Refrigerating and AirConditioning Engineers (ASHRAE), 2001; Ghali et al., 2017; Neville, 2012).

The higher specific heat capacity of the Dolomite mix indicates that more energy is required to heat the Dolomite mix by 1 °C than the Dolerite mix. This characteristic makes Dolomite-based concrete potentially more resistant to rapid temperature fluctuations, which is a critical consideration for thermal load management in structural applications.

4.4 Coefficient of Thermal Expansion

This section details the determination of the Coefficient of Thermal Expansion (CTE) of the two concrete mixes (Dolerite mix and Dolomite mix). The cylinder shapes (230mm diameter by 500mm height) were used to determine the coefficient of thermal expansion. As shown in Figure 3.15, the concrete cylinders were placed on a wooden pallet with the Vibrating Wire Strain Gauge (VWSG) positioned to measure vertical strains. This setup

minimised restraint along the vertical axis, providing a realistic representation of the concrete thermal and shrinkage response with limited structural interference. The choice of cylinders for the prediction of CTE and shrinkage was motivated by their largely unrestrained vertical expansion and contraction, which allowed for accurate thermal expansion and shrinkage measurements, essential to isolate these effects in L-Shape, Cube and Flange.

To isolate the CTE for each concrete mix, a systematic approach tracked the development of the strain in response to temperature variations over a period of 12 weeks. The 12 week period started at the end of curing (03-06-2024) and ended at the end of the experiment (03-09-2024). This methodology allowed for a detailed view of the thermal strain behaviour over time. The initial step involved plotting the strain versus temperature data points at weekly intervals for each mix, as shown in Figure 4.5. Here, (a) represents the Dolerite mix and (b) the Dolomite mix. A plasma colour scale was applied, with weekly intervals indicated by a colour bar to the right of each plot, allowing a clear visual assessment of strain development in response to temperature changes. In Figure 4.5, a clear weekly drift with a more or less constant slope was observed. The daily loop pattern in the strain vs. temperature plots reflects the cyclic thermal response of the concrete due to environmental temperature fluctuations. The gradual downward shift of the strain vs. temperature loops over time indicates a continuous strain accumulation unrelated to temperature changes, caused by drying shrinkage.

The superimposition of shrinkage on the thermal strain response highlights the dual influences of temperature and drying on the overall strain behaviour. The consistent slope of the loops, coupled with the gradual downward shift, underscores the stability of the thermal expansion of the material (α_c) while also capturing the cumulative effects of long-term shrinkage.

Subsequently, a weekly regression analysis was performed for each mix to capture the linear relationship between temperature and strain. The regression analysis is described by Equation 4.6.

$$\varepsilon_{\text{measured},wi} = \alpha_{c,wi} T_{wi} + \varepsilon_{0,wi} \tag{4.6}$$

Where,

$\varepsilon_{\text{measured},wi}$ = Measured strain for week i ($\mu\varepsilon$)
T_{wi} = Measured temperature for week i (°C)
$\alpha_{c,wi}$ = Slope (weekly coefficient of thermal expansion, $\mu\varepsilon/°C$)
$\varepsilon_{0,wi}$ = Intercept (weekly baseline strain, $\mu\varepsilon$)

Figure 4.6 (a) and (b) (Dolerite) and Figure 4.6 (c) and (d) (Dolomite) illustrate this process. In these figures:

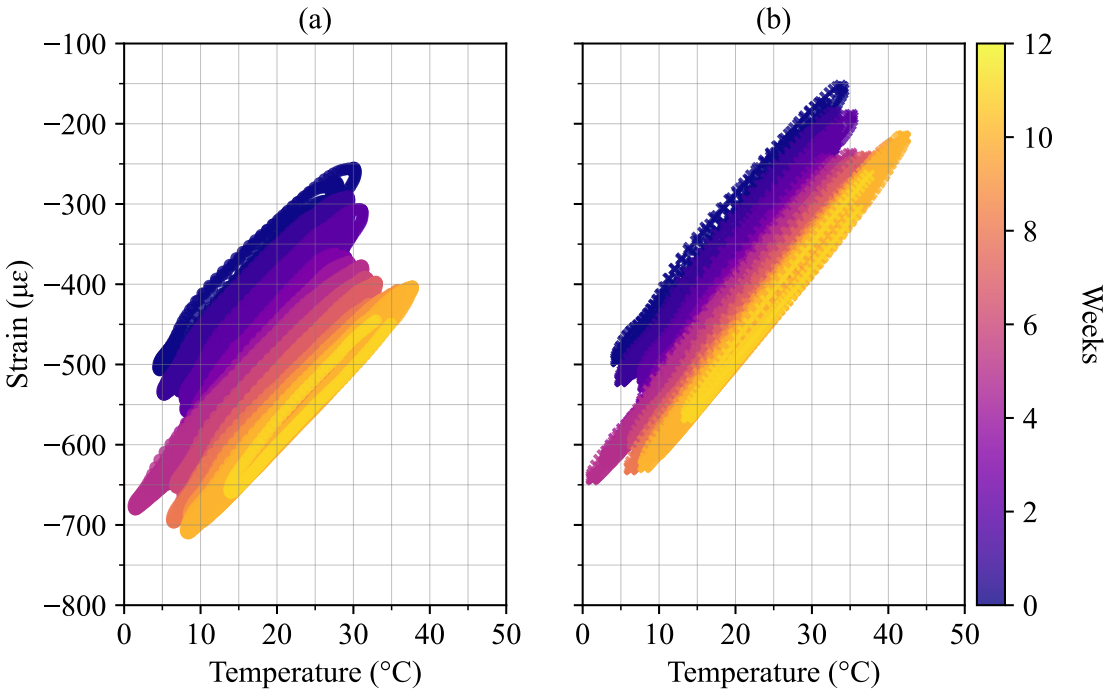

Figure 4.5: Secondary shapes (cylinders) weekly strain development plotted against temperature. (a) Dolerite mix and (b) Dolomite mix

- **(a)** Shows temperature (x-axis) versus strain (y-axis) data points with the corresponding weekly regression lines fitted to the data to calculate $\alpha_{c,wi}$ and $\varepsilon_{0,wi}$.
- **(b)** Shows the weekly progression of the regression analyses, with:
  - The primary y-axis representing the slope ($\alpha_{c,wi}$).
  - The secondary y-axis showing the weekly intercept values ($\varepsilon_{0,wi}$).

This approach provided an independent determination of α_c for each mix (Dolerite and Dolomite) over time. The adequacy of the regression analysis was confirmed by calculating the coefficient of determination (R^2) for each weekly data set, which was consistently equal to or greater than 0.93 (displayed in the legends of Figure 4.6 Dolerite (a) and 4.6 Dolomite (c)). This strong correlation underscores the adequacy of the linear fits in determining $\alpha_{c,wi}$ across the 12 weeks.

The component of thermal strain, $\varepsilon_{thermal}$, depends on the thermal expansion coefficient (α_c) for each mixture and the temperature change (ΔT), as shown in Equation 4.7.

$$\varepsilon_{thermal} = \alpha_c \Delta T \tag{4.7}$$

Where,

$\varepsilon_{thermal}$ = Thermal strain ($\mu\varepsilon$)

ΔT = Change in temperature (°C)
α_c = Coefficient of thermal expansion ($\mu\varepsilon/°C$)

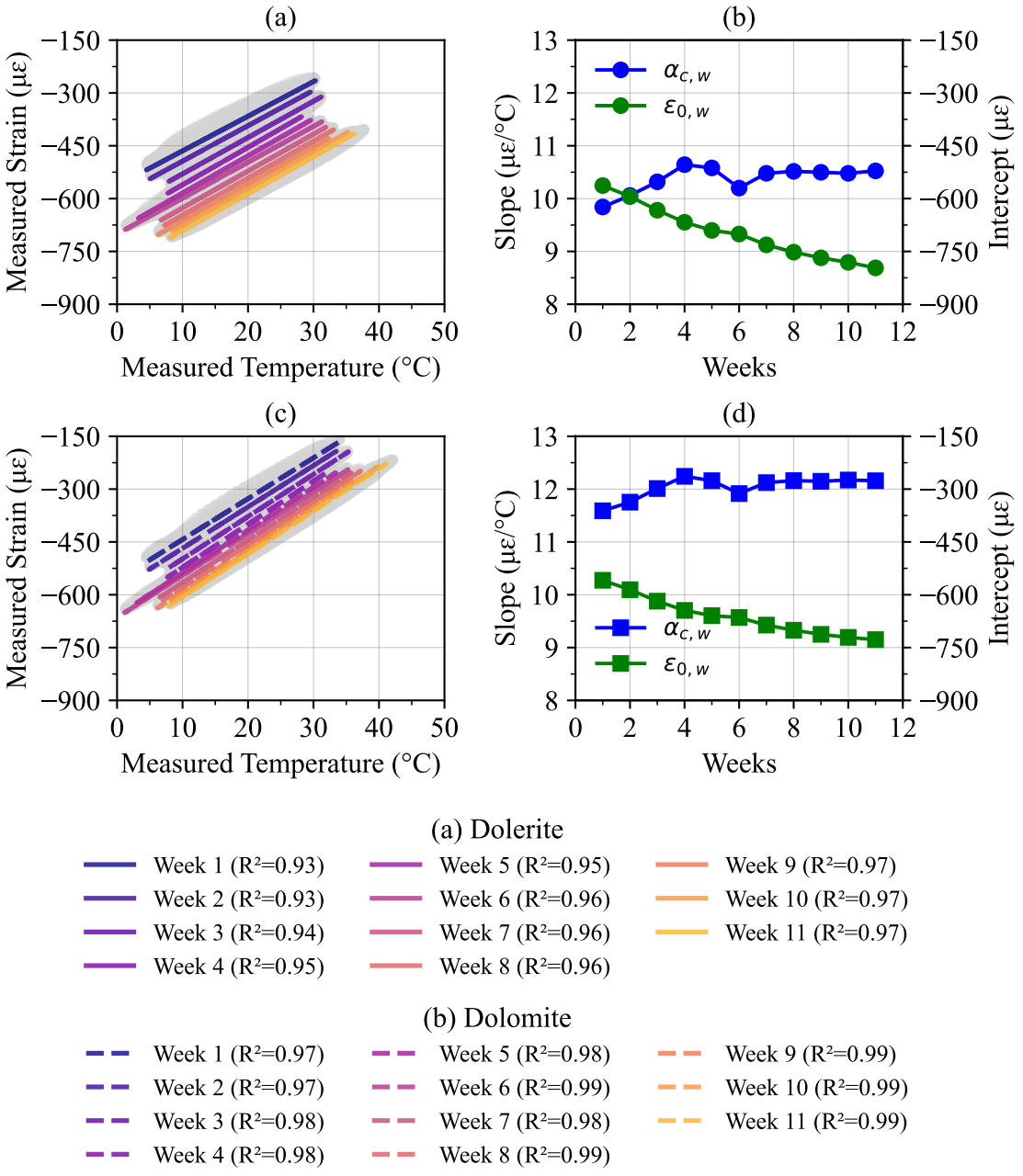

Figure 4.6: Weekly regression analysis of temperature vs strain. Dolerite: (a) data points with weekly regression lines and (b) weekly progression showing $\alpha_{c,wi}$ and $\varepsilon_{0,wi}$. Dolomite:(c) data points with weekly regression lines and (d) weekly progression showing $\alpha_{c,wi}$ and $\varepsilon_{0,wi}$.

Given the higher shrinkage rates at the start of the experiment, the values of α_c at week 11

of 10.5 $\mu\varepsilon/°C$ for Dolerite and 12.2 $\mu\varepsilon/°C$ for Dolomite were selected as effective thermal expansion coefficients. Weekly intercepts also showed a downward trend, attributed to progressive shrinkage, further distinguishing thermal from shrinkage strains.

4.5 Summary

In Chapter 4, the mechanical and thermal properties of concrete containing Dolerite and Dolomite aggregates were systematically evaluated to provide a understanding of their structural and thermal performance. The investigation focused on compressive strength, splitting tensile strength, modulus of elasticity (E-value), specific heat capacity, and thermal expansion coefficient (α_c).

The compressive and tensile strengths showed distinct trends for the two mixes. The Dolerite mix achieved higher compressive strength but a lower modulus of elasticity compared to the Dolomite mix. The EN1992-1-1 (2004a) guidelines recommend adjustments to the calculated elastic modulus (E_{cm}) based on the type of aggregate, with an increase 20% for basalt aggregates (for example, Dolerite) and a reduction 10% for limestone aggregates (for example, Dolomite). These adjustments account for the influence of aggregate stiffness on the overall modulus of elasticity. However, the adjusted E_{cm} values showed substantial discrepancies compared to the measured values in this study. For Dolerite, the adjustment overestimated stiffness by 27%, while for Dolomite, it underestimated stiffness by 19%.

The study revealed that the unadjusted E_{cm} values calculated using EN1992-1-1 (2004a) aligned closely with the measured water-cured E values and representative samples exposed to environmental conditions. This suggests that unadjusted values may provide a more accurate representation of stiffness for local aggregates, reducing the risk of overestimating or underestimating thermal strains in design applications. These findings highlight the limitations of EN1992-1-1 (2004a)'s adjustment factors for South African aggregates, emphasising the need for further research to develop locally calibrated adjustments. Until such adjustments are developed, unadjusted E_{cm} values are recommended for Dolerite and Dolomite aggregates to ensure reliability in design.

The specific heat capacity of the concrete was determined using calorimetric experiments. The Dolomite mix exhibited a higher specific heat capacity (1135 J/kg·°C) compared to the Dolerite mix (970 J/kg·°C), indicating greater thermal energy storage and slower heat release for the Dolomite mix. These thermal properties will be incorporated into the numerical model in Chapter 6 to refine the analysis of thermal conductivity and solar absorptivity.

The coefficient of thermal expansion (α_c) was derived from regression analyses of strain versus temperature data, with long-term shrinkage effects accounted for. The Dolerite mix exhibited a lower α_c value (10.52 $\mu\varepsilon/^{\circ}$C) compared to the Dolomite mix (12.16 $\mu\varepsilon/^{\circ}$C). The higher E value of the Dolomite mix implies that it would experience higher thermal stress under the same temperature gradients. Shrinkage contributed to a downward trend in strain over time, highlighting the importance of distinguishing between thermal and shrinkage strains. The combination of high shrinkage and underpredicted stiffness for the Dolomite mix underscores the necessity of accurate characterisation to avoid underestimating structural deformations and stresses.

In summary, this chapter investigates the mechanical and thermal behaviour of concrete, focussing on the interaction between the E-value and concrete's coefficient of thermal expansion in predicting thermal stresses. These findings provide input for the subsequent stress analysis in Chapter 6, ensuring that the thermal and mechanical behaviours of these mixes are accurately represented in numerical simulations. The results emphasise the importance of aggregate-specific properties in applying design codes to structural concrete and highlight the need for locally calibrated models for South African aggregates.

5 Environmental Loading and Thermal Response

5.1 Introduction

Concrete structures are frequently exposed to environmental conditions that substantially influence their thermal and mechanical behaviour. Parameters such as ambient temperature, relative humidity (RH), solar radiation, and wind speed contribute to the development of temperature gradients, thermal stresses, and drying shrinkage strains, all of which play a role in the long-term durability and performance of concrete elements. Understanding the effects of these environmental factors is important for designing resilient structures, particularly in regions characterised by highly variable climatic conditions, such as South Africa.

The properties of concrete are strongly influenced by its constituent materials. Aggregates, which comprise the majority of the concrete volume, play a critical role in modulating the thermal and shrinkage responses. The two aggregates investigated in this study, Dolerite and Dolomite, differ in their thermal conductivity, coefficient of thermal expansion, and drying shrinkage potential, making them suitable for comparative analysis under environmental loading. In addition, the geometry of concrete elements affects their response to external conditions. Elements with smaller notional sizes (h_0), such as Flanges, are more prone to drying shrinkage due to the increased volume to surface area ratios, whereas larger shapes, such as Cubes and L-Shaped shapes, exhibit more complex thermal and shrinkage behaviour.

This chapter examines the effects of environmental loading on concrete elements of varying shapes (Cube, Flange, and L-Shape) containing Dolerite and Dolomite over a three-month period of winter exposure. Data from a SenseCAP S2120 weather station (Seeed Technology Co., Ltd, 2022) provided measurements of ambient conditions, which were analysed to quantify their impact on concrete elements. These environmental factors were then incorporated into a solar radiation prediction model and an adjusted EN1992-1-1 (2004b) shrinkage prediction model to simulate and validate the thermal and shrinkage responses of concrete elements.

This chapter aims to provide a comprehensive understanding of how environmental loading interacts with aggregate properties and geometric configurations to shape the thermal and mechanical responses of concrete elements. The insights gained from this

analysis contribute to the development of better design practices for concrete structures exposed to fluctuating environmental conditions.

5.2 Weather Station Results

The environmental loading data were measured using the SenseCAP S2120 weather station, as detailed in Chapter 3, from 2024-06-03 to 2024-09-03. Key parameters, including ambient temperature, relative humidity, solar radiation, and wind speed, were recorded every 10 minutes. The data were processed by averaging over different intervals for each environmental factor to account for outliers and ensure an accurate representation. No rain was observed during this period of time, which ensured that the samples were exposed solely to the specified environmental conditions. The data provides the foundation for understanding the thermal and mechanical responses of the concrete samples to their environment.

5.2.1 Ambient Temperature

The hourly averaged ambient temperatures recorded by the weather station used in this experiment are shown in Figure 5.1. The data shows daily variations over the three-month monitoring period. The ambient temperature ranged from a minimum of -2.9 °C (2024-07-09 at 05:40) to a maximum of 29.5 °C (2024-08-22 at 14:30). To verify the accuracy of these results, data from a nearby weather station (*Pretoria UNISA)*, located approximately 4 km from the experimental site, were consulted. This station reported a temperature range of -1.4 °C to 30 °C (*Historical weather data for Pretoria,South Africa | Visual Crossing* 2024). The distribution of ambient temperatures over the monitoring period is further illustrated using a histogram and a normal probability function (Figure 5.2). The normal probability curves were generated using the probability density function (PDF) for the normal distribution, defined as in Equation 5.1 (Montgomery and Runger, 2010).

$$f(x_T) = \frac{1}{s\sqrt{2\pi}} e^{-\frac{(x_T-\mu)^2}{2s^2}} \tag{5.1}$$

Where,

x_T = Temperature value (°C)
μ = Mean (°C)
s = Sample standard deviation (°C)
$f(x_T)$ = Probability density for x_T
e_C = Euler's constant ≈ 2.718 (Montgomery and Runger, 2010)

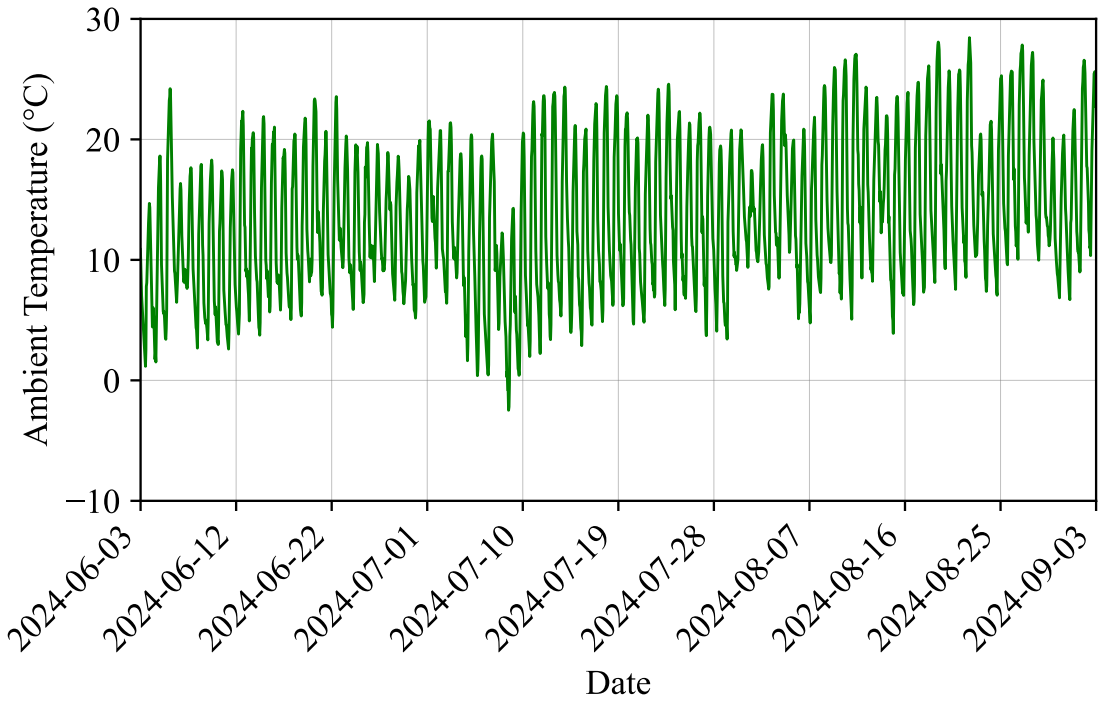

Figure 5.1: Hourly averaged ambient temperature over three months, recorded by the weather station used in this experiment.

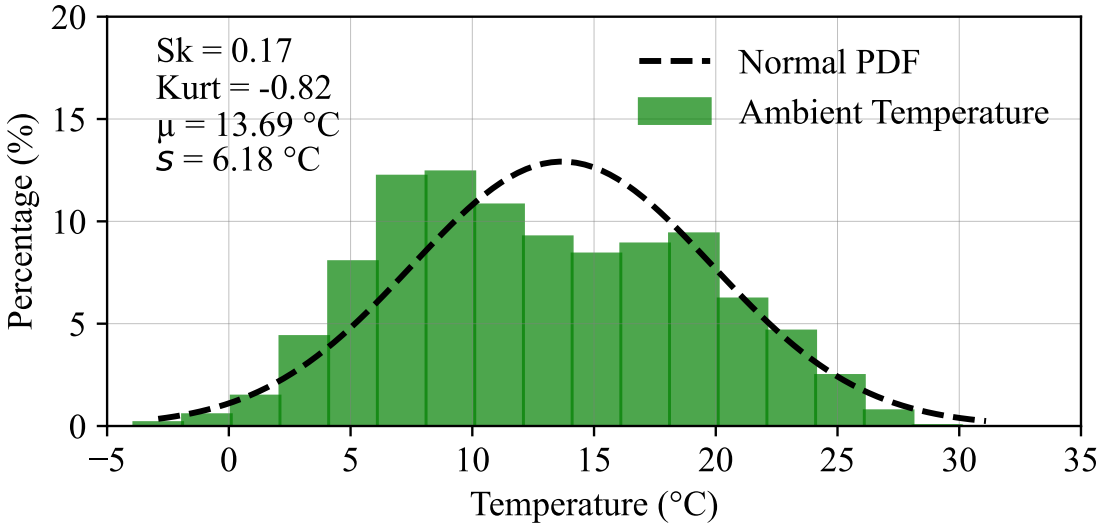

Figure 5.2: Histogram of ambient temperature distribution (2 °C bins) with PDF overlay for normality assessment.

The skewness (*Sk*) and kurtosis (*Kurt*) values provided information on the symmetry and peakedness of the ambient temperature distributions. Figure 5.2 shows the frequency of various temperature ranges, highlighting typical environmental conditions during the study period. The mean temperature was measured as 13.69°C, with a sample standard deviation of 6.18°C. The Coefficient of Variation (CV) is 45. 1%, indicating high variability in the temperature data. The distribution is slightly skewed to the right ($Sk = 0.17$) with a flatter than normal peak ($Kurt = -0.82$), suggesting that most of the temperatures clustered around $10°C - 15°C$. No extreme freezing events were observed. These results show relatively mild winter conditions, characterised by occasional colder days near 0 °C, but generally centred around a temperate range. The alignment with the normal distribution indicates consistent temperature variability typical of the winter season.

5.2.2 Relative Humidity

Relative humidity (RH) is a key environmental factor that influences drying shrinkage, as it directly affects the rate of moisture loss from the concrete surface (Neville, 2012). High RH slows moisture loss, reducing shrinkage rates, while low RH accelerates drying. However, significant fluctuations in RH and its temporal inconsistencies pose challenges for inclusion in shrinkage models. For example, EN1992-1-1 (2004a) provides predictive models for drying shrinkage based on average RH levels, but such predictions may be less reliable in environments with highly variable RH.

The RH results from the weather station were averaged daily to factor out outliers. Figure 5.3 shows the variation in daily RH during the 3-month monitoring period. RH levels showed substantial variability, with a mean value of 43.5%, a sample standard deviation of 13.4%, and extreme values ranging from 19.9% on 10 August 2024 to 72.3% on 24 June 2024. The coefficient of variation (CV) is 30.80%, supporting the observed variability. High levels of RH were predominantly observed during the early mornings, in correlation with cooler temperatures, while lower RH values were recorded during the afternoons as a result of solar heating and reduced moisture in the air.

Importantly, there were no rain events during the study period. Rainfall typically leads to near-saturation of the air with moisture, causing relative humidity to approach 100% due to the release of water vapour into the atmosphere. This process is closely tied to the concept of the dew point, the temperature at which air becomes saturated, as described by Manandhar et al. (2018). The absence of rainfall ensured that the RH fluctuations in this study were not influenced by sudden increases in moisture, which could mask other environmental effects. Instead, these variations were driven by the diurnal temperature cycle.

While EN1992-1-1 (2004a) provides a robust framework for predicting shrinkage, it relies on the assumption of stable RH conditions. The fluctuating RH observed in this

study, with large deviations from the mean, underscores the complexity of incorporating RH into shrinkage models. As such, this study excludes RH as a parameter in predicting drying shrinkage strains and instead focusses on environmental factors with more consistent influences, such as temperature and solar radiation. This decision is consistent with similar studies that emphasise the reliability of these parameters in predicting shrinkage (Kovler and Zhutovsky, 2006; Sakata and Shimomura, 2004).

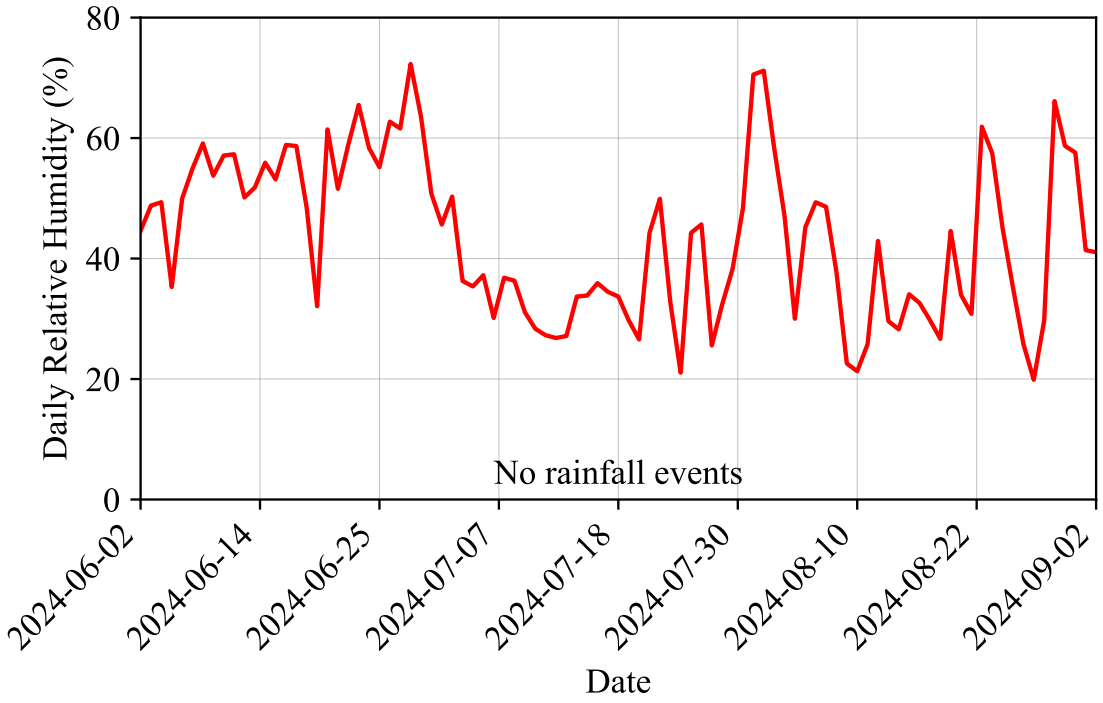

Figure 5.3: Daily averaged relative humidity (RH) over the three-month study period.

5.2.3 Solar Radiation

Solar radiation data, derived from the weather station's light intensity measurements, were analysed to quantify the thermal energy impacting the concrete samples. The light intensity (I_{lux}) measured in *lux* was converted to solar radiation (I_{measured}) in W/m^2 using a conversion factor provided in the literature. Michael et al. (2020) recommended a factor of $1\,\text{W/m}^2 = 122 \pm 1\,\text{lx}$ for outdoor solar measurements under natural sunlight conditions. This relationship is expressed in Equation 5.2. The conversion factor from light intensity(illuminance) to solar radiation (irradiation) has been widely studied and varies depending on the light source and environmental conditions. In natural sunlight, $1\,\text{W/m}^2$ of solar radiation corresponds to approximately $120\,\text{lx}$. The research carried out by Qahtan and Almawgani (2022) confirmed a similar conversion factor for outdoor sunlight, although they noted slight deviations under artificial lighting conditions 116 $lx/W/m^2$. Michael et al. (2020) provided a detailed analysis of the luminous

efficacy values, reporting a range of 121-131 $lx/W/m^2$ under varying conditions, which aligns with the factor used in this study. These variations demonstrate the importance of selecting an appropriate conversion factor tailored to natural sunlight conditions.

$$I_{\text{measured}} = \frac{I_{\text{lux}}}{C} \tag{5.2}$$

Where,

I_{measured} = Solar radiation (W/m^2)
I_{lux} = Light intensity (lx)
C_{lux} = Conversion factor ($122\,lx/W/m^2$, based on Michael et al. (2020))

Figure 5.4 illustrates the variability of solar radiation and light intensity throughout the study period. The variability in solar radiation, as shown in Figure 5.4, was used to accurately predict solar radiation on the surfaces of concrete shapes (Chapter 6). The average peak daily solar radiation for the three-month study period was $613.07\,W/m^2$, which typically occurred around 12:10 each day. The highest recorded solar radiation was $799.85\,W/m^2$ (2024-08-31), while the minimum value was $0.00\,W/m^2$ (2024-06-03). These variations may influence the thermal response of concrete, contributing to temperature gradients and thermal stresses, which are later incorporated into the study's numerical analyses (Chapter 6).

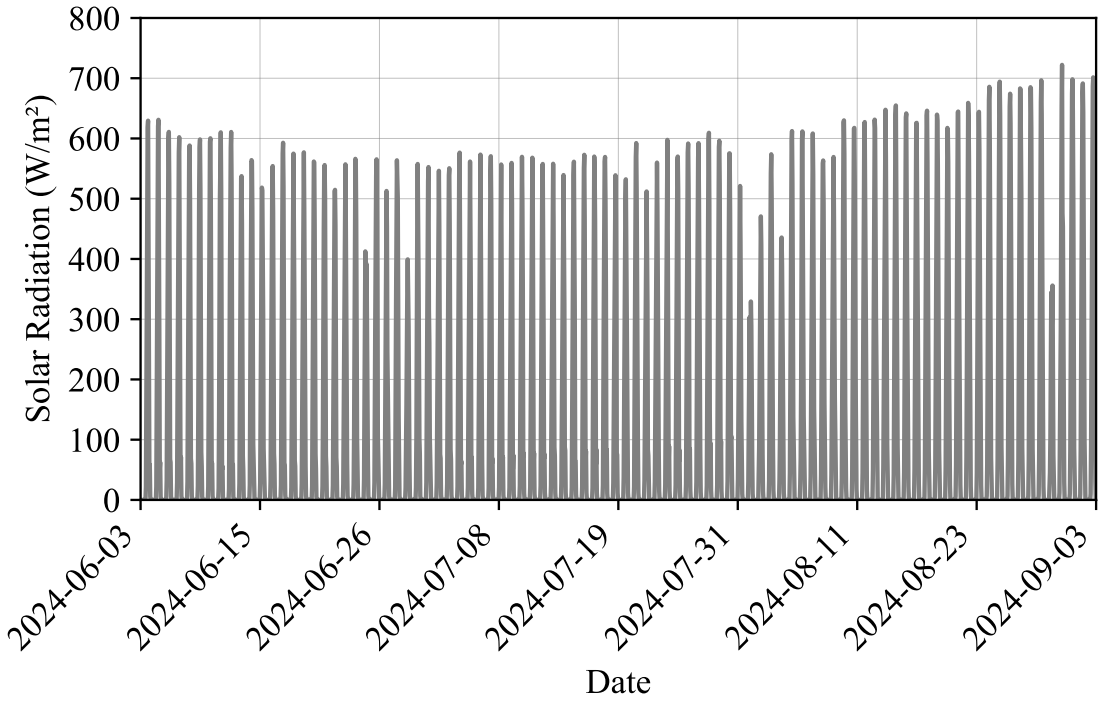

Figure 5.4: Averaged hourly solar radiation over the three-month study period.

The observed solar radiation measurements align closely with typical winter solar radiation patterns reported in the literature. Skorpen et al. (2020) showed that the winter solar radiation in central South Africa peaks at approximately 600 W/m^2 at noon, nearly a third lower than the summer maximum of 1000 W/m^2. The consistency between the measured values and those documented in the literature validates the reliability of the solar radiation data collected during the study.

5.2.4 Wind speed and Direction

Wind speed data, measured using the SenseCAP S2120 weather station, provided information on the environmental conditions surrounding the concrete samples. Figure 5.5 illustrates the averaged hourly wind speeds over the three-month study period, while Figure 5.6 presents a wind rose diagram summarising the predominant wind directions and their respective frequencies.

The analysis of wind speed data revealed the following statistics:

- **Mean wind speed:** 1.53 m/s.
- **Maximum wind speed:** 11.00 m/s (2024-07-08 @ 09:30).
- **Sample standard deviation:** 1.32 m/s.
- **Coefficient of variation:** 86.27%, indicating high variability in wind speeds over the study period.

The high CV reflects substantial variability in the wind speed data, which is characteristic of fluctuating environmental conditions. Such variability is important to consider when interpreting the thermal responses of the concrete samples.

The wind rose diagram (Figure 5.6) provides additional information on the predominant wind directions and their frequencies:

- Dominant wind direction: South (25.10%).
- Other dominant directions include:
  - North-west (18.47%),
  - West (12.03%),
  - South-west (11.19%).
- Winds from the north represented 8.50% of the observed wind patterns.

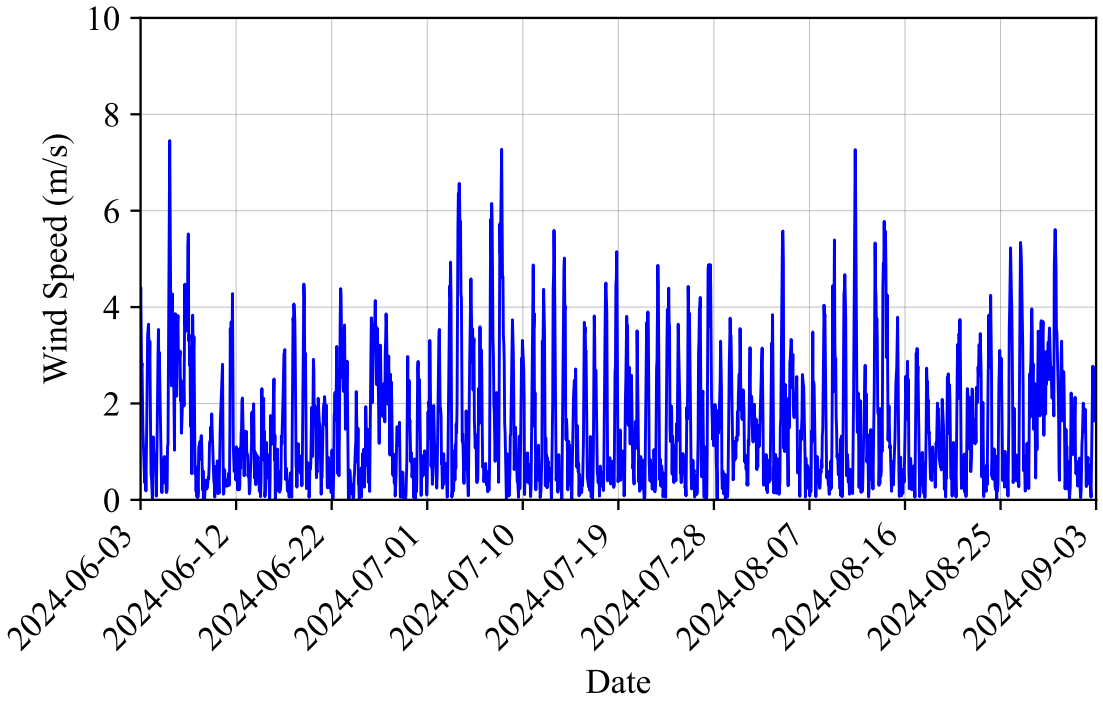

Figure 5.5: Averaged hourly wind speed (all directions) over the three-month study period.

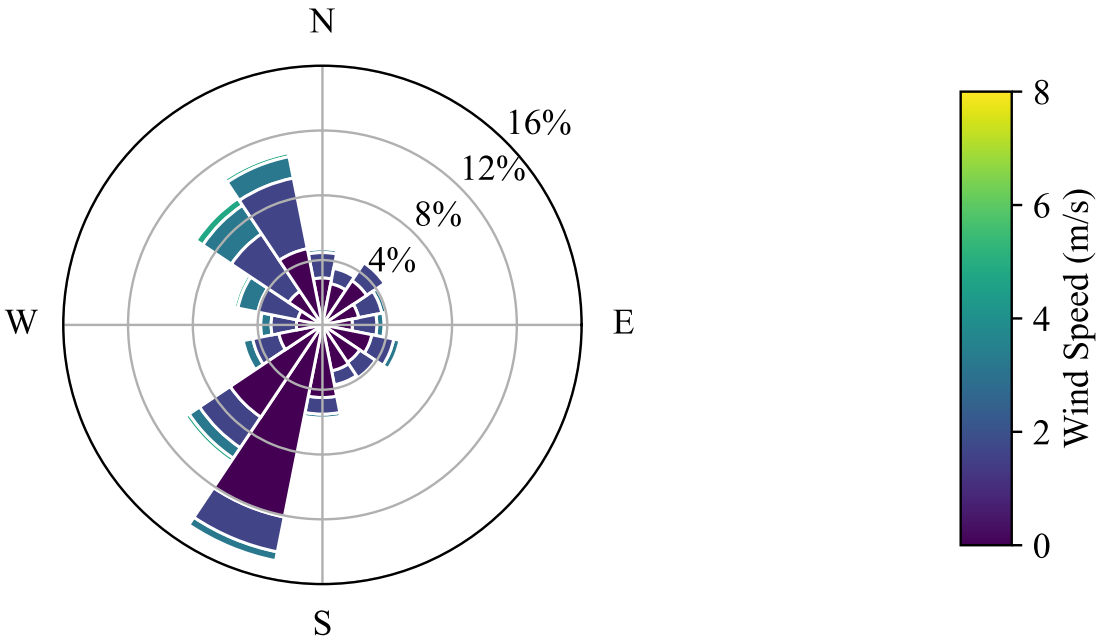

Figure 5.6: Wind rose diagram showing the predominant wind directions and speeds over the three-month study period.

The samples were placed with their southern side protected by a concrete wall, as shown in Figure 3.14. This placement influenced airflow and exposure to the prevailing winds.

- **Shielding from southern winds:** The southern wall effectively blocked the dominant winds from the south and the south-west, as identified in the wind rise. This reduced direct wind exposure to the concrete elements and created a relatively sheltered microenvironment.
- **Limited northern exposure:** Winds from the north were relatively infrequent (8.50%) and weaker in intensity compared to southern winds, further limiting the direct impact of the wind on the samples.

The samples were shielded from Southern winds, the use of the average wind speed in the numerical model is justified as it accounts for winds from other directions that likely affected the samples over the three-month period. Including southern wind speeds in the average also provides a conservative estimate, ensuring that the model does not underestimate wind (cooling) effects. Furthermore, using the average simplifies the modelling process while still reflecting the overall variability in wind conditions. However, it is acknowledged that this approach may introduce a limitation, as the shielding effect likely reduced the actual wind exposure experienced by the samples, particularly from the predominant Southern winds. Despite this, the chosen approach balances simplicity with a reasonable approximation of environmental effects.

5.3 Solar Prediction Model

The solar prediction model was implemented to calculate the solar radiation load applied to the surface elements throughout the experiment. This model takes into account the geographical location of the structures, the tilt angle of each surface, and the position of the sun over time, as described in the Chapter 2. The total solar radiation on the top, bottom, south, and north facing surface surface was computed by considering three components: direct radiation, diffuse radiation, and reflected radiation.

To ensure the precision of the solar prediction model, the calculated solar radiation values were compared with the measured solar radiation data (Figure 5.4). This comparison confirmed the reliability of the model in predicting the solar energy flux on concrete surfaces. The validation process provided confidence that the model could be used to accurately represent the thermal loads applied to the concrete elements in the numerical analysis.

5.3.1 Solar Incident and Zenith Angles

The position of the sun was calculated for each day of the year using the equations for solar incident and zenith angles. The solar zenith angle (θ_z) was calculated using Equation 2.34, which incorporates the latitude ($\phi = -25.74°$), solar hour angle (w) and the declination angle (δ). The angle of declination, dependent on the number of days (n), was calculated using Equation 2.36.

The solar hour angle (w) was calculated as a function of the time of day relative to solar noon, where $w = 0°$ at solar noon (Equation 5.3 in Kalogirou (2009)). The solar hour angle changes by 15° for every hour from solar noon.

$$w = 15° \times (t_{\text{solar}} - 12) \tag{5.3}$$

Where,

w = Solar hour angle (°)

t_{solar} = Solar time in hours ($t_{\text{solar}} = 12$ at solar noon)

Equation 5.3 allowed for tracking the position of the sun throughout the day, with positive values of w in the afternoon (west of solar noon) and negative values in the morning (east of solar noon).

The solar declination angle (δ) varies throughout the year, influencing both the θ_z and the incident angles. Figure 5.7 shows the variation of the angle of declination for 365 days, with dashed vertical lines indicating the start and end days of the experiment (Day 154 and Day 231, respectively). These values were used to calculate the solar incident angle during the experimental period.

Concrete elements (L-Shape, Cube, and Flange) have varying surface orientations and tilt angles (β) that influence the amount of solar radiation each surface receives. As shown in Figure 5.8, the top surfaces of the elements were considered to have a tilt angle of 0 ° ($\beta = 0°$), while the northern faces had a tilt angle of 90 ° ($\beta = 90°$). The southern and bottom surfaces were assumed to receive no direct solar radiation, and only reflected radiation was considered for these surfaces. The surface azimuth angle (λ) for the concrete elements was set at 10 ° east of north, as indicated in Figure 5.8.

The solar incident angle (θ) was then calculated with Equation 2.33, considering the angle of surface tilt and the solar azimuth angle (λ), which was derived using Equation 2.35. The southern and bottom surfaces were only subjected to diffuse and reflected radiation, and therefore direct solar radiation was excluded from the calculations for these surfaces.

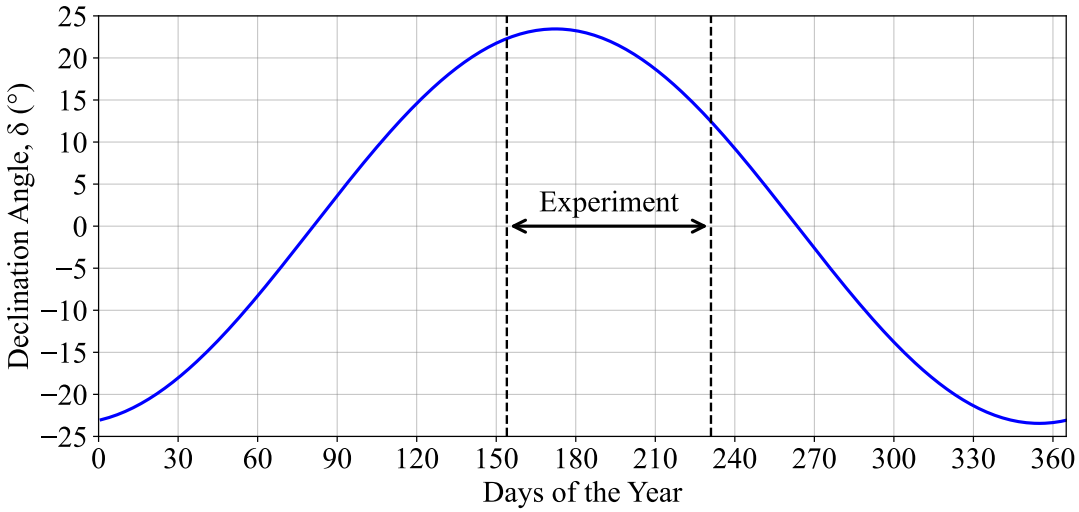

Figure 5.7: Graph of the declination angle (δ) over 361 days, indicating the start and end days of the experiment (Days 154 and 231, respectively).

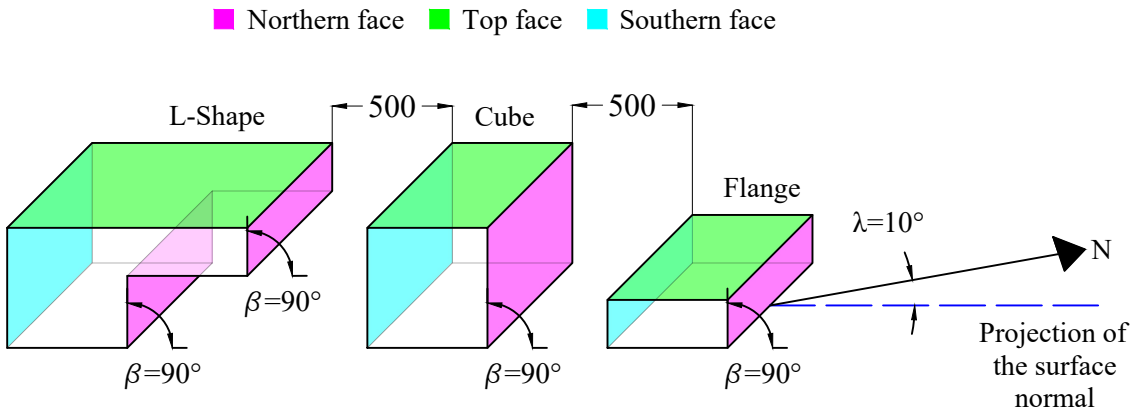

Figure 5.8: Surface orientation and tilt angles used for calculating solar radiation on the concrete elements.

Figure 5.9 shows the calculated solar incident angle for the duration of the experiment, with a colour bar indicating days of the year. The graphs show comparisons between surfaces at (a) 0 ° (top surface) and (b) 90 ° (northern surface) tilt angles. This visualisation highlights how the incident angle changes over the course of the day for different surface orientations and how it evolves throughout the experiment.

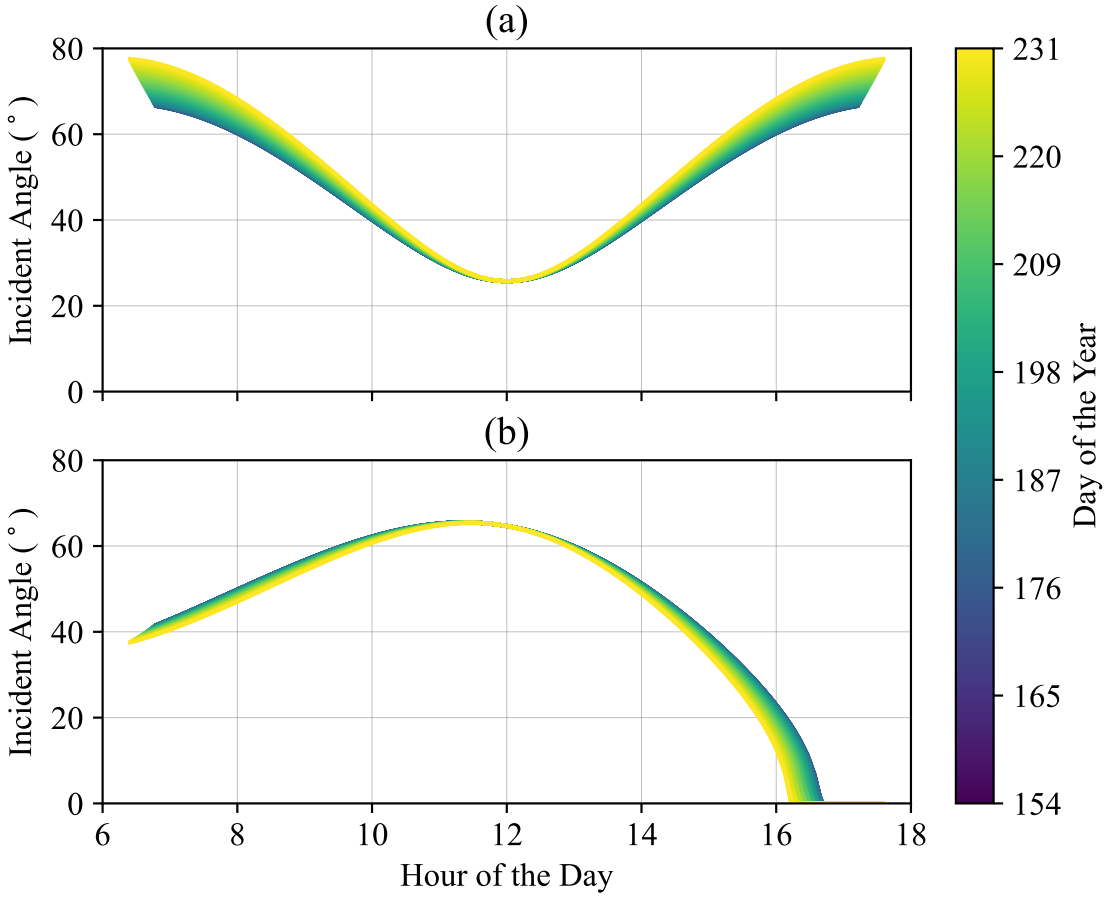

Figure 5.9: Calculated solar incident angle for the first day (Day 154) and the last day (Day 231) of the experiment for (a) 0° (top surface) and (b) 90° (northern surface) tilt angles.

5.3.2 Procedure for Calculating Total Solar Radiation

The total solar radiation on the surfaces of the concrete elements was calculated on the basis of the methodology described in Chapter 2. The components of solar radiation (direct beam radiation, diffuse radiation, and reflected radiation) were computed using the established equations for inclined surfaces.

The primary input parameters for the radiation calculations were the following:

- Beam radiation (I_{BH}) and diffuse radiation (I_{DH}) measured in the horizontal plane.

- Surface tilt angle (β) and solar incident angle (θ) for each surface.
- Zenith angle (θ_z) based on the position of the sun.
- Extraterrestrial radiation (G_{sc}) was calculated for each day of the year, as shown in Chapter 2, using the solar constant and day number (n).

Extraterrestrial radiation (G_{sc}), which represents the radiation of the beam outside the atmosphere of the Earth, was computed using Equation 2.32. This provided the base value for further adjustments based on atmospheric effects and surface orientation.

To account for atmospheric attenuation, the optical air mass (A_m) was calculated using the solar zenith angle (θ_z) as shown in Equation 2.41. The beam transmission coefficient (τ_B) was then determined using the optical air mass and the optical depth (A_d), based on Equation 2.40. These adjustments were used to modify both the beam and diffuse radiation components.

Direct beam radiation on each tilted surface (I_{BT}) was computed by adjusting extraterrestrial radiation for the solar incident angle (θ) and applying the transmission coefficient (τ_B), as shown in Equation 2.37 from Chapter 2. The formula for I_{BT} accounted for the orientation and tilt angle of the surface.

The diffuse radiation on the tilted surfaces (I_{DT}) was calculated using the diffuse fraction (k_{td}), which relates the diffuse radiation and the beam radiation, as shown in Equation 2.42. The total diffuse radiation was then adjusted on the basis of the tilt angle and sky view factor (F_{wb}).

Reflected radiation from the ground and surrounding surfaces (I_G) was included in the total solar radiation calculation using the ground view factor (F_{wd}) and the ground reflectance value (ρ_g), based on Equation 2.47 from Chapter 2.

The total solar radiation ($I_{Total,\beta=0}$, $I_{Total,\beta=90}$ and $I_{Total,Reflected}$) on each surface was calculated by summing the direct beam radiation on the tilted surfaces (I_{BT}), diffuse radiation on the tilted surfaces (I_{DT}), and reflected radiation (I_G) as shown in Chapter 2. This approach ensured that both direct and diffuse components, along with reflections from the ground, were accurately represented in the model.

Here, $I_{Total,\beta=0}$ represents the total radiation on the top surfaces of all shapes, $I_{Total,\beta=90}$ represents the total radiation on the north-facing surfaces, and $I_{Total,Reflected}$ represents the total radiation on the bottom and south-facing surfaces.

5.3.3 Model Calibration and Fit

The total solar radiation calculations, outlined in the previous sections, were calibrated by comparing the model's predictions to the measured solar radiation data. While there are established methods for determining the optical depth (A_d), as discussed in Chapter 2, an empirical and simple approach was deemed sufficient for the purposes of this study. The calibration process involved iteratively adjusting the optical depth to match the measured peak solar radiation during clear and cloudy conditions. The optical depth was manually varied and the resulting model predictions were compared to the measured data to achieve the closest alignment of the predicted and measured peaks.

Special consideration was given to calibrating the surfaces with a 0° tilt, since the weather station measured direct beam radiation on horizontal surfaces. For periods with cloudy conditions, the optical depth was adjusted to simulate the reduction in solar radiation caused by cloud cover, ensuring accurate modelling of both beam and diffuse radiation over time. This empirical calibration method was considered appropriate to refine the model and achieve predictions under the specific conditions of this study.

Figure 5.10 shows the variation of optical depth (A_d) over time, highlighting periods of clear and cloudy conditions. During clear-sky conditions, a lower optical depth was used as input, while during cloudy conditions, optical depth was increased to reflect the increased scattering and absorption of solar radiation by the atmosphere.

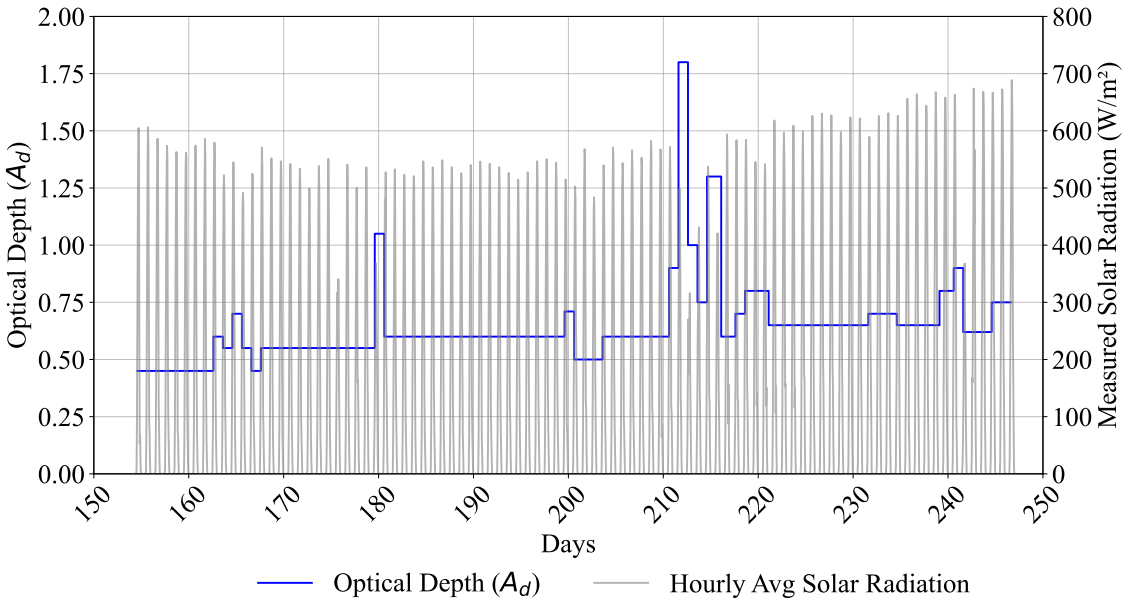

Figure 5.10: Optical depth (A_d) variation over time, with adjustments for clear and cloudy conditions.

Figure 5.11 shows a comparison between the measured and predicted solar radiation for the horizontal (0° tilt) surface. The calibration was performed using the measured direct radiation, as the weather station provided radiation data for horizontal surfaces. The model was calibrated to match the measured data during both clear and cloudy conditions.

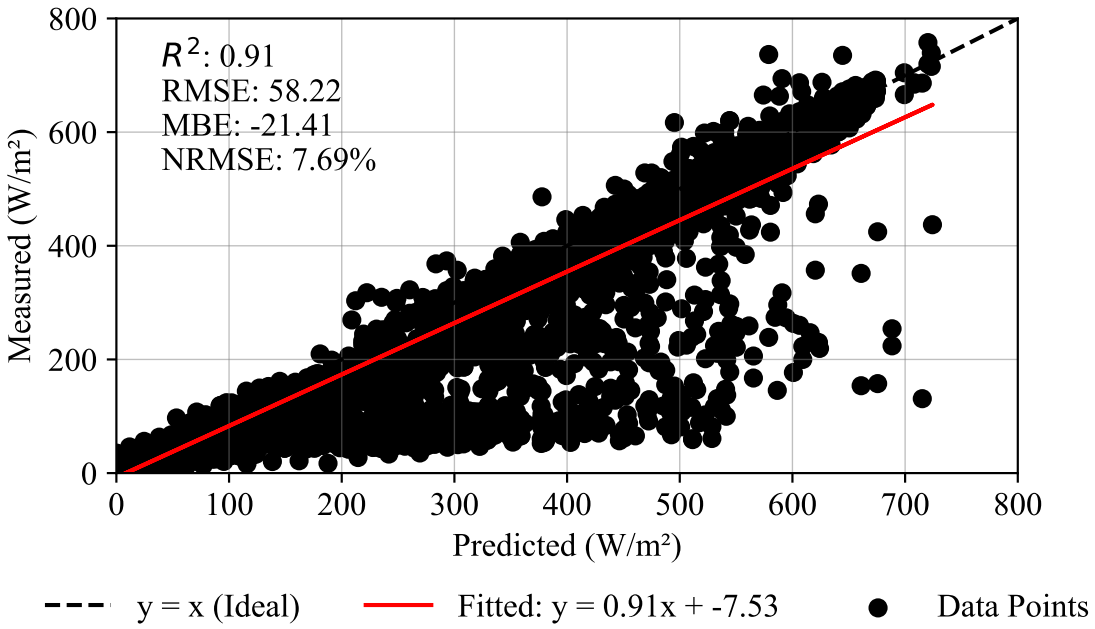

Figure 5.11: Comparison between measured and predicted solar radiation on the horizontal (0° tilt) surface.

Figure 5.11 illustrates the relationship between the measured and predicted solar radiation values, revealing a strong correlation with a coefficient of determination ($R^2 = 0.91$). This high R^2 value indicates that 91% of the variance in the measured solar radiation is explained by the model, demonstrating its adequacy in capturing daily fluctuations across both clear and cloudy periods. However, while the high R^2 reflects strong correlation, it does not necessarily imply perfect prediction accuracy.

To assess the model's predictive accuracy, the Root Mean Square Error (RMSE) was calculated relative to the $y = x$ reference line. The RMSE for this alignment was 58.22 W/m², indicating the typical deviation between the predicted and measured values. RMSE quantifies the average absolute deviation between predictions and observations, with lower values indicating better accuracy. The best-fit equation ($y = 0.91x - 7.53$) further reveals a slight underestimation at higher radiation values, suggesting that the model tends to underestimate peak solar radiation. To further evaluate model accuracy, the Normalized Root Mean Square Error (NRMSE) was calculated, which expresses RMSE

as a percentage of the mean measured values. The NRMSE for the $y = x$ alignment was 7.69%, indicating limited variability.

Furthermore, the Mean Bias Error (MBE) was calculated to assess systematic bias in the predictions. The MBE for this model was -21.41 W/m², indicating a tendency to over-predict solar radiation. An ideal MBE would be close to zero, which implies that there is no systematic bias (Moustris et al., 2010). The negative MBE value suggests that the model may consistently overestimate radiation levels, likely due to assumed atmospheric conditions or simplifications in cloud transmissivity effects.

The calibration process involved adjusting the optical depth to account for atmospheric variability, including changes in cloud cover and aerosol concentrations. While the model closely follows the ideal $y = x$ trend, the best-fit slope of 0.91 indicates a slight under-prediction of solar radiation, particularly at higher intensities. This underestimation is likely due to limitations in cloud transmissivity representation or residual errors in diffuse radiation modelling. Despite this, the high R^2 value and RMSE analysis suggest that the iterative calibration of the optical depth effectively improved model performance, allowing it to capture both short-term variations and long-term trends in solar attenuation. However, the moderate NRMSE and negative MBE highlight the presence of prediction errors and a tendency to overestimate radiation levels, which could be refined through further adjustments to cloud correction factors or alternative calibration approaches.

In South Africa, aerosol optical depth (AOD) is a key parameter for understanding the influence of aerosols on solar radiation, climate, and air quality. Extensive studies, using both satellite and ground-based observations, have shown significant spatial and temporal variability in AOD due to factors such as biomass burning, dust storms, and seasonal meteorological patterns (Adesina et al., 2016; Eck et al., 2003; Habib et al., 2019; Hersey et al., 2015; Kumar et al., 2020; Tesfaye et al., 2011). In Pretoria, aerosol optical depth values exhibit marked seasonal trends, with higher concentrations during periods of increased aerosol loading. For example, Kumar et al. (2014) reported that AOD values in South Africa can frequently exceed 0.3 during such periods, reflecting substantial aerosol concentrations. Similarly, Adesina et al. (2016) observed that AOD values could reach between 0.7 and 1.7, particularly during biomass burning seasons, highlighting the regional impact of these events on atmospheric conditions.

Given the variability of optical depth over the duration of the experiment, no fixed A_d value was used in the model. Instead, a daily adjustment of A_d was employed to optimise the fit to the measured solar radiation data. This method ensured that the model captured the dynamic nature of atmospheric changes, aligning the predicted and observed solar radiation with high accuracy under varying conditions. By calibrating the model using the 0° tilt surface, where direct radiation was measured, and fine-tuning the optical depth

each day, the model successfully simulated both clear and cloudy conditions. Figure 5.12 shows the predicted solar radiation over the three month experimental period.

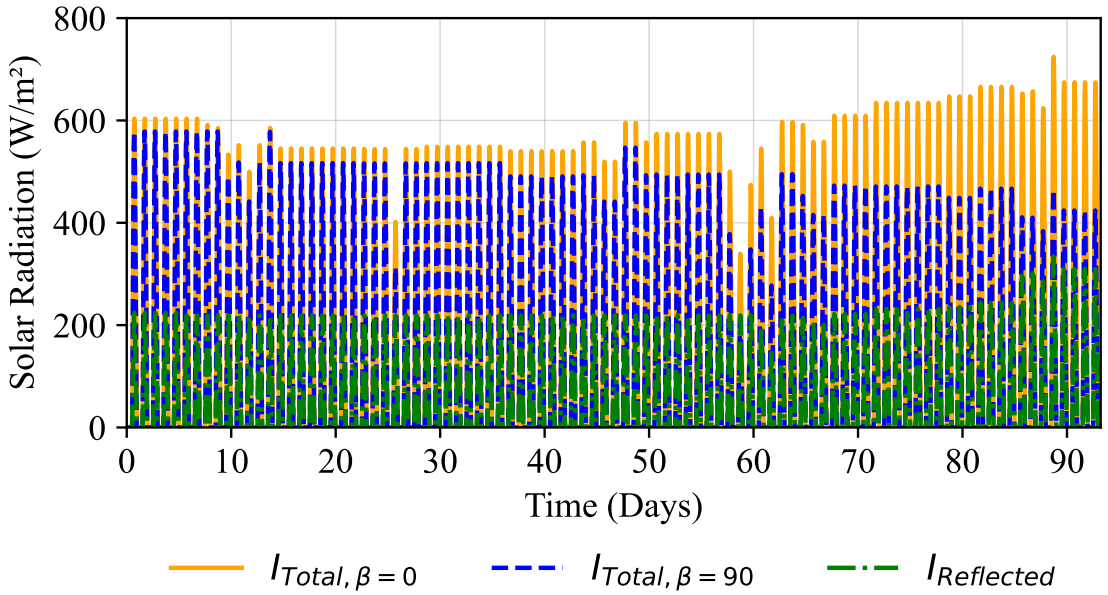

Figure 5.12: Predicted solar radiation over experimental period (top ($I_{Total,\beta=0}$), north ($I_{Total,\beta=90}$), and south and bottom ($I_{Reflected}$))

5.4 Thermal Response Results

To facilitate data interpretation, the position of each sensor and the corresponding naming convention are shown in Figure 5.13. The figure shows the locations of thermocouples and VWSGs across the L-Shape (a), Cube (b), and Flange (c) with a consistent labelling structure to distinguish each sensor based on its shape and depth.

The temperature variations recorded from 06-05-2024 (cast) to 03-09-2024 (end of experiment) are shown in Figure 5.14. The graph shows the period of environmental exposure (03-06-2024 to 03-09-2024), during which the concrete specimens were subjected to daily and seasonal fluctuations (winter). The temperature data are grouped and colour-coded to represent the specific sensors of each concrete shape. Figure 5.14 provides an overview of the measured temperature data, serving as a visual representation of the recorded temperatures during the experimental period.

The period after the relocation of the samples to the outdoor environment (*Moved Outside* in Figure 5.14) was then isolated, allowing for a focused analysis of the effective temperature response of each shape during exposure to real environmental conditions. The effective temperatures resulting for each shape during the exposure period are shown in Figure 5.15.

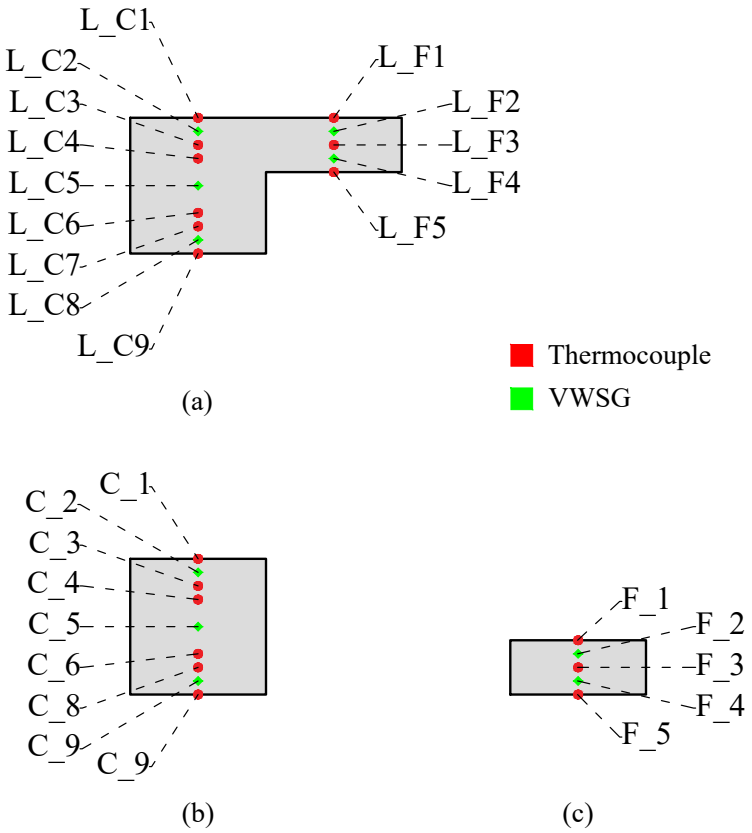

Figure 5.13: Sensor naming convention for temperature sensors in (a) L-Shape, (b) Cube, and (c) Flange.

To determine the effective temperature for each concrete shape, the concept of the effective bridge temperature (EBT) was applied using Equation 2.1, adapted to compute the weighted average temperature across the concrete shapes. The effective temperature, T_{eff}, was calculated as shown in Equation 5.4, where the contribution of each sensor was weighted according to its corresponding area within the shape.

$$T_{\text{eff}} = \frac{\sum_{i=1}^{n} A_i \cdot T_i}{\sum_{i=1}^{n} A_i} \tag{5.4}$$

Where,

T_{eff} = Effective temperature of the concrete shape (°C)
T_i = Temperature recorded by sensor i (°C)
A_i = Area associated with sensor i (m^2)
n_s = Total number of sensors in the concrete shape

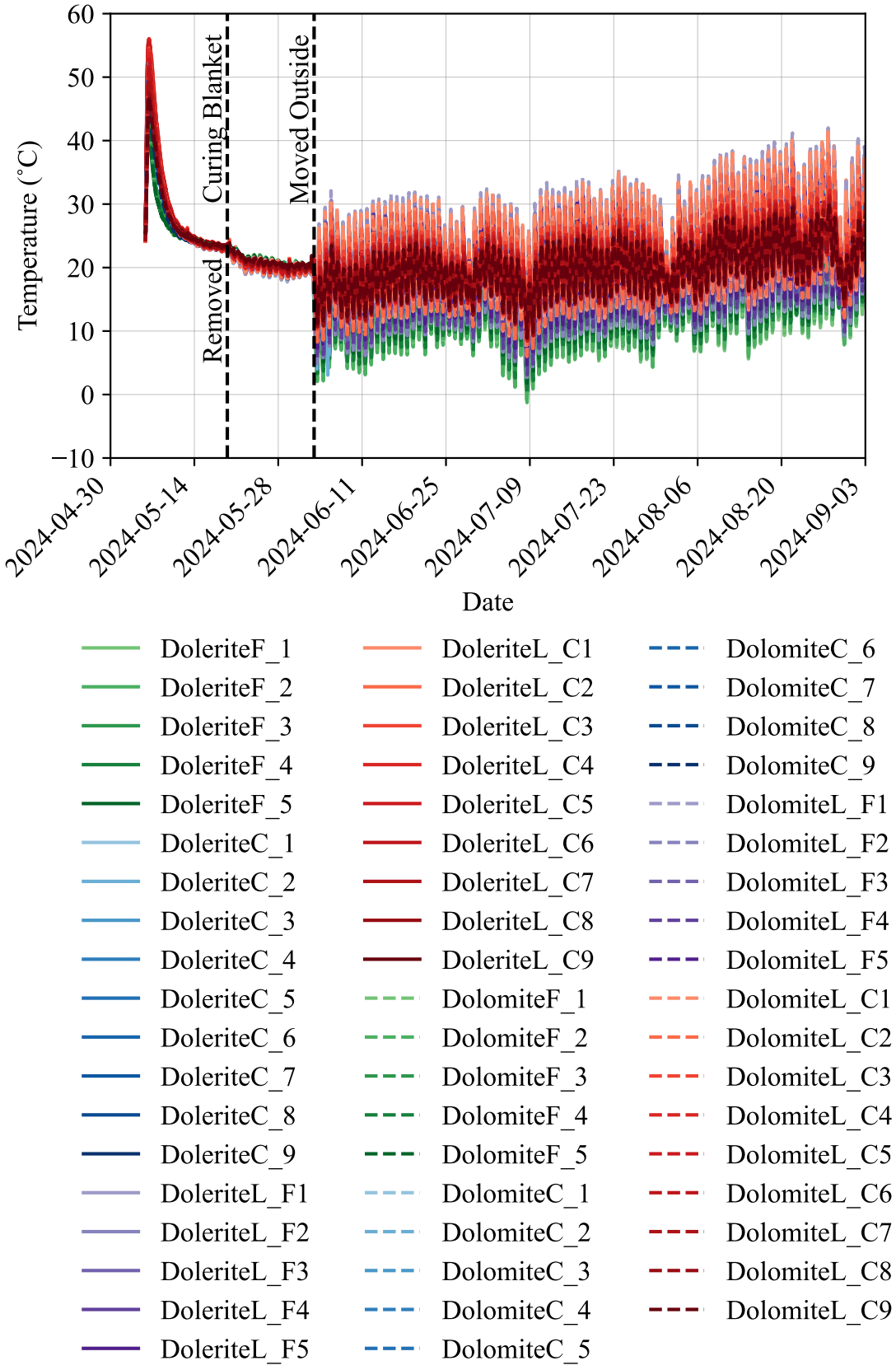

Figure 5.14: Measured temperature results from the start of the experiment.

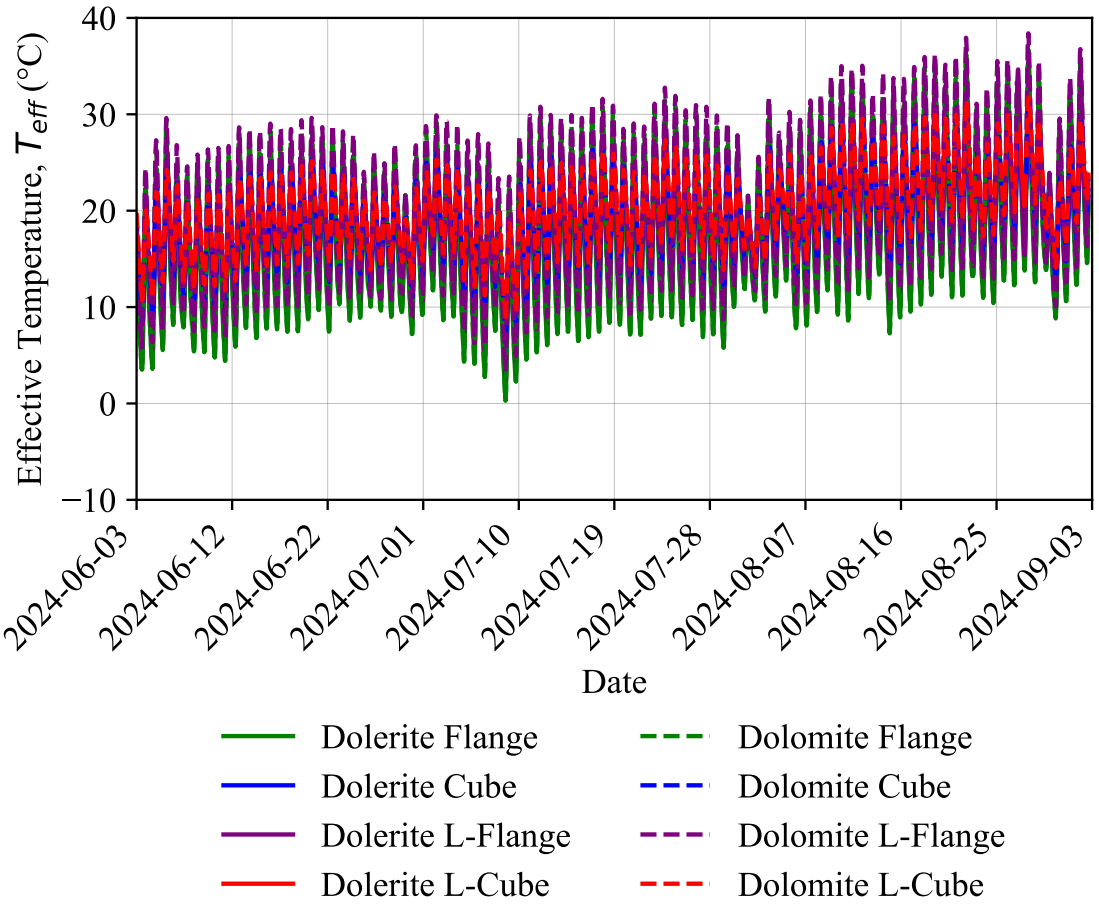

Figure 5.15: Calculated effective temperature for each shape over the three month exposure period.

5.4.1 Effective Temperature Normal Distribution Analysis

The distribution and skewness of the effective temperature data were evaluated by plotting normal probability curves for each shape and aggregate type over the three-month experimental period (Figure 5.16). These distributions were constructed using Equation 5.1, similar to the method applied for ambient temperature analysis. The effective temperature data were grouped into 2 °C bins to ensure robust comparisons between the Dolerite and Dolomite mixes.

For the Dolomite mix, skewness (*Sk*) values ranged from 0.02 to 0.27, while the kurtosis (*Kurt*) values ranged from −0.43 to −0.89, indicating slightly asymmetric distributions with flatter peaks than normal. Similarly, the Dolerite mixture exhibited a skewness ranging from 0.01 to 0.24 and kurtosis between −0.27 and −0.74. These results suggest that both mixes experienced mild winter conditions, with temperature distributions

approximately normal but slightly skewed to the right, consistent with ambient winter conditions (Figure 5.2).

The mean effective temperatures for Dolomite ranged between 18.18 °C and 20.39 °C, while the Dolerite mix exhibited means between 16.87 °C and 19.17 °C. Although this difference suggests a warmer temperature for Dolomite, the high CV observed in the data indicates substantial variability within each mix. The variability in distributions, represented by the sample standard deviations (s), was similar for both mixes, ranging between 3.66–6.43 and 4.12–6.45 for Dolerite and Dolomite, respectively. This high variability suggests that the observed differences in mean temperatures may not be significant and are influenced by environmental fluctuations during the experimental period.

The L-Shape Cube (Dolomite) showed the highest mean temperature (20.39°C), while the Flange (Dolerite) had the lowest (16.87°C), indicating a difference of approximately 3.5°C. The Cube and L-Shape Cube generally had higher mean temperatures than their corresponding Flange shapes, suggesting a greater heat retention capacity in more compact geometries. Sample standard deviations were higher in Flange and L-Shape Flange elements, indicating greater temperature variability compared to the more thermally stable Cube sections. Although these differences highlight some trends in thermal behaviour between shapes, the overlapping ranges and similar skewness and kurtosis values suggest that the variations, although notable, may not be highly substantial.

By isolating the effective temperature data into these distributions, the 5^{th} and 95^{th} percentiles were applied to determine the upper and lower bounds of the temperature ranges while excluding extreme values or outliers.

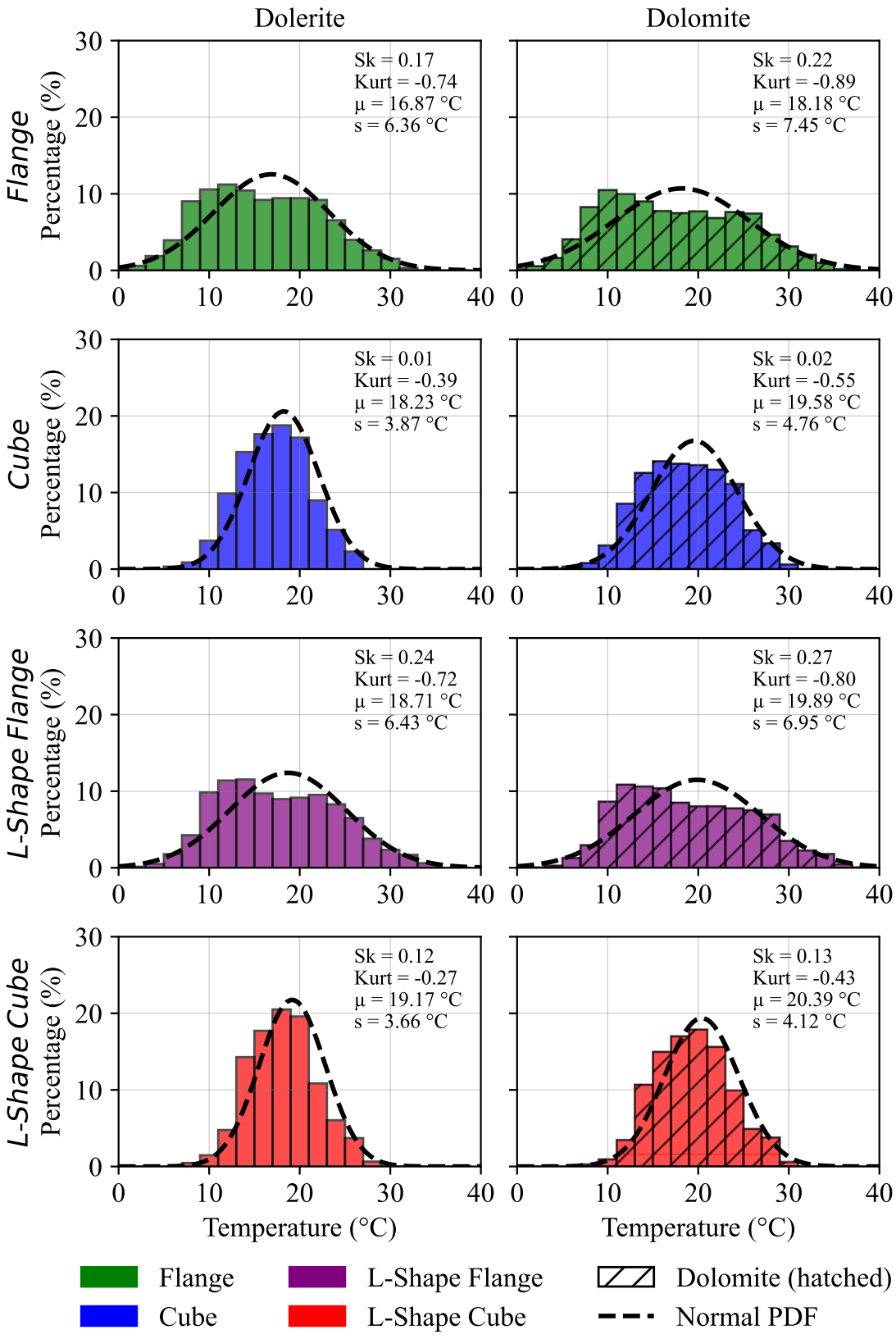

Figure 5.16: Normal probability curves for the measured effective temperatures of all shapes (3-month period).

5.4.2 Extreme Range of Effective Temperature

To assess the variation in effective temperatures under winter conditions, an "equivalent winter day" was constructed by plotting the effective temperatures of 5^{th} and 95^{th} percentiles for each shape and aggregate type at every hour of the day. This approach resulted in shaded regions representing the extreme temperature ranges for each shape, while the average effective temperatures for the Dolerite and Dolomite mixes were superimposed as solid and dashed lines, respectively, for comparison (Figure 5.17).

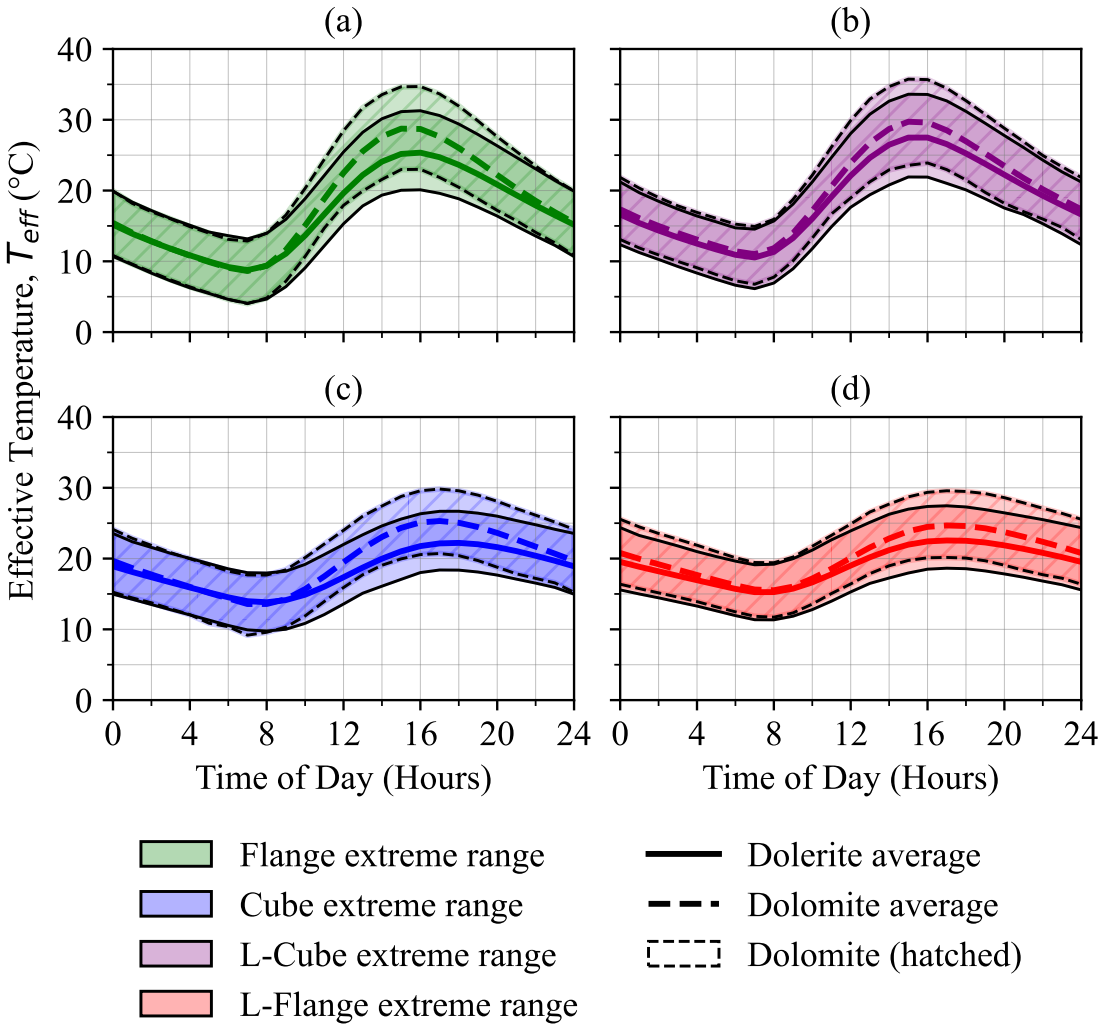

Figure 5.17: Winter (June to September) vertical effective temperature T_{eff}: (a) Flange, (b) L-Shape Flange, (c) Cube, (d) L-Shape Cube.

The results suggest differences in the thermal behaviour between the two mixes, with Dolomite shapes generally showing larger temperature fluctuations throughout the day. For instance, the Dolomite Flange shows an extreme temperature range of approximately

11 °C to 36 °C, compared to the Dolerite Flange, which ranges from 9 °C to 33 °C. However, the high CV observed in both mixes indicates considerable variability in the data. While the larger temperature fluctuations in the Dolomite mix may be attributed to its higher thermal conductivity and solar absorptivity, the observed differences could also be influenced by environmental factors and inherent variability within the experimental data. In contrast, the narrower temperature range in the Dolerite shapes reflects reduced thermal fluctuations under the same environmental conditions, though this behaviour may also be affected by experimental variability.

The average daily effective temperature changes varied substantially across different shapes. The Flange (Dolomite) showed the highest temperature fluctuation (20.12°C), while the L-Shape Cube (Dolerite) showed the lowest (7.30°C). Flange and L-Shape Flange elements experienced larger daily temperature variations compared to Cube and L-Shape Cube elements, indicating that the former were more responsive to external temperature fluctuations. This is further supported by the higher sample standard deviations observed in the Flange and L-Shape Flange shapes, with values ranging from 6.36°C to 7.45°C, compared to the Cube shapes, which had lower sample standard deviations between 3.66°C and 4.75°C. The greater thermal stability of the Cube sections can be attributed to their increased depth, which provides greater thermal mass, reducing the rate of heat transfer and moderating temperature fluctuations.

To better understand the distribution of effective temperatures throughout the experimental period, a box-and-whisker plot was constructed for each shape and mix, using the 5^{th} and 95^{th} percentiles as limits (Figure 5.18).

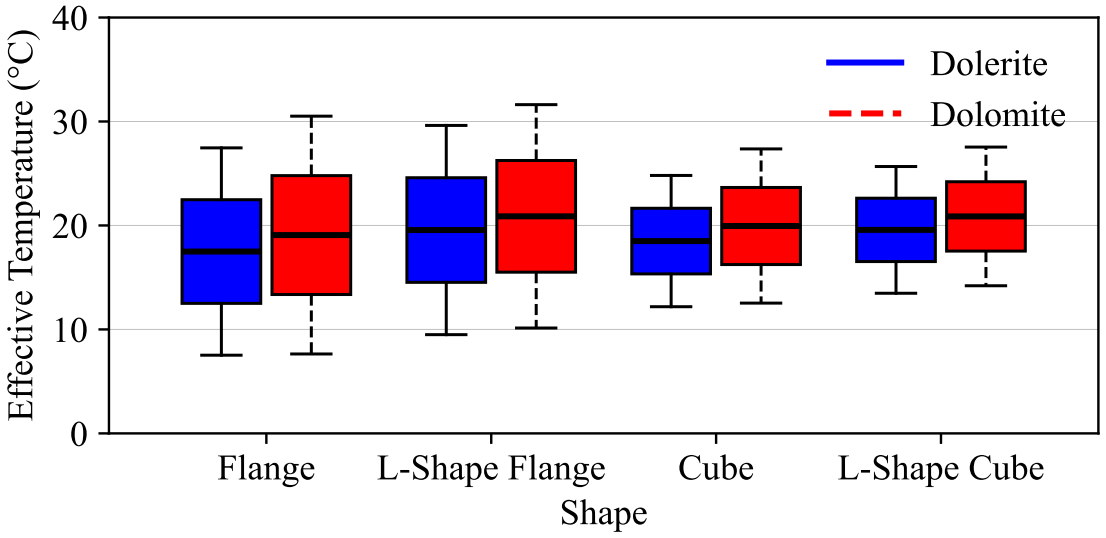

Figure 5.18: Box-and-whisker plot of effective temperature (T_{eff}) ranges for each shape and mix, based on the 5^{th} and 95^{th} percentiles.

The box-and-whisker plot highlights the trends measured on an equivalent winter day. While Dolomite shapes exhibit slightly larger interquartile ranges (IQR), indicating marginally greater variability in effective temperatures, the differences between the mixes may not be statistically significant. For instance, the Dolomite Flange has an IQR of 8 °C, compared to 6 °C for the Dolerite Flange. Similarly, the Dolomite L-Shape Cube has a median effective temperature of 20.4 °C, which is approximately 1.2 °C higher than the Dolerite L-Shape Cube. However, statistical tests confirmed that these differences fall within the bounds of variability and cannot be attributed to the inherent thermal properties of the mixes alone. This suggests that the thermal responses of Dolerite and Dolomite mixes to environmental conditions are comparable.

The differences in thermal behaviour of the shapes are also evident in the overall temperature range distributions captured in the box-and-whisker plots. The Flange and L-Shape Flange elements showed the largest temperature ranges, with the Dolomite Flange reaching the highest overall range (36.07°C) and a maximum temperature of 36.57°C. These elements also had the largest interquartile ranges (IQR), indicating higher variability in daily temperature fluctuations. In contrast, the Cube and L-Shape Cube elements displayed narrower temperature distributions, with lower maximum values and reduced IQRs. The Dolerite Cube had the smallest range (21.22°C), reinforcing the role of depth in stabilising temperature fluctuations by reducing heat loss and gain. While the L-Shape Cube (Dolomite) had a slightly higher temperature range (22.48°C), it remained substantially lower than the Flange elements.

The combined results from Figures 5.17 and 5.18 indicate that while the Dolomite mix exhibited slightly higher effective temperatures and larger temperature fluctuations than the Dolerite mix, the high variability within both datasets suggests that these differences may not be statistically significant. Flange and L-Shape Flange elements consistently showed greater temperature ranges and variability compared to Cube and L-Shape Cube sections, reinforcing the role of shape in moderating thermal behaviour. The deeper Cube sections showed smaller temperature variations due to their increased thermal mass, which buffers against rapid environmental fluctuations. The findings highlight that within the scope of this study, aggregate type had a limited influence on the overall thermal response of concrete elements, with shape playing a more dominant role in temperature variations.

5.4.3 Temperature Gradients

To analyse the temperature gradients within the concrete samples, winter gradient data was processed in a similar approach to the effective temperature. The hourly average temperatures were calculated for each sensor, allowing for a depth-based analysis of temperature changes through each shape. The equivalent winter day was then constructed

by averaging the hourly temperature values per sensor, with the 95^{th} and 5^{th} percentile values calculated to represent extreme gradient conditions. This approach provides a visualisation of the gradient development over a typical winter day, while also capturing the potential variability in extreme conditions.

Figure 5.19 presents the hourly temperature gradients over an equivalent day for each shape and aggregate type. The x-axis represents temperature, while the y-axis represents depth within the concrete element. This figure visually presents the hourly changes in temperature gradients, showing the heat flow and dissipation vertically through each shape throughout the day.

To quantify the temperature gradients, the temperature differences (from Figure 5.19) between points along the depth of the concrete shapes were calculated:

- **Top-to-Centre**: The temperature difference between the top surface and the mid-depth (centre) point.
- **Bottom-to-Centre**: The temperature difference between the bottom surface and the mid-depth (centre) point.
- **Top-to-Bottom**: The temperature difference between the top and bottom surfaces.

No immediate differences between the Dolerite and Dolomite mixes were observed in Figure 5.19, nor are the distinct variations between the shapes immediately evident. To quantify these differences, Table 5.1 was created to summarise the thermal behaviour of Dolerite and Dolomite in various concrete shapes under winter temperature variations. The table presents the maximum hourly differences, while the surface temperature ranges (*Top Temp. Range* and *Bottom Temp. Range*) are shown in Figure 5.20.

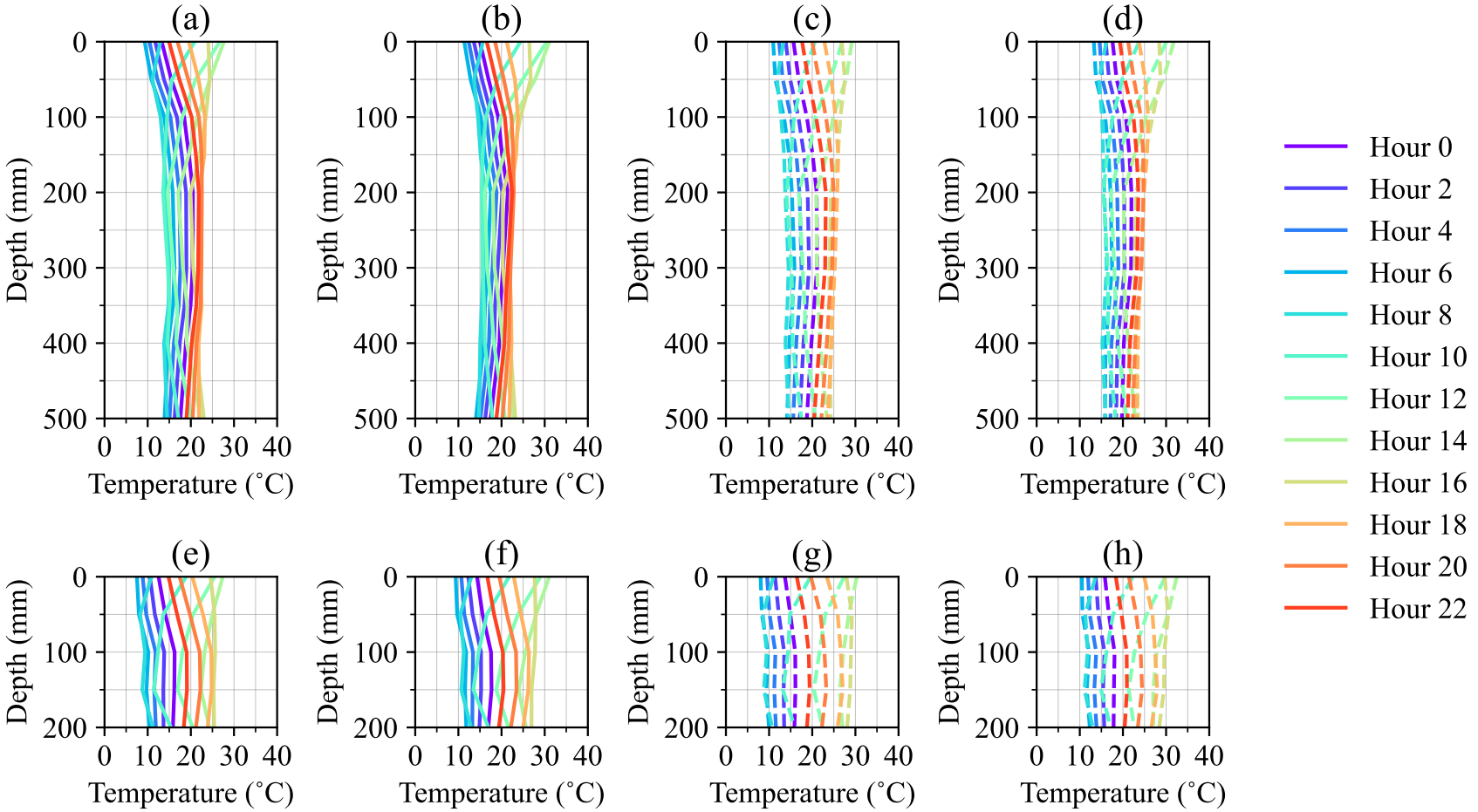

Figure 5.19: Averaged hourly temperature gradient for (a) Dolerite Cube, (b) Dolerite L-Shape Cube, (c) Dolomite Cube, (d) Dolomite L-Shape Cube, (e) Dolerite Flange, (f) Dolerite L-Shape Flange, (g) Dolomite Flange, and (h) Dolomite L-Shape Flange.

Table 5.1 summarises the maximum temperature differences for the Top-to-Centre, Bottom-to-Centre, and Top-Bottom metrics across all concrete shapes from Figure 5.19. These differences were statistically analysed within the hour at which each maximum occurred. Notably, all maximum Top-to-Centre and Top-to-Bottom differences occurred at 12:00. The Bottom-to-Centre differences varied:

- 12:00 – Dolerite Cube, Dolomite Cube, Dolomite L-Shape Cube
- 10:00 – Dolerite Flange, Dolerite L-Shape Flange, Dolomite Flange
- 14:00 – Dolerite L-Shape Cube
- 16:00 – Dolomite L-Shape Cube

Table 5.1: Summary of temperature differences between top, centre, and bottom measurements, as well as the Coefficient of Variation (CV) for each shape and mix.

Mix	Shape	Metric	Mean (°C)	*s* (°C)	CV (%)
Dolerite	Flange	Top-to-Centre	7.45	1.38	18.52
		Bottom-to-Centre	3.01	0.63	20.99
		Top-to-Bottom	5.03	1.14	22.57
	Cube	Top-to-Centre	12.15	2.34	19.24
		Bottom-to-Centre	5.50	1.24	22.60
		Top-to-Bottom	6.65	1.60	24.02
	L-Shape Flange	Top-to-Centre	8.48	1.46	17.25
		Bottom-to-Centre	2.26	0.53	23.23
		Top-to-Bottom	7.40	1.41	19.04
	L-Shape Cube	Top-to-Centre	14.42	2.65	18.40
		Bottom-to-Centre	4.83	1.02	21.31
		Top-to-Bottom	9.69	1.75	18.07
Dolomite	Flange	Top-to-Centre	5.72	1.03	18.05
		Bottom-to-Centre	1.54	0.36	23.61
		Top-to-Bottom	5.02	0.97	19.33
	Cube	Top-to-Centre	10.06	1.82	18.13
		Bottom-to-Centre	3.84	0.85	22.25
		Top-to-Bottom	6.23	1.29	20.75
	L-Shape Flange	Top-to-Centre	7.18	1.21	16.91
		Bottom-to-Centre	1.19	0.28	23.93
		Top-to-Bottom	7.26	1.29	17.76
	L-Shape Cube	Top-to-Centre	12.84	2.22	17.33
		Bottom-to-Centre	3.58	0.79	22.12
		Top-to-Bottom	9.26	1.68	18.17

Across all shapes, Dolerite appears to consistently show higher maximum hourly differences compared to Dolomite. For instance, in the L-Shape Cube, Dolerite's Top-to-Centre difference is 14.42 °C, compared to 12.84 °C for Dolomite. However, the sample standard deviations of 2.65 °C and 2.22 °C, respectively, indicate moderate variability in both cases. The CV further suggests that the relative variability of these gradients is similar, with Dolerite at 18.40% and Dolomite at 17.33%. This indicates that while Dolerite retains heat longer and results in steeper temperature gradients, the difference may not be substantial when considering the variability in the data.

- **Flange:** Due to its smaller depth (200 mm), the Flange shows smaller Top-to-Bottom differences, with mean values of 5.03 °C for Dolerite and 5.02 °C for Dolomite. The similarity in means suggests minimal variation between the two mixes. The sample standard deviation values (s = 1.14 °C for Dolerite and s = 0.97 °C for Dolomite) indicate some variability within each mix.
- **Cube:** With a greater depth (500 mm), the Cube exhibits larger thermal gradients, particularly in the Top-to-Bottom metric, where Dolerite (6.65 °C) shows a slightly higher difference than Dolomite (6.23 °C). However, the sample standard deviations (s = 1.60 °C and s = 1.29 °C, respectively) indicate that temperature variations within the Cube are considerable. The CV values are 24.02% for Dolerite and 20.75% for Dolomite, implying that the difference between the mixes may not be substantial when considering the inherent variability.
- **L-Shape Flange and Cube:** These shapes exhibit the largest temperature differences due to the combined effects of depth and flange geometry. The L-Shape Cube has the highest Top-to-Bottom differences, reaching 9.69 °C for Dolerite and 9.26 °C for Dolomite. While the mean values suggest Dolerite retains slightly more heat, the sample standard deviation values (s = 1.75 °C for Dolerite and s = 1.68 °C for Dolomite) indicate substantial variability. The CV values of 18.07% and 18.17% suggest that the differences in thermal behaviour between the mixes are minimal relative to the fluctuations observed within each mix.

Figure 5.19 demonstrates how the shape affects the thermal behaviour. The Flange shows relatively uniform temperature gradients, with small differences between the top and bottom. This is supported by Table 5.1, where the differences between the top and bottom of the Flange are only 5 °C for Dolerite and 5 °C for Dolomite. In contrast, deeper shapes such as the Cube and L-Shape Cube show substantial stratification. For example, the Dolerite L-Shaped Cube has a Top-to-Bottom difference of 9.7 °C, which corresponds to the sharp gradients observed in the figure.

The surface temperature ranges, shown in Figure 5.20, do not indicate a consistent trend between Dolerite and Dolomite across all shapes. While Dolomite shows a slightly wider

top surface range in some cases, such as the Flange (0.07–38.98 °C vs. −0.63–35.87 °C for Dolerite), this trend is not consistent across all shapes. For instance, the L-Shape Cube shows nearly identical maximum values (Dolomite: 6.32–41.17 °C; Dolerite: 4.23–41.05 °C), indicating that the thermal response is more depth-dependent rather than material-dependent.

Moreover, the CV values for both mixes remain within a similar range (approximately 17–23%), suggesting that the observed differences in temperature range could be influenced by external factors such as exposure to daily solar radiation exposure rather than a fundamental difference in material properties.

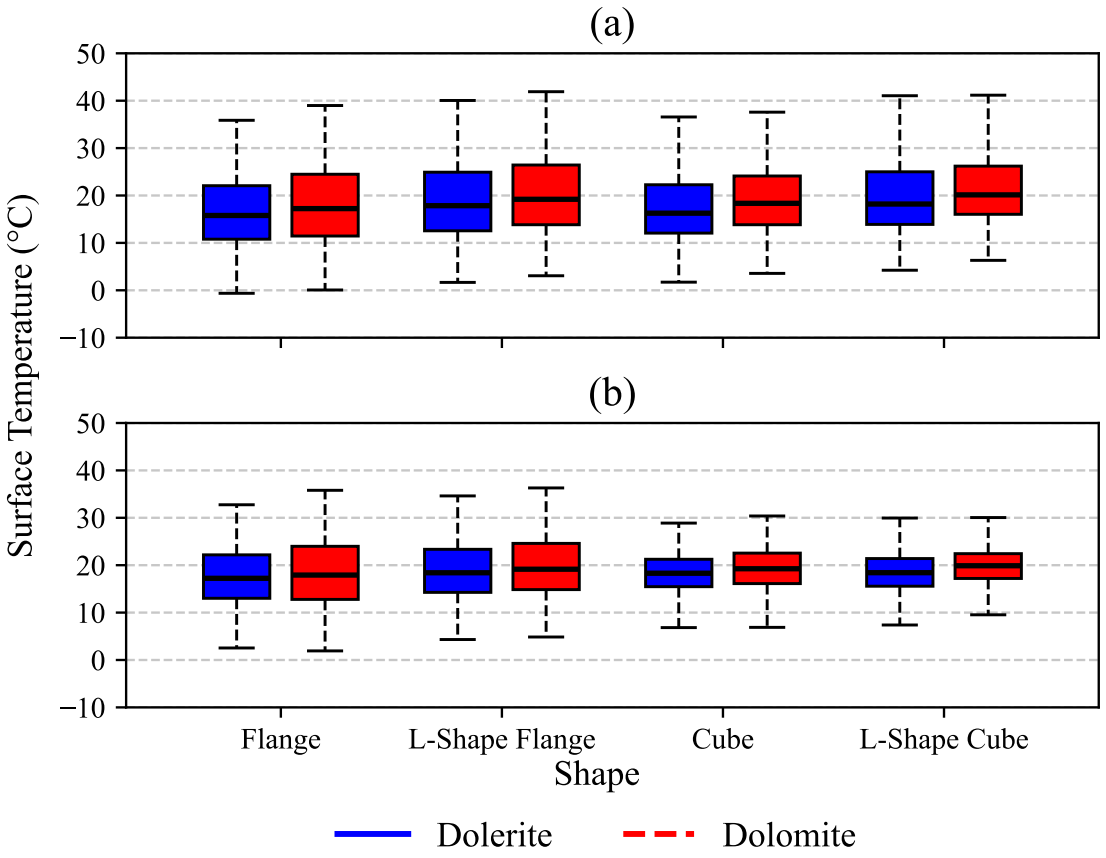

Figure 5.20: Temperature range distributions for the (a) top and (b) bottom surfaces of each shape.

For all shapes, the bottom sensors show less variation compared to the top surface, as shown in both Table 5.1 and Figure 5.20 (b). This thermal stability at depth can be attributed to reduced convective heat transfer and the influence of the ground, since the samples were placed only 0.99 m above the surface. For example, the bottom temperature range for the Dolerite Cube is 6.83–28.88 °C, compared to a substantially wider top surface range of 1.72–36.57 °C. A similar pattern is observed in the L-Shaped Cube,

where the bottom range (7.38–30.27 °C for Dolerite) is notably narrower than the top range (4.23–41.05 °C).

The analysis of temperature gradients indicates that element depth has a greater influence on thermal behaviour than aggregate type. Deeper sections, such as the Cube and L-Shape Cube, show greater temperature differences due to increased thermal stratification, whereas the Flange experiences smaller gradients due to its reduced depth. While Dolerite generally shows slightly higher temperature differences than Dolomite, the CV values suggest that the observed differences may be within the range of natural variability. Furthermore, surface temperature ranges do not show a consistent trend between the two mixes, indicating that section depth and exposure conditions play a more substantial role in temperature distribution than aggregate selection.

5.5 Drying Shrinkage

This section provides an overview of the shrinkage prediction methodology, highlighting the principles and numerical techniques applied to separate shrinkage strains in concrete samples. The approach included determining the coefficient of thermal expansion (α_c) and fitting an adjusted EN1992-1-1 (2004a) shrinkage prediction model to measured strain data from concrete cylinders, which were used as a basis to remove shrinkage effects from other shapes in this study.

The focus of this study was limited to shrinkage strains occurring after the samples were moved outdoors. This decision was made to account for the change in environmental conditions as the transition from a controlled laboratory environment to outdoor exposure. Consequently, the EN1992-1-1 (2004a) shrinkage prediction model was calibrated with data collected from 03-06-2024, to 20-08-2024, as shown in Figure 5.21. This time frame, which spanned approximately 12 weeks, captured the behaviour of the concrete under environmental exposure, allowing a comparison between the measured and predicted shrinkage behaviour in the cylinders.

Figure 4.6 shows the regression models for the determination of the coefficient of thermal expansion, highlighting the steady shrinkage behaviour. This analysis isolated thermal strains from the overall strain measurements. Subsequently, the shrinkage prediction was carried out by removing the thermal strain ($\varepsilon_{thermal}$) component from the cylinder data and fitting the remaining strain data to an adjusted EN1992-1-1 (2004a) drying shrinkage formula.

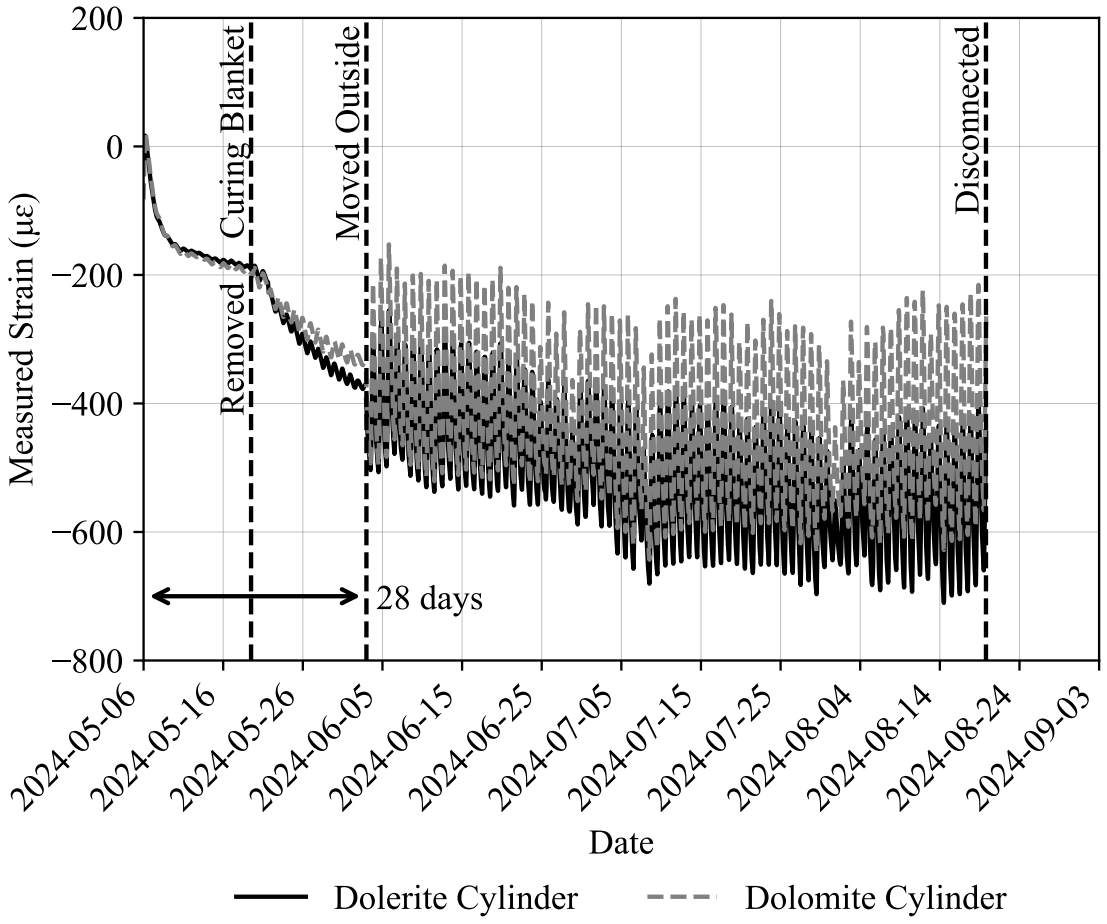

Figure 5.21: Measured strain development in the Dolerite and Dolomite cylinders.

Chapter 2 presents the total strain (ε_{total}) in a concrete structure (Equation 2.10). The focus of this study was on environmental loading, and therefore elastic and creep strains were neglected. Therefore, the total strain measured ($\varepsilon_{measured}$) within this study was the components of thermal strain, shrinkage strain, and creep strain (Equation 5.5). As the cylinders were effectively free to expand vertically (Figure 3.15), the creep strain was assumed to be negligible. This assumption allowed for Equation 5.6, where the measured strain of the cylinders ($\varepsilon_{measured,cyl}$) only has thermal ($\varepsilon_{thermal,cyl}$) and shrinkage ($\varepsilon_{shrinkage,cyl}$) components.

$$\varepsilon_{\text{measured}} = \varepsilon_{\text{thermal}} + \varepsilon_{\text{shrinkage}} + \varepsilon_{\text{creep}} \tag{5.5}$$

$$\varepsilon_{\text{measured,cyl}} = \varepsilon_{\text{thermal,cyl}} + \varepsilon_{\text{shrinkage,cyl}} \tag{5.6}$$

The shrinkage strains were isolated from the measured strains by subtracting the thermally induced strains in each cylinder. Thermally induced strains were calculated using

Equation 4.7 with the relevant thermal expansion coefficient ($\alpha_c = 10.5\,\mu\varepsilon/°\text{C}$ for Dolerite and $\alpha_c = 12.2\,\mu\varepsilon/°\text{C}$ for Dolomite) and the measured change in temperature.

After removing thermally induced strains, Figure 5.22 shows the development of the shrinkage strain over time, spanning 03-06-2024 to 20-08-2024. It is important to note that the strains in Figure 5.22 do not start from zero. This is attributed to the plastic deformation that occurred during the initial 28 days after casting, as illustrated in Figure 5.21. The adjusted EN1992-1-1 (2004a) shrinkage prediction model accounts for this by assuming an initial offset value at 28 days and incorporating the non-linear time-dependent factor proposed in EN1992-1-1 (2004a) (Equation 2.18).

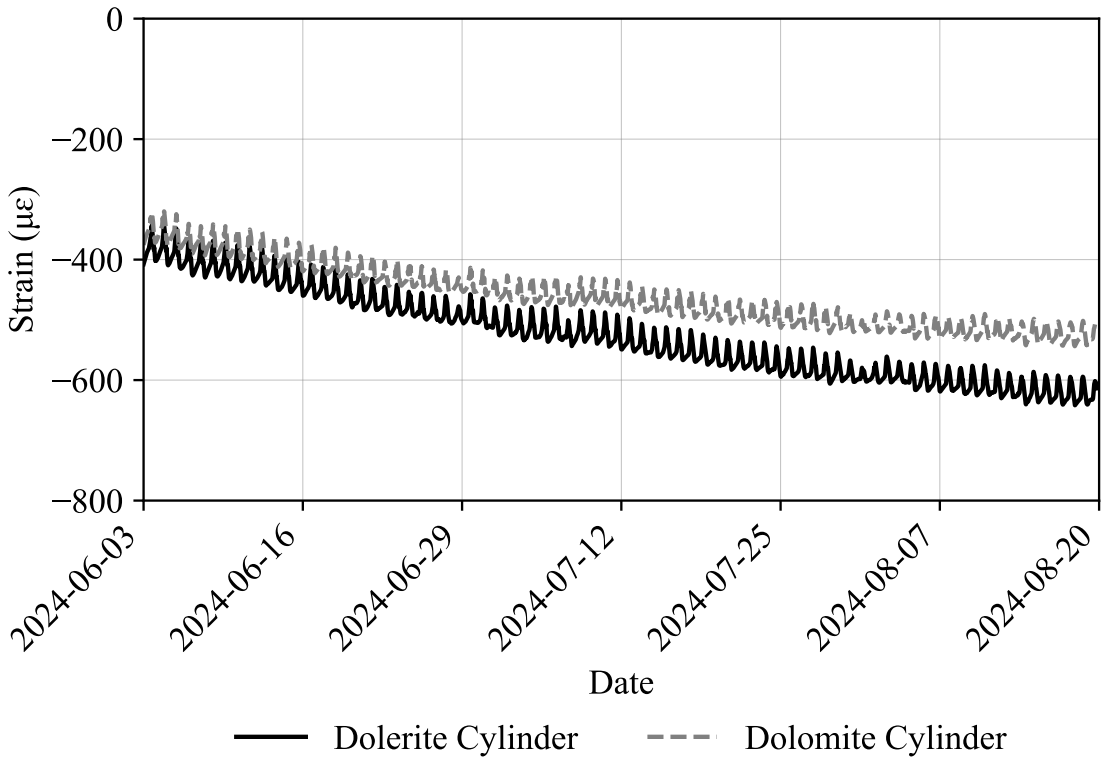

Figure 5.22: Shrinkage strain $\varepsilon_{shrinkage,cyl}$ development (after 28 days) in the Dolerite and Dolomite cylinders.

5.5.1 Shrinkage Prediction Using the 1992 EN1992-1-1 (2004a) Model

To model shrinkage in concrete elements of varying shapes, the EN1992-1-1 (2004a) shrinkage model was selected. The EN1992-1-1 (2004a) model introduces the concept of notional size (h_0), which accounts for the effects of shape. This parameter was defined in Chapter 2 (Equation 2.16). h_0 depends on both the cross-sectional area (A_c) and the perimeter exposed to drying (u). Figure 5.23 illustrates these parameters for each shape used in the study.

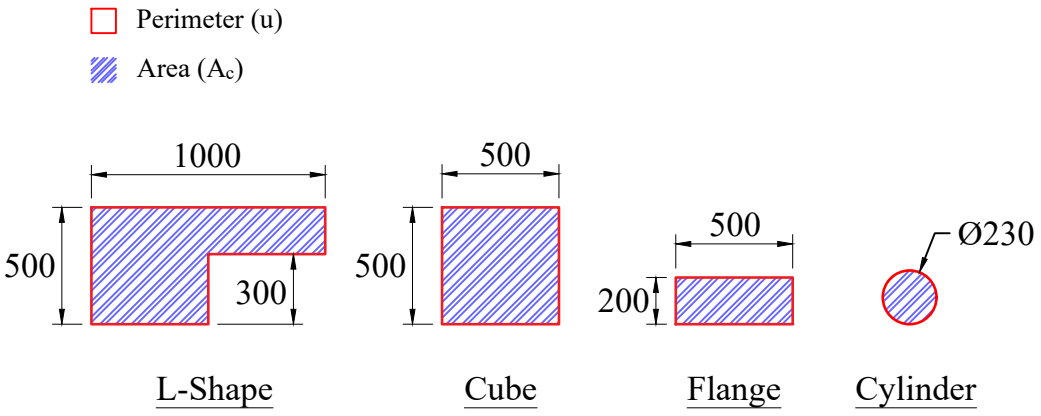

Figure 5.23: Cross-sectional area and perimeter exposed to drying for the shapes used in the study.

Table 5.2 presents the calculated values A_c, u, and h_0 values for each shape, demonstrating the size effect that the EN1992-1-1 (2004a) model can accommodate.

Table 5.2: Samples used for mechanical property tests on concrete (per mix).

Shape	A_c (mm^2)	u (mm)	h_0 (mm)
L-Shape	350 000	3 000	233
Cube	250 000	2 000	250
Flange	100 000	1 400	143
Cylinder	41548	723	115

The EN1992-1-1 (2004a) model predicts shrinkage as the sum of autogenous and drying shrinkage strains. Autogenous shrinkage is mainly influenced by early-age chemical processes in concrete and is considered a short-term shrinkage effect (Neville, 2012). Since autogenous shrinkage occurs rapidly, as discussed in Chapter 2, it was assumed that it had stabilised largely at the end of the curing period (28 days). Thus, the initial shrinkage strain value, ε_{28}, derived from data beyond 28 days, implicitly incorporates autogenous shrinkage of the early age.

Data recorded more than 28 days after casting were analysed in this study to eliminate the effects of curing conditions within the first two weeks. The samples were kept indoors under a curing blanket for the first 14 days and then exposed to drying conditions without a curing blanket for 14 days (see Figure 5.21). All ongoing shrinkage after 28 days was attributed solely to drying shrinkage, calculated using the EN1992-1-1 (2004a) drying shrinkage function Equation 2.18.

The EN1992-1-1 (2004a) drying shrinkage model incorporates the effects of relative humidity (RH) through the parameter ε_{cd0}, which is calculated using Equation 2.17. This parameter considers RH and cement type but does not account for aggregate type. However, as discussed in Chapter 2, aggregate type plays a substantial role in drying shrinkage and must be considered in predictive models.

Relative humidity fluctuates substantially over time, as shown in Figure 5.3 and discussed in Chapter 5. These fluctuations complicate the direct application of the EN1992-1-1 (2004a) model to real-world conditions. However, EN1992-1-1 (2004a) follows the practice of using a single representative RH value (typically the long-term average or a characteristic RH value) for shrinkage predictions rather than time-dependent variations. This study adopted the same approach, fitting an adjusted shrinkage model using a single RH input value to remain consistent with EN1992-1-1 (2004a) and to facilitate practical engineering applications.

To incorporate aggregate type, the EN1992-1-1 (2004a) drying shrinkage prediction model was adjusted by modifying the parameter ε_{cd0} to better reflect the measured shrinkage strains of the Dolerite and Dolomite mixes. A single adjusted ultimate drying shrinkage parameter, ε_{ae}, was defined for each mix to account for the combined effects of RH, cement type, and aggregate type. This approach assumes that RH variability is inherently captured within ε_{ae}, eliminating the need to recalculate ε_{cd0} for time-dependent RH fluctuations. Equation 5.7 was used to represent shrinkage strain after removing thermal effects.

$$\varepsilon_{shrinkage}(t) = \varepsilon_{28} + \beta_s(t, t_s) \cdot \varepsilon_{ae} \tag{5.7}$$

Where,

$\varepsilon_{\text{shrinkage}}(t)$	= Predicted shrinkage (adapted from EN1992-1-1 (2004a))
$\beta_s(t, t_s)$	= Time-dependent factor (same as EN1992-1-1 (2004a))
ε_{28}	= Shrinkage strain 28 days post casting
ε_{ae}	= Adjusted EN1992-1-1 (2004a) ultimate drying shrinkage strain

Using a curve fitting approach, the parameters ε_{28} and ε_{ae} were optimised to best fit the measured shrinkage data, as illustrated in Figure 5.24. Figure 5.24 displays both the measured shrinkage strain and the fitted EN1992-1-1 (2004a) shrinkage curve for each mix. The fitting process was validated using the root mean square error (*RMSE*) and the determination coefficient (R^2), both indicating strong correlations between the measured and predicted values. The results are summarised as follows:

- Dolerite: $\varepsilon_{28} = 232$, $\varepsilon_{ae} = 598$, RMSE = 16, $R^2 = 0.95$
- Dolomite: $\varepsilon_{28} = 253$, $\varepsilon_{ae} = 424$, RMSE = 13, $R^2 = 0.94$

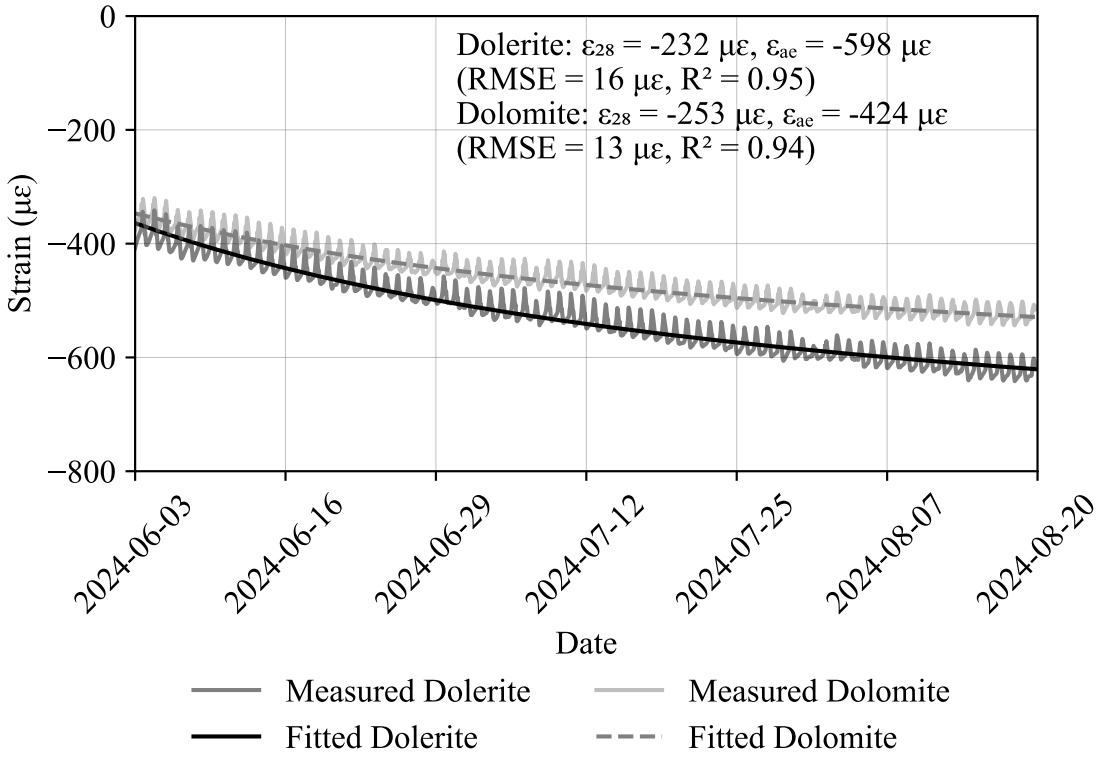

Figure 5.24: Shrinkage strain prediction for Dolerite and Dolomite cylinders using EN1992-1-1 (2004a) model, showing measured and fitted values over time.

The adjusted EN1992-1-1 (2004a) drying shrinkage model was successfully applied to predict the shrinkage strains in the cylinders for both mixes (Dolerite and Dolomite). Using the concept of notional size (h_0), defined in Chapter 2 (Equation 2.16), and a simplified approach to account for RH conditions, the shrinkage strains were modelled as a function of time (t) using Equation 5.7. The curve fitting process optimised the parameters ε_{28} (initial shrinkage strain) and ε_{ae} (ultimate drying shrinkage strain) for each mixture, as illustrated in Figure 5.24. The results indicate strong correlations between the measured and predicted shrinkage strains, with RMSE values of 16 and 13, and R^2 values of 0.95 and 0.94 for the Dolerite and Dolomite mixes, respectively.

While the model showed strong predictive capability within the RH conditions of this study, it is acknowledged that the fitted parameters are specific to the experimental RH levels. Both mixes were subjected to the same curing procedure and environmental conditions, including fluctuating RH, ensuring a consistent basis for comparison. However, since RH substantially influences drying shrinkage, the applicability of these fitted parameters to regions with substantially different RH levels (e.g., coastal environments) should be treated with caution.

5.5.2 Application to L-Shape, Cube and Flange Concrete Elements

The L-Shape, Cube and Flange measured strains over the duration of the experiment are presented in Figure 5.25. These concrete shapes were subjected to the same curing procedure as the cylinders (see Figure 3.10).

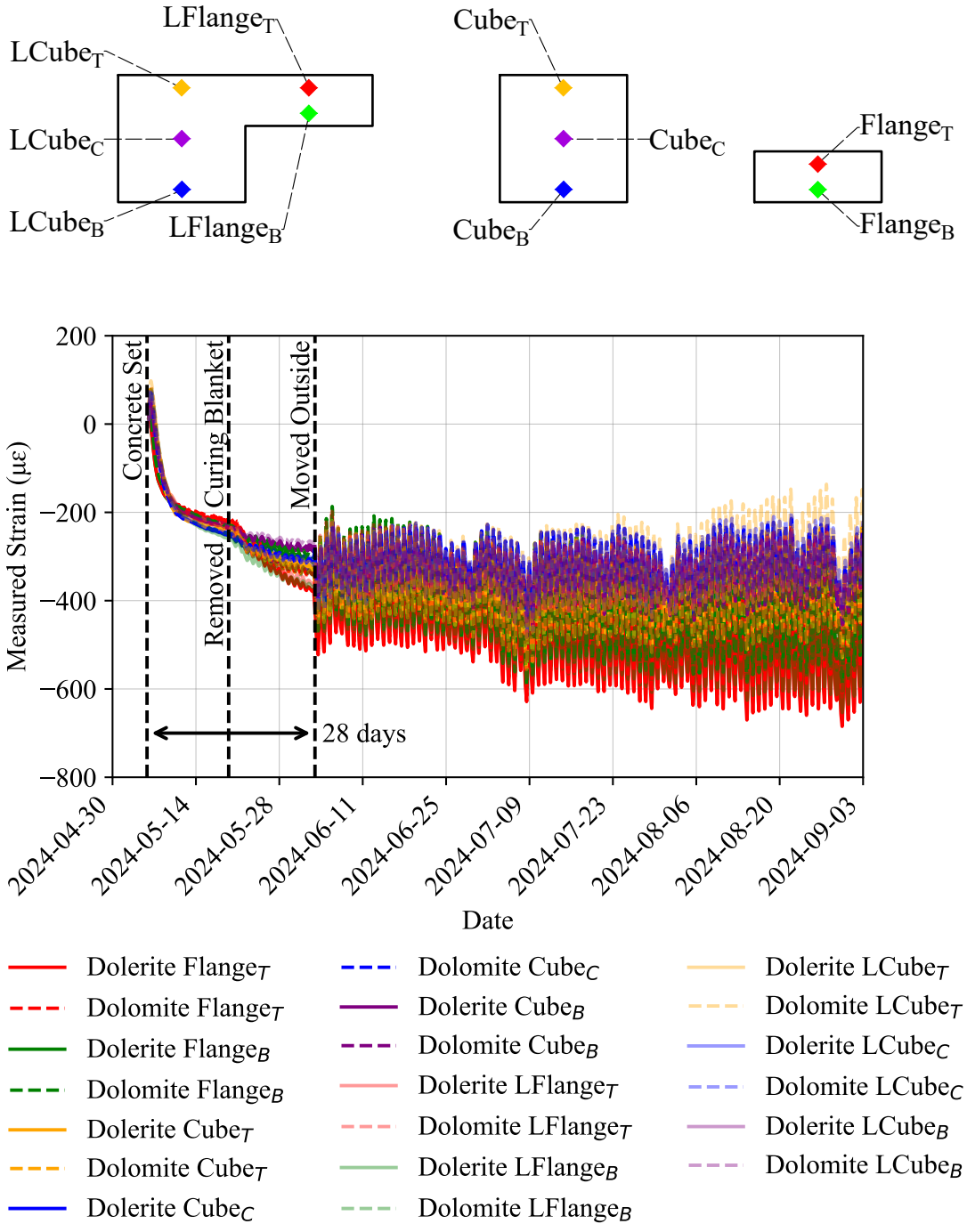

Figure 5.25: Measured strains over time from the start of the experiment, showing initial curing conditions followed by outdoor exposure.

Upon reaching 28 days, the concrete elements were moved outside and subjected to environmental conditions (seer Figure 5.25). In this analysis, only strain data after 28 days of curing are considered to assess the effects of environmental exposure.

The legend above the strain vs. time plot, in Figure 5.25, shows the location and colour of the strain readings in the concrete elements (from the VWSGs). The fitted shrinkage parameters ε_{28} and ε_{ae}, calibrated using 230mm diameter cylinders, are applied to the shapes in this section to isolate and analyse the shrinkage strain components effectively.

The initial peak of strain visible on the first day (06-05-2024) reflects swelling from the heat of hydration, as detailed in Chapter 3 (Figure 3.6).

5.5.3 Cube and Flange Sections

For each shape (Cube and Flange) h_0 was calculated using Equation 2.16, as provided in Table 5.2. The adjustment ensures that the effects of geometry and size on shrinkage are captured within the EN1992-1-1 (2004a) framework. Thermal effects were removed from the measured strains in the Cube and Flange sections using α_c for each mix, leaving only the shrinkage and creep strains (Equation 5.5). Using the adjusted shrinkage prediction model (Equation 5.7), the predicted shrinkage strains for the Dolerite and Dolomite mixes were calculated for the Flange and Cube shapes. The resulting shrinkage strain curves are shown in Figure 5.26.

The shrinkage behaviour of the Cube and the Flange was analysed, comparing the initial and final measured shrinkage values to the predicted shrinkage strains derived from the adjusted EN1992-1-1 (2004a) model. The Cube and Flange shapes were supported on their bottom surfaces while the top surfaces were free to expand or contract. The contact between the shapes and the steel frame introduced friction, which is assumed to provide sufficient horizontal restraint, limiting movement at the base. The measured and predicted shrinkage values for both mixes can be seen in Figure 5.26.

The shrinkage behaviour of the Dolerite and Dolomite mixes was found to be similar, with only marginal differences in initial and final shrinkage values. For the Flange specimens, the initial measured shrinkage for Dolerite (Top: 419.93 $\mu\varepsilon$, Bottom: 339.35 $\mu\varepsilon$) was slightly higher than that for Dolomite (Top: 370.10 $\mu\varepsilon$, Bottom: 322.69 $\mu\varepsilon$). Similarly, the final measured shrinkage for Dolerite (Top: 595.47 $\mu\varepsilon$, Bottom: 555.38 $\mu\varepsilon$) remained slightly above that for Dolomite (Top: 505.02 $\mu\varepsilon$, Bottom: 472.73 $\mu\varepsilon$). Despite these small numerical differences, the overall shrinkage trends between the two mixes followed a similar pattern, suggesting that the effect of aggregate type on the drying shrinkage was minimal in this study. The predicted shrinkage values closely matched the measured values, with initial and final shrinkage differences less than 1% for Dolerite and less than 2% for Dolomite, further indicating the comparable shrinkage behaviour of the two mixes.

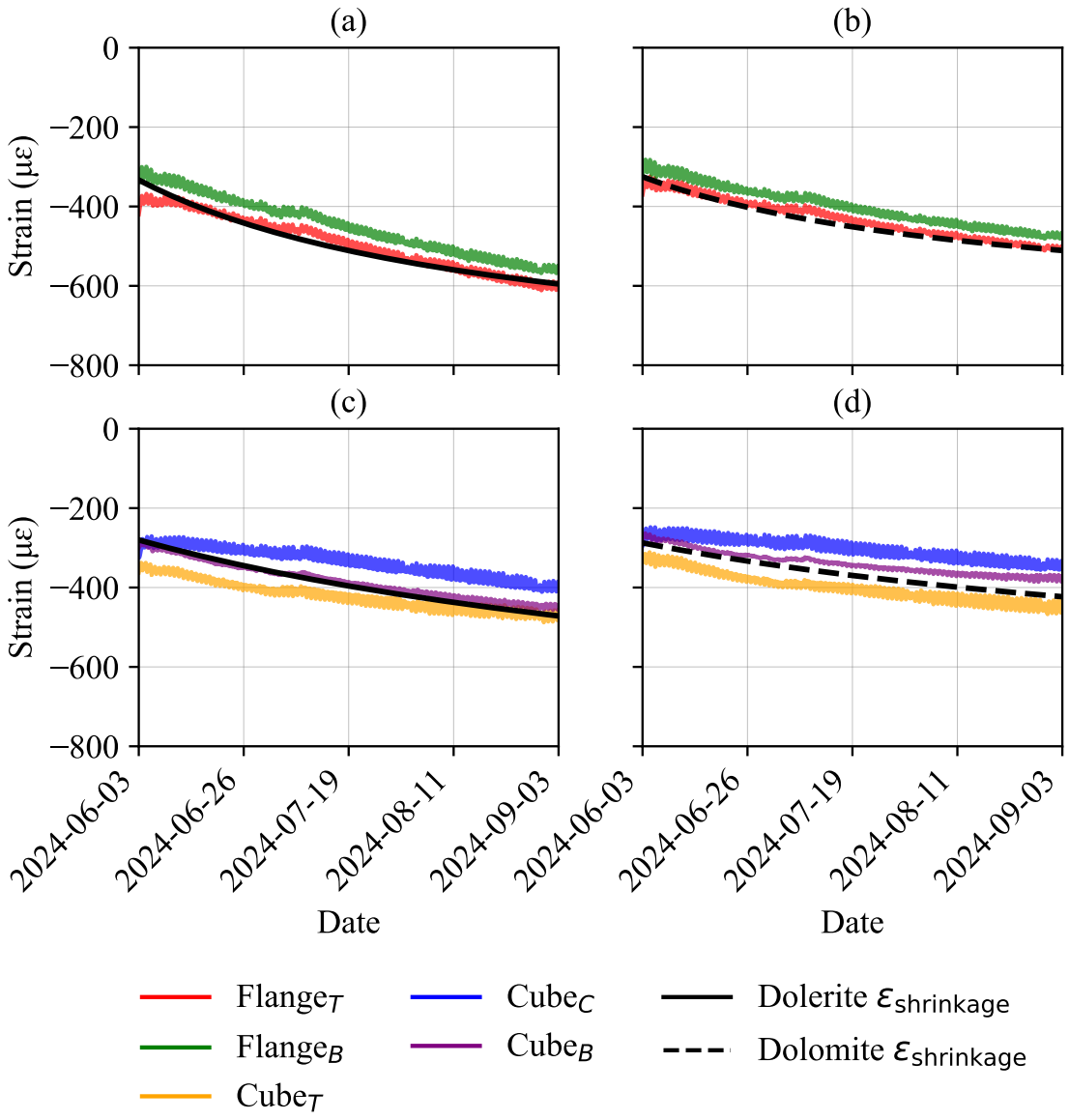

Figure 5.26: Shrinkage prediction for Dolerite and Dolomite mixes: (a) Dolerite Flange, (b) Dolomite Flange, (c) Dolerite Cube, (d) Dolomite Cube.

For the Cube specimens, the Dolerite mix exhibited slightly higher shrinkage strains compared to the Dolomite mix. The initial measured shrinkage for the top of the Dolerite Cube was 362.33 $\mu\varepsilon$ compared to 335.78 $\mu\varepsilon$ for the Dolomite Cube, while the final measured shrinkage values were 456.56 $\mu\varepsilon$ and 432.30 $\mu\varepsilon$, respectively. The bottom of the Dolerite Cube recorded a final shrinkage of 445.90 $\mu\varepsilon$, whereas the Dolomite Cube measured 373.45 $\mu\varepsilon$. While these values indicate that the Dolerite mix experienced slightly greater shrinkage, the differences remain relatively small, suggesting that aggregate type had only a minor influence on shrinkage in the Cube specimens. The predicted values for both mixes remained consistent with the measured values, with minor variations at

deeper locations attributed to restraint effects, as further detailed in Chapter 7.

The Flange exhibited slightly larger final shrinkage values compared to the Cube. For Dolerite, the final measured shrinkage for the Flange ranged between 555.38 $\mu\varepsilon$ at the bottom and 595.47 $\mu\varepsilon$ at the top, while for the Cube, it ranged between 392.92 $\mu\varepsilon$ at the centre and 456.56 $\mu\varepsilon$ at the top. Similarly, for Dolomite, the final measured shrinkage for the Flange ranged between 472.73 $\mu\varepsilon$ at the bottom and 505.02 $\mu\varepsilon$ at the top, compared to 349.86 $\mu\varepsilon$ in the centre and 432.30 $\mu\varepsilon$ at the top for the Cube. Although these results indicate that the Flange experienced higher shrinkage than the Cube, the differences are moderate and align with expectations based on the notional size (h_0). The smaller notional size of the Flange increases the rate and extent of drying shrinkage, explaining the observed variations. However, the overall shrinkage trends remain similar between the two shapes.

The agreement between the measured and predicted shrinkage strains supports the application of the adjusted EN1992-1-1 (2004a) model to the Cube and Flange shapes. The weighted coefficient of determination (R^2) values indicate strong correlation for the Dolerite Flange ($R^2 = 0.84$) and Dolomite Flange ($R^2 = 0.74$), while the Dolerite Cube ($R^2 = 0.64$) shows moderate agreement. However, the Dolomite Cube exhibits a lower correlation ($R^2 = 0.32$), suggesting that additional factors, such as local drying conditions or shape-specific effects, may influence shrinkage in this case. Notably, differences observed at deeper sensors, such as at the bottom of the Dolerite Cube (445.90 $\mu\varepsilon$ measured vs. 471.60 $\mu\varepsilon$ predicted), highlight potential limitations in capturing differential drying effects within the model.

5.5.4 L-Shape Sections

The strain analysis for the L-Shaped specimens focused on determining the impact of the combined Cube and Flange sections on the development of strain and stress. The analysis used the EN1992-1-1 (2004a) shrinkage prediction model adjusted for this study (see Equation 5.7) with h_0 calculated from the perimeter and area of the L shape, as described in Table 5.2 and shown in Figure 5.23. The predicted shrinkage strain for the Dolerite mix is shown in Figure 5.27 (a), and the predicted shrinkage for the Dolomite mix in Figure 5.27 (b). As with the Cube and Flange sections, thermal effects were removed from the measured strains, isolating shrinkage and creep strains for comparison against the adjusted shrinkage prediction model. Because the L-Shape was assumed as a single, uniform section, shrinkage was predicted for the entire section without distinguishing between the Cube and Flange regions.

For the Flange portion of the L-Shape, the Dolerite mix exhibited higher initial and final shrinkage values compared to the Dolomite mix. The initial measured shrinkage for the Dolerite mix ranged from 394.05 $\mu\varepsilon$ at the top to 385.21 $\mu\varepsilon$ at the bottom. The final

measured shrinkage values for the Dolerite Flange ranged from 588.68 $\mu\varepsilon$ to 572.67 $\mu\varepsilon$, exceeding the predicted shrinkage of 486.61 $\mu\varepsilon$ by approximately 17%. In comparison, the Dolomite mixture showed an initial shrinkage ranging from 362.16 $\mu\varepsilon$ (top) to 349.29 $\mu\varepsilon$ (bottom) and the final measured shrinkage values of 509.91 $\mu\varepsilon$ to 501.30 $\mu\varepsilon$. These values exceeded the predicted shrinkage of 433.85 $\mu\varepsilon$ by approximately 15%.

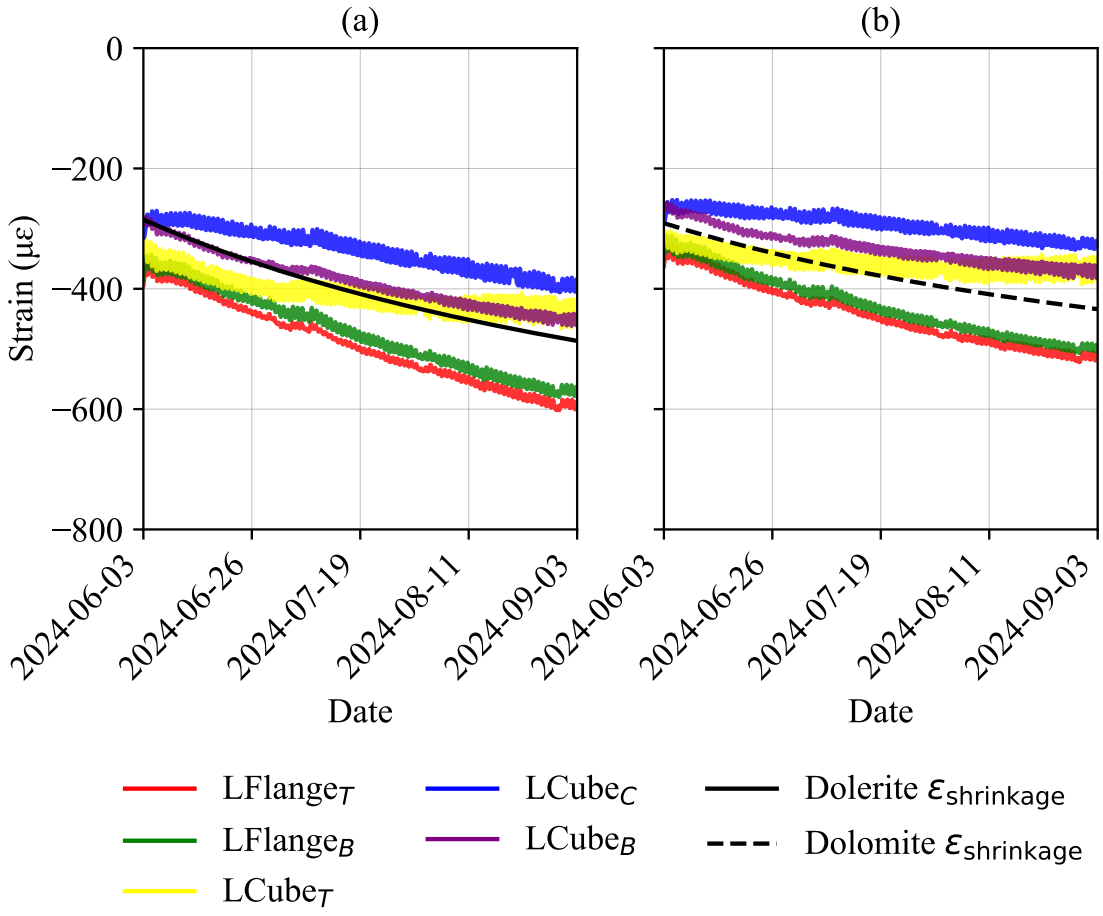

Figure 5.27: Shrinkage predictions for L-Shape elements: (a) Dolerite mix, (b) Dolomite mix.

For the Cube portion of the L-Shape, the Dolerite mix also demonstrated higher shrinkage values. The initial measured shrinkage ranged from 343.93 $\mu\varepsilon$ (top) to 292.75 $\mu\varepsilon$ (bottom), with the final measured shrinkage values ranging from 422.48 $\mu\varepsilon$ (top) to 448.23 $\mu\varepsilon$ (bottom). These values were slightly lower than the predicted shrinkage of 486.61 $\mu\varepsilon$, with deviations of up to 13%. For the Dolomite mixture, the initial shrinkage ranged from 320.65 $\mu\varepsilon$ (top) to 269.85 $\mu\varepsilon$ (bottom), with the final measured shrinkage values ranging from 348.91 $\mu\varepsilon$ (top) to 368.19 $\mu\varepsilon$ (bottom). These values were approximately 14% to 20% lower than the predicted shrinkage of 433.85 $\mu\varepsilon$.

The results indicate that the Dolerite mixture consistently showed greater shrinkage

strains than the Dolomite mixture on both the Flange and the Cube portions of the L-Shaped sections, consistent with the higher shrinkage potential of the Dolerite aggregate. Furthermore, the Flange portion showed a greater shrinkage than the Cube, reflecting the smaller notional size (h_0) of the Flange, which accelerates drying shrinkage. The top of the Flange exhibited greater shrinkage than the top of the Cube, a trend observed in both concrete mixes (Dolerite and Dolomite aggregates). This behaviour is attributed to the thinner Flange section's higher surface-area-to-volume ratio, leading to faster moisture loss and the abrupt thickness change at the Flange-Cube junction, which can induce localised stress concentrations. This differential shrinkage increases the risk of cracking in the thickness transition, which could compromise structural integrity.

5.6 Summary

The results of this study highlight the influence of both shape and aggregate type on the thermal and shrinkage behaviour of concrete elements exposed to environmental loading. Conducted over a three-month period under realistic winter conditions, the study provided insights into the performance of Dolerite and Dolomite concrete mixes in different geometries (L-Shape, Cube, and Flange). While section depth played a dominant role in temperature variations and shrinkage trends, aggregate effects were found to be minimal. The key findings are summarised below.

Thermal Response

- **Aggregate effects:** While Dolomite mixes showed slightly higher mean effective temperatures and larger daily fluctuations than Dolerite mixes, the high variability in both datasets suggests that these differences may not be statistically significant. Dolerite mixes tended to show steeper temperature gradients, possibly due to lower thermal diffusivity, leading to slower heat dissipation. However, further studies with a larger sample size are needed to better isolate the influence of aggregate type on thermal response.
- **Shape effects:** Shallower elements, such as the Flange and L-Shape Flange, showed higher temperature ranges and responded more rapidly to environmental changes, while deeper sections, such as the Cube and L-Shape Cube, showed lower effective temperature variations but more pronounced thermal gradients. The L-Shape geometry introduced additional complexity in heat distribution, influencing localised temperature variations. These findings highlight the influence of section depth on thermal behaviour, with deeper elements providing greater thermal stability while also experiencing steeper internal temperature differentials.

- **Thermal stresses and restraints:** The observed temperature gradients suggest that thermal stresses may develop within the concrete elements, particularly in deeper sections where increased thermal stratification occurs. The Cube and L-Shape Cube showed greater temperature differences, which could lead to higher internal restraint stresses, while the Flange experienced smaller gradients, potentially reducing restraint effects. External supports may further influence the thermal response by restricting expansion and contraction, increasing the likelihood of stress build-up. While this chapter focused on temperature distributions, the implications for thermal stress development will be explored in subsequent chapters.
- **Environmental exposure:** The study period was characterised by mild winter conditions, with variable temperatures, fluctuating relative humidity, and an absence of rainfall. These factors contributed to natural thermal variations in the concrete elements. While shielding reduced direct wind exposure, the overall environmental conditions remained representative of typical winter fluctuations. Further studies with controlled exposure conditions could help isolate the direct impact of environmental factors on thermal behaviour.

Shrinkage Response

- **Aggregate effects:** The shrinkage behaviour of the Dolerite and Dolomite mixes was similar, with only minor differences in shrinkage strains across all shapes. While Dolerite showed slightly higher shrinkage, the differences were small and within expected variability. These findings suggest that aggregate type had a minimal influence on drying shrinkage in this study.
- **Shape effects:** The Flange sections showed greater shrinkage than the Cube sections, consistent with their smaller notional size (h_0). The L-Shape sections showed intermediate shrinkage behaviour between the two. The top of the Flange consistently shrank more than the top of the Cube, likely due to increased moisture loss from its thinner section. These findings highlight the role of section size in drying shrinkage behaviour.
- **Model accuracy:** The adjusted EN1992-1-1 (2004a) shrinkage prediction model provided accurate predictions for the Dolerite and Dolomite mixes, with strong correlations between measured and predicted shrinkage strains in cylinder specimens. The model also performed well for Cube and Flange sections, though moderate deviations were observed, particularly in the Dolomite Cube, suggesting potential influences from local drying conditions or shape-specific effects. While the model effectively captured shrinkage trends under the RH conditions of this study, its applicability to regions with different RH levels should be treated with caution.

6 Calibration of Heat Transfer Models

6.1 Introduction

Concrete elements are subjected to various heat transfer mechanisms, including conduction, convection, and radiation, which govern their thermal response to environmental conditions. The development of a reliable heat transfer model is essential to accurately simulate these interactions and refine the material properties that influence heat transfer, such as thermal conductivity (k) and solar absorptivity (a_s).

The Finite Element Method (FEM) was selected as the primary numerical approach for this study due to its ability to accurately model heat transfer in complex geometries, such as the L-Shape, Flange, and Cube elements used in the experimental phase. The capacity of FEM to simulate transient thermal responses is aligned with the time-dependent temperature data captured from the sensors embedded in the concrete samples. Moreover, its flexibility in incorporating heterogeneous material properties, such as the thermal conductivity differences between Dolerite and Dolomite aggregates, ensures a detailed representation of the experimental conditions.

This chapter presents the development and calibration of a finite element-based heat transfer model for concrete elements, implemented using ABAQUS/CAE (2023). The model integrates environmental factors, such as ambient temperature and solar radiation, to predict the temperature distributions within concrete specimens of varying shapes and material properties. A separate numerical model was used to predict solar radiation, accounting for direct, diffuse, and reflected components. These solar radiation predictions were then converted into heat flux boundary conditions, allowing for a realistic simulation of environmental thermal loads.

The primary objective of this chapter is to determine the thermal conductivity and solar absorptivity for concrete mixes containing Dolerite and Dolomite and to assess their impact on effective temperature and temperature gradients. The model calibration focused on matching the measured effective temperatures of the Cube specimens during the first week of the experimental period. Sensitivity analyses were performed to evaluate the influence of thermal conductivity and solar absorptivity on thermal behaviour, while the validation of the model over the 3-month exposure period confirmed the assumption that the thermal properties remained constant throughout.

The results of this chapter not only provide insight into the thermal response of concrete elements but also establish the foundation for understanding the thermal strain behaviour that arises due to temperature variations. The following sections detail the methodology, the sensitivity analysis, the calibration results, and the implications of these findings for concrete performance under environmental loading.

6.2 Overview of Heat Transfer Model

The development of the heat transfer model followed a structured sequence, as outlined in Figure 6.1. The Finite Element Method (FEM) was chosen as the numerical analysis approach, implemented using the software ABAQUS/CAE (2023). This method was selected for its ability to simulate complex heat transfer phenomena in concrete elements, including the effects of environmental conditions.

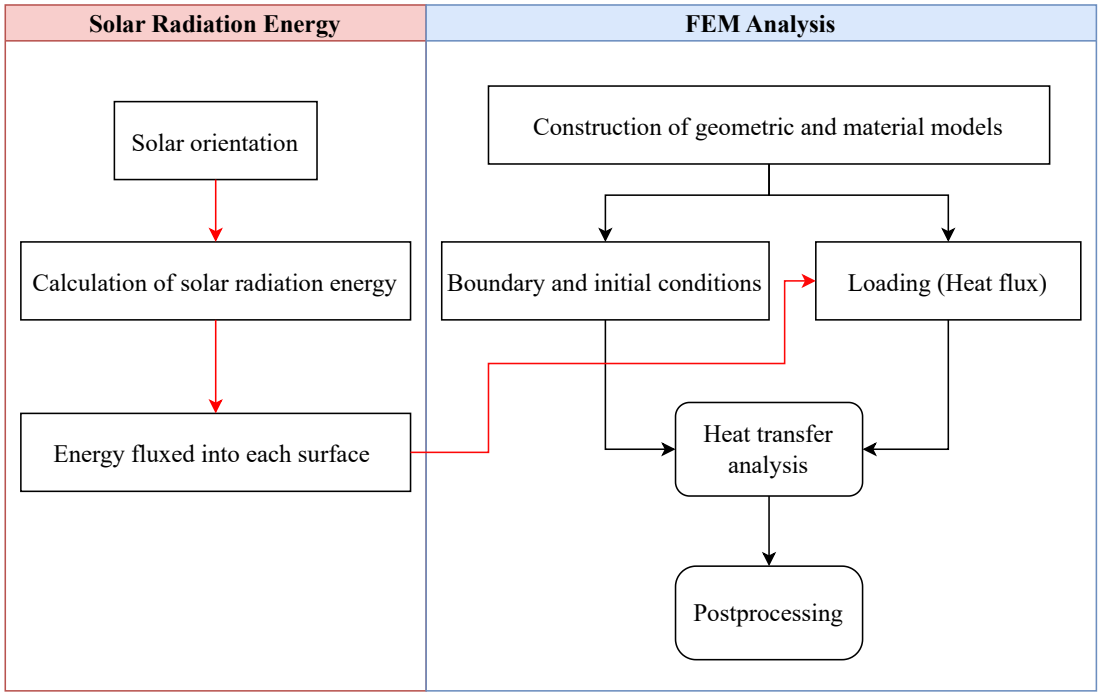

Figure 6.1: Flowchart of the numerical model integrating solar radiation energy prediction with FEM heat transfer analysis in ABAQUS.

In addition to Finite Element Analysis (FEA), a separate numerical model was developed to predict solar radiation energy, as detailed in Chapter 5. The solar radiation model calculated the total solar radiation on the surfaces of the concrete specimens, accounting

for direct, diffused, and reflected radiation. These values were then converted into heat flux, which was applied as a boundary condition in the ABAQUS heat transfer analysis. This integration allowed for a realistic representation of the thermal environmental loads in the FEA model.

The first step in building the numerical model was the construction of a simplified two-dimensional geometric and material model in ABAQUS. This simplification was justified by the insulation applied to certain surfaces, which allowed the problem to be effectively modelled in two dimensions without compromising accuracy. The model included the shapes, sizes, and thermal properties of the concrete elements. The initial conditions, including the starting temperature of the concrete elements, were then applied, followed by boundary conditions that accounted for the environmental factors. Key boundary conditions included solar radiation heat flux applied as a surface load to exposed areas, convective heat transfer to exposed surfaces, and insulated conditions for surfaces in contact with the ground or shielded from direct exposure.

Figure 6.1 illustrates the overall process of integrating the solar radiation model with the FEM heat transfer analysis in ABAQUS. This workflow ensured that the predicted solar energy flux directly informed the heat transfer simulation, providing a comprehensive analysis of the thermal response of concrete elements under realistic environmental conditions.

6.3 Introduction to ABAQUS Interface

ABAQUS is a versatile finite element programme capable of conducting structural, thermal, and dynamic analyses. In this study, ABAQUS/CAE (2023) was used to build and calibrate a heat transfer model to predict the thermal behaviour of concrete elements. This directly supports the objective of the chapter of determining the thermal conductivity (k) and the solar absorptivity for the two concrete mixes and evaluating their impact on effective temperatures.

ABAQUS employs numerical methods to solve the governing 2D heat transfer equation, as introduced in Chapter 2 (Equation 2.23). This partial differential equation (PDE) models heat conduction through concrete elements, integrating material properties, boundary conditions, and initial conditions to simulate heat transfer behaviour under environmental loading. By solving this equation, ABAQUS predicts the transient and steady-state temperature distributions, which are critical to calibrating the thermal properties (k and the solar absorptivity). ABAQUS uses the finite element method (FEM) to discretise the heat transfer equation across the concrete elements. The 2D domain is divided into smaller elements, each with a degree of freedom of nodal temperature. The heat transfer equation is applied to these elements and a global temperature distribution is calculated.

Transient heat transfer is solved using the backward Euler method, also known as the modified Crank-Nicolson operator, which ensures stability and accuracy (Dassault Systèmes, 2023). This method calculates the temperature field at each time increment, using the results from the previous step as input, and is particularly suited for capturing the time-dependent thermal response of concrete elements.

Material properties were assumed to be constant, as temperature-dependent behaviour was not considered in this study due to the relatively small temperature range observed during the experimental period.

Boundary conditions were applied to simulate environmental interactions, including:

- Heat Flux: Solar radiation calculated using the prediction model (Chapter 5) was input as surface heat flux on exposed boundaries (top, bottom and side surfaces).
- Convective Heat Transfer: Applied to exposed surfaces using coefficients derived from environmental data, representing air-surface interactions.

These inputs align with the chapter's aim of integrating environmental data and material properties into the heat transfer analysis.

The 2D domain was discretised into finite elements using ABAQUS mesh generation tools. Linear elements (first-order) were used for simplicity and computational efficiency, given the relatively uniform temperature gradients observed.

The calibrated heat transfer model was used to refine the thermal conductivity and solar absorptivity values for the Dolerite and Dolomite mixes. By inputting the solar heat flux and environmental data as boundary conditions, the model was adjusted to match the observed temperature distributions from the experimental data. Furthermore, a sensitivity analysis was performed to evaluate the influence of concrete's thermal conductivity and solar absorptivity on effective temperature predictions, fulfilling a key objective of this chapter.

6.4 Geometric and Material Models

The geometric and material models used in this study consisted of two different concrete mixes: Dolerite Mix and Dolomite Mix. Each mix was characterised by specific heat capacities and densities, as shown in Table 6.1. The primary difference between the two mixes lies in their thermal properties. The thermal conductivity of both mixes was varied in an extreme range of 1.0 to 3.6 $W/m/C$ to evaluate the sensitivity of the model. This range was chosen to include the typical values of concrete thermal conductivity found in the literature (Chapter 2).

For sensitivity analysis and calibration, only the Cube shape was used to represent the first week of the study. This allowed for a focused analysis on how variations in thermal conductivity affected heat transfer within a symmetric shape. The calibrated parameters from the Cube were then applied to the other two shapes (Flange and L-Shape) to confirm the results. The Flange and L-Shaped served as validation cases, verifying that the Cube calibration provided accurate heat-transfer predictions in these more complex shapes.

Table 6.1: Summary of thermal properties of Dolerite and Dolomite mixes.

Thermal Property	**Dolerite Mix**	**Dolomite Mix**
Density, ρ (kg/m^3)	2420	2380
Specific Heat Capacity, c_p $(J/(kgC))$	970	1135
Thermal Conductivity Range, k $(W/m/C)$	1.0 - 3.6	1.0 - 3.6

Since the east and west faces of the elements were insulated, the 3D problem was reduced to a 2D heat transfer model, simplifying the analysis (see Figure 6.2). This reduction was appropriate because insulation minimised heat flow in the out-of-plane direction, allowing the analysis to focus on heat transfer through the top and bottom faces of the elements.

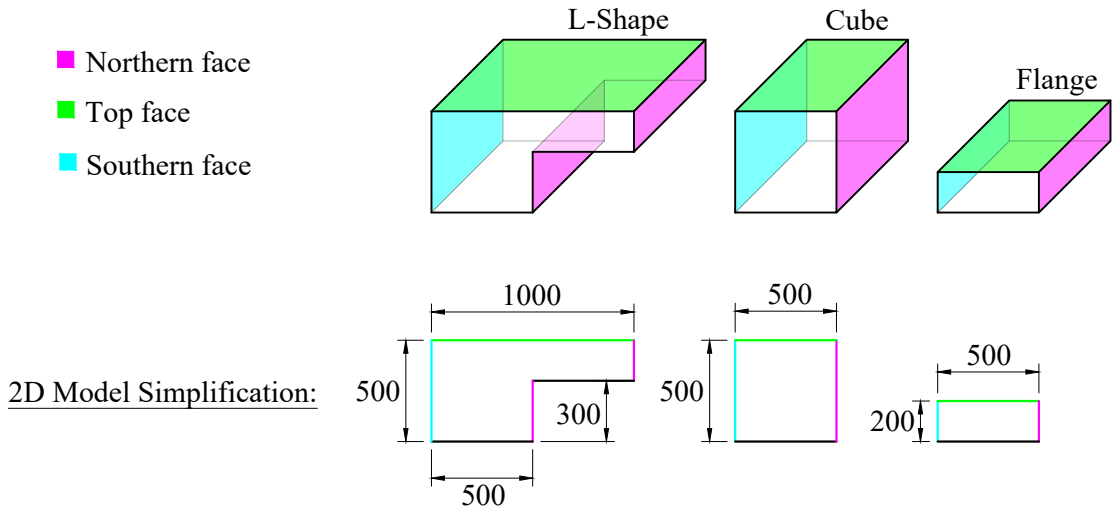

Figure 6.2: Simplification of 3D shapes into 2D models for heat transfer analysis

In finite element analysis, finer mesh sizes are generally chosen to enhance solution accuracy by minimising discretisation errors. As described in Zienkiewicz and Zhu (2005),

selecting an appropriately fine mesh size, such as 10 mm in this study, aligns with standard practices to reduce errors in computational simulations. Although a mesh sensitivity analysis was not conducted in this study, iterative mesh refinement or sensitivity analyses are widely recommended to verify convergence in finite element solutions, as they allow assessment of whether further refinement would significantly impact results. This study assumes that the 10mm mesh size is sufficiently accurate (see Figure 6.3). The 10 mm mesh was assumed to be sufficient based on its ability to accurately represent all increments across the modelled shapes after calibration. This approach reflects a balance between computational efficiency and the necessary level of precision, in line with established principles in finite element modelling (Zienkiewicz and Zhu, 2005).

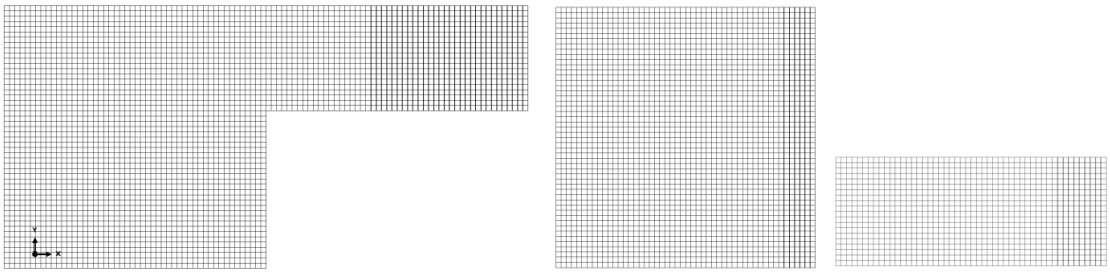

(a) (b) (c)

Figure 6.3: ABAQUS/CAE (2023) FEM model showing 10 mm mesh size for (a) L-Shape, (b) Cube and (c) Flange.

6.5 Boundary and Initial Conditions

The initial temperature distribution for the finite element analysis was taken from the first recorded data point after the concrete samples were moved outdoors (2024-06-03 18:40). This was used to define the starting thermal state of each shape, ensuring that the model accurately reflected the initial energy.

To assign this initial temperature distribution, a predefined field (analytical map) was used in the ABAQUS model. This method allowed for a detailed and spatially varying initial temperature profile to be applied to each shape, based on the actual measurements. Figure 6.4 presents the initial temperature distribution for each shape. The temperature profiles are plotted with distance from the top of the shape on the y-axis and temperature on the x-axis.

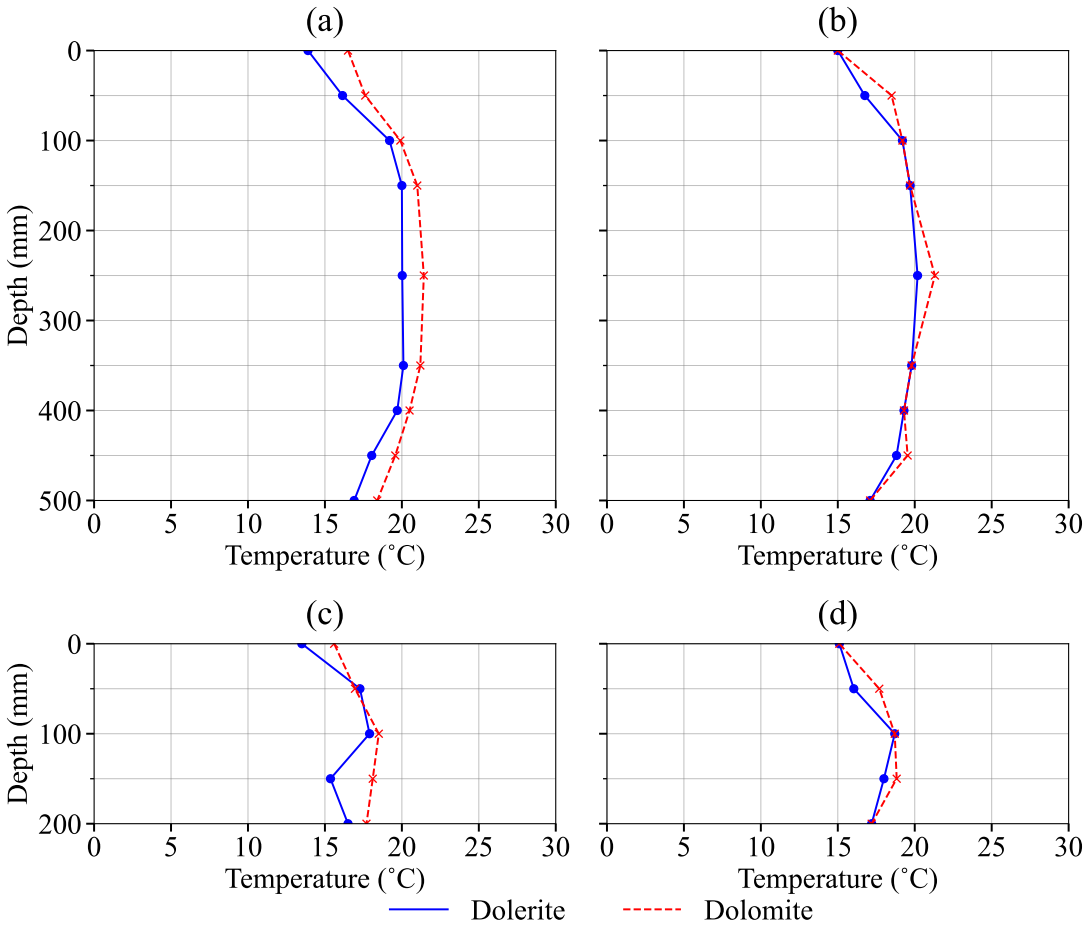

Figure 6.4: Initial temperature condition: (a) Cubes, (b) L-Shape Cubes, (c) Flange, (d) L-Shape Flange, showing Dolerite and Dolomite mixes (measured temperature at 03-06-2024 18:40).

In terms of boundary conditions, the east and west faces of each shape were assumed to be insulated. Convective boundary conditions were applied to the north, south, top, and bottom surfaces of each shape to simulate heat exchange with the surrounding environment. These boundary conditions were consistent across all shapes and ensured that the model accurately reflected the real world constraints experienced by the concrete elements.

To model the heat transfer occurring on the surface of each concrete element, a convective boundary condition was applied using the surface interaction feature in ABAQUS. The heat transfer coefficient (h_c) for convection was determined using an empirical formula (Equation 2.30), as detailed in Chapter 2, which relates the coefficient to the wind speed (v). Wind speed was averaged over the duration of the experiment and is shown in Figure 6.5.

The calculated heat transfer coefficients are shown in Table 6.2. For the bottom surface,

a convective heat transfer coefficient of 2.17 was chosen. This value corresponds to the minimum value h_c of the empirical formula when the wind speed is zero (Equation 2.30). As shown in Figure 6.6, the frame and angle irons blocked much of the airflow, reducing the wind speed on the bottom surface and resulting in a lower convective heat transfer coefficient.

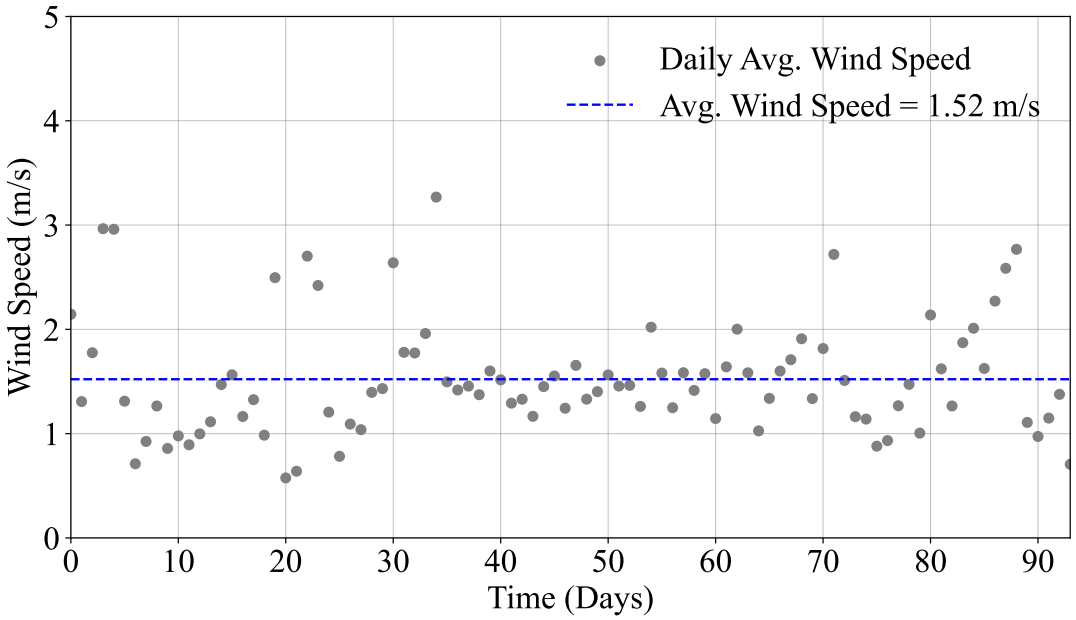

Figure 6.5: Average measured wind speed over time after moving the concrete samples outside (starting from 2024-06-03 18:40)

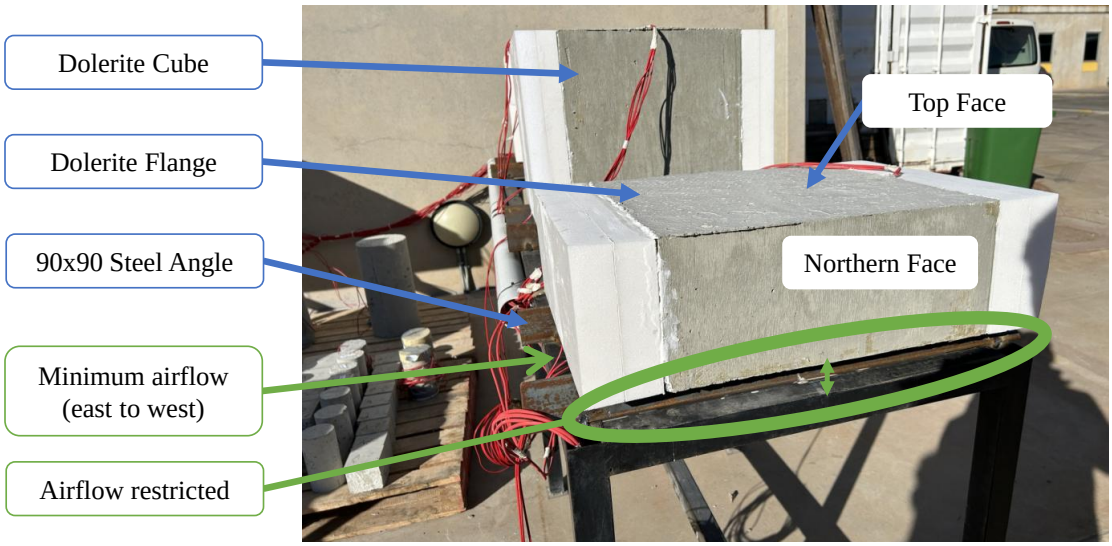

Figure 6.6: Support conditions of the steel frame and angle irons (Dolerite Flange section).

Table 6.2: Convective heat transfer coefficient.

Face	Convective heat transfer coefficient (h_c)
North Face	9.52
Top Face	10.52
South Face	9.52
Bottom ($v = 0$)	2.17

Long-wave radiation was modelled in ABAQUS using cavity radiation, under the assumption that the emissivity of concrete is 0.9, as indicated in the relevant literature (see Table 2.5). The Stefan-Boltzmann constant ($5.67 \times 10^{-8}\,\mathrm{W/m^2K^4}$) was used to represent radiative heat transfer, and it was assumed that the temperature of the surrounding environment was equal to the ambient temperature (Figure 6.7). Shade effects were deemed negligible for this study.

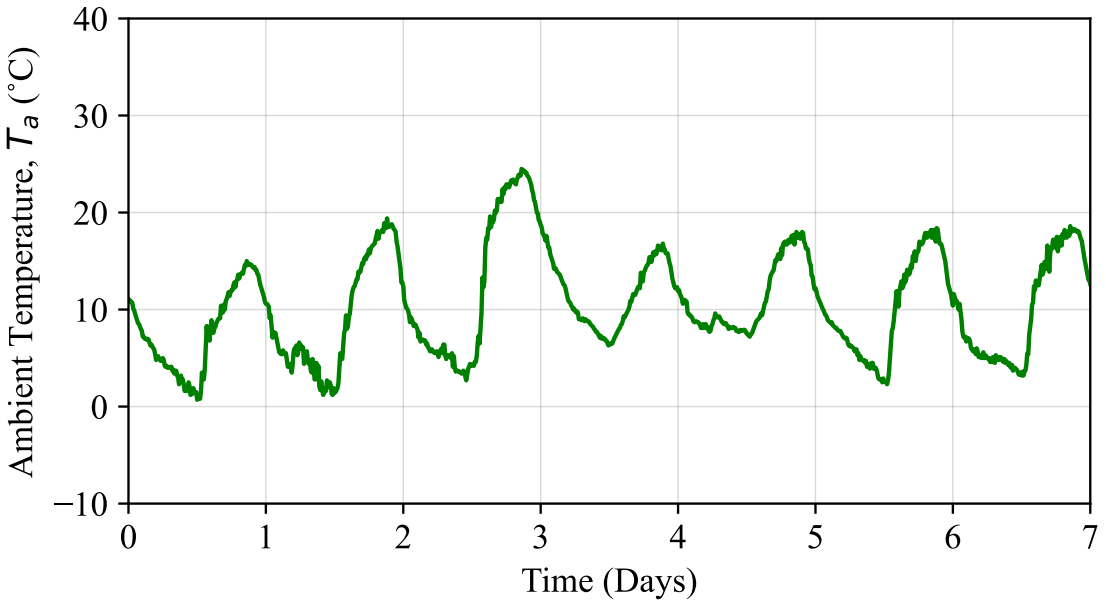

Figure 6.7: Recorded ambient temperature (T_a) over first week of experimental period.

The cavity radiation capability within ABAQUS/Standard was applied to simulate radiative heat exchange between surfaces. This approach allows for the analysis of thermal radiation between surfaces without accounting for mechanical deformation. This formulation assumes that all surfaces radiate to an exterior medium, represented by the ambient temperature. This assumption simplifies the model by eliminating the need to account for more complex surroundings or reflective surfaces. Additionally, the model assumes that temperature gradients within the concrete surfaces are gradual, thereby minimising any potential oscillations or numerical instabilities. This method was applied consistently to all surfaces throughout the duration of the experiment.

6.6 Application of Thermal Loading

This section explains the application of load conditions on each sample during the finite element analysis, specifically the ambient temperature (T_a) and the short-wave solar radiation (I_{Total}). The ambient temperature and short-wave solar radiation models were incorporated into the ABAQUS heat transfer model as time-varying surface heat fluxes. The model was calibrated using the ambient temperature data for the first week (Figure 6.7) and the predicted solar radiation for the first week (Figure 6.8). The predicted solar radiation for the first week remained fairly constant, as atmospheric conditions and cloud cover showed minimal variation during this period, resulting in similar daily radiation trends.

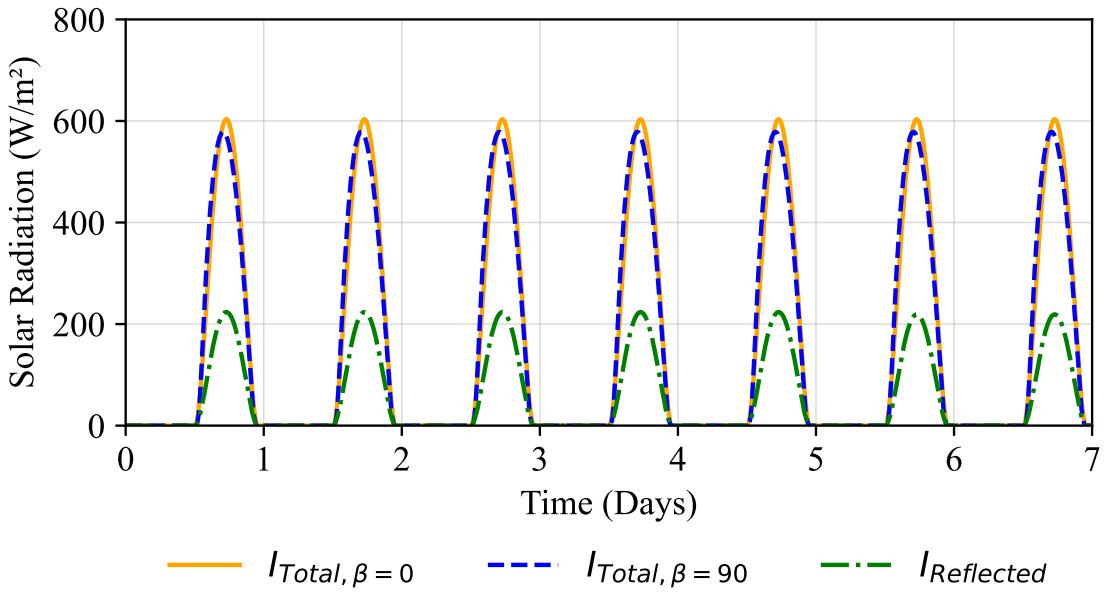

Figure 6.8: Predicted solar radiation for first week applied to top surface ($I_{Total,\beta=0}$), north facing surface ($I_{Total,\beta=90}$), south facing surface and bottom surface ($I_{Reflected}$).

The ambient temperature was uniformly applied to all the surfaces of the concrete elements, based on the weather station data recorded during the experiment. This initial period was chosen to ensure that the thermal response of concrete under realistic environmental conditions could be accurately captured, without the influence of non-linear thermal properties. The uniform application across all surfaces assumes that the concrete elements are subjected to the same ambient thermal environment on all sides, a valid assumption due to the relatively small scale of the representative samples.

Short-wave solar radiation (Figure 5.12) was applied to the surfaces shown in Figure 6.2. The predicted solar radiation intensities, $I_{Total,\beta=0}$ and $I_{Total,\beta=90}$, were applied to the top and northern surfaces of the concrete elements, respectively. The southern and lower

surfaces were assumed to receive only reflected solar radiation as predicted by the solar radiation model ($I_{Reflected}$). The equation governing the short-wave heat flux from solar radiation, Equation 2.29, was used for this purpose.

The absorptivity (a_s) values were varied between 0.4, 0.6, and 0.8 during sensitivity analysis and calibration. These values reflect typical solar absorptivity ranges for concrete surfaces based on colour, as established in Chapter 2. The extreme values of 0.4 and 0.8 were chosen as limits between the ranges listed in Table 2.5. For the purpose of this analysis, the values chosen encompass the potential variation in the surface finishes or conditions of the concrete elements.

6.6.1 Sensitivity Analysis Results

Sensitivity analysis was performed to evaluate the influence of thermal conductivity (k) and solar absorptivity (a_s) on the effective temperature and top-bottom temperature gradients of the concrete elements. This analysis provides insight into how variations in these thermal properties impact the thermal behaviour of concrete mixes, fulfilling a key objective of this chapter.

The effect of k and a_s on the effective temperature was assessed by calculating the daily change in effective temperature (T_{eff}) over a week-long period. The results were averaged to provide a representative value for each combination of k and a_s. These daily average changes in effective temperature were plotted against thermal conductivity (k) for various values of a_s in Figure 6.9.

The analysis confirmed the following trends:

- Thermal Conductivity (k): As k increases, the daily change in T_{eff} increases. This is attributed to the higher ability of materials with a higher k to dissipate heat, increasing temperature fluctuations within the concrete.
- Solar Absorptivity (a_s): Higher values of a_s result in greater daily changes in T_{eff}, as increased solar absorptivity amplifies the absorption of solar radiation, leading to greater diurnal temperature fluctuations.

To assess whether the observed trends are substantial, the sample standard deviations (s) and coefficients of variation (CV) reported in Chapter 5 for the measured effective temperatures were considered. The experimental results, recorded over a three-month period, showed variability in effective temperatures ranging between 3.66–6.43°C for Dolerite and 4.12–6.45°C for Dolomite, with CV values indicating substantial fluctuation within each mix. In contrast, the sensitivity analysis was conducted over a one-week period and assessed the daily change in effective temperature (ΔT_{eff}), which varied between 6.53°C and 14.06°C for Dolerite and 5.97°C and 12.78°C for Dolomite, depending on the thermal conductivity (k) and solar absorptivity (a_s) values.

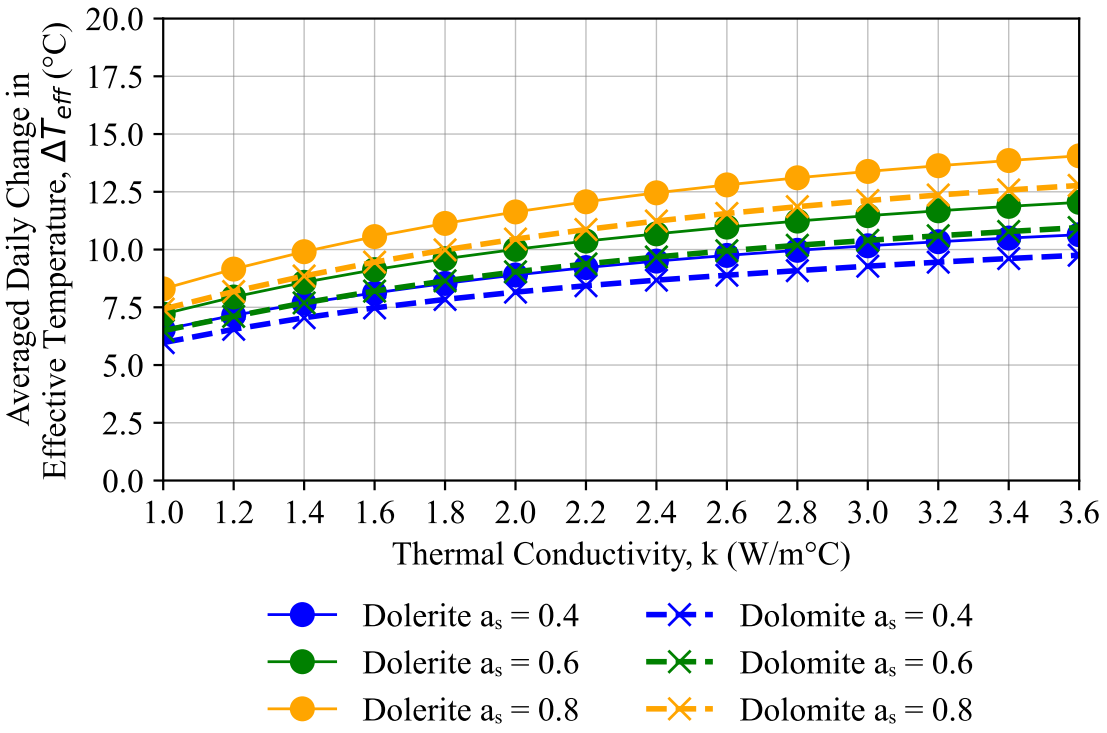

Figure 6.9: Averaged daily change in effective temperature plotted against k with range of a_s values.

By comparing these results, the modelled daily temperature fluctuations exceed the measured sample standard deviation range, suggesting that variations in k and a_s have a substantial impact on effective temperature. However, the high CV values in the experimental data indicate that environmental fluctuations also contributed substantially to the temperature variations. Given that the experimental data captures long-term seasonal trends, while the sensitivity analysis focuses on short-term variations, these results should be interpreted within the context of inherent experimental variability. While the trends observed in the sensitivity analysis align with expected thermal behaviour, the magnitude of the modelled changes should be assessed with caution due to the influence of external environmental factors over longer durations.

The sensitivity of the temperature gradients to k and a_s was assessed by calculating the maximum positive and negative *upper-lower* temperature differences over a week. Positive gradients ($T_{\text{top}} - T_{\text{bottom}} > 0$) and negative gradients ($T_{\text{top}} - T_{\text{bottom}} < 0$) were considered separately to account for the directional nature of heat transfer. These maximum gradients were plotted against the thermal conductivity (k) for various values a_s, as shown in Figure 6.10.

The results indicated:

- Positive Gradients: The maximum positive gradient decreased with increasing k, consistent with the improved heat dissipation in materials with higher thermal conductivity. Higher a_s values intensified positive gradients, reflecting the greater absorption of solar radiation at the top surface.
- Negative Gradients: The maximum negative gradient followed a similar trend but was not as evident. This was attributed to the low convective heat transfer of the lower surface, similar to the gradient results (see Table 5.1). Lower values of k lead to steeper gradients. Higher a_s values also amplified negative gradients by increasing heat loss from the top surface during cooler periods.

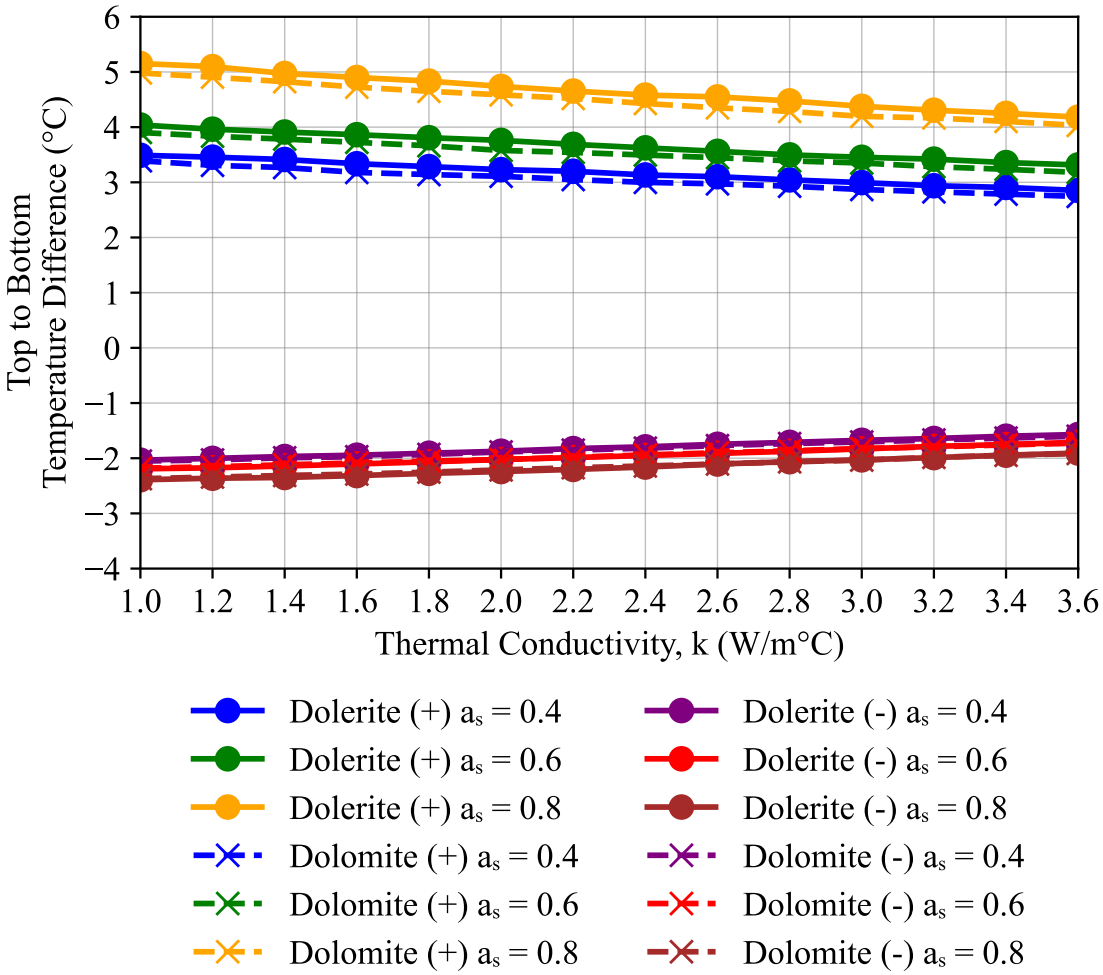

Figure 6.10: Maximum temperature difference between top and bottom surfaces plotted against k with a range of a_s values.

The experimental results showed variability in measured Top-to-Bottom temperature gradients ranging between 1.14–2.65°C for Dolerite and 0.97–2.22°C for Dolomite, with

CV values spanning 17.25–24.02%, indicating substantial fluctuation within each mix. In contrast, the sensitivity analysis, conducted over a one-week period, recorded less than 1°C change in both positive and negative gradients when k and a_s were varied.

When comparing these results, the modelled variations in top-to-bottom gradients are small relative to the measured sample standard deviations, suggesting that changes in k and a_s have a limited influence on thermal gradient magnitudes within the experimental variability range. The high CV values in the experimental data indicate that the environmental conditions and inherent variability contribute more substantially to the gradient fluctuations than the tested material parameters. Given that the experimental results account for long-term seasonal variations while the sensitivity analysis examines short-term fluctuations, this suggests that the effects of k and a_s on top-bottom gradients may not be substantial within the context of real-world environmental conditions.

6.7 Calibration Results

This section outlines the calibration process used to determine the optimal values of thermal conductivity (k) and solar absorptivity (a_s) for the concrete mixes of Dolerite and Dolomite. The model was calibrated to the first week of the experiment and validated for the entire three-month exposure period. This validation confirmed the assumption that the thermal properties remained relatively constant throughout the duration of the exposure. The calibration emphasised effective temperature predictions as the primary metric for refining thermal properties and verifying temperature gradients across the samples.

6.7.1 Rationale for Effective Temperature Calibration

The calibration focused on the effective temperature (T_{eff}) due to its reliability in capturing the global thermal response of the samples. This metric effectively integrates the thermal behaviour influenced by solar radiation, conduction, and minor convective heat transfer within the experimental environment. Additionally, the effective temperature served as a reference point to verify the consistency of the top-minus-bottom temperature gradients.

The experimental setup aimed to validate the model's capability to predict thermal gradients, using the top-minus-bottom temperature difference as an indicator. However, the calibration did not address non-linearities within the thermal gradient, such as those related to central temperatures, as the focus was on global responses rather than localised variations.

6.7.2 Calibration of Thermal Properties

The calibration process systematically varied solar absorptivity (a_s) and thermal conductivity (k) to achieve a close match between measured and predicted effective temperatures. The following steps were undertaken:

- **Absorptivity Variation:** Solar absorptivity (a_s) was tested at values of 0.4, 0.6, and 0.8 to represent a range of surface reflectivities typical of concrete.
- **Conductivity Variation:** Thermal conductivity (k) was incrementally adjusted between 1.0 and 3.6 $W/m \cdot^\circ C$, capturing the expected ranges for concrete with different aggregates.
- **Model Accuracy Assessment:** For each combination of a_s and k, the predicted effective temperature was compared with the measured data and the precision was evaluated by calculating R^2.

6.7.3 Results of Calibration and Validation

The calibrated thermal properties for effective temperature predictions were as follows:

- **Dolerite:** $k = 2.00\,W/m \cdot^\circ C$, $a_s = 0.4$, yielding $R^2 = 0.9471$.
- **Dolomite:** $k = 3.60\,W/m \cdot^\circ C$, $a_s = 0.6$, yielding $R^2 = 0.9252$.

Figure 6.11 shows a contour map of the values of R^2 for effective temperature predictions, with (a) Dolerite and (b) Dolomite. These maps illustrate the relationship between a_s, thermal conductivity, and the precision of the model, helping to select the thermal properties that best match the experimental data.

The calibrated model was validated by comparing the predicted and measured temperature gradients through the depth of all specimens during the three-month experimental period. Figure 6.12 shows the comparison between the measured and predicted values of effective temperature (T_{eff}) for (a) Cube, (b) Flange, (c) L-Shape Cube and (d) L-Shape Flange. The results confirm that the model accurately replicates the thermal behaviour of the samples and captures global temperature differences. However, non-linearities in the thermal gradient, such as central temperature variations, were not addressed within the calibration scope.

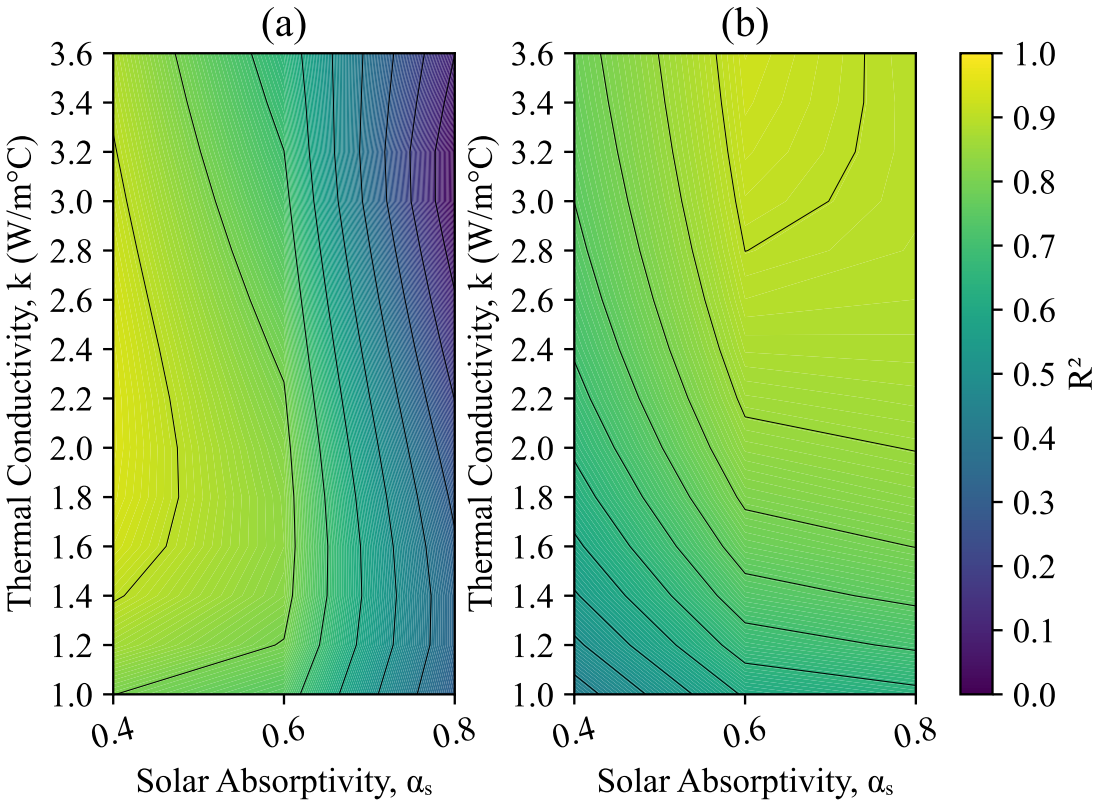

Figure 6.11: R^2 contour map for effective temperature predictions: (a) Dolerite and (b) Dolomite, with axes representing solar absorptivity and thermal conductivity.

Figure 6.13 shows the comparison between the measured and predicted values of gradient temperature ($Top - Bottom$) for (a) Cube, (b) Flange, (c) L-Shape Cube and (d) L-Shape Flange.

The three-month calibration results confirm the robustness of the finite element model in predicting both T_{eff} and Top-to-Bottom temperature gradients for a range of geometries and material properties. Key findings include:

- The high R^2 values (> 0.9) for Cubes, Flanges, and L-Shape Flanges indicate that the model accurately captures effective temperature across different shapes and materials, validating the assumption that thermal properties (k and a_s) remained consistent throughout the experimental period.
- The slightly lower R^2 values for the L-Shape Flange (0.86 dolomite, 0.80 dolerite) suggest minor deviations in predicted vs. measured T_{eff}, likely due to increased geometric complexity and heat flow interactions in the combined Flange-Cube configuration.
- For temperature gradients, the model maintains strong predictive capability ($R^2 > 0.7$) for most shapes but shows slightly reduced accuracy ($R^2 = 0.66$) for the

dolerite L-Shape Cube. This suggests that localised heat flow mechanisms, possibly influenced by mix-dependent thermal diffusivity, contribute to increased variability.

- Overall, the model's ability to accurately capture both global thermal responses (T_{eff}) and localised temperature gradients reinforces its applicability in evaluating the thermal behaviour of concrete elements across geometries and material properties.

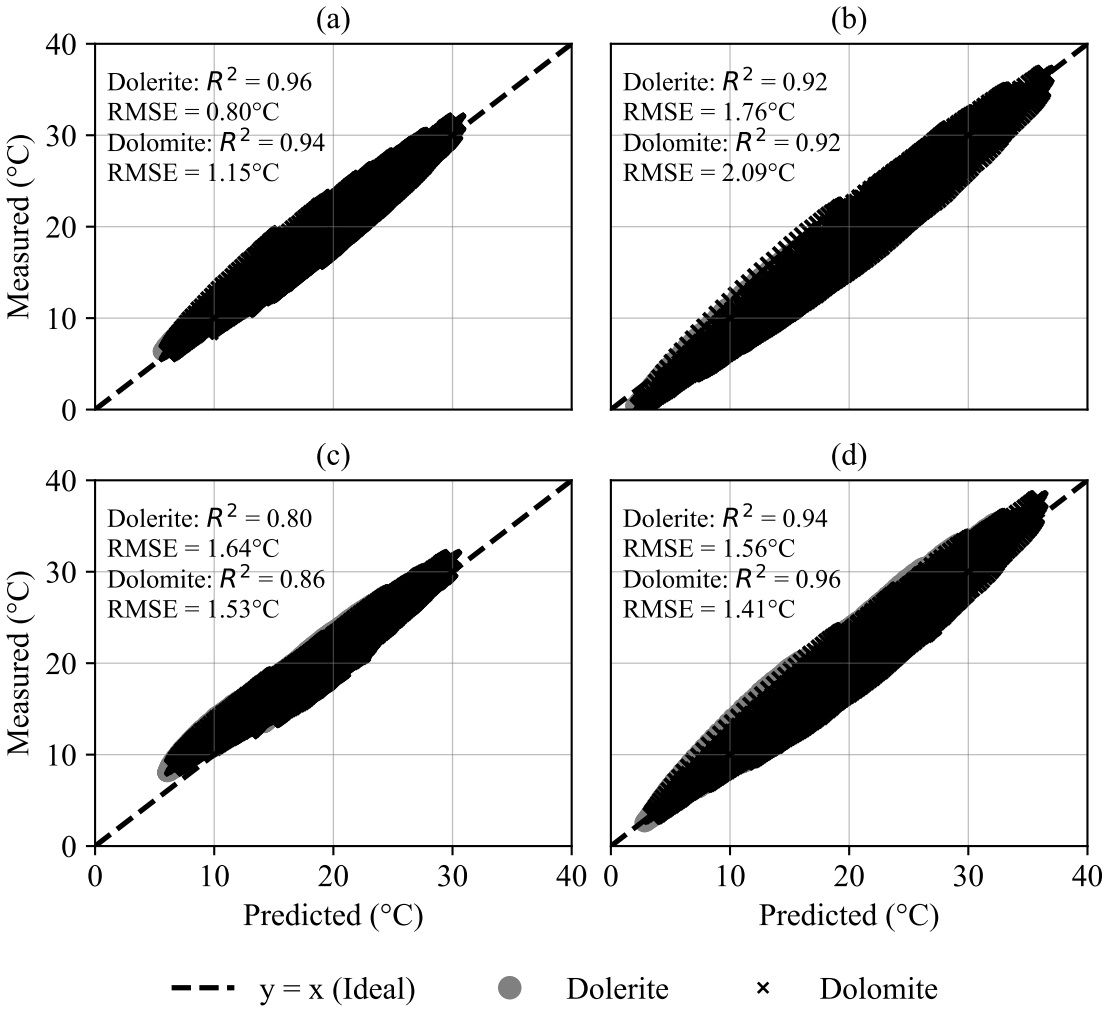

Figure 6.12: Comparison of three-month measured and predicted effective temperature (T_{eff}) for (a) Cube, (b) Flange, (c) L-Shape Cube and (d) L-Shape Flange.

These results provide a strong foundation for linking thermal behaviour with thermal strain and stress development, as explored in Chapter 7. By accurately simulating temperature distributions, the model enables reliable predictions of structural performance under environmental loading, supporting the design of more durable and thermally efficient concrete structures.

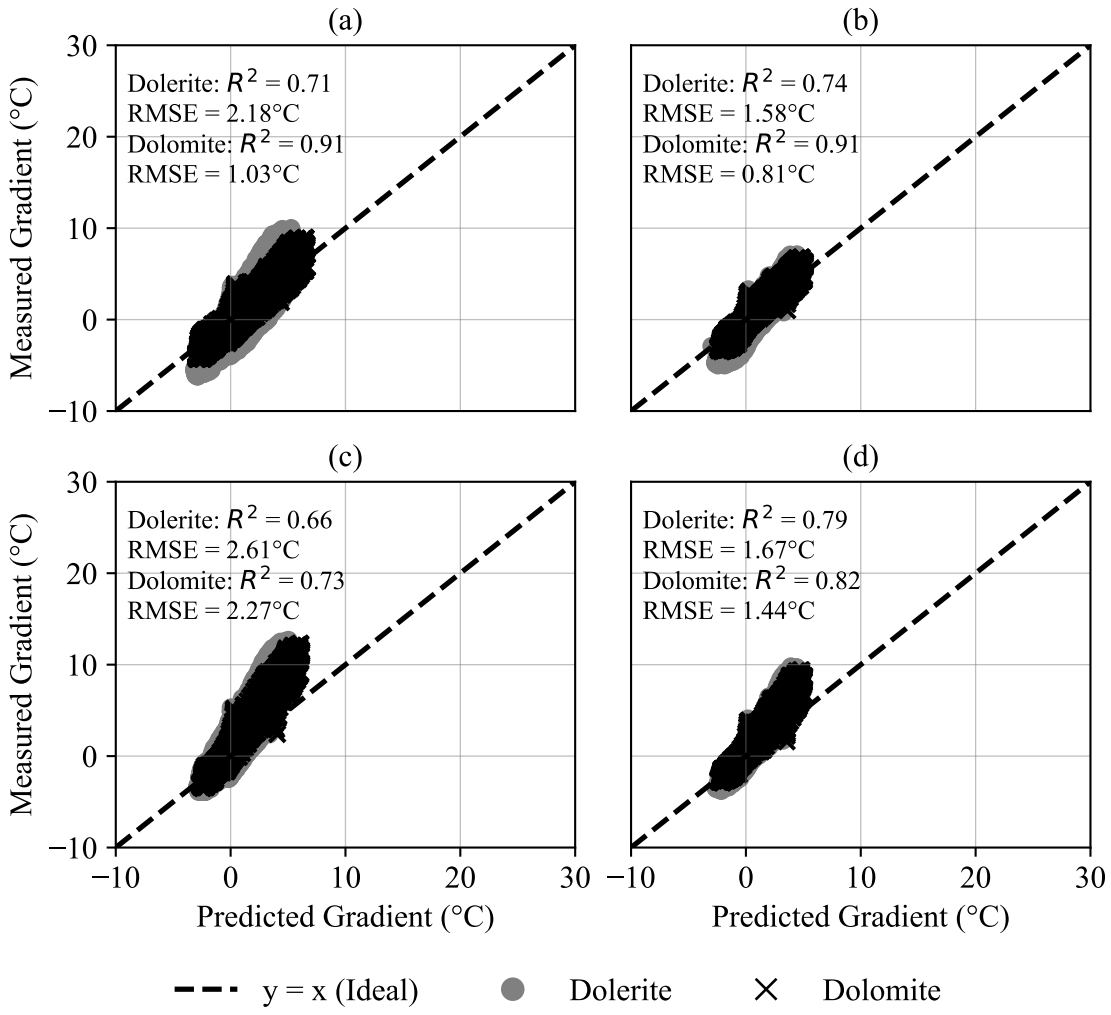

Figure 6.13: Comparison of three-month measured and predicted gradient temperature ($Top - Bottom$) for (a) Cube, (b) Flange, (c) L-Shape Cube and (d) L-Shape Flange.

6.8 Summary

This chapter successfully demonstrated the integration of a solar radiation prediction model (Chapter 5) and experimentally derived material properties (Chapter 2) to develop a heat transfer model for concrete elements in this study. The model incorporated ambient temperature data from a weather station and took into account various heat transfer mechanisms, including convection, conduction, and radiation. By calibrating and validating the model, it was possible to refine the thermal conductivity (k) and solar absorptivity (a_s) values for Dolerite and Dolomite concrete mixes.

The sensitivity analysis confirmed that thermal conductivity (k) and solar absorptivity

(a_s) influence effective temperature fluctuations and thermal gradients, with higher thermal conductivity values reducing gradients and higher a_s values amplifying diurnal fluctuations. However, within the context of real-world environmental conditions, these effects were small compared to the variability introduced by environmental fluctuations.

The model calibration over the three-month period successfully matched measured and predicted effective temperatures across all shapes, with strong correlation coefficients ($R^2 > 0.9$). The model also maintained good predictive capability for temperature gradients ($R^2 > 0.7$), though minor deviations were observed in the L-Shape sections, likely due to geometric complexity. These findings confirm that thermal properties remained consistent throughout the study period and validate the model's applicability for predicting thermal behaviour in concrete elements. The calibrated model provides a reliable basis for linking temperature distributions to thermal stress and strain development in subsequent analyses.

This chapter concludes by highlighting the differences in thermal conductivity and solar absorptivity between the two aggregates. While these properties influence the thermal response of concrete elements, their impact on effective temperature was found to be limited within the scope of this study. Dolomite showed slightly greater temperature variations, consistent with its higher thermal conductivity and absorptivity, but the variability introduced by environmental conditions and section geometry played a more dominant role. The influence of these temperature variations on thermal strains was examined in the subsequent section, providing further insight into the deformation behaviour of concrete and its implications for structural performance under environmental exposure.

7 Stress Analysis

7.1 Introduction

The behaviour of concrete elements under environmental loading is influenced by a combination of material properties, geometric factors, and constraint conditions. These factors interact to produce temperature gradients, shrinkage effects, and the resulting stresses that can substantially impact the durability and performance of concrete structures. Understanding these interactions is particularly important in South Africa, where concrete structures are exposed to variations in diurnal temperature and drying conditions that are unique to the region.

This chapter investigates the stress development in three primary concrete shapes—Cube, Flange, and L-Shaped—constructed using two aggregate types, Dolerite and Dolomite. These aggregates, which are widely used in South Africa, exhibit distinct thermal and mechanical properties that influence the response of concrete to environmental conditions. The study focuses on isolating the effects of thermal expansion, shrinkage, and residual strains to provide a complete understanding of the distribution of stress in these shapes.

The findings of this chapter are especially relevant as South Africa transitions to adopting the EN1992-1-1 (2004a) standard for concrete design. The results presented here will offer information on how South African aggregates perform under environmental loading and how the EN1992-1-1 (2004a) predictions align with experimental observations. By addressing these considerations, this chapter aims to provide a framework for improving the design and performance of concrete structures in the local context.

The analysis begins with a detailed methodology for isolating thermal and shrinkage strains, followed by a presentation of residual strains and stresses in the Cube, Flange, and L-Shaped sections. The discussion integrates these findings with the measured properties of South African aggregates, highlighting their implications for the adoption of EN1992-1-1 (2004a) in the region.

7.2 Geometric Restraint

If the concrete elements had been fully restrained, no strains would have been recorded, as the internal stresses within the structure would have been dictated solely by the concrete stiffness and the strain prevented from occurring. However, in this study, the concrete elements were not restrained, allowing movement to occur freely. Despite this, the measured strains differed from the predicted shrinkage and thermal strains (Chapter 5). These differences are identified as residual strains within the concrete.

This section examines the stress development in the L-Shape, Cube, and Flange concrete elements exposed to environmental conditions during the experimental period (03-06-2024 to 03-09-2024). The methodology involves isolating thermal and shrinkage strains, deriving residual strains, and ultimately calculating residual stresses. The approach is aligned with the relevant standards, calibration techniques, and theoretical models discussed in previous chapters.

The strains were measured using Vibrating Wire Strain Gauges (VWSGs) positioned at various depths along the centrelines of the concrete shapes (see Chapter 3). The sensor naming convention is detailed in Figure 7.1, which provides a clear representation of sensor placement and the nomenclature used to differentiate between shapes, mixes, and sensor depths.

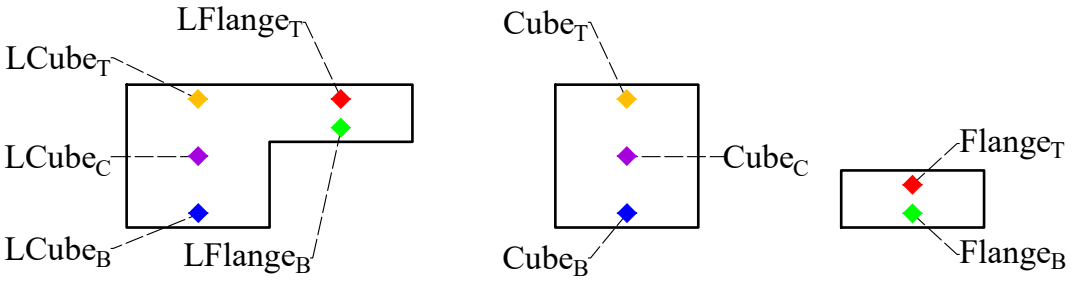

Figure 7.1: Sensor naming convention for Vibrating Wire Strain Gauges (VWSGs) in concrete shapes: (a) L-Shape, (b) Cube, and (c) Flange.

The methodology for isolating strain components consisted of the following steps:

1. Shrinkage Strains: The drying shrinkage strains were calculated using an adjusted version of the EN1992-1-1 (2004a) shrinkage *prediction model* (Chapter 5). This calibration was performed on free cylindrical concrete elements exposed to the same environmental conditions as the primary shapes. The simplified shrinkage model (Equation 5.7) incorporates relative humidity, temperature, and geometry, providing an accurate representation of shrinkage behaviour for this experimental setup.

2. Thermal Strains: Thermal strains were isolated using the coefficient of thermal expansion, α_c, *derived* through weekly regression analysis of strain versus temperature in cylindrical shapes (see Chapter 4). These cylinders, which were free to expand and contract, provided a reliable calibration of α_c for the Dolerite and Dolomite mixes. The thermal strain at each VWSG location was subsequently calculated using Equation 4.7, incorporating the measured temperature variations recorded at each sensor. By subtracting the calculated thermal strains at each sensor position from the measured strains, the influence of linear thermal strain variations was effectively removed, enabling the remaining strain components to be attributed to mechanisms such as drying shrinkage, creep, or secondary thermal effects.

3. Residual Strains: The residual strains were obtained by subtracting the isolated thermal and shrinkage strains from the measured strains at each sensor location, as shown in Equation 7.1. This equation systematically accounts for the contributions of measured, thermal, and shrinkage strains:

$$\underset{}{\varepsilon_{\text{residual}}} = \underset{\text{(Measured)}}{\varepsilon_{\text{measured}}} - \underset{\text{(Derived)}}{\varepsilon_{\text{thermal}}} - \underset{\text{(Modelled)}}{\varepsilon_{\text{shrinkage}}} \tag{7.1}$$

The residual strains, $\varepsilon_{\text{residual}}$, isolated through this process, are interpreted as a combination of the following components:

1. **Creep Strains:** Time-dependent deformations resulting from sustained internal stresses induced by environmental loading or differential drying.
2. **Differential Shrinkage Strains:** Variations in shrinkage along the depth or geometry of the sample due to uneven drying.
3. **Secondary Thermal Strains:** Self-equilibrating strains caused by internal temperature gradients that are not captured by the linear thermal strain assumptions.

Bending effects were deemed negligible due to the continuous support in the direction of the strain measurements, which prevented significant bending moments (see Chapter 3 and Figure 3.15).

This approach assumes uniform material properties and negligible contributions from external mechanical loads, which were validated by consistent strain distributions across similar elements. This methodology accounts for both time-dependent and spatially varying effects that influence residual strain development. Figure 7.2 shows the residual strain distributions for the Cube and Flange sections after removing thermal and shrinkage strains.

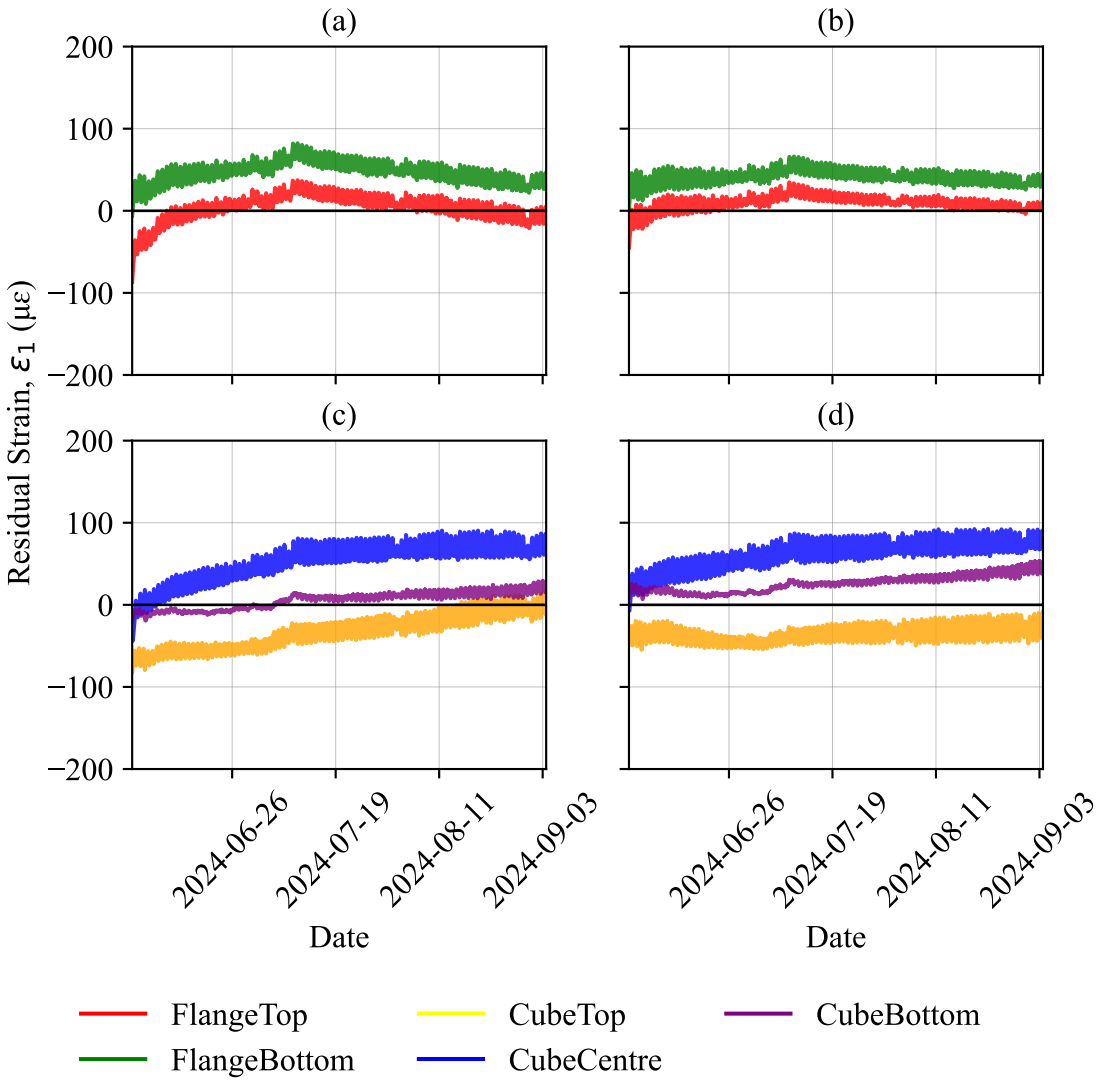

Figure 7.2: Residual strains after removing shrinkage and thermal strains for (a) Dolerite Flange, (b) Dolomite Flange, (c) Dolerite Cube, (d) Dolomite Cube.

The Flanges for both mixes showed minimal residual strain, with maximum positive residual strains of 83 $\mu\varepsilon$ (Dolerite Flange$_B$) and 66 $\mu\varepsilon$ (Dolomite Flange$_B$) near the bottom sensors and slightly lower values of 37 $\mu\varepsilon$ (Dolerite Flange$_T$) and 35 $\mu\varepsilon$ (Dolomite Flange$_T$) near the top sensors. The negative strain values in the Flanges were similarly small, with a minimum of -86.6 $\mu\varepsilon$ for the Dolerite Flange$_T$ and -44.9 $\mu\varepsilon$ for Dolomite Flange$_T$. These results indicate that there was no substantial increase in residual strain during the exposure period, which confirms that the shrinkage prediction model, along with thermal isolation, was successful.

In the Cube sections, the bottom sensors (Dolerite Cube$_B$ and Dolomite Cube$_B$) showed

minimal residual strain development due to the support condition, with maximum positive residual strains of 29 $\mu\varepsilon$ (Dolerite) and 53 $\mu\varepsilon$ (Dolomite) and maximum negative residual strains of $-20\,\mu\varepsilon$ and $6\,\mu\varepsilon$, respectively. The top sensors (Dolerite Cube$_T$ and Dolomite Cube$_T$) showed an increase in residual strain development, with strains increasing by 97 $\mu\varepsilon$ and 63 $\mu\varepsilon$, respectively. In contrast, the central sensors (Dolerite Cube$_C$ and Dolomite Cube$_C$) showed the highest variation and residual strain development, with maximum positive residual strains of 91 $\mu\varepsilon$ and 93 $\mu\varepsilon$ and maximum negative residual strains of $-44\,\mu\varepsilon$ and $-7\,\mu\varepsilon$, respectively.

Residual stresses ($\sigma_{residual}$)were calculated from residual strains ($\varepsilon_{residual}$) using Equation Equation 7.2 which applies Hooke's Law (Equation 2.11).

$$\sigma_{\text{residual}} = E \cdot \varepsilon_{\text{residual}} \tag{7.2}$$

Where,

$\varepsilon_{\text{residual}}$ = Residual strain (dimensionless)
E = Young's modulus of the concrete (GPa) (summarised in Table 7.1)
σ_{residual} = Residual stress (MPa)

E-values used in this analysis were experimentally determined from representative cylindrical samples (100mm diameter and 200mm height) for each type of mixture (Dolerite and Dolomite), as discussed in Chapter 3. These samples were exposed to the same environmental conditions as the concrete elements, ensuring that they accurately represented the experimental mixes. The experimentally determined E-values were used to transform the strains into stresses, allowing an assessment of the residual stress distributions (Equation 7.2).

The experimentally derived E-values (representative E-values) were compared with the EN1992-1-1 (2004a) predicted values, which include adjustment factors based on aggregate types. Chapter 4 discusses how these adjustment factors result in underestimations and overestimations for South African aggregates. Specifically, Chapter 4 demonstrates that South African aggregates differ from the assumptions made in EN1992-1-1 (2004a), and good alignment with experimental results was achieved when aggregate adjustment factors were omitted.

The representative E-values and the adjusted EN1992-1-1 (2004a) E_{cm} values for the Dolerite and Dolomite mixes are summarised in Table 7.1. Throughout the results and discussions, the experimentally determined E-values are referred to as representative E-values, while the code-derived values are referred to as the adjusted EN1992 E_{cm} values. It is important to note these distinctions, as they directly influence the interpretation of residual stress results.

Table 7.1: Modulus of Elasticity of representative samples and EN1992-1-1 (2004a) predicted values.

Property	Dolerite Mix	Dolomite Mix
Measured E-value (GPa)	30.0	34.8
EN1992-1-1 (2004a) Aggregate adjusted E-value, E_{cm} (GPa)	41.1	30.4

The observed discrepancies between the representative E-values and the adjusted EN1992 E_{cm} values are noteworthy. For the Dolerite mix, the representative E-value was approximately 27% lower than the code-predicted value, while for the Dolomite mix, the representative E-value was approximately 12% higher. These deviations are substantial because the calculated residual stresses are linearly proportional to the elastic modulus (Equation 7.2).

Residual stresses were calculated from residual strains using the representative E-values (Measured E-value in Table 7.1), as shown in Figure 7.3. These results show the depth-dependent variation in residual stress and emphasise the importance of using representative material properties for accurate stress estimation. The sign convention for stresses are as follows: tensile stresses $(+)$ and compressive stresses $(-)$. This convention is used consistently throughout the analysis.

The Flange sections exhibited relatively consistent stress levels, with maximum tensile stresses (2.5 MPa for Dolerite and 2.3 MPa for Dolomite) and minimal depth sensitivity. The stresses in the Flange sections indicate that the shrinkage and thermal models effectively removed the strains, leaving minimal residual stresses. Additionally, the smaller surface area-to-volume ratio and symmetric environmental exposure contributed to lower residual stresses compared to the Cube sections. This behaviour reflects the reduced susceptibility of the Flange to differential drying and thermal gradients. Despite these differences, both mixes showed similar residual stress development over time.

The cubic sections exhibited slightly higher maximum tensile stresses at the central depth (2.8 MPa for Dolerite and 3.2 MPa for Dolomite), with Dolomite showing a modest increase. However, the depth-dependent stress gradients were more pronounced in Dolomite, as indicated by the larger stress reduction toward the bottom surfaces (0.9 MPa for Dolerite and 1.8 MPa for Dolomite).These stress distributions can be attributed to:

- **Differential restraint:** The bottom of the Cube was supported and partially restrained, while the top was free to shrink and expand, leading to non-uniform stress distributions.
- **Surface exposure effects:** Higher exposure to drying and thermal gradients near the surfaces resulted in higher residual stresses at shallower depths.

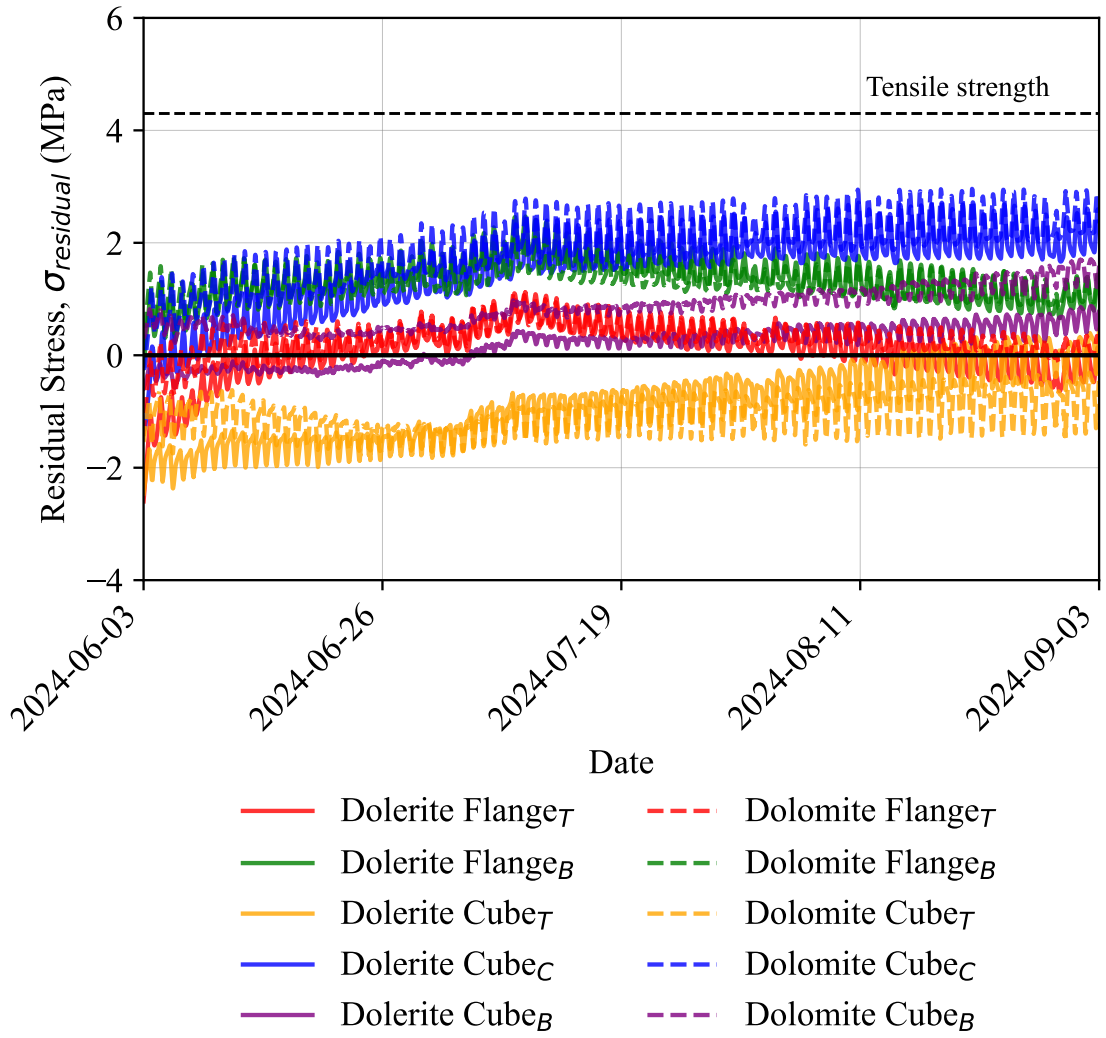

Figure 7.3: Residual stress development over time for (a) Dolerite Flange, (b) Dolomite Flange, (c) Dolerite Cube, (d) Dolomite Cube. Dashed lines represent tensile strength limits.

The residual stresses in the Cube sections approached the mean tensile strength (f_{ctm}) of the mixes (4.2 MPa for Dolerite and 4.0 MPa for Dolomite), but remained below these values at all depths. However, the maximum tensile stresses, particularly at central depth, exceeded the 5^{th} percentile tensile strength ($f_{ctk,0.05}$), which is 2.9 MPa for Dolerite and 2.8 MPa for Dolomite. This suggests a potential risk of restrained cracking developing internally, especially at the central depth where the highest tensile stresses were observed. In contrast, the Flange sections exhibited lower stresses that remained below the characteristic tensile strength for both mixes, reflecting the reduced influence of differential gradients.

Although Figure 7.3 represents stresses calculated using the representative E-values, additional calculations using the EN1992-1-1 (2004a) predicted E_{cm}-values revealed differing trends between the mixes:

- **Dolerite Mix:** The EN1992-1-1 (2004a) E_{cm}-value (42.6 GPa) overestimated the elastic modulus compared to the representative value (31.0 GPa). Consequently, the calculated stresses were higher when using the EN1992-1-1 (2004a) modulus. For example, the central Cube section showed an increase in maximum tensile stress from 2.8 MPa (representative E-value) to 3.9 MPa (EN1992-1-1 (2004a) E_{cm}).
- **Dolomite Mix:** Conversely, the EN1992-1-1 (2004a) E_{cm} value (31.4 GPa) underestimated the elastic modulus compared to the representative value (37.3 GPa). This resulted in lower calculated stresses for Dolomite when using the EN1992-1-1 (2004a) modulus. For example, the central Cube section showed a maximum tensile stress of 2.9 MPa (EN1992-1-1 (2004a) E_{cm}), compared to 3.2 MPa with a representative value of E.

An overestimation of E_{cm} for Dolerite could exaggerate the risk of cracking in the stress predictions, while an underestimation of Dolomite could lead to the failure to identify critical stress conditions, particularly in deeper depth sections where environmental gradients are most pronounced.

The stress results demonstrate the critical role of concrete element thickness, constraint conditions, and elastic modulus in the development of stress within the restricted concrete. The Cube sections exhibited the highest residual stresses, largely due to their differential restraint and environmental exposure. Although the Flange sections showed lower stress levels, their uniform behaviour validates the effectiveness of the shrinkage and thermal models in strain removal. The comparison with EN1992-1-1(2004a) highlights the importance of using realistic material properties to avoid overestimating the cracking potential.

7.2.1 Residual Strains in L-Shape Sections

The same procedure applied to the Cube and Flange sections was followed for the L-Shaped sections. The shrinkage prediction model was adapted to account for the unique geometry of the L-Shape, predicting the global shrinkage of the cross section. The effects of thermal expansion were isolated by temperature compensating each gauge, ensuring that the remaining strains represented the defined residual strains (Equation 7.1). The residual strains were then plotted in Figure 7.4, highlighting the strain distribution in the L-Shaped sections.

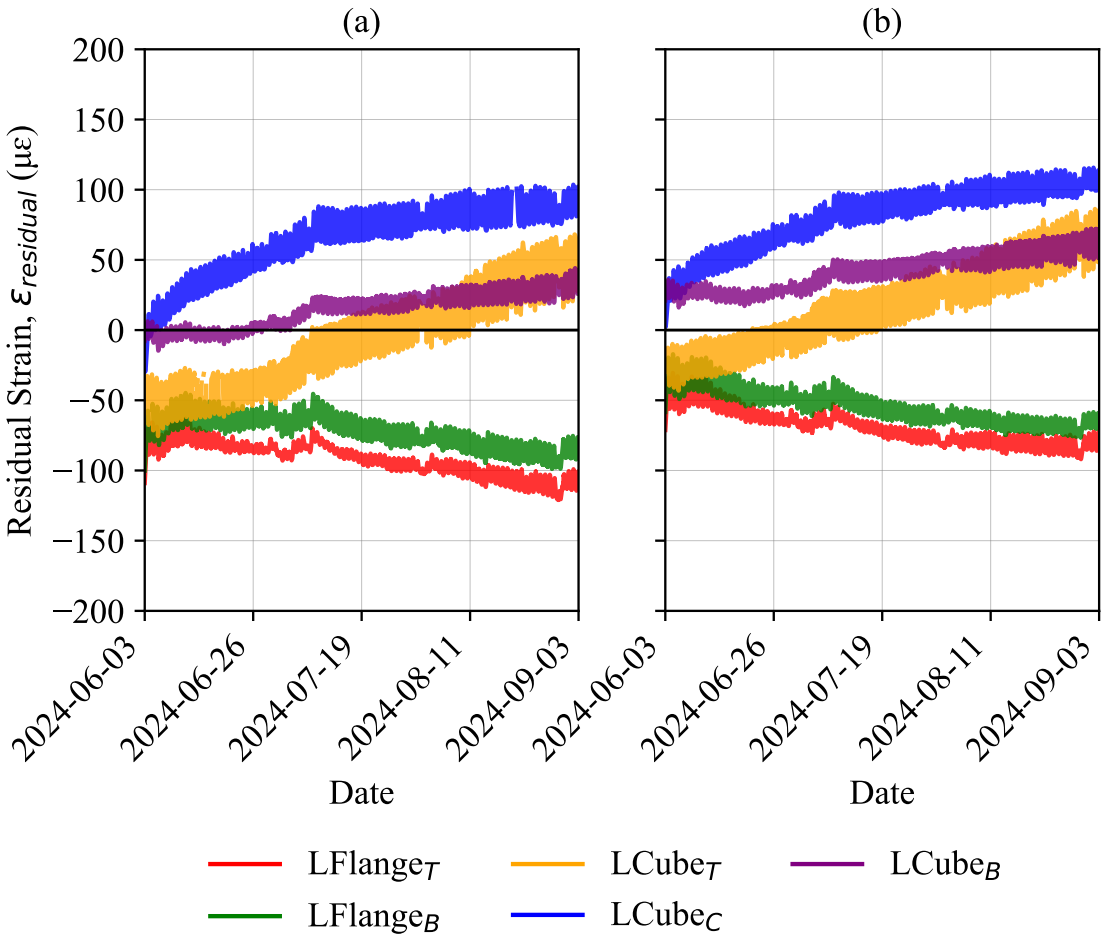

Figure 7.4: Residual strain development over time for (a) Dolerite and (b) Dolomite L-Shaped sections.

Figure Figure 7.4 presents the residual strains for the L-Shaped sections, (a) representing the Dolerite mix and (b) the Dolomite mix. The results show distinct trends between the Flange and Cube portions of the L-Shape:

For both Dolerite and Dolomite mixes, the Flange sections exhibited a gradual decrease in strain over time, indicating that the Flange shrank more than predicted by the shrinkage model. This is consistent with the smaller depth of the Flange, which leads to faster drying. The maximum negative strain observed on the Flange was $-121\,\mu\varepsilon$ for Dolerite and $-92\,\mu\varepsilon$ for Dolomite, both recorded by the bottom sensors. It is worth noting that the Flange was only restrained by the Cube. The top and bottom of the Flange were free from restraint.

The Cube portions for both mixes showed gradual expansion over time, with the top of the Cube experiencing the most substantial development of strain. The bottom of the

Cube exhibited the least strain, reflecting the partial restraint provided by its support condition. The maximum positive strain in the Cube was 103.6 $\mu\varepsilon$ for Dolerite and 115.7 $\mu\varepsilon$ for Dolomite.

A clear trend of contraction in the Flange and expansion in the Cube was observed for both mixes, highlighting the interaction between these two components of the L-Shape. This interaction was most pronounced at the top of the L-Shape, where the Cube exhibited the highest expansion and the Flange the highest contraction. This differential behaviour reflects the combined effects of drying, thermal expansion, and the unique geometry of the L-Shaped cross section.

The L-Shaped Cube was supported at its base, introducing a restraint condition that may restrict movement. To isolate the influence of the Flange on the Cube while factoring out the support conditions, the residual strains measured in a free Cube (without the Flange and with support restraint) were subtracted from the residual strains in the L-Shape Cube (Cube with Flange on supports). The resulting difference isolates the additional effect of the Flange on the Cube (see Equation 7.3). The differential development of strain between the Flange and the Cube is shown in Figure 7.5.

$$\varepsilon_{\text{Flange Effect}} = \varepsilon_{\text{L-Shape Cube}} - \varepsilon_{\text{Free Cube}} \tag{7.3}$$

Where,

$\varepsilon_{\text{Flange Effect}}$ = Strain component attributed to the presence of the Flange
$\varepsilon_{\text{L-Shape Cube}}$ = Measured residual strain in the L-Shaped Cube
$\varepsilon_{\text{Free Cube}}$ = Measured residual strain in the standalone Cube

The strain difference obtained from Equation 7.3 was subsequently converted into stress using Equation 2.11, applying the representative elastic modulus (measured) values from Table 7.1 for each mix. Figure 7.5 presents the difference in stress between the top sensors of the Cube and Flange ($\sigma_{1,\text{Cube}} - \sigma_{1,\text{Flange}}$) for the Dolerite and Dolomite mixes over time. The graph shows an increasing trend in the stress difference, indicating that the Cube experienced higher tensile stresses relative to the Flange as the experiment progressed.

The stress difference first exceeded the tensile strength of 4.3 MPa at different times for the Dolerite and Dolomite sections:

- The Dolomite exceeded the tensile strength almost a month earlier than the Dolomite, on **2024-07-04**.
- Dolomite exceeded the tensile strength later, on **2024-08-06**.

The maximum stress differences were observed as follows:

- For Dolomite, the maximum stress difference reached 6.3 **MPa**, exceeding the tensile strength and indicating a high risk of cracking on the Flange.
- For Dolomite, the maximum stress difference reached 5.3 **MPa**, the highest observed stress.

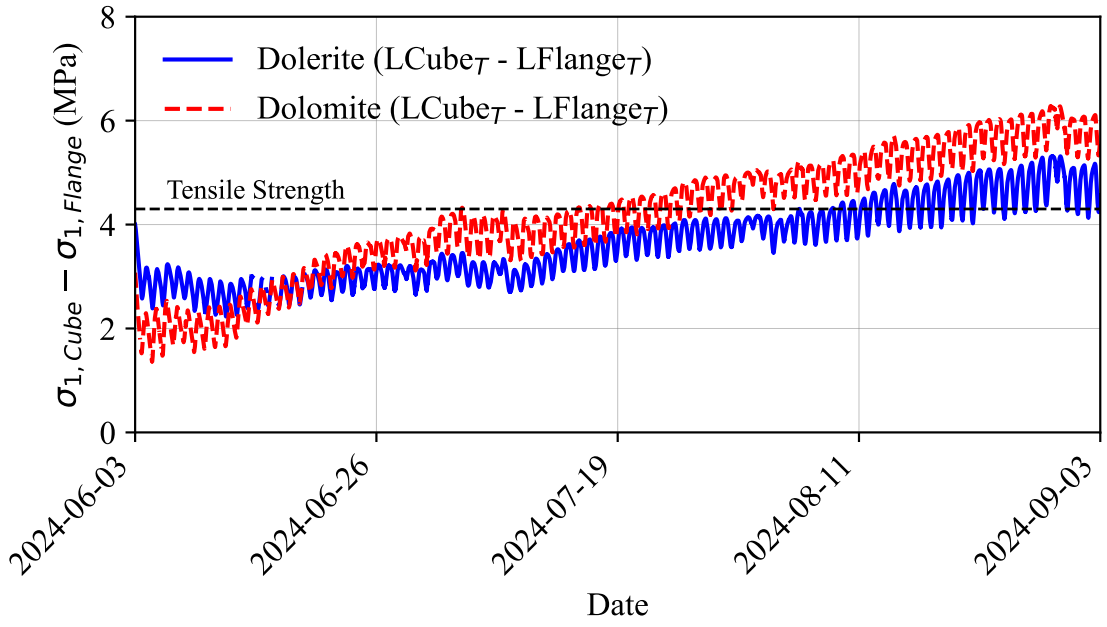

Figure 7.5: Stress development in L-Shaped concrete elements between the top of Cube section and top of Flange section over time.

The results presented in Figure 7.5 demonstrate the progressive development of differential stresses between the Flange and Cube components of the L-Shape for both Dolerite and Dolomite mixes. The following conclusions can be drawn from the observed trends:

1. Increasing Stress Difference Over Time: The stress difference between the Cube and the Flange increased steadily throughout the experiment. This indicates a progressive redistribution of stress within the L-Shaped cross-section, driven by differential strain behaviours caused by the distinct geometries and restraint conditions of the Cube and Flange.

2. Earlier Onset of Critical Stress in Dolomite: The stress difference exceeded the tensile strength (4.3 MPa) earlier for the Dolomite mix (**2024-07-04**) compared to the Dolerite mix (**2024-08-06**). This earlier onset in Dolomite reflects the increased differential behaviour of shrinkage and creep through the depth of the Dolomite section. However, the

Dolerite section seemed to develop strains at a slower rate with differential contraction and expansion less rapid.

3. Maximum Stress Differences: The maximum stress differences observed in the L-Shaped sections for both mixes exceeded the tensile strength, indicating a high risk of cracking due to differential stresses. After three months of outdoor exposure, the two mixes reached maximum stress, with the Dolomite mixture exhibiting a 15% higher differential stress compared to Dolerite.

Although the results highlight the potential for increased stress development in Dolomite due to differential shrinkage and thermal effects, it is important to acknowledge that these findings are based on a single tested sample per mix. As such, while the observed trends are insightful, more tests would be required to confirm whether these differences are statistically significant or consistent across multiple samples.

Despite the stress differences exceeding the tensile strength, no visible cracking was observed on the exposed surfaces of the L-Shaped Cube. This could be attributed to a combination of factors, including but not limited to:

- **Internal Stress Redistribution:** Tensile stresses may have been concentrated internally rather than on the outer surface.
- **Microcracking Below Detection Threshold:** Small-scale internal cracks may have formed within the concrete matrix but remained below the threshold for visual detection.
- **Concrete Toughness and Time-Dependent Relaxation:** The stress development occurred gradually over the three-month period, potentially allowing for stress redistribution through creep.
- **Environmental and Material Variability:** External factors such as moisture variations, temperature fluctuations, and specific material properties may have influenced the response to cracking in ways that were not directly observed.

While the absence of visible cracks suggests that the structural integrity of the L-Shaped Cube was maintained throughout the experimental period, it remains possible that undetected internal cracking or stress redistribution mechanisms played a role in preventing surface crack formation. The increasing stress differences and exceedance of tensile strength in both mixes emphasise the importance of accounting for differential stresses in L-Shaped cross-sections. The combination of Cube expansion and Flange contraction drives stress redistribution, which can lead to cracking under prolonged environmental exposure.

7.3 Thermal Stresses

In this study, thermal properties were determined using both experimental and numerical methods, providing a foundation for comparing temperature distributions and thermal gradients with precision. Key thermal properties were determined as follows:

- **Specific Heat Capacity (c_p)**: The specific heat capacity was experimentally determined in Chapter 3 using calorimetric principles, providing a direct measurement of the heat storage capacity of each concrete mix.
- **Density**: The density of each concrete mix was assumed to be equal to its *theoretical density*, determined based on mix proportions rather than direct measurement.
- **Thermal Conductivity (k) and Solar Absorptivity (a_s)**: Thermal conductivity and solar absorptivity were determined by calibrating a numerical heat transfer model in ABAQUS/CAE (2023), ensuring alignment between measured and predicted temperature distributions.

A summary of the thermal properties is shown in Table 6.1.

Table 7.2: Thermal Properties of Dolerite and Dolomite Mixes

Thermal Property	Dolerite Mix	Dolomite Mix	Defined in Chapter
Density, ρ (kg/m^3)	2500	2451	3
Specific Heat Capacity, c_p ($J/(kg \cdot^\circ C)$)	970	1111	4
Thermal Conductivity Range, k ($W/m/^\circ C$)	2.0	3.6	6
Solar Absorptivity, a_s (Dimensionless)	0.4	0.6	6
Coefficient of Thermal Expansion, α_c ($\mu\varepsilon/^\circ$C)	10.5	12.2	4

Although density could have been measured directly during the experimental campaign, theoretical density values were used in this study to ensure consistency with standard engineering practice. Design engineers typically rely on theoretical values for thermal and mechanical analyses, as these are considered representative for modelling purposes. Additionally, variations in in-situ density were expected to have a negligible impact on the overall thermal response of the concrete elements. Given that the primary objective of this study was to investigate temperature and strain development rather than material property characterisation, the use of theoretical density was deemed appropriate.

The Dolerite mixture showed lower thermal conductivity (2 W/m/°C) and solar absorptivity (0.4) compared to the Dolomite mixture (3.6 W/m/°C and 0.6, respectively). As

discussed in Chapter 2, a lower thermal conductivity in Dolerite indicates slower heat transfer, which can increase thermal gradients within concrete sections during environmental temperature fluctuations. This behaviour makes Dolerite a better thermal insulator, as heat is retained within the structure for longer periods, leading to localised temperature differentials. In contrast, the higher thermal conductivity of the Dolomite mix facilitates faster heat transfer and results in a higher thermal diffusivity, as defined by Equation 2.3. While these properties suggest that Dolomite should exhibit greater fluctuations in effective temperature (T_{eff}), the results in Chapter 5 indicate that aggregate type had only a minimal impact on thermal response within the scope of this study, with section geometry and environmental variability playing a more dominant role.

The variation in effective temperature directly influences the thermal movement of the concrete, which is quantified by thermal strain using the coefficient of thermal expansion (α_c). The Dolerite mixture, with a lower α_c (10.5 $\mu\varepsilon/^{\circ}$C), exhibited reduced thermal movement compared to the Dolomite mixture, which had a higher α_c (12.2 $\mu\varepsilon/^{\circ}$C). This means that for the same temperature fluctuation, Dolomite concrete experienced greater deformation due to its higher sensitivity to thermal changes.

These thermal strains, in turn, generate thermal stresses that are influenced by the modulus of elasticity (E-value). The Dolomite mix, with a higher E-value (34.8 GPa) compared to Dolerite (30.1 GPa), amplifies the resulting stresses for the same level of strain. This characteristic makes Dolomite concrete more susceptible to stress accumulation under temperature-induced movements, increasing the potential for cracking under restricted conditions.

If the thermal response of these concrete elements were restrained, internal stresses could develop, which could lead to cracking. For example, bridge decks or integral abutment structures, restrained thermal expansion during high-temperature fluctuations may induce tensile stresses that exceed the tensile strength of the material, causing surface cracking. In contrast, restrained contraction during cooling periods can result in compressive stresses, which can cause spalling or buckling in thin sections.

To evaluate the thermal response and its implications for structural performance, the effective temperature (T_{eff}) was calculated and used to transform global (uniform) deformations or strains of each concrete element into equivalent stresses. By converting ΔT_{eff} into stress using experimentally determined coefficients of thermal expansion (α_c) and elastic moduli (E), the global stress analysis provided a unified comparison of thermal effects across different shapes, mixes, and boundary conditions. This methodology quantifies the impact of thermal variations on structural performance and highlights critical areas susceptible to thermal stress accumulation.

7.3.1 Calculation Methodology

The effective temperature (T_{eff}) of each section was first zeroed at the start of the equivalent day (00:00) to provide a change in effective temperature, ΔT_{eff}:

$$\Delta T_{eff} = T_{eff} - T_{eff,00:00}. \tag{7.4}$$

Using ΔT_{eff}, the effective thermal strain ($\varepsilon_{\text{thermal}}$) was calculated for each aggregate type using the respective coefficient of thermal expansion, α, as follows:

$$\varepsilon_{\text{thermal}} = \alpha_c \cdot \Delta T_{eff}. \tag{7.5}$$

Finally, thermal stress (σ_{thermal}) was determined by applying Hooke's Law, using the elastic modulus (E) specific to each mix:

$$\sigma_{\text{thermal}} = E \cdot \varepsilon_{\text{thermal}}. \tag{7.6}$$

For the L-shape section, the effective temperature (T_{eff}) was not separated into L-shape Cube and L-shape Flange components, as was done in Chapter 5. Instead, the entire L-shape section was analysed as a single entity. This approach allowed for a unified evaluation of the thermal response of the combined geometry and facilitated comparisons with the Cube and Flange sections.

The variation in ΔT_{eff}, $\varepsilon_{\text{thermal}}$, and σ_{thermal} for Dolerite and Dolomite mixes is shown in Figure 7.6. Dolomite exhibited higher ΔT_{eff} due to its greater thermal conductivity and higher solar absorptivity, as highlighted in Figure 6.9. The increased solar absorptivity (a_s) of Dolomite allowed more heat to be absorbed, while its higher thermal conductivity facilitated efficient heat transfer between sections, resulting in more pronounced temperature changes.

The results presented in Figure 7.6 reflect the changes in temperature and stress experienced by the different shapes and aggregate types during an equivalent winter day, as discussed in Chapter 5. The minimum temperature did not drop substantially due to the microclimatic conditions created by the limited breathing distance under the samples and the reduced wind exposure, which provided thermal buffering (see Chapter 5).

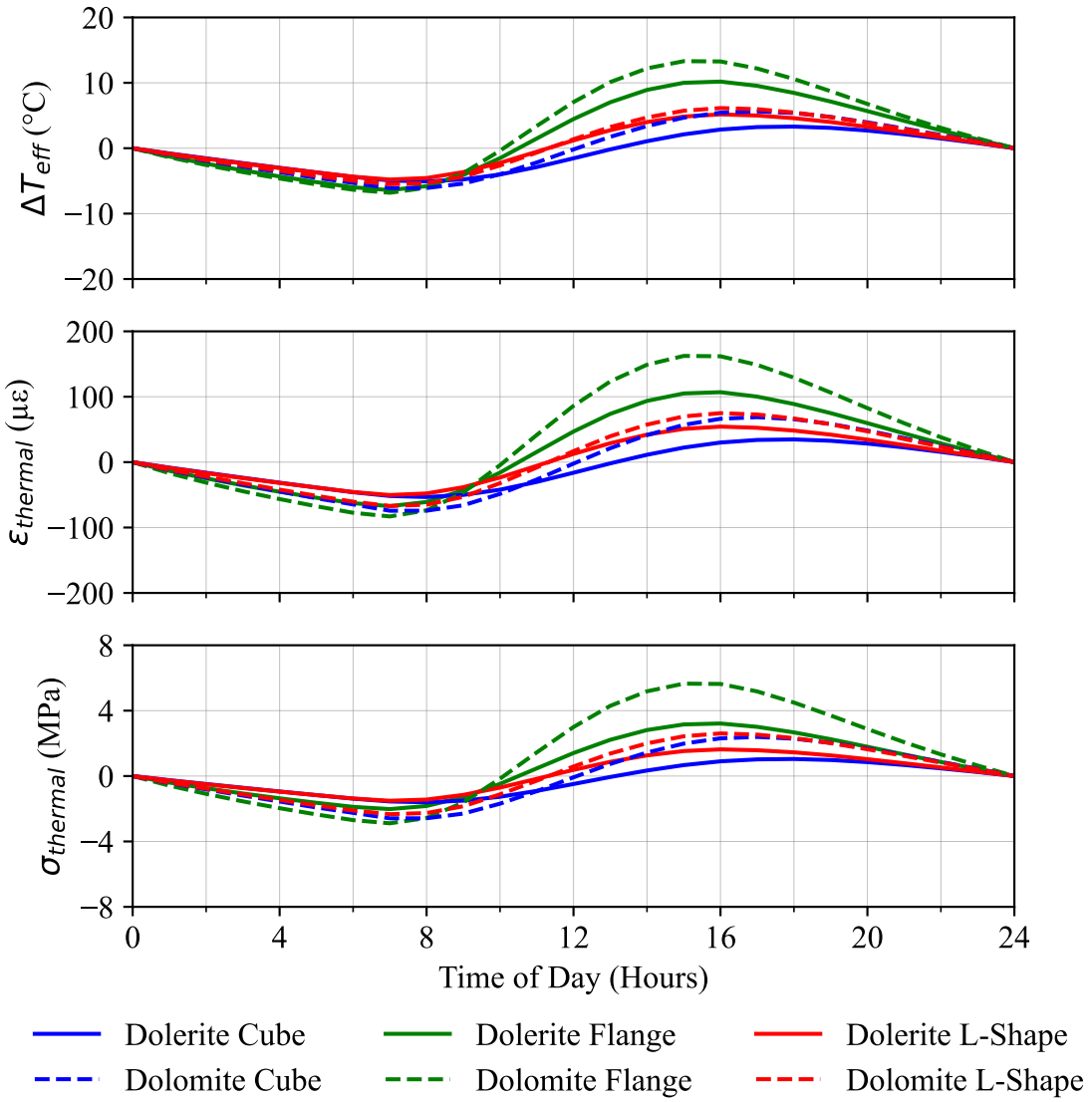

Figure 7.6: Effective temperature (ΔT_{eff}), thermal strain ($\varepsilon_{\text{thermal}}$), and thermal stress ($\sigma_{\text{thermal}}$) for Dolerite and Dolomite mixes over equivelant winters day.

Dolerite exhibited lower temperature changes (ΔT) in all shapes compared to Dolomite, consistent with its lower thermal conductivity and solar absorptivity.

- **Flange:** The Flange section experienced the largest temperature fluctuation in Dolerite, with a maximum ΔT of 10.2°C and a minimum of -6.4°C. These temperature changes resulted in a maximum thermal stress of 3.3MPa and a minimum stress of -2.1 MPa.
- **Cube:** The Cube exhibited a smaller temperature range, with a maximum ΔT of 3.3°C and a minimum of -5.1°C. Consequently, the thermal stress was substantially lower, with a maximum stress of 1.1MPa and a minimum stress of -1.7MPa.

- **L-Shape:** The L-Shape had intermediate temperature changes, with a maximum ΔT of 5.2°C and a minimum of -4.8°C, resulting in a maximum stress of 1.7MPa and a minimum stress of -1.6MPa.

The lower values of ΔT in Dolerite align with its lower thermal conductivity, which theoretically slows heat transfer and moderates temperature fluctuations. However, among all shapes, the Flange section exhibited the largest difference in ΔT, likely due to its smaller depth, making it more sensitive to environmental gradients and resulting in higher stress amplification.

Dolomite showed higher temperature and stress changes in all shapes because of its higher thermal conductivity and solar absorptivity.

- **Flange:** The Flange in Dolomite experienced the largest temperature fluctuations, with a maximum ΔT of 13.3°C and a minimum of -6.8°C, resulting in a maximum thermal stress of 6.1 MPa and a minimum stress of -3.1 MPa. Note: This stress exceeds the tensile cracking strength of 4.3 MPa, indicating a high probability of cracking in the Flange.
- **Cube:** The Cube exhibited smaller temperature changes compared to the Flange, with a maximum ΔT of 5.6°C and a minimum of -6.1°C, leading to a maximum thermal stress of 2.6 MPa and a minimum stress of -2.8 MPa.
- **L-Shape:** The L-Shape experienced moderate temperature fluctuations, with a maximum ΔT of 6.1°C and a minimum of -5.5°C, resulting in a maximum stress of 2.8 MPa and a minimum stress of -2.5 MPa.

The higher ΔT values in Dolomite correlate with Dolomite's thermal conductivity, which theoretically allows for more efficient heat transfer and greater temperature fluctuations. This, combined with the higher coefficient of thermal expansion (α_c) and the elastic modulus (E-value), amplified the thermal stresses observed in Dolomite compared to Dolerite.

Across both mixes, the Flange consistently showed the highest temperature and stress fluctuations, highlighting its sensitivity to environmental conditions because of its shallow geometry and larger surface area-to-volume ratio. The Cube, on the other hand, exhibited the lowest temperature and stress changes, likely due to its greater depth, which provides thermal stability by reducing the extent of environmental gradients.

The L-Shape exhibited intermediate behaviour, effectively combining the characteristics of the Cube and Flange. Although the Flange alone experienced the highest temperature fluctuations and stress levels, its integration with the Cube in the L-Shape geometry moderated these extremes. This interaction likely provided a degree of thermal buffering, where the Cube reduced the extreme thermal effects experienced by the Flange, and

conversely, the Flange mitigated the Cube's stability by introducing its own thermal dynamics.

However, the combined geometry of the L-Shape also introduced complexity in the stress distribution, as internal gradients between the Cube and Flange could lead to localised zones of stress amplification. For example, the interface region between the Cube and Flange may have been subjected to differential stresses due to variations in temperature response and thermal expansion between the two components.

These findings underscore the importance of considering the effects of shape interaction in design, particularly for elements exposed to environmental thermal loading. Inclusion of features such as haunches, which act as transitional elements between sections, could further reduce localised stress concentrations by distributing thermal gradients more evenly. For instance, a haunch between the Cube and Flange could enhance thermal continuity and minimise abrupt changes in temperature and stress, ultimately reducing the likelihood of cracking or other thermal damage (see Figure 7.7). Such design considerations are particularly relevant for bridge decks, integral abutments, and other concrete elements subjected to cyclic thermal loading, where combined geometries often play a critical role in performance.

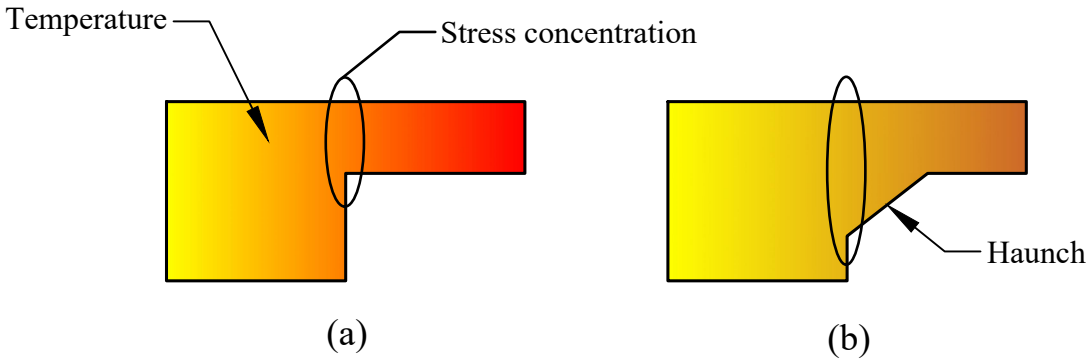

Figure 7.7: Comparison of temperature distribution in an L-shaped section: (a) L-shape showing and (b) L-shape with a haunch.

7.4 Summary

This chapter investigated the development of thermal stresses in concrete elements subjected to environmental loading, focusing on the effects of section geometry and aggregate type. The analysis considered three concrete shapes—Cube, Flange, and L-Shaped

sections—constructed with Dolerite and Dolomite aggregates. The findings provide insight into how these factors influence temperature distributions, thermal expansion, and stress development.

Aggregate type played a role in stress development primarily through its influence on stiffness and thermal expansion. The Dolerite mix, with its lower thermal conductivity and solar absorptivity, exhibited slightly reduced effective temperature fluctuations, but its higher stiffness resulted in increased restraint, contributing to higher stress concentrations. Conversely, the Dolomite mix, with its higher thermal conductivity and solar absorptivity, experienced slightly greater temperature variations. However, section geometry had a more pronounced effect on temperature fluctuations. The increased thermal expansion of the Dolomite mix led to larger thermal strains and, subsequently, higher thermal stresses. These findings highlight the interplay between material properties and stress development, with aggregate selection influencing the magnitude of stresses, while section geometry governed their distribution.

Additionally, the study revealed interactions between shape and geometry in thermal behaviour. The L-Shape section, which combines Cube and Flange geometries, moderated the extreme thermal responses observed in the individual shapes but introduced complex thermal gradients. The inclusion of a haunch or transition between the Cube and Flange is recommended to reduce localised temperature differentials at the junction, minimising stress concentrations and mitigating the risk of cracking.

The study also examined the applicability of the EN1992-1-1 (2004a) standard in predicting stress development for South African aggregates. The adjusted elastic modulus (E_{cm}) values, which incorporate aggregate adjustment factors, substantially influenced the calculated thermal stresses. For the Dolerite mix, the adjusted E_{cm} overestimated stiffness, leading to an overprediction of stress and an exaggerated risk of cracking. In contrast, for the Dolomite mix, the adjusted E_{cm} underestimated stiffness, resulting in an underestimation of stress and a failure to accurately identify critical conditions. These findings underscore the need for further refinement of aggregate adjustment factors to improve the accuracy of stress predictions in local conditions.

The calibrated physics-based model provided accurate thermal predictions for unreinforced concrete elements; however, future research should explore its applicability under additional factors such as mechanical loading and reinforcement. Internal restraint from embedded steel would reduce free thermal and shrinkage strains, leading to increased internal stresses, which may require refinements to the model. A hybrid approach integrating physics-based modelling with data-driven techniques could further enhance predictive accuracy by incorporating real-time experimental data and adaptive parameter adjustments. Investigating reinforcement interactions would provide a more comprehensive understanding of stress development in restrained concrete elements.

8 Conclusions and Recommendations

This study provides a comprehensive investigation of the thermal and mechanical behaviour of concrete elements under environmental loading, with a specific focus on South African aggregates and climatic conditions. Through a combination of experimental and numerical approaches, the research addressed the objectives outlined in Chapter 1, exploring the interaction between material properties, environmental factors, and geometric influences on structural performance. The findings offer critical insights into the applicability of the EN1992-1-1 (2004a) standard and its relevance to local conditions.

Experimental measurements of restricted strains in the Cube, Flange, and L-Shaped sections provide a detailed perspective on the impact of concrete's Coefficient of Thermal Expansion (CTE) under environmental loading. These insights contribute to the refinement of design practices for thermally stressed concrete structures, addressing critical challenges such as internal stress development, cracking, and long-term durability.

By calibrating the solar model with measured data, the FEM simulations effectively linked experimental observations with theoretical predictions of heat transfer mechanisms. This approach highlights the versatility of FEM to coupling environmental heat transfer processes, such as conduction, convection, and radiation, with structural responses. The integration of solar radiation theory further enhances the model's ability to analyse the impact of climatic factors on temperature gradients and thermal distributions in concrete elements. This combined experimental and numerical framework validates FEM as a robust tool to investigate the thermal behaviour of concrete structures exposed to environmental conditions.

Key Findings and Contributions

- The study revealed differences in the thermal properties of Dolerite and Dolomite aggregates; however, these differences resulted in only slight variations in effective temperature. Dolerite showed marginally lower effective temperature fluctuations but steeper internal gradients due to its lower thermal conductivity. Conversely, Dolomite, with its higher thermal conductivity and solar absorptivity, showed slightly larger effective temperature variations. While these findings highlight the

role of aggregate-specific thermal behaviour, the overall temperature differences between the two mixes were small. Section geometry had a more dominant influence on temperature distributions.

- Thermal stresses were primarily governed by the interaction between temperature variations, the thermal expansion coefficient (α_c), and the modulus of elasticity (E). Dolomite, with its higher the CTE and E-value, experienced greater stress development, increasing the potential for cracking. In contrast, Dolerite, despite exhibiting higher shrinkage, showed more controlled thermal deformation due to its lower the CTE and E-value. These findings highlight the need for tailored design approaches that consider both material properties and structural geometry to optimise performance under environmental loading.

- The study highlights the limitations of applying EN1992-1-1 (2004a) directly to South African aggregates without calibration, particularly aggregate-specific adjustments to the E-value. The standard recommended increase of 20% for basalt aggregates substantially overestimated stiffness, while the reduction of 10% for limestone aggregates underestimated stiffness. These discrepancies could result in overly conservative or unsafe designs by misrepresenting thermal strains and structural deformations. The findings suggest that unadjusted E_{cm} values align more closely with measured data for Dolerite and Dolomite mixes and may provide a more reliable basis for design in the absence of locally calibrated adjustment factors. Additionally, the validated shrinkage prediction model provided reliable results for most shapes but highlighted areas where refinement is needed for complex geometries.

- **Numerical Modelling and Validation**: The finite element model, calibrated with effective temperature data, successfully replicated the thermal behaviour of concrete elements over a three-month experimental period. Sensitivity analyses demonstrated the substantial influence of thermal conductivity (k) and solar absorptivity (a_s) on effective temperatures and gradients. This robust validation confirmed the reliability of the model and its applicability to different types of aggregates and environmental conditions. The calibration process revealed the interplay between material properties and environmental exposure, paving the way for broader application in other climatic regions and geometries.

Broader Implications

The findings of this study extend beyond the immediate experimental results, offering insights for the design and performance of concrete structures in South Africa and other regions with similar climatic and material challenges. By addressing aggregate-specific properties, environmental factors, and geometric influences, this research bridges the gap

between international design standards and local conditions. The study emphasises the need to incorporate material-specific behaviours into structural design, particularly thermal properties and shrinkage characteristics, to ensure resilience, durability, and cost-effectiveness.

Importantly, the results highlight the need for standardised testing methods to accurately characterise the thermal properties of South African aggregates. Developing reliable and accessible tests for parameters such as thermal conductivity, specific heat capacity, and coefficient of thermal expansion will be essential to produce consistent data that can inform both research and practice. These standardised tests would support the regional calibration of design codes and enable engineers to make more informed decisions about material selection and structural performance under environmental load.

Recommendations

Based on the results, several recommendations are proposed for design practices and future research:

- Incorporate calibrated material properties, such as shrinkage coefficients and coefficient of thermal expansion values, into the prediction models for South African aggregates to ensure accurate thermal strain predictions.
- Update *EN 1992-1-1* assumptions for E-values and thermal properties to account for regional variability in aggregate types and environmental conditions. This would involve refining the standard's aggregate-specific adjustment factors and thermal property models to better reflect the performance of South African materials. Such updates would improve the applicability of the standard to local contexts, ensuring safer and more accurate structural designs.
- Recognise the amplified effects of high thermal variations, the CTE, and E values in concrete mixes, particularly for restricted geometries. This combination presents a higher risk of thermal cracking and stress development.
- Develop standardised testing protocols to determine key thermal properties of aggregates, ensuring consistency and reliability in the construction industry and research efforts.
- Explore advanced numerical methods to account for non-linear temperature distributions and their impact on localised strain behaviour, especially in complex geometries like L-Shapes.

Future Directions

Building on the foundation of this study, future research could expand into:

- Investigating the effects of seasonal variations, such as summer exposure, to understand the full range of thermal responses and their implications for long-term performance.
- Integrating creep behaviour and long-term deformation mechanisms into numerical models for more comprehensive predictions of structural performance.
- Applying findings to larger-scale elements, such as bridge decks and retaining walls, to evaluate the broader implications of material and geometric variability in real-world structures.
- Further refinement of shrinkage prediction models to account for complex geometries and their interaction with environmental conditions.
- Developing and validating standard testing methods for thermal properties, creating a robust database of material-specific data for design codes and numerical modelling.
- Investigate the incorporation of haunches at transitions between Cube and Flange geometries in complex elements like L-Shapes. A gradual change in geometry may help distribute thermal stresses more evenly and improve structural durability under environmental loading.
- Future research should incorporate a larger sample size to enhance the statistical robustness of the findings within this study.
- Study the impact of environmental conditions on concrete structures subjected to service loads, either through field monitoring of real structures or controlled experiments with simulated loading.
- Explore machine learning and other computational techniques to complement physics-based models for predicting thermal response, particularly for complex geometries. A hybrid approach could improve predictive accuracy by integrating real-time data and refining model parameters.

A Material Property Test Results

This appendix presents the results of the material property tests conducted on the Dolerite and Dolomite concrete mixes used in this study. The tests include cube compressive strength, splitting tensile strength, modulus of elasticity (E-value), and density measurements. These properties were determined from laboratory testing of both dry-cured and water-cured specimens, which were prepared under controlled curing conditions. The results are summarised in Table A.1, which provides a comprehensive overview of the material properties at various curing ages:

- **Compressive Strength:** Measurements were taken at 1, 7, 14, 28, and 56 days under dry curing conditions, with additional 28-day results for water-cured specimens.
- **Splitting Tensile Strength:** Tests were conducted at 1, 7, 14, 28, and 56 days, comparing the development of tensile capacity over time.
- **Modulus of Elasticity (E-value):** E-values were determined at different curing ages, providing insight into the stiffness characteristics of the concrete mixes.
- **Density:** The density of 100mm cubes was measured at different curing ages to assess variations in material composition and porosity.

Table A.1: Material Property Test Results for Dolerite and Dolomite Mixes

Mix Type	Day	Curing Method	Compressive Strength (MPa)					
			1	2	3	4	5	6
Dolerite	1	Dry	16.3	17.0	16.5	17.8	-	-
	7	Dry	42.7	38.0	39.4	41.4	-	-
	14	Dry	44.8	47.2	43.1	45.4	-	-
	28	Dry	56.0	53.7	53.9	52.7	53.4	51.2
	56	Dry	57.0	57.0	57.0	-	-	-
	28	Water	51.9	52.9	56.0	56.9	56.7	54.5
Dolomite	1	Dry	17.8	17.8	15.8	15.4	-	-
	7	Dry	38.5	37.5	34.0	32.5	-	-
	14	Dry	43.1	43.2	39.0	39.7	-	-
	28	Dry	50.8	51.9	52.3	48.0	53.6	48.9
	56	Dry	49.5	51.4	49.0	-	-	-
	28	Water	52.4	55.5	50.2	48.1	55.0	51.5

Continued on next page

Continued from previous page

Mix Type	Day	Curing Method	Density (kg/m^3))					
			1	**2**	**3**	**4**	**5**	**6**
Dolerite	1	Dry	2474	2497	2481	2481	-	-
	7	Dry	2486	2498	2470	2497	-	-
	14	Dry	2487	2477	2478	2472	-	-
	28	Dry	2440	2437	2371	2442	2438	2419
	56	Dry	2427	2440	2411	-	-	-
	28	Water	2495	2419	2484	2513	2487	2490
Dolomite	1	Dry	2419	2395	2425	2439	-	-
	7	Dry	2415	2418	2413	2438	-	-
	14	Dry	2415	2418	2413	2438	-	-
	28	Dry	2435	2401	2393	2354	2387	2397
	56	Dry	2428	2406	2426	-	-	-
	28	Water	2420	2424	2430	2439	2439	2439

Mix Type	Day	Curing Method	Splitting Tensile Strength (MPa)				
			1	2	3	4	5
Dolerite	1	Dry	1.9	2.0	1.9	2.1	-
	7	Dry	3.2	3.5	3.2	3.3	-
	14	Dry	3.2	3.8	3.4	3.6	-
	28	Dry	4.2	4.6	3.9	4.1	4.2
	56	Dry	3.9	4.1	-	-	-
	28	Water	4.0	4.1	4.4	4.2	4.2
Dolomite	1	Dry	2.2	2.3	2.3	2.1	-
	7	Dry	3.4	3.3	2.9	3.4	-
	14	Dry	3.2	3.7	3.3	3.7	-
	28	Dry	4.6	4.5	4.1	4.1	4.3
	56	Dry	4.3	4.0	-	-	-
	28	Water	4.1	4.3	4.2	4.6	4.2

Mix Type	Day	Curing Method	E-Value (GPa)		
			1	2	3
Dolerite	1	Dry	20.5	22.5	–
	7	Dry	27.4	28.6	–
	14	Dry	28.7	29.2	–
	28	Dry	30.3	29.8	30.1

Continued on next page

Continued from previous page

	56	Dry	28.4	28.9	–
	28	Water	30.3	31.6	31.0
	1	Dry	23.9	23.8	–
	7	Dry	30.0	33.9	–
	14	Dry	34.3	35.0	–
Dolomite	28	Dry	35.4	34.3	34.8
	56	Dry	33.7	33.8	–
	28	Water	36.7	37.9	37.3

References

Abid, S. R., N. Tayşi, and M. Özakça (Mar. 2016). "Experimental analysis of temperature gradients in concrete box-girders". In: *Construction and Building Materials* 106, pp. 523–532.

Abid, S. R., N. Tayşi, M. Özakça, J. Xue, and B. Briseghella (Oct. 2021). "Finite element thermo-mechanical analysis of concrete box-girders". In: *Structures* 33, pp. 2424–2444.

Abuhmida, M. (2023). "Concrete Subsurface Crack Detection Using Thermal Imaging in a Deep Neural Network". In: *Ijccs (Indonesian Journal of Computing and Cybernetics Systems)* 17.2.

ACI Committee 209 (2002). *ACI 209R-92: Prediction of Creep, Shrinkage, and Temperature Effects in Concrete Structures*. American Concrete Institute, Detroit Michigan.

Adesina, J. A., K. R. Kumar, and V. Sivakumar (2016). "Aerosol-Cloud-Precipitation Interactions Over Major Cities in South Africa: Impact on Regional Environment and Climate Change". In: *Aerosol and Air Quality Research* 16.1, pp. 195–211.

Afrimat (2022). *Regional Stone Supply*. Afrimat.

AfriSam (South Africa) (Pty) Ltd (2017). *Afrisam Technical Reference*. 9.0. Weltevredenpark, South Africa: Promise.

Albarwary, I. H., Z. N. Aldoski, and L. K. Askar (2017). "Effect of Aggregate Maximum Size Upon Compressive Strength of Concrete". In: *The Journal of the University of Duhok* 20.1, pp. 790–797.

Alexander, M. and S. Mindess (Apr. 2014). *Aggregates in Concrete*. London: CRC Press.

Alhussainy, F., H. A. Hasan, M. N. Sheikh, and M. N. Hadi (2019). "A New Method for Direct Tensile Testing of Concrete". In: *Journal of Testing and Evaluation* 47.2, pp. 704–718.

American Association of State Highway and Transportation Officials (AASHTO) (2007). *Standard specification for highway bridges*. Washington, D.C.: AASHTO.

American Society of Heating, Refrigerating and AirConditioning Engineers (ASHRAE) (2001). *2001 ASHRAE handbook: fundamentals*. eng. SI ed. OCLC: 49408272. American Society of Heating, Refrigerating and AirConditioning Engineers, Atlanta, Georgia, USA.

Ångström, A. (Aug. 1929). "On the Atmospheric Transmission of Sun Radiation and on Dust in the Air". fr. In: *Geografiska Annaler* 11.2, pp. 156–166.

Aniskin, N. A. and T.-C. Nguyen (2018). "The Thermal Stress of Roller-Compacted Concrete Dams During Construction". In: *Matec Web of Conferences* 196, p. 04059.

ASTM Standard (2022). *C469/C469M -22: Static Modulus of Elasticity and Poisson's Ratio of Concrete in Compression*. ASTM International, United Sates.

Bahnick, R., M. Joshaghani, O. Ghasemi-Fare, and Z. Sun (2020). "Exploring the Curing Condition and Age Effect on Thermal Conductivity of Concrete". In: *E3s Web of Conferences* 205, p. 06012.

Bazant, Z. P. and S. Baweja (Aug. 1995a). "Justification and refinements of model B3 for concrete creep and shrinkage 1. statistics and sensitivity". In: *Materials and Structures* 28.7, pp. 415–430.

Bazant, Z. P. and S. Baweja (Oct. 1995b). "Justification and refinements of model B3 for concrete creep and shrinkage 2. Updating and theoretical basis". In: *Materials and Structures* 28.8, pp. 488–495.

Benoudjafer, I., I. Benoudjafer, and M. Tomoaia-Cotişel (2021). "The Effect of Granulate Porosity on the Evolution of the Thermal Conductivity of an Resin Concrete Exposed to High Temperatures". In: *Revista Romana De Inginerie Civila/Romanian Journal of Civil Engineering* 12.2, pp. 253–262.

Bentz, D., M. Peltz, A. Durán-Herrera, P. Valdez, and C. Juárez (Jan. 2011). "Thermal properties of high-volume fly ash mortars and concretes". en. In: *Journal of Building Physics* 34.3. Publisher: SAGE Publications Ltd STM, pp. 263–275.

Branco, F. A. and P. A. Mendes (Aug. 1993). "Thermal Actions for Concrete Bridge Design". EN. In: *Journal of Structural Engineering* 119.8. Publisher: American Society of Civil Engineers, pp. 2313–2331.

Brink, M. (2024). "Thermal Effects on Concrete Properties". Doctor of Philosophy. Pretoria: University of Pretoria.

Brown, M. D., G. Sellers, K. Folliard, and D. Fowler (June 2001). "Restrained Shrinkage Cracking of Concrete Bridge Decks: State-of-the-art Review". In.

Cai, C., S. Huang, X. He, T. Zhou, and Y. Zou (Jan. 2022). "Investigation of concrete box girder positive temperature gradient patterns considering different climatic regions". In: *Structures* 35, pp. 591–607.

Campbell Scientific, Inc. (2025). *CR6 Measurement and Control Data Logger: Operator's Manual*. Tech. rep. Logan, UT.

Cao, V. D., S. Pilehvar, C. Salas-Bringas, et al. (2017). "Microencapsulated Phase Change Materials for Enhancing the Thermal Performance of Portland Cement Concrete and Geopolymer Concrete for Passive Building Applications". In: *Energy Conversion and Management* 133, pp. 56–66.

Cengel, Y. (2004). *Heat Transfer: A Practical Approach*. en. McGraw-Hill Education.

Chen, B.-L., L. Rockett, and R. Mallick (Jan. 2008). "A laboratory investigation of temperature profiles and thermal properties of asphalt pavements with different subsurface layers". In: *Asphalt Paving Technology: Association of Asphalt Paving Technologists-Proceedings of the Technical Sessions* 77, pp. 327–359.

Chung, S.-Y., M. A. Elrahman, and D. Stephan (2017). "Effect of Different Gradings of Lightweight Aggregates on the Properties of Concrete". In: *Applied Sciences* 7.6, p. 585.

Chung, Y. and H.-C. Shin (2011). "Characterization of the Coefficient of Thermal Expansion and Its Effect on the Performance of Portland Cement Concrete Pavements". In: *Canadian Journal of Civil Engineering* 38.2, pp. 175–183.

Dassault Systèmes (2023). *ABAQUS/CAE*.

Dassault Systemes (2023). *ABAQUS/Standard User's Manual, Version 6.9*. Dassault Systemes Simulia Corp.

Davis, D. and M. Alexander (1994). *Properties of aggregates in concrete. Part 1 and Part 2*. 2nd Ed. Sandton: Hippo Quarries.

Demirtürk, D., H. Öztürk, and M. Güler (Oct. 2023). *Using Calorimetry-Based Method for Measuring Specific Heat Capacity of Asphalt Concrete*.

Deng, J., C. W. Liu, and J. Liu (2012). "Effect of Dynamic Loading on Mechanical Properties of Concrete". In: *Advanced Materials Research* 568, pp. 147–153.

Dincer, I. and D. Erdemir (Jan. 2021). "Chapter 4 - System Analysis". In: *Heat Storage Systems for Buildings*. Ed. by I. Dincer and D. Erdemir. Elsevier, pp. 115–178.

Ding, S., Z. H. Shui, T. Pan, and W. Chen (2014). "Study on Preparation of Low-Thermal Expansion Coefficient Concrete With Fly Ash". In: *Key Engineering Materials* 599, pp. 89–92.

Duffie, J. A., W. A. Beckman, and N. Blair (Mar. 2020). *Solar Engineering of Thermal Processes, Photovoltaics and Wind*. English. 5th edition. Hoboken, New Jersey: Wiley.

Dunić, V., N. Busarac, V. Slavkovic, et al. (2015). "A Thermo-Mechanically Coupled Finite Strain Model Considering Inelastic Heat Generation". In: *Continuum Mechanics and Thermodynamics* 28.4, pp. 993–1007.

Eck, T. F., B. N. Holben, D. E. Ward, et al. (2003). "Variability of Biomass Burning Aerosol Optical Characteristics in Southern Africa During the SAFARI 2000 Dry Season Campaign and a Comparison of Single Scattering Albedo Estimates From Radiometric Measurements". In: *Journal of Geophysical Research Atmospheres* 108.D13.

Elbadry, M. M. and A. Ghali (Oct. 1983). "Temperature Variations in Concrete Bridges". EN. In: *Journal of Structural Engineering* 109.10. Publisher: American Society of Civil Engineers, pp. 2355–2374.

Elwakeel, A., M. K. Shehzad, K. E. Khoury, et al. (2022). "Assessment of Cracking Performance in Edge Restrained RC Walls". In: *Structural Concrete* 23.3, pp. 1333–1352.

Emerson, M. (1973). "The Calculation of The Distribution of Temperature in Bridges". In.

Emerson, M. (1976). *Extreme Values of Bridge Temperatures for Design Purposes*. en. Transport and Road Research Laboratory.

Erbs, D. G., S. A. Klein, and J. A. Duffie (Jan. 1982). "Estimation of the diffuse radiation fraction for hourly, daily and monthly-average global radiation". In: *Solar Energy* 28.4, pp. 293–302.

Etxeberria, M., A. Gonzalez-Corominas, and P. G. Pardo (2016). "Influence of Seawater and Blast Furnace Cement Employment on Recycled Aggregate Concretes' Properties". In: *Construction and Building Materials* 115, pp. 496–505.

European Committee for Standardization (2004a). *EN 1992-1-1: Eurocode 2: Design of Concrete Structures – Part 1-1: General Rules and Rules for Buildings*. Brussels: European Committee for Standardization.

European Committee for Standardization (2004b). *EN-1991-1-1: Eurocode 1, Actions on Structures—Part 1-1: General Actions —Densities, Self-Weight, Imposed Loads for Buildings*. Brussels: European Committee for Standardization.

European Committee for Standardization (2004c). *EN-1991-1-2: Eurocode 2: Design of concrete structures - Part 1-2: General rules - Structural fire design*. Brussels: European Committee for Standardization.

Feng, Z., L. Jinyi, and G. Lei (June 2022). "Experimental investigation of temperature gradients in a three-cell concrete box-girder". In: *Construction and Building Materials* 335, p. 127413.

Flitta, I., T. Hatzenbichler, and B. Buchmayr (2013). "Investigation and Comparison of Heat Transfers Analysis Used in Commercial FEM for Metal Forming". In: *Materials Science Forum* 773-774, pp. 176–185.

Foteinaki, K., R. Li, A. Heller, M. H. Christensen, and C. Rode (2019). "Dynamic Thermal Response of Low-Energy Residential Buildings Based on in-Wall Measurements". In: *E3s Web of Conferences* 111, p. 04002.

Fourier, J. B. J. (1878). *The analytical theory of heat*. eng. Cambridge [Eng.] : University Press.

Fu, W. Q. (Jan. 2006). "Radiative Transfer". In: *Atmospheric Science (Second Edition)*. Ed. by J. M. Wallace and P. V. Hobbs. San Diego: Academic Press, pp. 113–152.

Gao, H. and G. Wei (2014). "Stress Intensity Factor for Interface Cracks in Bimaterials Using Complex Variable Meshless Manifold Method". In: *Mathematical Problems in Engineering* 2014, pp. 1–8.

Gao, Y., X. Ren, J. Zhang, et al. (2020). "Proposed Constitutive Law of Uniaxial Compression for Concrete Under Deterioration Effects". In: *Materials* 13.9, p. 2048.

Gardner, N. and M. Lockman (2001). "Design Provisions for Drying Shrinkage and Creep of Normal Strength Concrete". In: *ACI Materials Journal* 98, pp. 159–167.

Ge, Z., K. Wang, P. Sandberg, and J. Ruiz (Oct. 2009). "Characterization and Performance Prediction of Cement-Based Materials Using a Simple Isothermal Calorimeter". In: *Journal of Advanced Concrete Technology - J ADV CONCR TECHNOL* 7, pp. 355–366.

Ghali, A., R. Favre, and M. Elbadry (Jan. 2017). *Concrete Structures: Stresses and Deformations: Analysis and Design for Serviceability, Third Edition*. 3rd ed. London: CRC Press.

Ghannam, M. (2019). "Proposed Models for Concrete Thermal Expansion With Different Aggregate Types and Saturation Conditions". In: *Sn Applied Sciences* 1.5.

Graphtec Corporation (2010). *GL820 Midi Logger User's Manual*. Tech. rep. Yokohama, Japan.

Gribniak, V., G. Kaklauskas, and D. Bacinskas (Dec. 2007). "State-Of-Art Review of Shrinkage Effect on Cracking and Deformations of Concrete Bridge Elements". In: *The Baltic Journal of Road and Bridge Engineering* II, pp. 183–193.

Gribniak, V., G. Kaklauskas, and D. Bacinskas (Mar. 2008). "Shrinkage in reinforced concrete structures: A computational aspect". In: *Journal of Civil Engineering and Management* 14, pp. 49–60.

Gribniak, V., G. Kaklauskas, D. Bacinskas, W.-P. Sung, A. Sokolov, and D. Ulbinas (June 2011). "Investigation of Shrinkage of Concrete Mixtures Used for Bridge Construction in Lithuania". en. In: *The Baltic Journal of Road and Bridge Engineering* 6.2, pp. 77–83.

Gueymard, C. A. (Mar. 2009). "Direct and indirect uncertainties in the prediction of tilted irradiance for solar engineering applications". In: *Solar Energy* 83.3, pp. 432–444.

Gui, L., M. T. Hasholt, and O. M. Jensen (2020). "Environmental Assessment of Frost-Resistant Concrete With Superabsorbent Polymers". In: *Nordic Concrete Research* 63.2, pp. 43–62.

Habib, A., B. Chen, B. Khalid, et al. (2019). "Estimation and Inter-Comparison of Dust Aerosols Based on MODIS, MISR and AERONET Retrievals Over Asian Desert Regions". In: *Journal of Environmental Sciences* 76, pp. 154–166.

Hall, K. and S. Tayabji (Oct. 2011). "Coefficient of Thermal Expansion in Concrete Pavement Design". In.

Hersey, S. P., R. M. Garland, E. Crosbie, et al. (2015). "An Overview of Regional and Local Characteristics of Aerosols in South Africa Using Satellite, Ground, and Modeling Data". In: *Atmospheric Chemistry and Physics* 15.8, pp. 4259–4278.

Historical weather data for Pretoria,South Africa | Visual Crossing (2024).

Holben, B. N., T. F. Eck, I. Slutsker, et al. (Oct. 1998). "AERONET—A Federated Instrument Network and Data Archive for Aerosol Characterization". In: *Remote Sensing of Environment* 66.1, pp. 1–16.

Hołowaty, J. (2015). "Creep and Shrinkage of Concrete in Eurocode 2 and Polish Bridge Standards—Necessity for Implementation". In: *Journal of Civil Engineering and Architecture* 9.4.

Hossain, M. M., S. Al-Deen, K. Hassan, S. K. Shill, A. Kader, and W. D. Hutchison (2021). "Mechanical and Thermal Properties of Hybrid Fibre-Reinforced Concrete Exposed to Recurrent High Temperature and Aviation Oil". In: *Materials* 14.11, p. 2725.

Hou, L., H. M. Cheng, J. Y. Li, B. D. Shao, and J. Hou (2013). "Comparison of Surface Heat-Transfer Coefficient of GCr15 Steel Quenched by Clear Water and Nitrogen-Spray Water". In: *Applied Mechanics and Materials* 444-445, pp. 1290–1294.

Hu, J., K. Wang, and Z. Ge (2012). "Study of Concrete Thermal Properties for Sustainable Pavement Design". In: *Journal of Sustainable Cement-Based Materials* 1.3, pp. 126–137.

Hussein, H. H. and O. S. Saeed (2016). "Effect of Additive of Expanded Polystyrene and Perlite on Some Mechanical Properties and Thermal Conductivity for Mass Concrete". In: *Tikrit Journal of Engineering Sciences* 23.1, pp. 78–86.

Hwang, E., G.-Y. Kim, K.-M. Koo, et al. (2021). "Compressive Creep and Shrinkage of High-Strength Concrete Based on Limestone Coarse Aggregate Applied to High-Rise Buildings". In: *Materials* 14.17, p. 5026.

Incropera, F., D. DeWitt, T. Bergman, and A. Lavine (Jan. 2007). *Fundamentals of Heat and Mass Transfer*.

Ivanov, O. and S. Thelandersson (Oct. 2011). "Estimating extreme values of thermal gradients in concrete structures". In: *Materials and Structures/Materiaux et Constructions* 44, pp. 1491–1500.

Jędrzejewska, A., M. Zych, F. Kanavaris, et al. (2023). "Standardized Models for Cracking Due to Restraint of Imposed Strains—The State of the Art". In: *Structural Concrete* 24.4, pp. 5388–5405.

Jiang, Y., E. Li, X. Zhang, Q. Wu, and Y. Yap (2018). "Superposition Method for the Simulation of Heat Transfer". In: *International Journal of Heat and Mass Transfer* 120, pp. 914–922.

Jin, H., G. Wang, and Z. Chen (2021). "Temperature Control Technology for Construction of Jinsha River Bridge". In: *Advances in Civil Engineering* 2021.1.

Jurowski, K. and S. Grzeszczyk (2018). "Influence of Selected Factors on the Relationship Between the Dynamic Elastic Modulus and Compressive Strength of Concrete". In: *Materials* 11.4, p. 477.

Kalogirou, S. A. (Jan. 2009). "Chapter two - Environmental Characteristics". In: *Solar Energy Engineering*. Ed. by S. A. Kalogirou. Boston: Academic Press, pp. 49–762.

Kang, X., H. Lei, and Z. Xia (Mar. 2020). "A comparative study of modified fall cone method and semi-adiabatic calorimetry for measurement of setting time of cement based materials". In: *Construction and Building Materials* 248.

Kehlbeck, F. (Jan. 1975). *Einfluss der Sonnenstrahlung bei Brückenbauwerken*. German. Düsseldorf: Werner.

Khalifa, M., M. A. Youssef, and M. M. A. Alhadid (2020). "Heat of Hydration Stresses in Stainless-Steel-Reinforced-Concrete Sections". In: *Sustainability* 12.12, p. 4852.

Kim, J. J., K.-S. Youm, and M. M. Reda Taha (2014). "Extracting Concrete Thermal Characteristics from Temperature Time History of RC Column Exposed to Standard Fire". en. In: *The Scientific World Journal* 2014.1. kothra kothr, p. 242806.

Kim, K.-H., S.-E. Jeon, J.-K. Kim, and S. Yang (Mar. 2003). "An experimental study on thermal conductivity of concrete". In: *Cement and Concrete Research* 33.3, pp. 363–371.

Kim, W., K. Jeong, T. Lee, and S.-G. Park (2022). "A Study on Correlation Between Ultrasonic Pulse Velocity Method and Coarse Aggregate for Estimating Residual Modulus

of Elasticity of Concrete Exposed to High Temperatures". In: *Applied Sciences* 12.13, p. 6644.

Kodur, V. (2014). "Properties of Concrete at Elevated Temperatures". In: *Isrn Civil Engineering* 2014, pp. 1–15.

Kodur, V. and M. A. Sultan (2003). "Effect of Temperature on Thermal Properties of High-Strength Concrete". In: *Journal of Materials in Civil Engineering* 15.2, pp. 101–107.

Kothandaraman, C. P. (2006). *Fundamentals of Heat and Mass Transfer*. en. New Age International.

Kovler, K. and S. Zhutovsky (Nov. 2006). "Overview and Future Trends of Shrinkage Research". en. In: *Materials and Structures* 39.9, pp. 827–847.

Kumar, K. R., V. Sivakumar, Y. Yin, et al. (2014). "Long-Term (2003–2013) Climatological Trends and Variations in Aerosol Optical Parameters Retrieved From MODIS Over Three Stations in South Africa". In: *Atmospheric Environment* 95, pp. 400–408.

Kumar, K. R., R. Boiyo, R. Khan, et al. (July 2020). "Multi-year analysis of aerosol optical properties and implications to radiative forcing over urban Pretoria, South Africa". en. In: *Theoretical and Applied Climatology* 141.1, pp. 343–357.

Lee, J. Y., J. S. Choi, T. Yuan, Y. S. Yoon, and D. Mitchell (2019). "Comparing Properties of Concrete Containing Electric Arc Furnace Slag and Granulated Blast Furnace Slag". In: *Materials* 12.9, p. 1371.

Lee, T. G., G.-Y. Kim, Y. S. Kim, and G. Y. Park (2011). "Mechanical Properties of Concrete With Aggregate Type at Elevated Temperature". In: *Advanced Materials Research* 311-313, pp. 1840–1846.

Li, G. (2019). "Formation of Temperature Cracks of Concrete in High-Rise Buildings and the Corresponding Measures". In: *Archives of Civil Engineering* 65.4, pp. 177–188.

Li, Q., L. Liu, Z. Huang, and G. Yuan (2018). "Degradation of the Elastic Modulus of Cement-Based Grouting Material With Early Ages After Fire". In: *Construction and Building Materials* 187, pp. 510–518.

Li, Q., H. Sun, M. Wang, and P. Liu (2021). "Effects of Moisture Content and Heating Temperature on the Thermal Expansion Deformation of Concrete". In: *Structural Concrete* 23.4, pp. 2301–2312.

Li, S. C., T. Yao, Y. J. Wang, et al. (2014). "Determination of Tensile Creep and Stress Relaxation of Concrete by Ring Test". In: *Applied Mechanics and Materials* 584-586, pp. 1172–1175.

Li, S., J. Liu, C. Cui, Z. Yu, Z. Fan, and J. Hou (2020). "Carbonation Process of Reinforced Concrete Beams Under the Combined Effects of Fatigue Damage and Environmental Factors". In: *Applied Sciences* 10.11, p. 3981.

Li, W., W. Sun, and J. Jiang (2012). "Damage of Concrete Subjected to Simultaneous Fatigue Load and Thermal Effect". In: *Magazine of Concrete Research* 64.1, pp. 35–42.

Li, X., J. Taylor, and P. Symonds (2019). "Indoor Overheating and Mitigation of Converted Lofts in London, UK". In: *Building Services Engineering Research and Technology* 40.4, pp. 409–425.

Liang, Y. (2024). "Analysis of Thermal Behavior of Prestressed Double T Beam Made of Sustainable Carbon-Capturing Concrete". In: p. 26.

Liang, Z., H. Zhou, C. Zhao, F. Wang, and Y. Zhou (June 2023). "Experimental and Numerical Study of the Influence of Solar Radiation on the Surface Temperature Field of Low-Heat Concrete in a Pouring Block". en. In: *Buildings* 13.6, p. 1519.

Liu, L. and J. C. Wang (Jan. 2022). "Test and Calculation Model of Thermal Conductivity of Concrete". In: *Key Engineering Materials* 905, pp. 314–319.

Lu, Y., D. Li, K. Wang, and S. Jia (Jan. 2021). "Study on Solar Radiation and the Extreme Thermal Effect on Concrete Box Girder Bridges". en. In: *Applied Sciences* 11.14. Number: 14 Publisher: Multidisciplinary Digital Publishing Institute, p. 6332.

Lu, Y., Y. Qin, C. Huang, and X. Pang (Jan. 2023). "Albedo of Pervious Concrete and Its Implications for Mitigating Urban Heat Island". en. In: *Sustainability* 15.10. Number: 10 Publisher: Multidisciplinary Digital Publishing Institute, p. 8222.

Manandhar, S., S. Dev, Y. H. Lee, S. Winkler, and Y. S. Meng (July 2018). "Systematic Study of Weather Variables for Rainfall Detection". In: *IGARSS 2018 - 2018 IEEE International Geoscience and Remote Sensing Symposium*. ISSN: 2153-7003, pp. 3027–3030.

Mehta, P. K. and P. J. M. Monteiro (2014). *Concrete: Microstructure, Properties, and Materials*. en. 4th Edition. New York: McGraw-Hill Education.

Michael, P. R., D. E. Johnston, and W. Moreno (Dec. 2020). "A conversion guide: solar irradiance and lux illuminance". en. In: *Journal of Measurements in Engineering* 8.4. Number: 4 Publisher: JVE International Ltd., pp. 153–166.

Min, H. G., W. P. Zhang, and X. L. Gu (2016). "Experimental Study on Temperature Response in Damaged Concrete Under Atmospheric Environment". In: *Key Engineering Materials* 711, pp. 404–411.

Montgomery, D. C. and G. C. Runger (Mar. 2010). *Applied Statistics and Probability for Engineers*. en. John Wiley & Sons.

Mosley, B., R. Hulse, and J. Bungey (Apr. 2012). *Reinforced Concrete Design: to Eurocode 2*. English. 7th edition. Basingstoke: Red Globe Press.

Moustris, K. P., I. C. Ziomas, and A. G. Paliatsos (June 2010). "3-Day-Ahead Forecasting of Regional Pollution Index for the Pollutants NO2, CO, SO2, and O3 Using Artificial Neural Networks in Athens, Greece". In: *Water, Air, & Soil Pollution* 209.1, pp. 29–43.

Murphy, K. D., J. S. McCartney, and K. S. Henry (2014). "Impact of Horizontal Run-Out Length on the Thermal Response of Full-Scale Energy Foundations". In: pp. 2715–2724.

Naik, T. R., R. N. Kraus, and R. Kumar (2011). "Influence of Types of Coarse Aggregates on the Coefficient of Thermal Expansion of Concrete". In: *Journal of Materials in Civil Engineering* 23.4, pp. 467–472.

Namiki, S., T. Iino, and Y. Okamoto (2020). "Evaluation of Localized Heat Transfer Coefficient for Induction Heating Apparatus by Thermal Fluid Analysis Based on the HSMAC Method". In: *Open Physics* 18.1, pp. 504–511.

Naterer, G. F. (Aug. 2002). *Heat Transfer in Single and Multiphase Systems*. Boca Raton: CRC Press.

Neville, A. M. (Sept. 2012). *Properties of Concrete: Fith Edition*. en. Wiley.

Norouzi, M., Seyed Ehsan Haji Agha Mohammad Zarbaf, A. Dalvi, V. J. Hunt, and A. J. Helmicki (2016). "A Study of Thermal Response of Concrete Towers Employing Linear Regression". In: 9804, 98040G.

Omega Test House (2022). *SANS 8301:2010 Thermal Insulation Test – Thermal Conductivity*. Test Report OTH-T-2204-01B. Omega Test House, Wierdapark, Centurion, p. 4.

Pan, J., R. Zou, and F. Jin (Jan. 2017). "Experimental Study on Specific Heat of Concrete at High Temperatures and Its Influence on Thermal Energy Storage". en. In: *Energies* 10.1. Number: 1 Publisher: Multidisciplinary Digital Publishing Institute, p. 33.

Pan, Z., D. Cao, B. Zeng, and Y. Wang (2022). "Nonlinear Creep Amplification Factor Considering Damage Evolution of Concrete Under Compression". In: *Materials* 15.19, p. 6742.

Park, S. S., S.-J. Kwon, and H. Song (2010). "Analysis Technique for Restrained Shrinkage of Concrete Containing Chlorides". In: *Materials and Structures* 44.2, pp. 475–486.

Pavlů, T., K. Fořtová, J. Diviš, and P. Hájek (2019). "The Utilization of Recycled Masonry Aggregate and Recycled EPS for Concrete Blocks for Mortarless Masonry". In: *Materials* 12.12, p. 1923.

Porges, F. (Dec. 2000). *HVAC Engineer's Handbook*. 11th ed. London: Routledge.

Potgieter, I. C. and W. Gamble (Apr. 1983). "Response of Highway Bridges to Nonlinear Temperature Distributions. Civil Engineering Studies. Final Report". In.

Prata, J., A. Tadeu, and N. Simões (2012). "Three-Dimensional Boundary Element Method Model in the Frequency Domain for Simulating Dynamic Heat Conduction". In.

Qahtan, A. and A. H. M. Almawgani (2022). "Experimental Evaluation of Thermal and Lighting Performance Using Double Dynamic Insulated Glazing". In: *Buildings* 12.8, p. 1249.

Qin, Y., C. Huang, and X. Pang (2023). "Albedo of Pervious Concrete and Its Implications for Mitigating Urban Heat Island". In: *Sustainability* 15.10, p. 8222.

Raheem, A. A., B. D. Ikotun, and S. O. Akinloye (2021). "Effects of Granite Sourced From Selected Locations in Ogbomoso, Nigeria on the Properties of Concrete". In: *Advances in Science and Technology* 107, pp. 113–121.

Ramachandran, V. S. (Dec. 1996). *Concrete Admixtures Handbook: Properties, Science and Technology*. en. thermal. William Andrew.

Remer, L. A., Y. J. Kaufman, D. Tanré, et al. (Apr. 2005). "The MODIS Aerosol Algorithm, Products, and Validation". en. In: Section: Journal of the Atmospheric Sciences.

Ren, X., Y. Ding, Q. Liu, S. Chen, and F. Song (Sept. 2022). "Effect of different volume fraction of steel fiber/graphite on thermal conductivity and compressive properties of concrete". In: *Frontiers in Materials* 9, p. 1003830.

Rezaei, H., B. Kayan, I. Asadi, and Z. Abu Hassan (Sept. 2020). "Investigation of Thermal Properties of Normal Weight Concrete for Different Strength Classes". In.

Richard, C., G. Doré, C. Lemieux, J.-P. Bilodeau, and J. Haure-Touzé (2015). "Albedo of Pavement Surfacing Materials: In Situ Measurements". In: pp. 181–192.

Rivera-Salinas, J.-E., K.-M. Gregorio-Jáuregui, H.-A. Fonseca-Florido, et al. (May 2021). "Numerical Study Using Microstructure Based Finite Element Modeling of the Onset of Convective Heat Transfer in Closed-Cell Polymeric Foam". en. In: *Polymers* 13.11, p. 1769.

RST Instruments LTD (2019). *Vibrating Wire Embedment Strain Gauge (VWSG-E) Manual*. Canada: RST Instruments LTD.

Ruano, G. (2024). "On the Effect of Thermal Expansion Coefficient in Prestressed Concrete Beams". In.

Sakata, K. and T. Shimomura (2004). "Recent Progress in Research on and Code Evaluation of Concrete Creep and Shrinkage in Japan". en. In: *Journal of Advanced Concrete Technology* 2.2, pp. 133–140.

Šarler, B. and D. W. Pepper (2004). "Application of Meshless Methods for Thermal Analysis". In.

Seeed Technology Co., Ltd (2022). *SenseCAP S2120 LoRaWAN 8-in-1 Weather Station User Guide*. Vol. 1.0.3. Seeed Technology Co., Ltd.

Shahedan, N. F., N. Mahmed, A. Kusbiantoro, M. Binhussain, and S. N. Zailan (2017). "Review on Thermal Insulation Performance in Various Type of Concrete". In.

Sheng, X., Y. Yang, W. Zheng, B. Zhou, S. Li, and L. Huang (2020). "Study on the Time-Varying Temperature Field of Small Radius Curved Concrete Box Girder Bridges". In: *Aip Advances* 10.10.

Sheng, X., T. Shi, W. Zheng, and P. Lou (Feb. 2022). "Time-varying non-uniform temperature distributions in concrete box girders caused by solar radiation in various regions in China". en. In: *Advances in Mechanical Engineering* 14.2. Publisher: SAGE Publications, p. 16878140221076458.

Silliman, K. R. and C. M. Newtson (2006). "Effect of Misting Rate on Concrete Shrinkage". en-US. In.

Skorpen, S. A., E. P. Kearsley, C. R. I. Clayton, and E. J. Kruger (Sept. 2020). "Structural monitoring of an integral bridge in South Africa". In: *Proceedings of the Institution of Civil Engineers - Smart Infrastructure and Construction* 173.3. Publisher: ICE Publishing, pp. 63–72.

Somerton, W. H. (Mar. 1992). *Thermal Properties and Temperature-Related Behavior of Rock/Fluid Systems*. en. Elsevier.

South African National Standard (2000). *SANS 10100-1:2000 The structural use of concrete: Part 1: Design*. Pretoria: The South African Bureau of Standards.

South African National Standard (2006a). *SANS 5863:2006 Concrete tests- Compressive strength of hardened concrete*. Pretoria: The South African Bureau of Standards.

South African National Standard (2006b). *SANS 6253:2006 Concrete tests- Tensile splitting strength of concrete*. Pretoria: The South African Bureau of Standards.

Stephen, H., S. Ahmad, and T. Piechota (Jan. 2010). "Land Surface Brightness Temperature Modeling Using Solar Insolation". In: *Geoscience and Remote Sensing, IEEE Transactions on* 48, pp. 491–498.

Sun, R. W. and G. Fanourakis (2021). "An Assessment of Factors Affecting the Elastic Modulus of Concrete". In: *Structural Concrete* 23.1, pp. 593–603.

Tatro, S. (Jan. 2006). "Chapter 22: Thermal Properties". In: *Significance of Tests and Properties of Concrete and Concrete-Making Materials*. Ed. by J. Lamond and J. Pielert. Vol. STP169D-EB. ASTM International, p. 0.

Tayşi, N. and S. Abid (Apr. 2015). "Temperature Distributions and Variations in Concrete Box-Girder Bridges: Experimental and Finite Element Parametric Studies". en. In: *Advances in Structural Engineering* 18.4. Publisher: SAGE Publications Ltd STM, pp. 469–486.

Tesfaye, M., V. Sivakumar, J. O. Botai, and G. M. Tsidu (2011). "Aerosol Climatology Over South Africa Based on 10 Years of Multiangle Imaging Spectroradiometer (MISR) Data". In: *Journal of Geophysical Research Atmospheres* 116.D20.

Thekaekara, M. P. and A. J. Drummond (Jan. 1971). "Standard Values for the Solar Constant and its Spectral Components". en. In: *Nature Physical Science* 229.1. Publisher: Nature Publishing Group, pp. 6–9.

Turns, S. R. and D. R. Kraige (2007). *Property tables for thermal fluids engineering: SI and U.S. customary units*. eng. OCLC: 181079272. New York, NY: Cambridge University Press.

Wang, H., H. A. Mang, Y. Yuan, and B. Pichler (2019). "Multiscale Thermoelastic Analysis of the Thermal Expansion Coefficient and of Microscopic Thermal Stresses of Mature Concrete". In: *Materials* 12.17, p. 2689.

Wang, Q., J. Xian, X. Jun, and S. Zou (2023). "Simulation Study on Sunshine Temperature Field of a Concrete Box Girder of the Cable-Stayed Bridge". In: *Sustainability* 15.9, p. 7541.

Wang, X.-Y., H.-K. Cho, and H.-S. Lee (Jan. 2011a). "Prediction of temperature distribution in concrete incorporating fly ash or slag using a hydration model". In: *Composites Part B: Engineering* 42.1, pp. 27–40.

Wang, X., M. G. Stewart, and M. Nguyen (2011b). "Impact of Climate Change on Corrosion and Damage to Concrete Infrastructure in Australia". In: *Climatic Change* 110.3-4, pp. 941–957.

Weiss, W. J. (Nov. 1999). "Prediction of early-age shrinkage cracking in concrete elements". PhD thesis.

Welty, J., C. E. Wicks, G. L. Rorrer, and R. E. Wilson (Nov. 2007). *Fundamentals of Momentum, Heat and Mass Transfer*. English. 5th edition. Hoboken, NJ: Wiley.

Westgate, R., K.-Y. Koo, and J. Brownjohn (May 2015). "Effect of Solar Radiation on Suspension Bridge Performance". en. In: *Journal of Bridge Engineering* 20.5. Publisher: American Society of Civil Engineers, p. 04014077.

Whitaker, S. (1977). *Fundamental Principles of Heat Transfer*. en. Elsevier Science & Technology Books.

Wu, H., Z. Liu, Y. Yang, and S. Bai (2017). "Characterizing Thermal Impacts of Pavement Materials on Urban Heat Island (UHI) Effect". In: *Destech Transactions on Engineering and Technology Research* ictim.

Xie, W., Y. Jin, and S. S. Li (2012). "Experimental Research on the Influence of Grain Size of Coarse Aggregate on Pebble Concrete Compressive Strength". In: *Applied Mechanics and Materials* 238, pp. 133–137.

Xu, Q. and M. Solaimanian (Apr. 2010). "Modeling temperature distribution and thermal property of asphalt concrete for laboratory testing applications". In: *Construction and Building Materials* 24, pp. 487–497.

Yan, E. (2014). "Finding Knowledge Paths Among Scientific Disciplines". In: *Journal of the Association for Information Science and Technology* 65.11, pp. 2331–2347.

Yang, W.-J., P. Li, L. Zhuo, M.-L. Pang, H.-Q. Xie, and M.-L. Xiao (2024). "Analytical and experimental analysis of concrete temperature and energy considering open-air environmental variations". en. In: *Scientific Reports* 14.1.

Yang, W., M. Pang, H. Xie, M. Xiao, J. Pei, and L. Zhuo (Jan. 2023). "Investigation and Analysis of the Influence of Environmental Factors on the Temperature Distribution of Thin-Walled Concrete". en. In: *Applied Sciences* 13.22. Number: 22 Publisher: Multidisciplinary Digital Publishing Institute, p. 12157.

Yeon, J. H., S. Choi, and M. C. Won (Jan. 2009). "Effect of Relative Humidity on Coefficient of Thermal Expansion of Hardened Cement Paste and Concrete". en. In: *Transportation Research Record* 2113.1. Publisher: SAGE Publications Inc, pp. 83–91.

Yeon, J. H., S. Choi, and M. C. Won (Jan. 2013). "In situ measurement of coefficient of thermal expansion in hardening concrete and its effect on thermal stress development". In: *Construction and Building Materials*. 25th Anniversary Session for ACI 228 – Building on the Past for the Future of NDT of Concrete 38, pp. 306–315.

Yu, Z., F. Zhao, X. Ma, F. Yang, D. Hu, and H. Zhou (2021). "Experimental Study on Thermal Expansion Behavior of Concrete Under Three-Dimensional Stress". In: *Advances in Civil Engineering* 2021.1.

Yuan, M., Q. Shen, Y. Xu, Y. Liu, and W. Xu (2021). "Research on Cracking Mechanism of Early-Age Restrained Concrete Under High-Temperature and Low-Humidity Environment". In: *Materials* 14.15, p. 4084.

Yun, T. S., Y.-I. Jeong, and K. S. Youm (2014). "Effect of Surrogate Aggregates on the Thermal Conductivity of Concrete at Ambient and Elevated Temperatures". In: *The Scientific World Journal* 2014, pp. 1–9.

Zehfuß, J., F. Robert, J. Spille, and R. N. Razafinjato (2020). "Evaluation of Eurocode 2 Approaches for Thermal Conductivity of Concrete in Case of Fire". In: *Civil Engineering Design* 2.3, pp. 58–71.

Zeng, H., C. Lu, L. Zhang, et al. (Jan. 2022). "Prediction of Temperature Distribution in Concrete under Variable Environmental Factors through a Three-Dimensional Heat Transfer Model". en. In: *Materials* 15.4. Number: 4 Publisher: Multidisciplinary Digital Publishing Institute, p. 1510.

Zhang, B. and C. S. Poon (2015). "Use of Furnace Bottom Ash for Producing Lightweight Aggregate Concrete With Thermal Insulation Properties". In: *Journal of Cleaner Production* 99, pp. 94–100.

Zhang, C., Y. Liu, J. Liu, Z. Yuan, G. Zhang, and Z. Ma (Oct. 2020a). "Validation of long-term temperature simulations in a steel-concrete composite girder". In: *Structures* 27, pp. 1962–1976.

Zhang, C., Z. Zhu, S. Zhu, et al. (2019). "Nonlinear Creep Damage Constitutive Model of Concrete Based on Fractional Calculus Theory". In: *Materials* 12.9, p. 1505.

Zhang, R., G. Jiang, and L. Jia (2015). "The Albedo of Pervious Cement Concrete Linearly Decreases With Porosity". In: *Advances in Materials Science and Engineering* 2015, pp. 1–5.

Zhang, W., M. Zakaria, and Y. Hama (2013). "Influence of Aggregate Materials Characteristics on the Drying Shrinkage Properties of Mortar and Concrete". In: *Construction and Building Materials* 49, pp. 500–510.

Zhang, Y. and Y. Jiang (Mar. 1999). "A simple method, the T-history method, of determining the heat of fusion, specific heat and thermal conductivity of phase-change materials". In: *Measurement Science and Technology* 10, p. 201.

Zhang, Y. (2021). "Modeling of Thermal Expansion Characteristics of Concrete in Agricultural Water Conservancy Projects". In: *Arabian Journal of Geosciences* 14.7.

Zhang, Y., C. Mao, J. Wang, Y. Gao, and J. Zhang (2020b). "Sustainability of Reinforced Concrete Beams With/Without BF Influenced by Cracking Capacity and Chloride Diffusion". In: *Sustainability* 12.3, p. 1054.

Zhao, Y., G. Li, C. Fan, W. Pang, and Y. Wang (Mar. 2021). "Effect of Thermal Parameters on Hydration Heat Temperature and Thermal Stress of Mass Concrete". en. In: *Advances in Materials Science and Engineering* 2021. Publisher: Hindawi, e5541181.

Zheng, S. (2023). "Enhancing Bridge Structural Stability: A Comprehensive Analysis of Thermodynamic Properties and Thermal Stress Performance". In: *International Journal of Heat and Technology* 41.3, pp. 761–768.

Zhou, F., C. Su, D. Wu, et al. (2022). "Concrete Elastic Modulus Experimental Research Based on Theory of Capillary Tension". In: *Materials* 15.10, p. 3734.

Zhu, L. (2024). "Experimental and Numerical Study on the Thermal Response of the Lightweight Aggregate Concrete Panels Integrated With MPCM". In: *Buildings* 14.1, p. 234.

Zienkiewicz, O. and J. Zhu (Jan. 2005). *The Finite Element Method: Its Basis and Fundamentals*. Vol. I. Journal Abbreviation: The Finite Element Method: its Basis and Fundamentals: Seventh Edition Publication Title: The Finite Element Method: its Basis and Fundamentals: Seventh Edition.